Investigation and Optimisation of an Array-on-device configuration for a Novel Wave Energy Converter

by

Emilio Faraggiana

Submitted to Swansea University
in fulfilment of the requirements for the Degree of

Doctor of Philosophy

at

Swansea University

2019

Declaration

This work has not previously been accepted in substance for any degree and is not being concurrently submitted in candidature for any degree.

Signed: ..... (candidate)

Date: .....

Statement 1

This thesis is the result of my own investigations, except where otherwise stated and that other sources are acknowledged by footnotes giving explicit references and that a bibliography is appended.

Signed: ..... (candidate)

Date: .....

Statement 2

I hereby give consent for my thesis, if accepted, to be made available online in the University's Open Access Repository and for inter-library loan after expiry of the bar on access, and for the title and summary to be made available to outside organisations.

Signed: ..... (candidate)

Date: .....

Acknowledgements

My first sincere gratitude is to my supervisor Ian Masters for guiding me and having the patience to help me during the problems faced during the PhD.
This work is part-funded by the European Social Fund (ESF) through the European Union's Convergence programme administered by the Welsh Government.
I would like to thank Marine Power Systems (MPS) for giving me the opportunity to work in a company environment. My lot of thanks is especially for John Chapman that helped me significantly in the problem solving and brainstorming during my research project. I have also really appreciated the time spent with the MPS team.
I would also express my friendly gratitude to my colleagues of the marine and coastal engineering group. My special thanks is to my friend Thomas that was sharing with me trekking adventures enabling me to discover the wonderful welsh landscape.
My enormous thank is to my mum for giving me helpful advice and to be very supportive.
Finally and most importantly I would like to thank my wife Sky for the wonderful time spent together and for let me understand the deep sense of life.

From the darkness towards the kingdom of the discoveries

Abstract

Wave energy has a huge potential to satisfy the global electricity demand from a renewable source. Many Wave Energy Converters (WECs) have been designed to harvest energy from sea waves but, to date, they cannot compete on the commercial energy market. However, the WaveSub, which is a point absorber developed by Marine power Systems Ltd, has a great potential to become one of the most promising future ways of wave energy extraction.

This research project aims to develop and validate a numerical model of a multi-float configuration of the WaveSub device, followed by an optimisation of the design parameters to minimize the Levelized Cost Of Energy (LCOE). The numerical methodology is based on open-source codes but a careful comparison with commercial codes has been considered demonstrating a good agreement between them. Then, the numerical model has been extended to include multi-directional waves. An important step of this research project has been the benchmarking of the numerical model with tank testing. The comparison was satisfactory with a relative mean total power difference between tank and model of around 10%. Finally, the optimisation of multi-float configurations have been investigated. A genetic algorithm combined with the Kriging surrogate model was mainly used to optimise the LCOE. The number of floats of a linear multi-float configuration has been optimised showing that a 6 float one decreases the LCOE by 21% compared to a single one. Then a linear, rectangular, triangular and circular 6 multi-float configurations were compared showing the circular one as the most competitive with a LCOE reduction around 12% relative to the worst configuration.

This work is a starting point for a more extended study of multi-float configurations, which can include more floats and complex geometries. These results will help to develop a future multi-float WaveSub design, which can harvest renewable energy competitively.

Author's publications

Journal publications

- Faraggiana E, Whitlam C, Chapman J, Hillis A, Roesner J, Hann M, Greaves D, Yu YH, Ruehl K, Masters I, Foster G, Stockman G. Computational modelling and experimental tank testing of the multi float WaveSub under regular wave forcing. Renewable Energy, 2020.

- Faraggiana E, Chapman J, Williams AJ, Masters I. Genetic based optimization of the design parameters for an array on device orbital motion wave energy converter. Paper submitted to the Ocean Engineering Journal and currently under review.

Conference publications

- Faraggiana E, Masters I, Chapman J, Foster G, Stockman G. Multi-directional waves and time domain perturbed field visualization of the WaveSub device. EWTEC 2019 Conference Proceedings.

- Faraggiana E, Masters I, Chapman J. Design of an optimization scheme for the WaveSub array. RENEW 2018 Conference Proceedings.

Contents

List of Figures

List of Tables

Nomenclature

Roman symbols		
Symbols	**Description**	**Units**
$\mathbf{A}$	Added mass matrix	kg
A	Added mass coefficient	kg
$\mathbf{A}_\infty$	Infinite added mass matrix	kg
A_∞	Infinite added mass coefficient	kg
A_D	Diffraction amplitude	m
$\mathbf{A_{Drag}}$	Drag characteristic area vector	m^2
A_I	Incident wave amplitude	m
A_R	Radiation amplitude	m
$Areaxy$	Reactor projection area on the xy plane	m^2
$AreaxyMin$	Reactor projection area on the xy plane referred to the smallest float spacing considered	m^2
$\mathbf{B}$	Radiation damping matrix	Nsm^{-1}
$BaselineMframeReactor$	Baseline frame mass of the reactor	kg
$BaselineMsubsystem$	Baseline mass of the subsystem of the reactor	kg
$BaselineNetBuoyancyReactor$	Baseline net buoyancy of the reactor	kg
$BaselineRL$	Baseline reactor length	m
c	Damping coefficient	Nsm^{-1}
$\mathbf{C_D}$	Drag coefficient vector	–
C_D	Drag coefficient	–
c_{ph}	Phase velocity	ms^{-1}
$\mathbf{C_{PTO}}$	PTO damping matrix	Nsm^{-1}
C_{PTO}	PTO damping coefficient	Nsm^{-1}
$c1$	Personal learning coefficient	–

Roman symbols		
Symbols	**Description**	**Units**
$c2$	Global learning coefficient	–
$CAPEX$	CAPital EXpenditure	£
$Cash$	Cash flow	£
$Cost_{Primary}$	Cost of the primary transmission of an hydraulic PTO	£
$Cost_{PTO}$	Cost of the PTO	£
$Cost_{Secondary/Storage}$	Cost of the secondary transmission/energy storage of an hydraulic PTO	£
$Cost_{SpecificRatedPower}$	Specific cost of the rated power of the PTO	£
d	Water depth	m
$D(\beta)$	Directional distribution	rad
D_{PTO}	Diameter of the PTO motor	m
$DECOM$	Decomissioning cost	£
E	Energy produced	kWh
$\overline{E}_{kinetic}$	Mean wave kinetic energy per metre of wave front	$kWhm^{-1}$
$\overline{E}_{potential}$	Mean wave potential energy per metre of wave front	$kWhm^{-1}$
$\overline{E}_{potential}$	Mean wave potential energy per metre of wave front	$kWhm^{-1}$
$\overline{E}_{w}$	Mean wave energy per metre of wave front	$kWhm^{-1}$
EP_{year}	Energy produced in an year	kWh
f	Wave frequency	Hz
$\mathbf{F_{MF}}$	Mechanical friction force vector	N
$\mathbf{F_{Coriolis}}$	Coriolis force vector	N
$\mathbf{F_{d}}$	Diffraction force vector	N
$\mathbf{F_{es}}$	End stop force vector of the PTO mechanism	N
$\mathbf{F_{ex}}$	Excitation force vector	N
F_{ex}	Excitation force written in a complex notation	N
$\mathbf{F_{F-K}}$	Froude-Krylov force vector	N
F_g	Gravitational force	N
$\mathbf{F_{H}}$	Hydrostatic force vector	N
F_i	Inertial force	N
$\mathbf{F_{M}}$	Mooring force vector	N
$\mathbf{F_{PTO}}$	PTO force vector	N

Roman symbols		
Symbols	**Description**	**Units**
$\mathbf{F_{rad}}$	Radiation force vector	N
$\mathbf{F_V}$	Viscous force vector	N
FNM	Float number multiplier	–
Fr	Froude number	–
FS	Float spacing	m
FSM	Float spacing multiplier	–
$\mathbf{g}$	Acceleration of gravity vector	ms^{-2}
g	Acceleration of gravity constant	ms^{-2}
gen	Number of generations	–
H	Wave height	m
$h_r(t)$	Impulse response function	Nm^{-1}
H_s	Significant wave height	m
I_{hu}	Inertia fluid coefficient for an hydraulic PTO	kgm^{-4}
IE	Incident energy	$kWhm^{-1}$
IRR	Internal rate of return	%
k	Wave number	m^{-1}
k_{ploss}	Coefficient of pressure loss in an hydraulic circuit	kgm^{-7}
K_d	Disturbance coefficient	–
$\mathbf{K_H}$	Linear restoring matrix	Nm^{-1}
$\mathbf{K_M}$	Mooring stiffness matrix	Nm^{-1}
$\mathbf{K_{PTO}}$	PTO stiffness matrix	Nm^{-1}
KC	Keulegan-Carpenter number	–
l	Characteristic length	m
L_{abs}	Absorption length	m
L_{Spring}	Load on the spring	N
L_{Tank}	Longitudinal length of the tank	m
$L_{Tank-ts}$	Transversal size of the cross-sectional area of the tanks	m
L_{ts}	Length of the time series	–
$LCOE$	Levelized Cost Of Energy	$£(kWh)^{-1}$
$\mathbf{M}$	Mass matrix	kg
M_{drag}	Drag momentum	Nm
M_F	Mass of the float	kg
M_{Fd}	Displaced mass of the float	kg
M_m	Numerical model motion amplitude	m
m_n	Spectral moment	$m^2 \cdot s^{-n}$

Roman symbols		
Symbols	**Description**	**Units**
M_R	Mass of the reactor	kg
M_{Rdb}	Baseline displaced mass of the reactor	kg
M_T	Tank motion amplitude	m
MAX	Maximum error	–
$MframeReactor_{Buoyancy}$	Buoyancy mass of the frame of the reactor	kg
$MframeReactor_{dryMass}$	Dry mass of the frame of the reactor	kg
MIR	Maintenance inflation rate	%
$Msubsystem_{Buoyancy}$	Buoyancy mass of the subsystem of the reactor	kg
$Msubsystem_{dryMass}$	Dry mass of the subsystem of the reactor	kg
$Mtank_{Buoyancy}$	Buoyancy mass of the tank of the reactor	kg
$Mtank_{dryMass}$	Dry mass of the tank of the reactor	kg
n	Unit vector	–
N_{OM}	Number of oscillatory modes	–
N_d	Number of directions	rad
N_{DOF}	Number of degrees of freedom	–
N_f	Number of frequencies	–
n_p	Number of points	–
NBM	Net Buoyancy Multiplier	–
NDR	Nominal Discount Rate	%
$NetBuoyancyReactor$	Net buoyancy of the reactor	kg
NF	Number of factors (Taguchi DOE)	–
$nfloats$	Number of floats	–
NPV	Net Present Value	£
$NRMSE$	Normalized Root Mean Square Error	%
$Ntanks$	Number of tanks of the reactor	–
O	Occurrence of a sea state	%
$OPEX$	OPerating EXpenditure	£
p	Fluid pressure	Pa
P_{Best}	Best position of the particle	–
P_{Old}	Old position of the particle	–
P_{Rated}	Rated power	kW
$\overline{P}_{abs}$	Mean absorbed power	kW

Roman symbols		
Symbols	**Description**	**Units**
P_{ex}	Excitation pressure	Pa
$\overline{P}_I$	Incident wave power per metre of wave front	kW/m
$\overline{P}_m$	Numerical model mean power	kW
P_{rad}	Radiation pressure	Pa
$\overline{P}_T$	Tank mean power	kW
P_{tank}	Mechanical power from the tank testing	kW
PIR	Profit Investment Ratio	%
PLT	Project life time	$years$
PVF_D	Present value factor of the decommissioning cost	–
PVF_E	Present value factor of the energy produced	–
PVF_{OP}	Present value factor of the operating cost	–
q	WEC array interaction factor	–
q_{flow}	Volume flow rate of the fluid of an hydraulic PTO	m^3/s
Ql	Number of levels for the Taguchi DOE	–
r	Discount rate	%
r_{RBF}	Distance expressed by an Euclidean form (RBF surrogate model)	–
R_{tank}	Radius of the tank of the reactor	m
RAO	Response Amplitude Operator vector	–
Re	Reynolds number	–
RL	Reactor length	m
RW	Reactor width	m
$S(f)$	Wave frequency spectrum	m^2s
$S(f,\beta)$	Wave frequency-directional spectrum	m^2srad^{-1}
S_b	Wave density spectrum	m^2s
S_c	Wave density spectrum	m^2s
SFL	Wave density spectrum	m^2s
SM	Wave density spectrum	m^2s
SNB_b	Baseline system net buoyancy	kg
t	Time	s

Roman symbols		
Symbols	**Description**	**Units**
T	Wave period	s
T_e	Mean energy period	s
T_{sim}	Duration of the simulation	s
T_{PTO}	Torque of the PTO	Nm
$T1$	Pre-load force applied on the mooring attachment point in the front of the triangle multi-float configuration	N
$T2$	Pre-load force applied on the mooring attachment point in the back of the triangle multi-float configuration	N
U	Flow velocity written in a complex notation	ms^{-1}
$\mathbf{u}$	Flow velocity vector	ms^{-1}
u	Flow velocity	ms^{-1}
V	Amplitude of the body velocity	ms^{-1}
$\mathbf{v}$	Body velocity vector	ms^{-1}
$\mathbf{v_{PTOline}}$	Velocity of the PTO line vector	ms^{-1}
$v_{PTOline}$	Velocity of the PTO line	ms^{-1}
v_g	Group velocity	ms^{-1}
v_p	Velocity of the particle (PSO algorithm)	–
$w_{inertia}$	Inertia term of the particle (PSO algorithm)	–
$\mathbf{X}$	Body position vector	m
$\dot{\mathbf{X}}$	Body velocity vector	ms^{-1}
$\ddot{\mathbf{X}}$	Body acceleration vector	ms^{-2}
X_c	Device motion written in a complex notation	m
x_{MSpac}	x spacing of the mooring attachment on the seabed	m
x_R	x coordinate of the mooring attachment point on the reactor.	m
x_S	x coordinate of the mooring attachment point on the seabed.	m
xd_{min}	Combination of design parameters that minimize the objective function (GA algorithm)	–

Roman symbols		
Symbols	**Description**	**Units**
$xd_{NewPoint}$	Combination of design parameters of the new point (GA algorithm)	–
xd_{range}	Searching space of the design variables (GA algorithm)	–
y_{MSpac}	y spacing of the mooring attachment on the seabed	m
y_i	Real value of the response	–
$\hat{y}_i$	Predicted value of the response	–
y_R	y coordinate of the mooring attachment point on the reactor.	m
y_S	y coordinate of the mooring attachment point on the seabed.	m
z	Vertical coordinate	m

Greek symbols		
Symbols	**Description**	**Units**
β	Wave/flow direction	rad
$\Gamma(\omega)$	Excitation force coefficient vector	Nm^{-1}
ϵ	Strain of the spring	–
η_D	Diffracted water free surface elevation	m
η_I	Incident water free surface elevation	m
η_P	Perturbed water free surface elevation	m
η_R	Radiated water free surface elevation	m
λ	Water wave length	m
μ	Dynamic viscosity	$kgm^{-1}s^{-1}$
ν	Kinematic viscosity	m^2s^{-1}
ρ	Fluid density	kgm^{-3}
ρ_w	Water density	kgm^{-3}
σ	Wave directional spread	rad
τ_0	Local shear stress on the body	Pa
ϕ	Velocity potential	m^2s^{-1}
ϕ_d	Diffraction velocity potential	m^2s^{-1}
ϕ_D	Diffraction wave phase	rad
φ	Excitation phase angle	rad
ϕ_i	Incident velocity potential	m^2s^{-1}
ϕ_I	Incident wave phase	rad
ϕ_r	Radiation velocity potential	m^2s^{-1}
ϕ_R	Radiation wave phase	rad
ω	Angular velocity	$rads^{-1}$

Acronyms	
Symbols	**Description**
BEM	Boundary Element Method
DOE	Design Of Experiments
GA	Genetic Algorithm
MPS	Marine Power Systems
PSO	Particle Swarm Optimisation
WEC	Wave Energy Converter
RBF	Radial Basis Function
TRL	Technology Readiness Level

Chapter 1

Introduction

1.1 Research Context

Ocean energy is a renewable resource of large potential. Wave energy is one of the most significant types of the amount of ocean energy and it is estimated it could be equivalent the global electrical energy consumption of almost 24 TWh [1]. The map in Figure 1.1 shows the wave potential around the world. It is possible to observe that the west coasts and the temperate climates have the highest energy potential [2]. Generally the wave energy

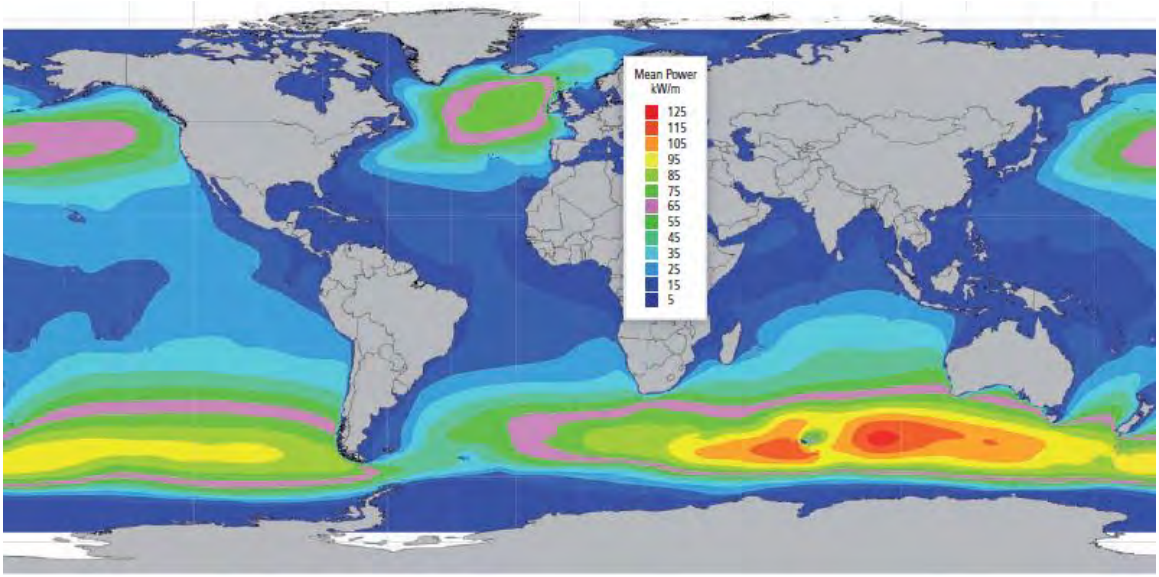

Figure 1.1: Global offshore annual wave power level distribution [2].

potential is more than the electricity consumption in most of the areas of our Planet (Table

1.1). Only North America and Asia have more electricity consumption than the wave energy potential due to the large continental area.
Wave energy has different advantages compared to other renewable resources such as a high energy density and a natural seasonal variability that follows the electricity demand in temperate climates. There are different definition of the wave energy resource based on the limits to the wave energy potential [3]. The accessible wave energy resource is limited by several factors such as:

- the efficiency of the device.
- sea depth less than 50m (could be increased dependent on the technology).
- areas further than 100km from coast.
- areas with uneconomically low wave power.
- Exclusion zones such as navigation lanes, fish farms and wind farms concessions.

The global accessible wave energy resource is around 4.6% of the total global theoretical one as reported in [4]. In particular the Pelamis device [5] has been used for this estimation. Table 1.1 shows the estimated yield of accessible wave energy relative to the theoretical wave power.
The wave energy technology is in an early development stage and it is not converged yet to

Table 1.1: Comparison between electricity energy consumption and wave energy potential in different areas [1, 2, 4].

	Electricity energy consumption, 2015 (TWh)	**Theoretical wave energy (TWh)**	**Yield of accessible wave energy (%)**
Europa	3791	4100	5.4
North america	4956	4000	4.8
South America	1536	4600	3.6
Asia	12587	6200	6.4
Oceania	300	5600	3.7
Africa	780	3500	4

a WEC. Research and innovation are very important to improve the technology giving more scientific insight. The optimisation of the WECs will be based mainly in decreasing the Levelized Cost of Energy (LCoE) based on a TRL 2-3 making competitive this technology with other ones.
There are different typologies of wave devices designed until now. Two different types of

classification can be identified. In the first type, the wave devices are divided dependent on the location if they are installed on-shore, near-shore or off-shore [6]. In the second type described in the book of Falcao [7], the wave devices are divided dependent on the working principle. There are three main classes of wave devices: Oscillating Water Column (OWCs), Oscillating bodies and Overtopping devices. The OWCs are typically on-shore devices and are characterized by a submersed part of the structure in which air is trapped inside. The incident waves on the chamber move the air through a turbine that drives an electrical generator. Oscillating bodies are mainly off-shore devices, they create energy from the relative movement of another body or the sea bottom. Finally the overtopping devices operate in a manner that is very similar to a low head hydroelectric plant. The energy comes from hydraulic turbines that exploit a reservoir at a higher level than the free surface of the sea.
A floating wave device can be identified in three categories as shown in the book of Cruz [8]. There are Point Absorbers, Terminators and Attenuators. Point absorbers have a small characteristic length compared to the wavelength of the incident waves, Terminator has the dominant direction perpendicular to the incident waves and finally the Attenuator is aligned along the incident waves directions.
There is a large number of companies that are competing in the wave energy market with different device concepts especially in UK that is one of the leading country in marine energy [9]. Table 1.2 shows the UK wave developers and their related WEC following the classification of the European Marine Energy Centre (EMEC) [10]. This research project is in collaboration with Marine Power Systems Ltd that is developing the WaveSub device. This device is a point absorber that extracts energy from the relative motion between a float and a reactor.

1.2 Industrial collaboration

This research project is a result of the collaboration between Swansea University and MPS Ltd. As a result of this, my research time was divided between academia and industry. Most of the time I was in the university but normally once a week I was in MPS. Progression meetings have been very usual in MPS where I could show the most updated research work. MPS supported me in a workshop at the beginning of my PhD that helped me significantly to develop the numerical model of a single float WaveSub. After that, I received still from MPS a numerical tool to model the frequency domain of the wave fields. This has been

Table 1.2: UK wave developers 2019 [10].

Company	Device name	Device type
Aimmer UK	Aimmer (Squid)	Other
AlbaTERN Ltd	WaveNET,SQUID	Other, Attenuator
AWS Ocean Energy	AWS III	Overtopping device
Caley Ocean Systems	Wave Plane	Other
Checkmate Seaenergy UK Ltd	Anaconda	Bulge wave
Ecotricity	Searaser	Point absorber
Greenheat Systems Ltd	Gentec WaTS	Other
Limerick Wave Ltd	Limerick Wave PTO	Other
M4Wave Power	M4	Attenuator
Marine Power Systems Ltd	WaveSub	Point absorber
Neptune Renewable Energy Ltd	Triton	Point absorber
Offshore Wave Energy Ltd (OWEL)	OWEL WEC	Oscillating wave surge converter
ORECon	MRC 1000	Submerged pressure differential
PAULEY (Phil Pauley Innovation)	Solar Marine Cells	Other
Polygen Ltd	Ocean WaveFlex, Volta WaveFlex	Oscillating wave surge converter, overtopping device
Sea Wave Energy Ltd (SWEL)	Waveline Magnet	Other
Seatricity	Oceanus 2	Point absorber
SEEWEC Consortium	FO3	Point absorber
Snapper Consortium	Snapper	Point absorber
The Bobber Company Ltd	Manchester Bobber	Point absorber
Trident Energy Ltd	PowerPod and PowerPod II (Linear Generator)	Point absorber
Wave-tricity	-	Other
Wavepower Technologies Ltd	-	Other
WITT Ltd	-	Other

very useful for a deeper understanding of the wave fields and it has been the starting point of further research. Numerical results of commercial codes such as Wamit and WaveDyn were obtained from MPS. A comparison between numerical results of them and from the numerical model chosen was of significant importance at this stage. Then, the experimental results of the tank testing undertaken in 2017 by MPS have been of great importance for the validation of the numerical model. The tank testing has been a collaboration between MPS and the University of Bath as an academic partner that was involved in the control system. MPS gave me directly the experimental data of the tank testing. Finally, my last significant collaboration with MPS has been the development of a cost model of a multi-float WaveSub. However, my contribution to this cost model are quite limited to account the influence of the design parameters on the LCOE.

Generally, the collaboration with MPS has been very positive throughout the PhD. A good

communication has been of crucial importance.

1.3 Aim of the Research

The WEC market is extremely competitive and does not show convergence on a particular device. The WaveSub device is a WEC developed by Marine Power Systems, that is based in Swansea. This research aims to investigate the competitiveness of a multi-float WaveSub device. In fact, a multi-float WaveSub expected to improve the design in terms of cost of energy because of the shared infrastructure. The investigation of the multi-float device at a TRL 2-3 [11] based on a numerical model promises to save lots of effort and money compared to a tank testing investigation. The validation of the numerical model is very important for this project to give confidence of the results obtained. The numerical model will be able to capture with reasonable accuracy the hydrodynamic interaction between the floats and the energy produced by the device. Finally, the optimisation of the device based on several design parameters will be the final step of this project. In this optimisation, a cost model will be coupled with the energy yield estimate obtained from the numerical model to show the competitiveness of the device in the energy market.

1.4 Contribution to Knowledge

This thesis makes the following contributions to knowledge in the field of wave energy:

- Numerical modelling of the multi-float WaveSub device.
- Comparison between open-source and commercial codes of the WaveSub numerical model.
- Benchmarking between the numerical model and the tank testing of a multi-float configuration of the WaveSub device.
- Extension of Wec-Sim open access software through multi-directional wave capability.
- The optimisation of a linear design concept of the multi-float WaveSub device.
- The optimisation of novel multi-float design concepts of the WaveSub device.

1.5 Content and Structure

The main chapters of the thesis are shown in the pyramid diagram (Figure 1.2). The research question aims to optimise a multi-float WaveSub device to minimise the cost of energy produced. This goal requires different steps that must be followed in order.
Chapter 1 introduces the context and the goal of this research. The main contribution to knowledge is also presented.
Chapter 2 reviews the literature related to this PhD proposal. The numerical modelling of Wave Energy Converters (WECs), the optimisation techniques for a WEC array, the tank testing, the WEC market and the wave field generated by a WEC have been discussed here. This review is the starting point of the choice of the numerical model.
Chapter 3 introduces the WaveSub device and the numerical methodology adopted to estimate the motion and the energy produced of the device. The choice of appropriate tools is obtained comparing commercial and open-source codes. Then the fluid resistance created by a WEC is investigated as well as the perturbed wave field generated.
Chapter 4 aims to validate the numerical model comparing experimental and numerical results. It is a very important step to give more confidence of the results obtained from the numerical model.
Chapter 5 and 6 are relative to the optimisation of a multi-float WaveSub design. Chapter 5 focuses on a linear multi-float WaveSub design based on a first design. The number of floats is investigated until a maximum number of 6. This upper limit is chosen due to computational time reasons. A second updated design is then used to optimise new multi-float design concepts in chapter 6. The optimisation is based on the Levelized Cost of Energy (LCOE) that takes both in account the cost and the energy produced from the device. It is the final goal of this research project and marked as the last level of the pyramid (Figure 1.2).
Chapter 7 concludes the thesis summarizing the main achievements and discussing the limitations and the further extension of this work.

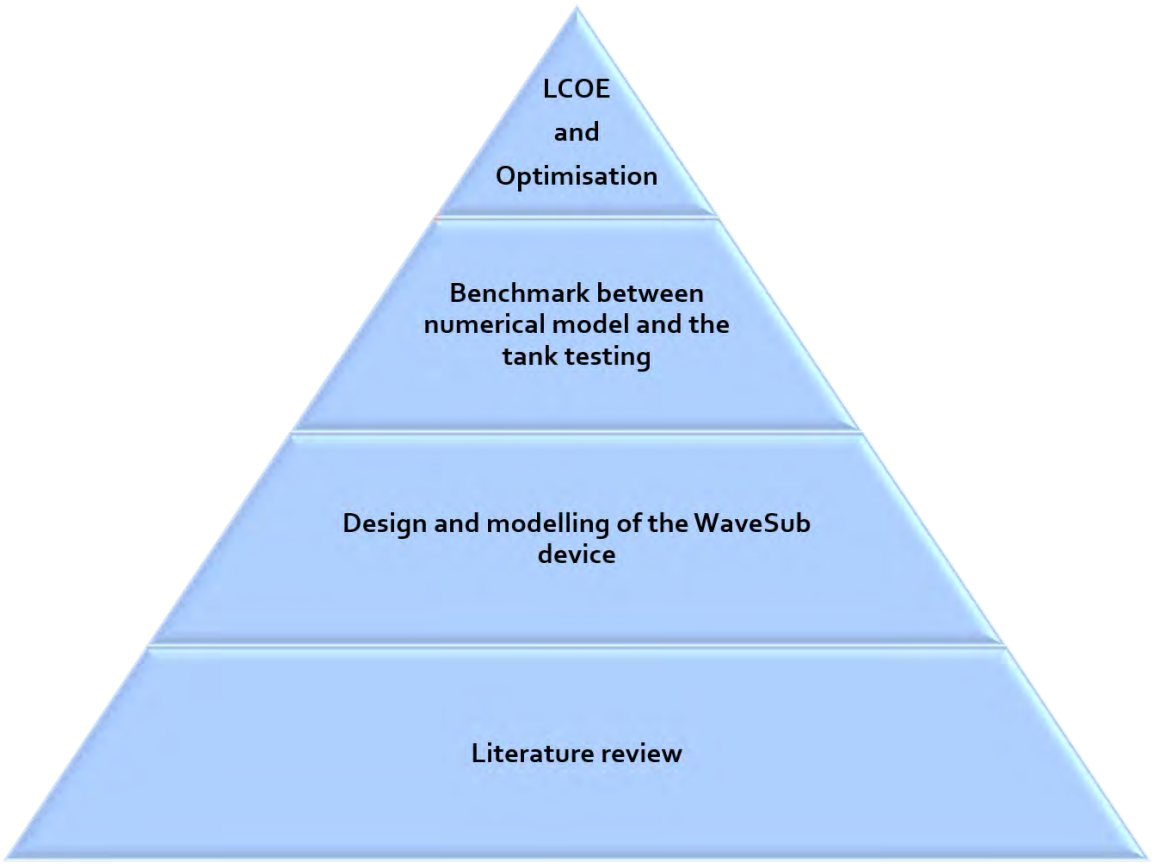

Figure 1.2: Thesis content pyramid.

Chapter 2

Literature review

2.1 Numerical modelling

2.1.1 Introduction

One of the main problems in the design of a novel WEC is to validate a numerical model to estimate the energy production [12]. There is a wide range of possibilities of modelling a particular wave energy converter due to the different device typologies. The choice of the numerical model is very critical and it could influence significantly the results. A general understanding of the limitations and benefits of each numerical model will help the choice of the most suitable numerical model of a multi-float configuration of the WaveSub device. The numerical model will need to account for the various hydrodynamic forces acting on the WEC. These are mainly: a hydrostatic force, a radiation force created by the motion of the device in absence of waves, an excitation force due to the modification of the incident wave field because of the presence of the WEC and a viscous force.
The motion of a WEC can be modelled as following [13]:

$$\mathbf{M}\ddot{\mathbf{X}} = \mathbf{F_{ex}} + \mathbf{F_{rad}} + \mathbf{F_{H}} + \mathbf{F_{PTO}} + \mathbf{F_{V}} + \mathbf{F_{es}} + \mathbf{F_{M}} + \mathbf{F_{Coriolis}} \tag{2.1}$$

in which:

- $\mathbf{X}$, $\dot{\mathbf{X}}$, $\ddot{\mathbf{X}}$ are the position, velocity and acceleration vectors of the WEC. The dimensions of the vectors depends on the number of degrees of freedom considered.
- $\mathbf{M}$ is the mass matrix of the device and it depends on the device and whether the equation of motion is linearised or not, it is not necessarily constant.

- $\mathbf{F_{ex}}$, and $\mathbf{F_{rad}}$ are respectively the wave excitation force and the radiation force.
- $\mathbf{F_H}$ is the hydrostatic force resulting from the combined action of the gravity and buoyancy force.
- $\mathbf{F_{PTO}}$ is the force applied by the Power Take Off (PTO) system.
- $\mathbf{F_V}$ is the viscous force that depends quadratically on the velocities, and which aims at taking into account the effect of viscous losses.
- $\mathbf{F_{es}}$ is a force which aims at taking into account the effect of end stops in the PTO mechanism, if any.
- $\mathbf{F_M}$ is the mooring force.
- $\mathbf{F_{Coriolis}}$ is a force which comes from non-linear terms in the mechanical part of the equation of motion.

In this analysis, drift forces, current forces and wind forces are not considered because it is supposed that they have a small influence on the energy absorption [13]. Drift forces becomes more important for larger wave amplitudes and so they are more important to design off-shore mooring systems. Current and wind forces can be approximated as constant forces and so they will determine mainly an additional off-set. The correlation between theory and experiment is generally good in small to moderate sea states while it becomes more inaccurate with severe sea states due to non-linear and viscous effects [13]. In particular linear theory [7] will produce an overestimation of the device response and energy production for large sea states [13]. Another approximation that is usually done is the mono-directionality of the waves. This assumption is more valid especially for axi-symmetric devices and when the mooring allow some alignment with the wave direction [13]. Finally the design of mooring systems requires generally to take in account non-linear effects generated by the waves that are usually not considered in the linear theory [7].
There are different numerical models described in the literature to simulate a WEC device including: linear potential flow (Frequency-Domain, Time-Domain and Spectral-Domain Models), non-linear potential flow, a Computational Fluid Dynamics (CFD) model and an identification model.

2.1.2 Frequency Domain Model

The hydrodynamic interaction between the WEC and the waves, the mooring and the electric generator forces are generally non-linear. However under some assumptions such as an inviscid, irrotational and incompressible flow, small waves compared to the wavelength and small amplitude of motion of the device compared to the characteristic dimension, the system can be linearised with a frequency-domain model. The agreement between numerical model under these assumptions and experiment is generally good from small to moderate sea states [13].
It is based on linear potential flow [7] in which the fluid can be represented by a velocity potential (ϕ):

$$\mathbf{u} = \nabla\phi \tag{2.2}$$

where $\mathbf{u}$ is the fluid velocity. Neglecting viscosity the Navier-Stokes equation is reduced to the Bernoulli equation [7]:

$$p + \rho_w g z + \rho_w \frac{1}{2}(\nabla\phi)^2 + \rho_w \frac{\partial\phi}{\partial t} = 0 \tag{2.3}$$

where p is the fluid pressure, g is the acceleration of gravity, z is the vertical coordinate with origin on the free surface and t is the time. The linear theory neglects the quadratic term because under the assumptions, it results in values of an order of magnitude less than the other terms.
The irrotational and the incompressible conditions are described by the following Equations [7]:

$$\nabla \times \mathbf{u} = 0 \qquad\qquad \nabla \cdot \mathbf{u} = 0 \tag{2.4}$$

From the definition of velocity potential and the incompressibility condition derives directly the Laplace condition defined on the fluid volume [7]:

$$\nabla^2\phi = 0 \tag{2.5}$$

Then there are the boundary conditions on the free surface, on the sea bottom and on the body surface. On the free surface there are the dynamic and the kinematic boundary conditions obtained assuming small wave amplitudes relative to the wavelength.
The dynamic and the kinematic free surface boundary condition are expressed respectively

as following [7]:

$$\left[\frac{\partial\phi}{\partial t}\right]_{z=\eta_I} \approx \left[\frac{\partial\phi}{\partial t}\right]_{z=0} = -g\eta_I \tag{2.6}$$

$$\frac{D\eta_I}{Dt} = \frac{\partial\eta_I}{\partial t} + \vec{u}\cdot\nabla\eta_I = -\left[\frac{\partial\phi}{\partial z}\right]_{z=\eta_I} \approx -\left[\frac{\partial\phi}{\partial z}\right]_{z=0} \tag{2.7}$$

From these 2 forms of the free surface boundary condition another expression of the velocity potential can be obtained [7]:

$$[\frac{\partial^2\phi}{\partial t^2}]_{z=0} = [-g\frac{\partial\phi}{\partial z}]_{z=0} \tag{2.8}$$

Finally there are the sea bottom (z=-d) and the body surface boundary conditions that are respectively [7]:

$$\frac{\partial\phi}{\partial z} = 0 \tag{2.9}$$

$$\frac{\partial\phi}{\partial n} = \mathbf{n} \tag{2.10}$$

where **n** is the unit vector normal to the body boundary and pointing out to the fluid domain. The expression of the incident velocity potential can be found from the boundary conditions as a function of the sea bottom (d), of the wave number (k), of the coordinate of the reference system (x,z), of the wave height (H) [14]:

$$\phi_i(x,z,t) = -\frac{\omega H}{2k}\frac{cosh[k(z+d)]}{sinh(kd)}sin[\omega t - kx + \Phi] \tag{2.11}$$

The wave parameters are represented in Figure 2.1.

The dispersion relationship can be found from equations 2.6 and 2.11:

$$\omega^2 = gktanh(kd) \tag{2.12}$$

The mean energy and incident power per metre of wave-front are expressed respectively as:

$$\overline{E}_w = \overline{E}_{potential} + \overline{E}_{kinetic} = \frac{1}{16}\rho_w g H^2 + \frac{1}{16}\rho_w g H^2 = \frac{1}{8}\rho_w g H^2 \qquad \overline{P}_i = \overline{E}v_g \tag{2.13}$$

In particular the mean potential energy and the mean kinetic energy are equal. v_g is instead the group velocity that is the velocity of propagation of the wave energy.
The dispersion relationship, the phase velocity, the group velocity and the mean incident

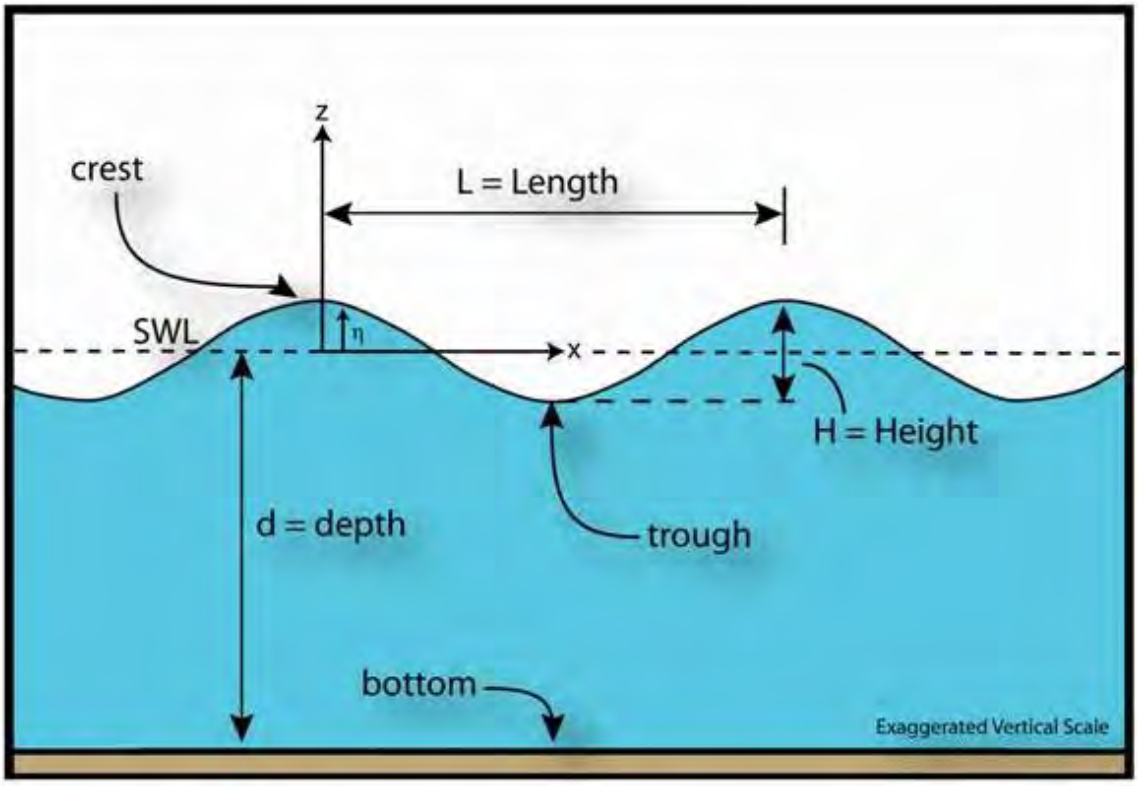

Figure 2.1: Representation of the wave parameters [15].

power can be summarized in Table 2.1 for different water depth range:

The velocity potential can be expressed as a superposition of the incident, diffraction and radiation wave field [16, 17]:

$$\phi = \phi_i + \phi_d + \phi_r \tag{2.14}$$

The diffraction wave field results from the interaction between the incident wave and a motionless body and the radiation wave field is produced by the body motion in the absence of an incident wave field. The diffraction and incident velocity potential should respect the following boundary condition [16, 17]:

$$\frac{\partial \phi_d}{\partial n} = -\frac{\partial \phi_i}{\partial n} \tag{2.15}$$

In fact, the velocity component normal to the body wetted surface must be zero on the wet surface S [16, 17]. After that the excitation and radiation pressures (P_{ex} and P_{rad}

Table 2.1: Linear wave theory relations for different classification of the water depth.

	Deep water ($d < \lambda/2$)	**Transitional depth** ($\lambda/20 < d < \lambda/2$)	**Shallow water** ($d < \lambda/20$)
Dispersion relationship	$\omega^2 = gk$	$\omega^2 = gktankd$	$\omega^2 = gk^2d$
Phase velocity (c_{ph})	$c_{ph} = \frac{g}{2\pi}T$	$c_{ph} = \frac{\lambda}{T} = \frac{\omega}{k} = \sqrt{\frac{g\lambda}{2\pi}tankd} = \frac{g}{2\pi}Ttanhkd$	$c_{ph} = \sqrt{gd}$
Group velocity (v_g)	$v_g = \frac{c_{ph}}{2}$	$v_g = \frac{\omega}{2k}(1 + \frac{2kd}{sinh2kd})$	$v_g = c_{ph}$
Mean incident power ($\overline{P}_I$)	$\overline{P}_I = \frac{\rho_w g^2}{4\omega}(\frac{H}{2})^2$	$\overline{P}_I = \frac{\rho_w g^2}{4\omega}(\frac{H}{2})^2(1 + \frac{2kd}{sinh2kd})tankd$	$\overline{P}_I = \frac{\rho_w g^2}{4\omega}(\frac{H}{2})^2 2kd$

respectively) and the relative forces ($\mathbf{F_{ex}}$ and $\mathbf{F_{rad}}$ respectively) can be found [7]:

$$P_{ex} = -\rho_w \frac{\partial(\phi_i + \phi_d)}{\partial t} \qquad P_{rad} = -\rho_w \frac{\partial(\phi_r)}{\partial t} \tag{2.16}$$

$$\mathbf{F_{ex}} = \int P_{ex}\mathbf{n}dS = \mathbf{F_{F-K}} + \mathbf{F_d} \qquad \mathbf{F_{rad}} = \int P_{rad}\mathbf{n}dS \tag{2.17}$$

where the $\mathbf{F_{F-K}}$ is the Froude-Krylov force that derives from the incident potential while $\mathbf{F_d}$ from the diffraction potential. In particular the diffraction force is negligible if the largest dimension of the immersed part of the body is very small compared with the wavelength. The source distribution method is implemented to find the solution of the velocity potential [18]. The Laplace equation and the boundary conditions must be solved using a boundary integral equation method (BIEM)[18]. The Green's theorem is used to simplify the volumetric problem (see Equation (2.5)) into a surfacic problem. It is usually implemented using a low order method where the body surface is approximated with a large number N of quadrilateral flat panels and the source strength is assumed constant on each panel [18]. The Green's function (G (p,q)) is expressed as [18]:

$$\alpha(p)\phi(q) + \int \phi(p)G_n(p,q) - \int \phi_n(p)G(p,q) = 0 \tag{2.18}$$

where p and q represent the field point and the source point, $\alpha(p)$ is the internal angle formed at the boundaries, $G_n = \nabla G \cdot n_q$, $\phi_n = \nabla\phi \cdot n_q$ and n_q is the normal vector at q. Finally the normal derivative of the potential is evaluated at the centroid of each panel, and set equal to the normal velocity at that point giving a total of N linear equations for the unknown source strengths [18]. This system of equations is solved and from the potential of each panel the pressure is found and finally the forces and moments acting on the body.

As a rule of thumb the characteristic size of the panels should be at least of the order of 1/8 of the wave length corresponding to the higher frequency used in the computations [19].
The calculation of the hydrodynamic coefficients could be very long especially for a large number of panels. When the number of bodies becomes larger, other theories must be adopted such as the multiple-scattering method or the direct matrix method (see Section 2.1.6). In fact, the panel method has some computational limit due to the fact that the CPU time is proportional to the square of the number of panels [20].
Wave effects on multiple bodies were analysed by Newman [21]. The excitation force can be expressed as

$$\mathbf{F_{ex}} = \sum_{m=1}^{M} \sum_{j=1}^{NDOF} F_{ex-jm} \tag{2.19}$$

while the radiation force as

$$\mathbf{F_{rad}} = \sum_{m=1}^{M} \sum_{n=1}^{M} \sum_{j=1}^{NDOF1} \sum_{k=1}^{NDOF2} F_{rad-jm,kn} = \sum_{m=1}^{M} \sum_{n=1}^{M} \sum_{j=1}^{NDOF1} \sum_{k=1}^{NDOF2} -A_{jm,kn}\ddot{\mathbf{X}} - B_{jm,kn}\dot{\mathbf{X}} \tag{2.20}$$

where m,n indicate the m-th and n-th bodies and j,k indicate the motion modes for the 2 different hydrodynamic bodies. $A_{jm,kn}$ and $B_{jm,kn}$ represent respectively the added mass and the radiation damping. If the body has zero forward speed and if there is no current $A_{jm,kn} = A_{jn,km}$ and $B_{jm,kn} = B_{jn,km}$ [19].
After having determined the hydrodynamic coefficients, the body motion (**X**) is obtained by solving the following frequency domain equation:

$$\begin{aligned}(\mathbf{M}+\mathbf{A})\ddot{\mathbf{X}} + (\mathbf{B}+\mathbf{C_{PTO}})\dot{\mathbf{X}} + (\mathbf{K_H}+\mathbf{K_{PTO}}+\mathbf{K_M})\mathbf{X} = \mathbf{F_d} \\ +\mathbf{F_{F-K}} + \mathbf{F_{es}} + \mathbf{F_V} + \mathbf{F_{Coriolis}}\end{aligned} \tag{2.21}$$

where the excitation force ($\mathbf{F_{ex}}$), the hydrostatic force ($\mathbf{F_H}$), the PTO force ($\mathbf{F_{PTO}}$) and the mooring force ($\mathbf{F_M}$) are expressed in this way:

$$\mathbf{F_{ex}} = \mathbf{F_d} + \mathbf{F_{F-K}} \tag{2.22}$$

$$\mathbf{F_H} = \mathbf{K_H}\mathbf{X} \tag{2.23}$$

$$\mathbf{F_{PTO}} = -\mathbf{K_{PTO}}\mathbf{X} - \mathbf{C_{PTO}}\dot{\mathbf{X}} \tag{2.24}$$

$$\mathbf{F_M} = -\mathbf{K_M}\mathbf{X} \tag{2.25}$$

The excitation force ($\mathbf{F_{ex}}$) is considered as the sum of the diffraction force and the Froude-Krylov force as explained before. The hydrostatic force is obtained by reference to a hydrostatic stiffness matrix K_H. It is modelled as a restoring force and it is the difference between the buoyancy and the gravity force. The PTO force ($\mathbf{F_{PTO}}$) is linearised and it is described with a stiffness and a damping term. The mooring force is expressed as a linear function of the device motion. These assumptions are needed if a frequency domain model will be chosen.

It is suggested to consider $\mathbf{F_V}$ especially for large WEC amplitude motion because will reduce more significantly the device motion. The drag force for a slender body is usually expressed as a quadratic term of the relative difference between the flow ($\mathbf{u}$) and the body velocity ($\mathbf{v}$) [16]:

$$\mathbf{F_V} = \frac{1}{2}\rho_w \mathbf{C_D} \mathbf{A_{Drag}} (\mathbf{u} - \mathbf{v}) |\mathbf{u} - \mathbf{v}| \tag{2.26}$$

where $\mathbf{C_D}$ is the drag coefficient, $\mathbf{A_{Drag}}$ is the characteristic area, $\mathbf{u}$ and $\mathbf{v}$ are the incident flow and body velocity. However this relationship is valid only for slender bodies or other similar geometries where the diameter is small compared to the wavelength (ratio less than 0.2) [22]. So it is assumed that the body is not influencing the wave field around it. The main problem of this formulation is the correct estimation of the drag coefficient.

Finally the end-stop forces are implemented when the amplitude of the PTO motion is larger than the amplitude constraint.

The Coriolis force is generally negligible while the end-stop force should be implemented for a more detailed PTO design.

The excitation force can be linearised and can be expressed as following [7]:

$$\mathbf{F_{ex}} = \Gamma(\omega) A_I cos(\varphi_{\mathbf{ex}}) \tag{2.27}$$

where A_I is the incident wave amplitude, $\Gamma(\omega)$ is the excitation force coefficient and $\varphi_{\mathbf{ex}}$ is the phase angle.

The device motion without considering the end-stop force of the PTO, the viscous and the Coriolis forces results equal to [7]:

$$X_c = |\mathbf{X}| e^{i\omega t} = \frac{\mathbf{F_{ex}}}{-\omega^2(\mathbf{M} + \mathbf{A}) + \mathbf{K_H} + \mathbf{K_{PTO}} + \mathbf{K_M} + i\omega(\mathbf{B} + \mathbf{C_{PTO}})} \tag{2.28}$$

where X_c is the device motion written in a complex notation.

It is possible finally to estimate the mean absorbed power. For a heaving oscillating body

it can be estimated by the following equation [7]:

$$\overline{P}_{abs} = \frac{1}{2}\omega^2 C_{PTO}|\mathbf{X}|^2 \tag{2.29}$$

If the motion is considered linear the RAO (Response Amplitude Operator) could be defined and it tells us for which frequencies there will be a larger motion. It is going to zero for low periods since the body acts as a filter and also for high periods because the body tends to move together with the wave. The maximum is for an intermediate frequency: the resonance frequency. It is defined as the ratio between the response amplitude and the wave height [23]:

$$\mathbf{RAO}(\omega) = \frac{\mathbf{X}}{H} \tag{2.30}$$

It is convenient to design the wave device with a resonance period equal to the most energetic period of the design installation location (for example, a wave energy test site). The most energetic period is not also the most powerful wave period because it accounts also the occurrence of the sea state. Linear theory will become less accurate, in particular, for sea states with large significant heights where non-linearities are more important.
A frequency domain model is usually based on a monochromatic wave field that is not an accurate representation of real waves. However it is also possible to model irregular waves thanks to the superposition principle of a large number of regular sinusoidal waves with different amplitude, frequency and phase.

2.1.3 Time Domain Model

A Time-Domain model could be used because it can consider the non-linearities in the system, which are mainly from PTO, mooring and larger waves. However it is more computational demanding than Frequency-Domain and so its application to WEC arrays is more limited. After the Time Domain hydrodynamic coefficients have been found, the Time-Domain Models can be applied.

A Time-Domain model is based on the Cummins Equation [24]:

$$[-\omega^2(\mathbf{M}+\mathbf{A}_\infty)+\mathbf{K}]\mathbf{X}+\int_0^t h_r(t-t')\dot{\mathbf{X}}\,dt' = \mathbf{F_{ex}}+ \\ \mathbf{F_{PTO}}+\mathbf{F_V}+\mathbf{F_{es}}+\mathbf{F_M}+\mathbf{F_{Coriolis}} \tag{2.31}$$

where A_∞ is the added inertia matrix for infinite frequency while $h_r(t)$ is the impulse response function of the radiation force.

The calculation of the radiation force is more complex compared to the other forces because of the convolution term that represents the fluid memory effect.

An example of a non-linear PTO is the hydraulic PTO and it is described in [7] (fig: 2.2).

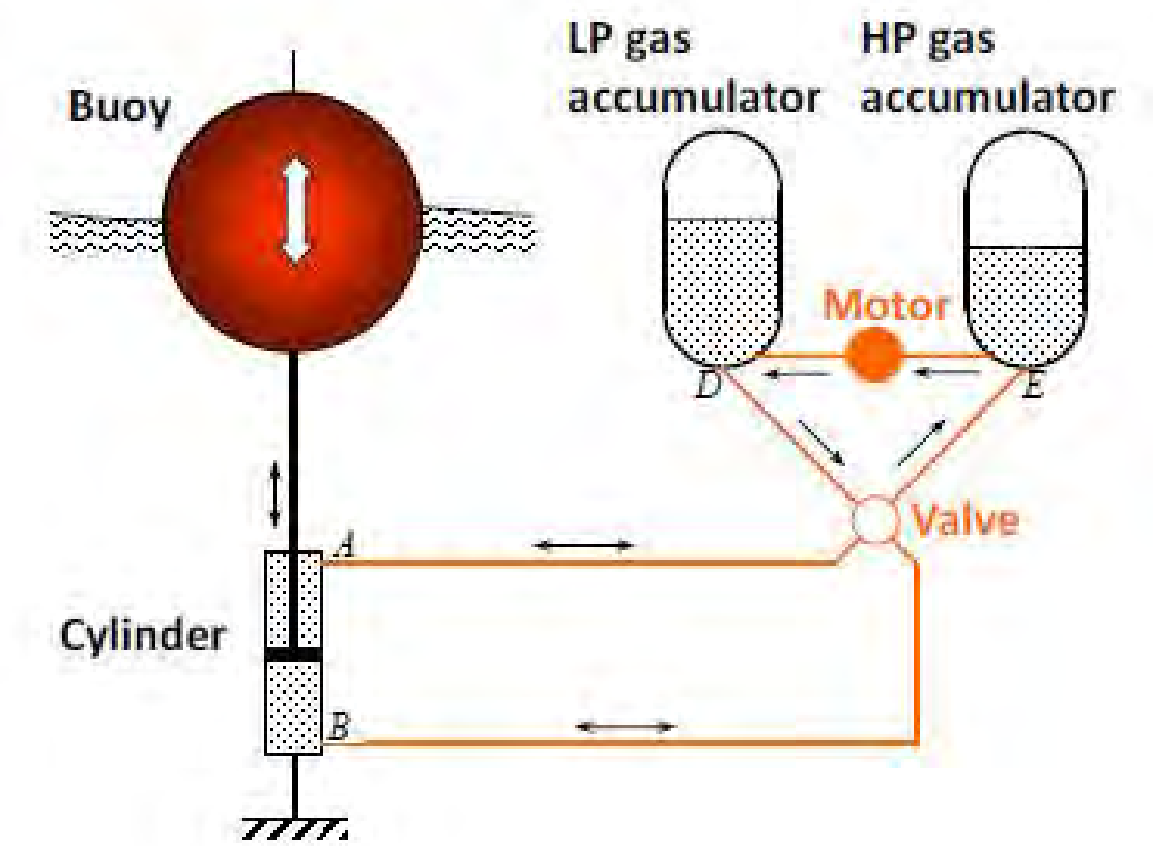

Figure 2.2: Simplified scheme of an hydraulic PTO [7].

The pressure difference between the accumulators can be written as [7]:

$$p_1 - p_2 = |p_A - p_B| - k_{ploss} q_{flow}^2 - I_{hu} \frac{dq_{flow}}{dt} \tag{2.32}$$

where k_{ploss} is a coefficient of pressure loss due to viscous effects along the circuit, q_{flow} is the volume flow rate and I_{hu} is a coefficient that takes into account the inertia of the fluid. The PTO force finally can be written as [7]:

$$\mathbf{F_{PTO}} = -sign(\dot{\mathbf{X}}) S_c (p_1 - p_2) \tag{2.33}$$

where S_c is the cylinder cross-sectional area. In particular the body will remain stationary until when the hydrodynamic force on the body overcomes the resisting force or Coulomb damping force ($S_c(p_1 - p_2)$).

The time domain hydrodynamic coefficients can be obtained from the frequency ones. The convolution term can be approximated with a linear ordinary differential equation or state-space model for this purpose [25]. The use of the state-space model instead of a direct convolution evaluation increase the simulation speed by almost 40 times. There are some relations between the frequency dependent hydrodynamic coefficients and the time domain ones. These are expressed by the equations derived from Ogilvie [25]:

$$A(\omega) = A_\infty - \frac{1}{\omega} \int_0^\infty h_r(t) sin(\omega t)\, dt \tag{2.34}$$

$$B(\omega) = \int_0^\infty h_r(t) cos(\omega t)\, dt \tag{2.35}$$

where $h_r(t)$ is the matrix of memory function.

Applying the Fourier transform the impulse response function in time domain can be found [25]:

$$h_r(t) = \frac{2}{\pi} \int_0^\infty B(\omega) cos(\omega t)\, d\omega \tag{2.36}$$

or in frequency domain [25]:

$$h_r(j\omega) = \int_0^\infty h_r(t) e^{-j\omega t}\, d\omega = B(\omega) + j\omega [A(\omega) - A_\infty] \tag{2.37}$$

The equations 2.36 and 2.37 are used to estimate the convolution term [25]:

$$\mathbf{F_{rad}} = \int_0^t h_r(t-t')\dot{\mathbf{X}}\,dt' \cong \begin{cases} \dot{\mathbf{X}} = A'\mathbf{X} + B'\dot{\mathbf{X}} \\ \mathbf{F_{rad}} = C'\mathbf{X} + D'\dot{\mathbf{X}} \end{cases} \tag{2.38}$$

The state-space model is obtained from the convolution term using the system identification [25].

2.1.4 Non-linear potential flow and CFD

The non-linear potential flow is an extension of the linear theory when the wave amplitude and the device motion become larger and they tend to be highly non-linear. However viscous effects are not considered. The quadratic terms of the dynamic and of the kinematic boundary condition of the free surface are not negligible as it was for the linear potential flow [12]:

$$\frac{\partial \phi}{\partial t} + \frac{1}{2}(\nabla\phi)^2 + g\eta_I = 0 \tag{2.39}$$

$$\frac{\partial \eta_I}{\partial t} + \frac{\partial \phi}{\partial x}\frac{\partial \eta_I}{\partial x} + \frac{\partial \phi}{\partial y}\frac{\partial \eta_I}{\partial y} + \frac{\partial \phi}{\partial z} = 0 \tag{2.40}$$

The boundary conditions are shown in Figure 2.3:

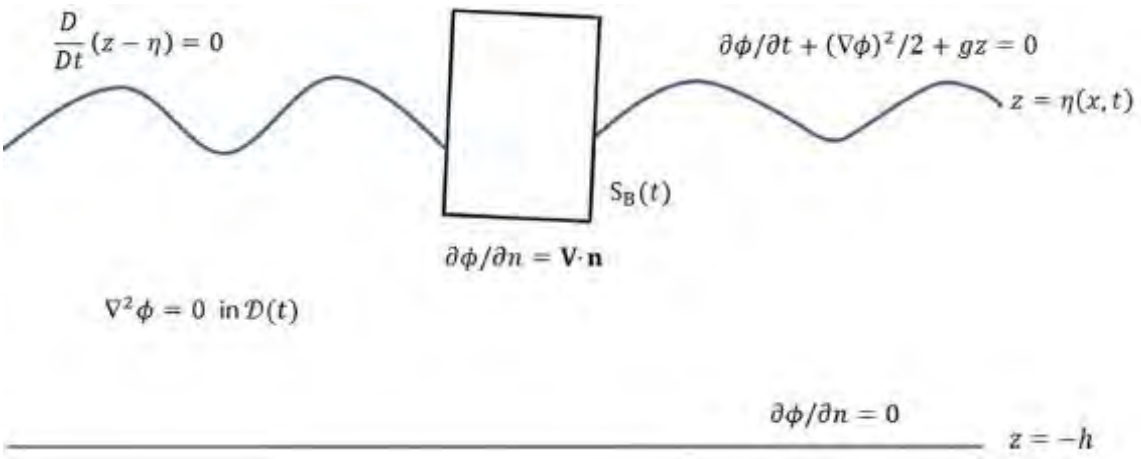

Figure 2.3: Boundary conditions of the nonlinear potential flow theory [12].

These models give more accurate results than linear potential flow.
There are 2 main nonlinear wave theories: the Stokes theory and the Cnoidal theory [26]. The application of these theories as a function of the wave parameters and the sea depth

is shown in Figure 2.4. The linear theory shows a good approximation for waves with small wave heights, large sea depth and wave periods. This theory has been chosen in the present work because it offers a reduced computational time and because some software implementations were available [27]. It is assumed deep water waves and the accuracy of the linear theory is quite good around until a 3 m wave height for a wave period of 10 s. Most of the occurrence of a certain location is, generally, under this wave height limit and so the numerical simulation of the device will estimate in a reasonable way the amount of energy produced.

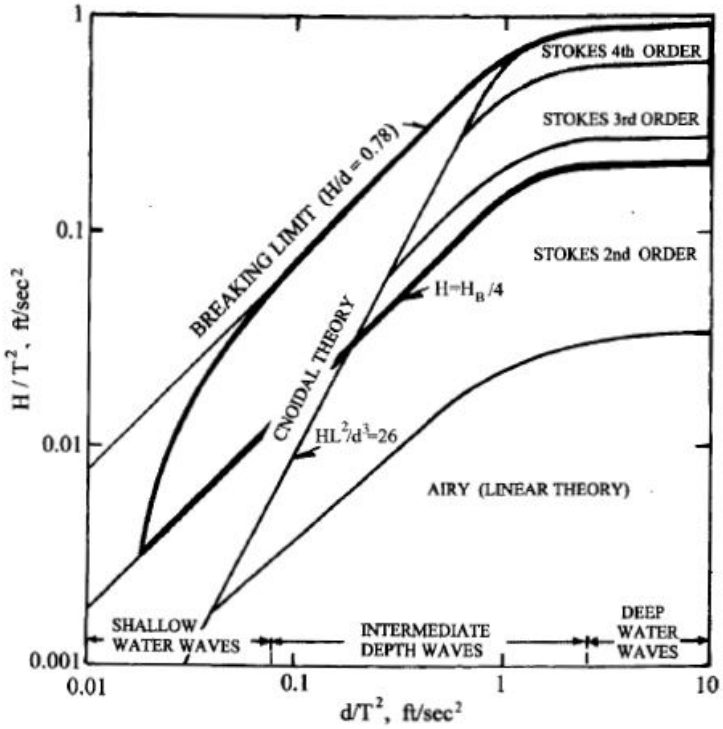

Figure 2.4: Wave theory identification from wave parameters and sea depth [28].

CFD models consider the viscosity of the fluid. In this model Navier-Stokes equations with the continuity equation are solved together with the internal and external boundary conditions and the initial conditions [12].

The continuity equation and Navier-Stokes equation are defined as following for an incompressible fluid [29]:

$$\nabla \cdot \mathbf{u} = 0 \tag{2.41}$$

$$\left(\frac{\partial \mathbf{u}}{\partial t} + \mathbf{u} \cdot \nabla \mathbf{u}\right) = -\frac{\nabla p}{\rho} + \mathbf{g} + \nu \nabla^2 \mathbf{u} \tag{2.42}$$

where **u** is the flow velocity, p is the flow pressure, ν is the kinematic viscosity and **g** is the acceleration of gravity.
There are mainly 2 CFD categories: Eulerian and Lagrangian [12]. In the first type the entire domain is discretized as a grid of points where is calculated the solution. In the second type the computational domain is set as a certain number of particles that move with a local velocity.
CFD could take into account multiple fluids [12]. So for example considering wave breaking, a WEC must be modelled using 2 fluids, water and air. However the compressibility of the air must be accounted in the simulation.
The main problem of a CFD model is the computational time which is highest when compared with the other methods [12]. The validation of the model is still necessary despite the more general assumptions compared with the other codes. In fact, there are always uncertainties related to the accuracy of the boundary conditions and if the model includes all the relevant physics. Finally microscopic flow physics is not accounted in a CFD model and this could determine some differences when air bubbles have an important role in the physics of the model [12].
A review of non-linear potential flow and CFD applied to WECs can be found in [12] and in [30]. Oscillating Water Columns (OWC) are the main wave devices in which these theories have been applied due to the large non-linearities of the physics involved. The hydrodynamics response is simplified for this case often in 2 dimensions. Examples of application of a non-linear potential flow theory for OWC device can be found in [31] and in [32]. The dynamics of a submerged cylinder undergoing large motion has been modelled in [33] using a linear potential flow theory with the intention to build a numerical tool that could simulate any submerged point absorber under large waves.
The simulation of the hydrodynamics of an OWC is obtained using CFD method for example in [34] and in [35] still using a 2 dimensions numerical approach. Most of the CFD numerical models that have been applied to a moving WEC are related to a heaving buoy such as in [36, 37, 38].

2.1.5 Numerical models (single device)

The limitations and the benefits of the numerical modelling applied to a single device are summarized in Table 2.2. Frequency domain models are the numerical models with the most simplifying assumptions of those considered but they have the potential to be used in

a more extended way for small WEC arrays. Time domain models relies on the frequency domain models for the calculation of the frequency hydrodynamic coefficients. After that, nonlinear forces can be added to the dynamic system for a more realistic representation of the device motion and power production such as the drag force. Nonlinear theories can be then used to overcome the limitations of the small amplitude of motion of the device and small wave amplitudes. CFD can reach a higher accuracy because they can account viscous effects and turbulence despite a large CPU required. Finally recorded data can be used to build the numerical model but the main problem is that it needs to face the scaling issues and the limited data.

Table 2.2: Numerical models (Single device).

Numerical models (Single device)	**Limitations**	**Benefits**
Frequency-Domain Models (WAMIT, ANSYS AQWA, NEMOH, OPENWARP, AQUAPLUS)	Inviscid, incompressible and irrotational fluid, small amplitudes of motion of the device relative to its dimension and small wave amplitudes relative to the wavelength, linear representation of reactive forces, flat seabed at a constant depth.	Possibility to use complex geometry and to apply to small WEC arrays.
Time-Domain Models (WaveDyn, WEC-Sim, OpenWEC, Simulink)	Inviscid, incompressible and irrotational fluid, small amplitudes of motion of the device relative to its dimension, small wave amplitudes relative to the wavelength, flat seabed at a constant depth.	Possibility to consider nonlinear reactive forces. Possibility to include drag forces.
Nonlinear Potential Flow Models (Wasim)	Inviscid, incompressible and irrotational fluid, flat seabed at a constant depth.	Accurate results considering second order terms in the free surface boundary condition.
CFD (AMAZON, Code-Saturne, ComFLOW, OpenFoam, CFX, Star-CD/CCM+, FLOW-3D, ANSYS Fluent)	Large CPU required, approximations on aerated fluid physics, approximations on turbulence physics.	Viscous effects and turbulence are considered.

2.1.6 Numerical models (array models)

The numerical modelling applied to the single device can be expanded to the use of WEC arrays. Frequency Domain models are the most used until now. The number of frequencies that must be simulated increases significantly when compared to a single device but this deficiency can be limited by reducing the range of frequencies in which the response is more

notable. Another important thing is that all the degree of freedom must be accounted including the non-generating modes because of the WEC interactions. WEC arrays modelled with other techniques than linear potential flow are not really developed essentially due to the complexity and the higher computational requirement. This conventional extension of a single device model to array is limited to small arrays of no more than 10 devices due to computational limitations [12].

This approach is computationally demanding and so semi-analytical Array Models could be preferred [12]. Semi-analytical Array Models have been created to solve the problem of hydrodynamic interactions between the WECs in an array. A great advantage is that they are more computationally efficient than the conventional numerical modelling. There are 4 main methods: the point absorber method, the plane wave method, the multiple scattering method and the direct matrix method [12]. The point absorber method consider only the radiated waves and not the scattered ones. It is assumed that the diameter of the devices is small compared to the wavelength and the device separation. The plane wave method approximates the radiated and the scattered waves by plane waves. It is more accurate than the point absorber method. These two first models are suited for widely spaced arrays. The multiple scattering method and the direct matrix method try to overcome the limitation of large separations between the WECs. The main assumption of these 2 methods is that the described cylinder to each WEC must not enclose the origin of any other WEC. There are common limitations of these methods such as the WECs in the array must be identical, with a single oscillating mode of motion (heave) and axisymmetric. There has been recently a coupling of the direct matrix method with the Boundary Element Method (BEM) solver that can overcome the limitation of the geometry [39].

Boussinesq and the mild-slope wave models can be also used to model WEC arrays [12]. These methods are suitable to model large domains at a reasonable computational cost. Specifically, this approach assumes a linear wave theory with an inviscid, incompressible and irrotational flow. The Boussinesq model enables to model the device also in shallow water. Using the mild-slope equations, that can be considered a linearised version of the Boussinesq equations, it is possible to model a varying bathymetry with mild slopes. A big limitation is that another model is required such as a potential-flow model or wave-tank/field data to know the required reflection, transmission, and absorption characteristics of the WEC.

The last type used for WEC arrays modelling is the spectral numerical model [12]. This is a probabilistic model and assumes statistical stationarity and Gaussian distribution of

the surface elevation. The wave is described through an energy spectrum while an appropriate transformation function is used to calculate a statistical representation of the device response and of the average power capture. Until now there are only few examples of its use because of the relatively new technique [12]. However they have been validated using tank testing showing that they can give an accurate estimation of the power produced. A good advantage is to be more computationally efficient for modelling non-linear systems than an equivalent deterministic model [12]. So they can be used in the parametric design process where a large number of simulations is required. Moreover it can be used to take in account the bottom friction and white-capping on wave growth. However it can only calculate average parameters of the response of the device.
The limitations of the numerical modelling applied to array devices are summarized in Table 2.3.

Table 2.3: Numerical models (Array models).

Numerical models (Array models)	**Limitations**	**Benefits**
Conventional Multiple Degree-of-Freedom Array Models	Increasing of the computational requirements.	Good accuracy in the results.
Semi-analytical Array Models (point absorber method, plane wave method, multiple scattering method, direct matrix method)	These models are limited to linear wave theory finding the hydrodynamic array interaction solution in the frequency domain. Flat seabed. Single oscillating mode of motion (heave), axisymmetric devices and identical WECs in the array.	Fast simulation and possibility of optimization changing a large variety of configuration parameters.
Boussinesq and mild-slope wave models (MILDwave, FUNWAVE, Mike21)	Limitation on the seabed slope, linear wave theory, small waves, not capable of modelling the response of a moving WEC.	Possibility to consider large wave field domains and accurate models for considering wave propagation and influence in the near shore.
Spectral-Domain Models (TOMAWAC, SWAN)	Inviscid, incompressible and irrotational fluid, small waves and small amplitudes of the WEC motion. It is limited to average response parameters, flat seabed at a constant depth. Not capable of modelling the hydrodynamics of a moving WEC.	Possibility of consider refraction, shoaling, wind forcing, white-capping, wave breaking, non-linear wave interactions. Possibility to simulate very large waves.

Finally, Table 2.4 represents the suitability of the various numerical methods [20]. The suitability is shown from a minimum of only one star which is not suitable to a maximum of

four stars which is highly suitable. Different modelling tasks are considered in this Table: localised effects, dynamic control, small WEC array, large WEC array and environmental impact. A detailed discussion of the suitability for the different models is given in [20]. This is given mainly by experience and by various considerations described in details in [20]. For example, CFD are very suitable for localised effects because they can account both evanescent waves and turbulence.

Table 2.4: Suitability of Numerical models [20].

	Lin. BEM	**Semi-analyt.**	**Time-domain**	**Nonlin. BEM**	**Bouss.**	**Mild-slope**	**Spectral**	**CFD**
Localised effects	***	*to***	***	***	**	**	*	****
Dynamic control	*	*	****	****	*	*	*	**
AEP (small WEC array)	***	***	**	**	***	***	***	**
AEP (large WEC array)	**	***	**	**	***	***	***	**
Environmental impact	*	*	*	*	***	***	****	**

2.2 WEC farm effect and optimisation

2.2.1 Introduction

Research in wave devices has increased since the beginning of this century due to the increased need of renewable resources [6]. The most analysed and investigated technology in the previous decades has been the Oscillating Water Columns (OWCs) [6]. However the wave resource is quite reduced on this device located on the coast because of the energy losses especially due to the bottom friction. For this reason the floating technology, that can be installed relatively far from the coast, has recently been chosen by several companies.
Different initiatives are helping the commercialisation process of marine technology reducing carbon emission towards a more sustainable future. A UK project called Marine Energy Accelerator (MEA) is accelerating the development of marine technology for energy capture [40]. This project was launched together by the Carbon Trust [41] and the Offshore Renewable Energy Catapult centre [42]. The aim of this project is to reduce the Cost Of Energy of the marine energy in the way to become competitive with the other renewable technologies by the mid of 2020s [43].
The aim of the funding is to develop a technology until its commercial phase. In particular a farm configuration is foreseen before reaching a full commercial device (fig: 2.5). The aim of a farm configuration is to decrease the Cost Of Energy of a single body configuration in the way to have a competitive device on the energy market.

Figure 2.5: Development phases of a marine development device [43].

The Pelamis device is an example of wave devices deployed in a park scale [6]. It is a submerged attenuator device that derives energy from the relative motion of the different cylindrical components linked by joints. Three Pelamis devices were installed along the coast of Agucadoura in Portugal in 2006. A Pelamis farm of 25 devices was also foreseen in 2008 (see Fig: 2.6). Since 2014 the developer company Pelamis Wave Power went into administration with the intellectual property transferred to Wave Energy Scotland [44]. Another example is the Seabased that has been contracted for a WEC park of 100MW in

Figure 2.6: Pelamis farm [45].

2018 by TC's Energy, a Ghanaian renewable energy production company [46]. Recently, Seabased has just completed a 14 MW wave power array [47].
There are also other wave farms that will be developed over the next years [48]. Ocean Power Technologies (OPT) is involved in the development of a wave farm of the PowerBuoy device at Cromarty Firth. OPT expressed his interest also in the development of a wave farm in the Wave hub site [49] in Cornwall. The PowerBuoy is a point absorber device that converts the heave motion in to hydraulic energy and then in to electric energy.
40South Energy cite [50] is also reaching a commercial stage with a planned project of developing a wave farm in Lavagna [48]. There are finally different WEC developers that are reaching a full scale deployment of their device or nearly. For example Bombora Wave Power [51] is working on a full scale device after have received £10.3 millions European Union funds while NEMOS [52] and AMOG [53] have reached $1/3^{rd}$ scale development.
This chapter will investigate 2 main topics related to WEC arrays: the WEC array effect and the WEC array optimization. The WEC array effect is very useful to understand the hydrodynamic interactions between the WECs. In particular, the visualization of the perturbed wave height could give an indication of this interaction. Literature regarding the optimiza-

tion of WEC array can be, instead, very useful to decide the optimization approach of a multi-float configuration of the WaveSub device.

2.2.2 WEC array effect

A WEC farm is expected to produce a "WEC array effect" that will have an effect on the energy production. The DHI (Danish Hydraulic Institute) has done several experiments to test this effect [54, 55]. An array has in particular two effects: an "intra-array effect" and an "extra-array effect" that are influencing respectively the energy production and the surrounding wave field.
A research project called "WECwakes" [55] has investigated WEC effects modifying the wave conditions (frequency and angle of the incident wave), WEC number, geometric configuration and position of the WECs. So a careful analysis is necessary to optimize the WEC farm. Two position configurations were studied: the first considers aligned devices and the second staggered devices. There is in both cases generally a wave height reduction in the downstream of the WEC arrays while there is an increase of the wave height just upstream of the arrays. In particular the wave height at a specific location was measured using resistive wave gauges. The influence of the position of the devices on the relative wave height or disturbance coefficient ($K_d = H_m / H_{m,ref}$) is shown in Figure 2.7. This image was obtained using a mild-slope propagation model called MILDwave. Generic wave energy converters of the overtopping type are considered. In particular observing the array configurations, the staggered array is characterized by a higher power absorption and by a higher WEC array interaction factor. This factor gives information about the influence of the intra-array interactions on the power absorbed by the array. It is defined as:

$$q = \frac{\sum_{i=1}^{N} \overline{P}_{abs,i}}{N\overline{P}_{abs}} \tag{2.43}$$

where $\overline{P}_{abs,i}$ is the mean absorbed power by the i-th WEC in the array while $\overline{P}_{abs}$ is the mean absorbed power by the case with an individual WEC and N is the number of WECs in the array. There is constructive effect when this factor is more than one while a destructive effect when it is less than one.
Different wave fields can be measured, especially the incident, the diffracted and the radiated field. The sum of the three types of wave field is called the perturbed field.

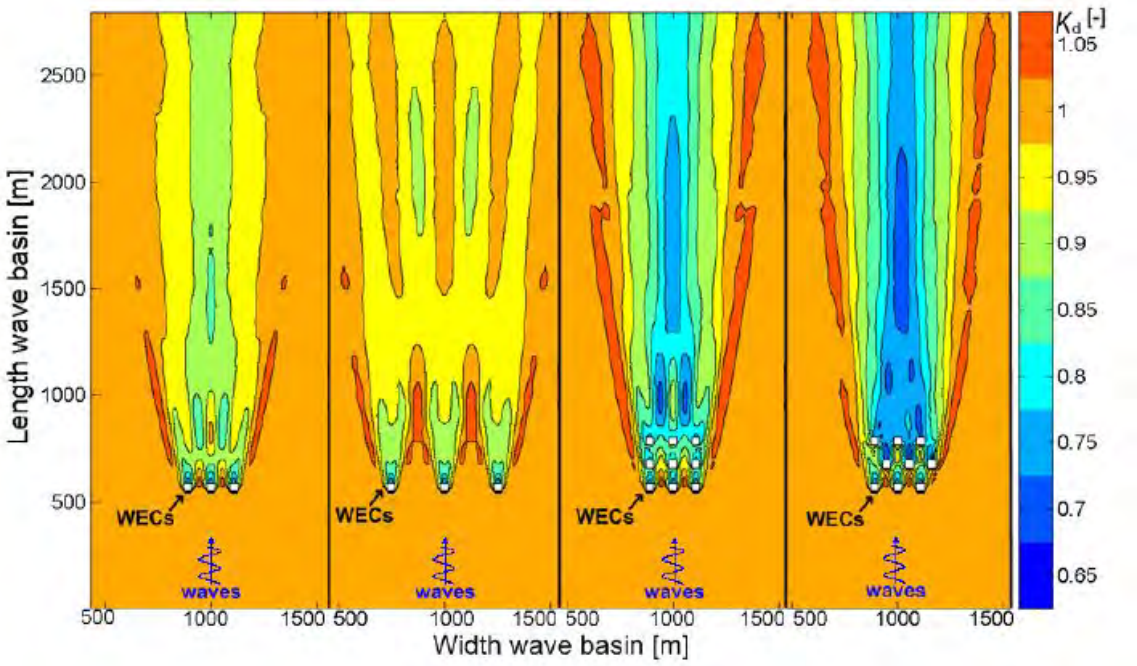

Figure 2.7: K_d for different configurations [55].

2.2.3 WEC array optimization

Optimization of WEC arrays is becoming an important issue because of the development of the wave energy sector. The cost of energy of this technology is still too high compared to other ways of energy production and there is the need to improve as much as possible its efficiency.

Different WEC arrays are generally compared using the absorption length. It is not sufficient to know the absorption power by the WEC but also the incident wave power. The absorption length is defined as following [8]:

$$L_{abs} = \frac{\overline{P}_{abs}}{\overline{P}_I} \tag{2.44}$$

where $\overline{P}_{abs}$ is the mean absorbed power and $\overline{P}_I$ is the mean incident wave power.

The interaction factor q (see Equation (2.43)) is used generally for the optimisation of the power produced from a WEC array. WEC devices in an array can have a constructive or destructive effect on the mean absorbed power. This strongly depends on the incident wave frequency and array layout [56].

The optimization of WEC farm, usually, is related to the power produced by the farm be-

cause it is supposed that the layout of the WECs will not influence the cost of the farm. In fact, the cost of the WEC farm is difficult to estimate and there could be lots of uncertainties especially regarding the grid connection and installation costs. Some research tried to take in account the cost of the WECs, for example in [57] a cost function was used, defined as the ratio between the power and the total mass of the devices. Wave direction and number of WECs are important parameters for the optimization of the WEC arrays as reported in the research of Andres et al. [58]. In this work a triangular and square array layout with two body oscillating WEC were analysed concluding that the triangular configuration is more suitable with irregular sea.

BEM enables the calculation of the hydrodynamic forces acting on the WECs with arbitrary shape (see Chapter 2.1.2). However other methods must be considered for large arrays due to the limitation of the computational time. When large WEC arrays are considered simplifying assumptions are necessary such as small and vertical axisymmetric bodies oscillating in one single or double modes of motion [59, 60, 61]. Semi-analytical Array models can be used for this purpose (see Section 2.1.6).

Most of the research currently available about optimization of WEC array is related to Oscillating Wave Surge Converters and point absorbers [62, 63, 64].

The Oscillating Wave Surge Converters or flaps in the front of the WEC farm are discussed to have generally a better performance than the ones in the back [62]. Then a WEC farm staggering configuration in a 'bowl' or 'chevron' configuration is shown to be more efficient than a linear configuration [65].

The energy produced from a single row of point absorbers perpendicular to the incident wave has been investigated in [66]. It is found out that it can produce 50% of the incident power if the bodies are operated in one mode (heave) while it could produce all the energy that comes from the waves if operated in two modes (heave and roll). Moreover when the distance between the WECs is λ and the number of devices tends to infinity the power absorption may increase of a maximum factor of π when compared to a configuration with isolated WECs. A limitation of this work is that it is limited to harmonic analysis. Ocean waves will produce a significant averaging effect and a slow fluctuation of the interaction factor.

Evans has found that the mean absorbed power for point absorbers can be expressed as [67]:

$$\overline{P}_{abs} = \frac{1}{8B}|F_{ex}|^2 - \frac{B}{2}|U - \frac{F_{ex}}{2B}|^2 \tag{2.45}$$

where U is the complex number of the velocity of the device.
In this case the power is optimized when the second term is equal to 0 and so when:

$$U_{opt} = \frac{F_{ex}}{2B} \tag{2.46}$$

There is also a relation between the complex velocity and the displacement of each WEC device:

$$U = -i A_I \omega X \tag{2.47}$$

where A_I is the incident wave amplitude and X is the displacement.
So the optimal displacement that maximise the mean absorbed power of the device can be also found:

$$X_{opt} = \frac{i F_{ex}}{2\omega A_I B} \tag{2.48}$$

In particular it can be demonstrated that the maximum absorption length for point absorber array is equal to [68]

$$L_{abs} = \frac{\overline{P}_{abs}}{\overline{P}_I} = \frac{\lambda}{2\pi} N q \tag{2.49}$$

where N is the number of the devices, $\overline{P}_{abs}$ is the mean absorbed power from the farm and $\overline{P}_I$ the mean incident wave power per metre of wave front.
There is another important relation that describes the interaction factor for point absorbers [68]:

$$\frac{1}{2\pi} \int_0^{2\pi} q(\beta) d\beta = 1 \tag{2.50}$$

In particular the optimization process should maximize the interaction factor.
In [68] the optimization of the linear array configuration was related to the angle of the direction of the wave train and the position of the wave devices (see Figure 2.8).

A linear array configuration was considered with point absorbers equally distributed. The best wave incident angle β was found to be equal to 0 for 5 point absorbers and for smaller a-dimensional factors (kL where L is the length of the array and k is the wavenumber) while it converges to $\pi/2$ for bigger values of the a-dimensional factor (see Figure 2.9). The spacing between the WECs in a linear array has been also analysed [68] and it has been found that the best configuration is not when the devices are equally spaced. In fact, some asymmetric solution optimize the energy production. An optimized solution for $\beta = 0$ shows the devices closer together in the front of the array due to the positive effect of the radiated field.

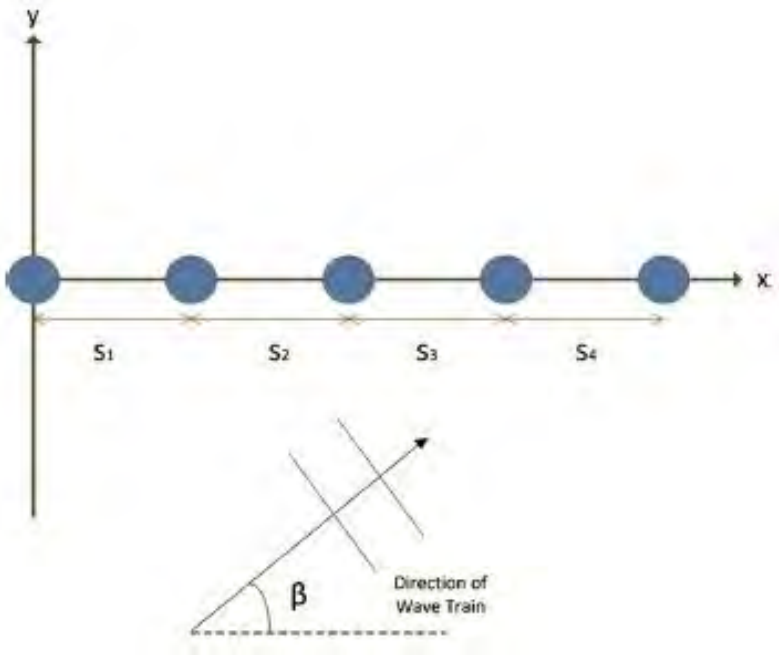

Figure 2.8: Linear array configuration [68].

A circular array has been also considered in this work showing larger values of the interaction factor [68]. In this case the best configuration has been obtained when the wave devices are in a semicircle.

Other WEC configuration could be considered such as an elliptical one but for the moment the results are not present in literature.

In the PhD thesis of Child [64] an optimization of an array configuration of point absorbers is considered using the direct matrix method (see Section 2.1.6). Two optimisation methods have been used to find the best array configurations: an heuristic approach called the Parabolic Intersection (PI) method and the Genetic Algorithm (GA). In particular each method was used to maximize the power produced with a given wave regular frequency and direction. Only the progressive terms of radiated and the scattered field were considered in the parabolic intersection. The evanescent terms are, in fact, negligible because they are generally smaller. This method enables only simplified calculation but with the advantage to be very fast. It is based on the fact that the constructive and destructive interference is given where the interactive wave field (scattered and radiated) are in or out of phase with the incident wave field [69]. In particular the strongest interference will be the closest in phase position to the device. The in-phase curves are approximated with parabolas. These parabolas shapes are constant because the relative phase keeps constant over time.

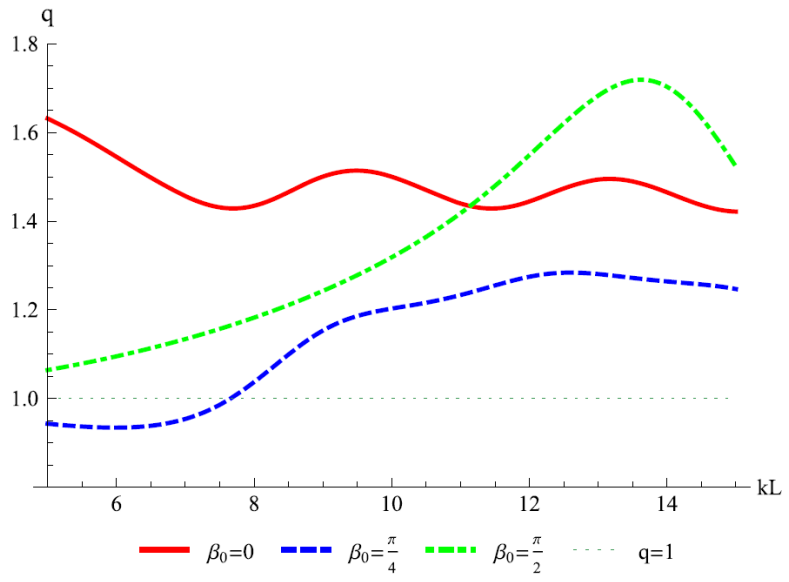

Figure 2.9: Interaction factor as a function of the a-dimensional length KL for a linear array of 5 point absorbers [68].

A farm of several hundreds of point absorbers can be optimized very efficiently using a multi-scattering method as described in [70]. This method has been then extended to allow WECs with different dimensions [71]. A hybrid array is optimized in [57].

A small array of four point absorbers connected to a coaxial moored disk has been optimized as a function of incident wave direction, separating distance between the absorbers and the PTO damping using a BEM approach [63]. All these factors have a great influence in the power absorption and have influence between each other. Looking in more details the power absorption as a function of the PTO damping, the power absorption first increases and then it starts to decrease slowly. It shows that there is an optimal PTO damping coefficient for each wave frequency. Different array layout were analysed in this work. In particular the square configuration compared with the rhombus and triangular configurations has given better results in terms of power production and a less sensitivity of the incident wave direction.

In the work of Borgarino et al. [72] a parametric analysis of a wave farm has been carried out, observing the influence of some parameters on the power production. In particular the influence of the device separation on the mean absorbed power is reduced if the PTO damping is optimized and if the WEC has a large power capture bandwidth. In this research a WEC farm between 9 and 25 devices have been considered using a BEM approach. Aquaplus [73] has been used for the computation of the hydrodynamic coefficients

of the WEC array. Generally a BEM approach is limited to small arrays but Aquaplus has recently been improved accelerating the hydrodynamic computation.
Generally, the computational time to simulate large WEC arrays using a BEM approach is too high. So a coupling with other methods is also possible. For example semi-analytical array models can be coupled with BEM to save computational time [74, 39]. Chakrabarti proposed a hybrid method that combines the BEM and the multiple-scattering method [74]. This hybrid method overcomes the limitation of the geometry of the multiple-scattering method and at the same time it requires less computational time than the BEM.
McNatt proposed in a similar way of Chakrabarti the coupling between the direct matrix method and the BEM [39]. McNatt developed a MATLAB open-source tool named mwave [75]. An application of mwave is possible to find in [76] for an array optimisation of fixed oscillating water columns.
Finally a coupled numerical model combining a wave propagation model (MILDwave) and a BEM (WAMIT) has been used by Stratigaky [77]. A large number of WEC point absorbers (25) has been considered in the optimization comparing experimental and numerical results.

2.3 Tank testing

2.3.1 Introduction

Tank testing is an important step to validate numerical results. So a careful and accurate gathering of the experimental data is necessary. In this chapter a description of the tank testing topic is presented with the aim of a better understanding of this complex subject.
WEC test experiments are used to simulate the energy capture investigating the parameters involved in the optimization [78]. Tests are done also to validate numerical models, in particular free oscillations and decay tests are necessary to calibrate input coefficients in the numerical model such as the viscous damping coefficient. Then survivability test could be carried out to simulate large device motion due to extreme sea waves and fatigue limit state tests to simulate fatigue limit states.
Useful information can be found from the recommended procedures of the International Towing Tank Conference (ITTC) [79, 78] and from [80, 81].
Technology Readiness Levels (TRLs) are used typically in industry environment to define the technology development [11]. The following stages are identified in the wave energy converter development (see fig: 2.10) [11]:

- The concept validation phase (TRL 1-3) validates the numerical model of the device and optimizes the device in relation to design variables. The device is usually tested with a scale range between 1:100 and 1:25.

- The design validation phase (TRL 4) develops PTO control strategies and verifies mooring system. Realistic survival conditions are also simulated in this stage. In this case the scale is between 1:25 and 1:10.

- The system validation phase (TRL 5-6) includes the testing of a fully operational PTO. It is tested at real sea at a sub-prototype size (1:4).

- The device validation phase (TRL 7-8) tests the device in full scale and it should validate the design already established experimenting new options.

- The economic validation stage (TRL 9) involves multiple device testing in small arrays (3-5 devices) in order to reduce the cost of energy.

The tank testing gives results about the motion of the devices, local wave elevations, wind and currents velocities, PTO quantities and mooring forces [78]. Different conditions

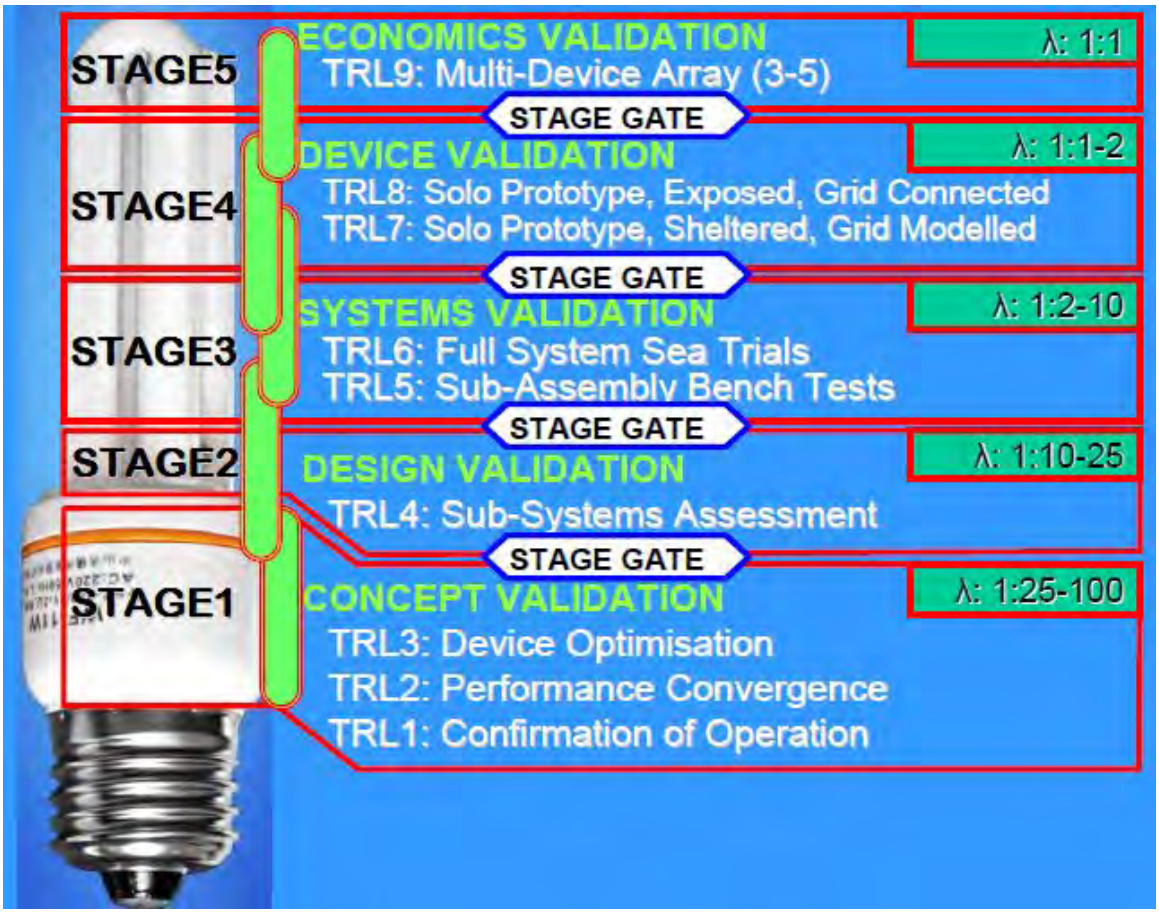

Figure 2.10: Stages of a wave energy converter [81].

should be verified for the accuracy of the experiments. These conditions are for example the test conditions that should be as similar as possible to the sea conditions. Currents, wind and mooring should be calibrated if used. The drift forces are due to cumulative wave actions and so they must be measured considering enough long runs. Moreover natural frequency should be considered carefully measuring the WEC device motion.

The tank testing must face scaling effects [78]. All the relevant forces of the real model cannot be simulated at the same time. For example the spring coefficient is not scaled correctly for a pneumatic PTO if geometric similarity is respected. Another problem for small scaled devices is the overestimation of the damping coefficients related to vortex shedding from sharp edges. The mechanical friction is also not scaled correctly assuming geometric similarity.

2.3.2 PTO and mooring modelling

The PTO is simulated at the beginning such as a simplified spring-damper system, then when it is reached an advanced phase a more realistic PTO is simulated. The various PTO have different ways to take measurements: the linear electric generator and the hydraulic system need a potentiometer for the measure of the velocity of the generator and of the piston respectively and a load cell to measure the force acting on them. Pneumatic PTO systems such as Oscillating Water Columns measure the pressure drop on the orifice thanks to a pressure gauge that is related with the flow rate on the air turbine. The last type is the overtopping PTO systems that just have the necessity to have the measures of the change in the reservoir level [78].

There are 2 main requirements that a WEC mooring system needs to satisfy that are to keep the device on station and to be cost effective [82]. In fact, a moored device will be offset mainly by steady wind, current and wave drift [83]. Then, the mooring system has an important impact on the economics and the challenge is to have low installation, maintenance and component costs and to be a reliable system [84]. More specifically, component costs are due to the mooring line and the anchor.

The mooring has a different influence on the WEC performance depending if it is catenary/slack or tight/taut. In particular, taut mooring should be simulated because it can have a significant impact on the WEC response [78]. Catenary mooring instead has generally less influence on the device motion. However, a wave device developer may want to exploit the high tensile forces of a taut mooring as part of the device design. A taut mooring could be made by a wire rope that is cheaper than the chain [82]. On the other side, a catenary mooring could use cheaper anchors such as gravity anchors because it needs to resist only horizontal forces [82].

As regards the numerical model of a mooring system, usually a taut mooring system can be simplified using a linear quasi-static method expressing the mooring force through the use of a stiffness and a damping matrix. More complexity is involved for a catenary system because inertia effects due to the larger weight of the mooring line are not negligible [85]. In this case a lumped mass system, that considers the mooring line as a series of short line elements, could be used [86]. A Finite Element Method could be also used to increase the accuracy of the results despite the increase in computational time. They are used especially for fatigue analysis and for extreme loads calculation [87].

A mooring can be use in passive, active or reactive functionality [88]. The WaveSub device is characterised by a mooring in a passive mode where the main purpose of it is the station

keeping of the reactor. So, its influence on the power production will be minimum.

2.3.3 Physical modelling, measurement and wave generation

There are three main topics related to tank testing: physical modelling, measurement and wave generation [89].
The WEC device concept design is investigated during the physical modelling. There are different laboratory facilities where the device could be tested:

- The wave flumes that are narrow tanks with a single paddle. The wave generated can be regular or irregular but only uni-directional.
- The towing tanks are similar to wave flumes but are usually longer and larger and have a mobile carriage to set in different position the models.
- The ocean wave basins are the largest one with a tendency to a squared ratio. In particular they are the only that can test the device using a 3D wave spectra. In this typology the wall effects are also reduced.

Figure 2.11 shows the Ocean Wave Basin at Plymouth University. In particular it offers the possibility to simulate waves and currents at any orientation and at different water depth.

The response of the WEC should be represented in a similar way between the model and the prototype. To obtain this there are different types of similarities: geometric, kinematic and dynamic [91]. Geometric similarity exists when the ratio between all the corresponding dimensions between prototype and model are the same; kinematic similarity when the ratio between the flow velocity at any point is the same and dynamic similarity when the ratio between the forces is equal. It is not possible to satisfy dynamic similarity of all the forces, so only the most important are considered such as the inertial force (F_i), the gravitational force (F_g) and the viscous force (F_V). These forces are expressed as following [91]:

$$F_i \propto \rho_w u^2 l^2 \tag{2.51}$$

$$F_g \propto \rho_w g l^3 \tag{2.52}$$

$$F_V \propto \mu u l \tag{2.53}$$

where l is the characteristic length.
In particular the relative influence of the inertial force on the gravitational and on the

Figure 2.11: Ocean Wave Basin at Plymouth University [90].

viscous force should be respected. The non-dimensional Froude number (Fr) and the Reynolds number (Re) are obtained [91]:

$$Fr = \frac{u}{\sqrt{gl}} \propto \frac{F_i}{F_g} \propto \frac{inertialforce}{gravitationalforce} \tag{2.54}$$

$$Re = \frac{\rho u l}{\mu} \propto \frac{F_i}{F_V} \propto \frac{inertialforce}{viscousforce} \tag{2.55}$$

However it is not possible to obtain a similarity for more than one non-dimensional number if it is used the same fluid and the same acceleration of gravity.

Another important topic is about the measurement in the wave tank. Sensors are necessary to measure the experimental results of a model. In particular displacement and velocity sensors should have low friction in the way to interfere as less as possible on the device motion. A cheap solution are potentiometers that can be used for rotational and linear motions. Another solution is the use of encoders with a digital output that are however more expensive. Higher accuracy is obtained using Linear and Rotary Variable Differential Transformers (LVDT and RVDT) but these instruments are still more expensive. Device motion can be measured also with optical capture. This method doesn't interfere mechanically. A leading provider of this kind of technology is Qualisys [92]. This method uses different markers on the the device and at least two cameras to cover the area in the device motion. The

cameras collect the position of the markers and then build the three-dimensional position of the markers. There are several good features of this approach such as the suitability for long distances between the cameras and the device and the possibility to know all the six degrees of freedom of the device.
The forces can be measured using strain gauges and piezoelectric sensors [89]. Strain gauges measure the force indirectly measuring the strain of the material. It is important to consider the influence of the temperature in the strain and to know the range of the forces that will be applied. Moreover also the geometry and the material of the device should be known. Piezoelectric sensors exploit the concept of electric charge accumulation in response to mechanical stress. These sensors however are not applied efficiently for static pressure because the voltage that they generate decrease with time. Moreover they can be used only in compression and so they are more limited compared with the strain gauges that can be used both in compression and in tension.
There are different types of wave gauges to measure waves [89]. For example float gauges measure the vertical displacement of the free surface. In particular the distance is calculated between the head of the transducer and the magnet inside the float.
Another type of gauge is the capacitance gauge [89]. It measures the depth of water measuring the capacitance caused by change in the partly immersed.
Ultrasound gauges are also used to measure waves [89]. They measure the time that the sound takes to return to the gauge after has been reflected by the water surface. In particular environmental factors should be accounted such as air temperature and humidity because they affect the speed of the sound in the air. The radar can be used to measure open sea areas. The process consists in irradiating the sea surface with electro-magnetic energy and detecting the corresponding reflection.
Conductive gauges are characterized by two vertical metal rods partly immersed [89] (2.12). The water height comes from the conductivity between the rods which increases with the immersion of the rods. Calibration is necessary quite often due to changes of conductivity of the water.

The last type are the optical gauges in which the spot generated by a laser light is detected by a camera [89].
Sometimes it is necessary to know the directional frequency spectrum [89]. In particular there are two ways to measure it: the first is to measure the surface elevation at at least three different locations while the second is based on a single point measurement but taking information about heave, pitch and roll of the buoy.

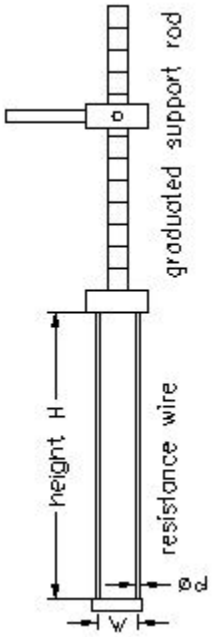

Figure 2.12: Conductive gauge [93].

The measurement obtained from the sensors has always some 'noise'. For this reason it is necessary to have signal processing. Low-pass filters are generally used to eliminate high frequency noise.

The last topic related to tank testing is wave generation [89]. Regular and irregular waves can be generated. Regular waves are used in the first stage of design, then irregular waves should be considered because they are more similar to a real sea. There are in particular two phases in wave generation: the first is the choice of the sea state that is sent to the wave maker and the second is the transfer function (Inverse Discrete Transfer Function) that converts the wave amplitudes of the irregular wave in the motion of the wave maker. There are different types of wavemaker: the main ones are the flap type and the piston type. The main distinction between the 2 is that the flap type is used to model waves in deep water while the piston type in shallow water because the horizontal water particle in the last one is approximately constant with the water depth [94].

Figure 2.13 shows an example of wave maker at the university of Naples [95]. In particular there are multiple flaps that can be used to create angle waves or to absorb cross waves. An example of software to control the paddles is the Wave Generating Software [96] developed by Edinburgh Designs Ltd .

Figure 2.13: Wave maker at University of Naples [95].

2.3.4 The WaveSub tank testing

In the last years the scale models of the WaveSub wave energy converter were tested in the Plymouth Ocean Basin. This Ocean Basin is 35 m long and 15.5 m wide. Waves are generated by a flap-type generator characterized by 24 flap wave makers of 2.0 m hinge depth. Different thesis were undertaken about the WaveSub tank testing especially for 1:30 Froude scaling [97, 98, 99, 100, 101].

The power performance of the WEC was investigated considering the characterization of the wave resource and the power matrix of the WEC. The wave resource is characterized with two methods: wave buoys and hind cast data obtained with numerical models. These two methods are often used together to define the wave resource. The difference between them is that the wave buoys give single local point while hind cast models give a field of points of wave data but more approximated. The wave resource is more difficult to characterize in shallow water because there are numerous effects to take in account: seabed friction reducing the wave height, refraction if the waves are not parallel to the contour of the seabed, diffraction due to obstacles in the wave fields, white-capping and wave-wave interactions. The FaBTest wave resource was chosen for the tank testing. This wave resource comes from 4 years of historical data from the wave buoy in FaBTest site.

During the tank testing different gauges were used: conductive wave gauges and load/strain

gauges. The position of the wave gauges were chosen in the way to measure directional waves and to take in account reflected and transmitted waves. Wave gauges signals were measured using Edinburgh Designs WG8USB Wave Gauge Controller while the waves where generated using the Edinburgh wave generating software. Load gauges were used to measure the PTO and mooring line forces.
Qualysis was used to measure the motion of the float and of the reactor. Different markers were positioned on them while a various number of infra-red cameras were used.
The local coordinates of the markers of the float and of the reactor were converted in global coordinates using a rotational matrix.

$$P_{global} = R \cdot P_{local} + P_{origin} \tag{2.56}$$

where P_{global} is the position of the point in the global reference system, P_{local} is the position of the point in the local reference system, P_{origin} is the position of the origin of the axes in the global reference system and R is the rotational matrix.
The data logging was done using National Instruments (NI) modular DAQ hardware. The NI modules were then connected to a laptop through USB connection. In [97] LabView was used to visualize in real time the electric output from the sensors. Moreover a trigger was used to correlate the time between all the instruments.
The PTO was simplified as a spring coefficient and a damping coefficient. The power was calculated from the product of the time derivation of the rope extension $L'(t)$ and the time dependent tension of the rope $F(t)$. The ropes were assumed rigid and so the time derivation of the rope extension was related with the time derivation of the spring extension. The power was obtained using this equation:

$$P(t) = \sum_{t=t_0}^{t_{end}} |F(t) \cdot L'(t)| \tag{2.57}$$

The model was also tested for extreme sea states [99, 100]. Real data from wave buoys were taken from a very energetic location located off the north coast of Belmullet. The significant height and the peak period, necessary for the calculation of the spectra, were then calculated with an extreme value theory called Peaks Over Threshold method. This method consists of fitting the generalised Pareto distribution to the peaks of excesses over a threshold. Two extreme sea states were considered: the Storm Default Case configured in its operational mode and the Storm Survival Case configured in survival mode. This last

configured with the float at the centre of the base but with the base at the same position.
In Paul [100] the PTO was simulated as a flat brushless AC motor where the motor controlled the extension and retraction force in the PTO lines and it was connected to a Simulink acquisition model. The mooring was a four lines taut system in high modulus polythylene.
Finally an investigation of the relationship between the power produced and the operational depth was made [102].

2.4 WEC market

2.4.1 Introduction

Wave energy technology is presented in this chapter in terms of economic competitiveness. The Cost of Energy is an important economic parameter that inform us about the economic competitiveness of a particular device. This parameter is influenced by different factors (see Figure 2.14): lifetime costs (capital and operating) and the energy produced. Introducing the discount rate to translate future costs and revenue to the present time, the Cost of Energy is better called Levelized Cost of Energy (LCOE). Capital costs are mainly at the beginning

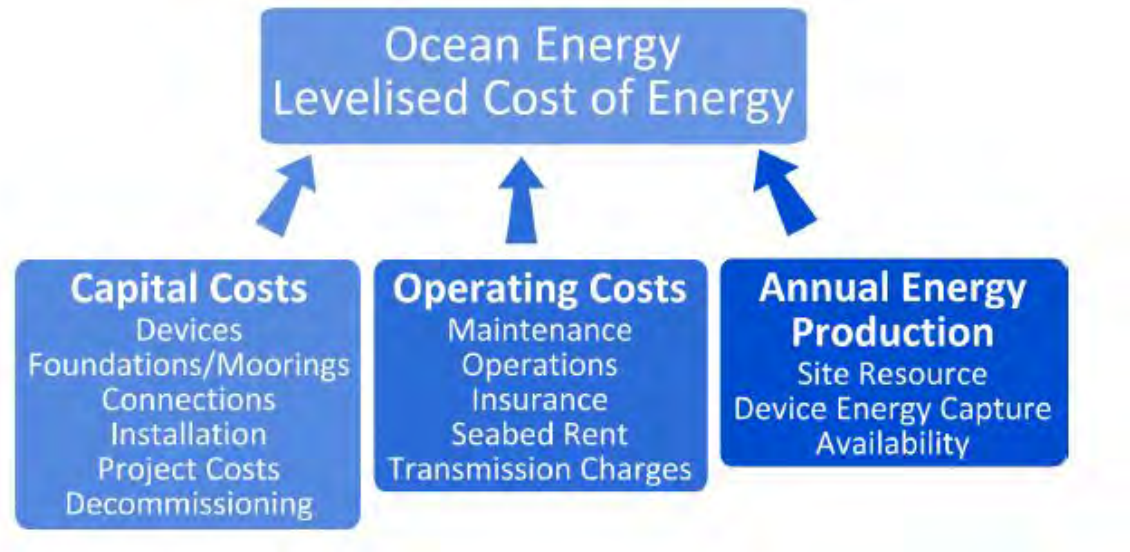

Figure 2.14: Factors influencing LCOE [103].

of the lifetime of the device while the operating costs are spread over the lifetime period. The capital costs can be divided in 7 components [104]:

- The structure can be obtained as a simple product of the material weight and the specific cost of the material. However the complexity of the shape structure should be taken in account but in a first approximation is negligible.

- The Power Take Off system is designed as a function of the peak power of the device. In particular the optimal PTO that minimize the cost of energy may not be the one that captures all the waves from the sea including the largest energy waves. This is because the largest waves occur quite rarely and so it would be not used most of the

time at these high power levels and the cost of it will be large. The cost of the PTO can be approximated proportional to the rated power of the PTO.

- The mooring costs could be taut or catenary. There are different types of anchoring and foundation available to suit the types of seabed. In particular the mooring system is designed to resist to extreme loads.
- The installation costs depends specifically on the device and on the choice of the vessel used for the installation process.
- The grid connection is strongly dependent on the distance from the shore, the condition and the depth of the sea bottom and the amount of power transmitted.
- The project and management is very hard to predict; so in a first analysis this cost is taken in account as a percentage of the overall costs.
- The decommissioning is estimated to be small compared to the initial capital costs. It is not considered in a first analysis.

The other main important source of costs are the operating costs. These costs can change quite significantly from year to year and are quite difficult to estimate especially given the lack of experience in the sector. There are in particular 2 types of maintenance: planned and unplanned. The costs of an unplanned maintenance can be very high due to the early development stage.
The LCOE can be found with the following Equation [105]:

$$LCOE = \frac{CAPEX + \sum_{t=1}^{PLT} \frac{OPEX_t}{(1+r)^t}}{\sum_{t=1}^{PLT} \frac{E_{year-t}}{(1+r)^t}} \tag{2.58}$$

where PLT is the project life time, r is the discount rate and E_{year-t} is the energy produced each year.
The typical considered discount rates are between 8% and 15% for marine energy [105]. Discount rates represent the risk of a project: the higher the discount rate the higher the expected income of the investor [104].
An ideal design methodology to estimate the LCOE is described in [106]. Four main modules are considered: Design and Analysis, Manufacturing and Deployment, Operation and Maintenance and Environmental Compliance.
There are other important economic parameters that can help for key decisions of a project:

the Net Present Value (NPV), the Internal Rate of Return (IRR) and the Profit Investment Ratio (PIR).
The NPV describes the cash flows over a certain period of time. It is used to have an estimation of the profit subtracting the present values of incoming and outgoing cash flows. In particular projects are designed when the NPV is positive that means that total benefits are more than total costs. Generically, the NPV can be expressed as following for a certain number of years (N) [107]:

$$NPV_{i,N} = \sum_{year=1}^{N} \frac{Cash_{year}}{(1+r)^{year}} \tag{2.59}$$

The IRR is a popular key decision economic parameter defined as the discount rate at which the NPV calculated for the lifetime of the project is equal to 0. Higher values of this values are preferable and generally projects should be chosen when this value is more than the company's average investment opportunity rate [108].
Finally the PIR gives information about the amount of value created per unit of investment and it is defined as following [109]:

$$PIR = \frac{NPV_{i,PLT} + CAPEX}{CAPEX} \tag{2.60}$$

The selection of a project is based on the value of this parameter: only projects with this economic parameter higher than 1 are accepted.
All these economic parameters could be used for the optimisation of a certain project. In particular the NPV gives more information about the final company profit while the IRR and the PIR give more an idea about the economic efficiency.

2.4.2 Current situation

The current ocean energy development is characterized by a high CAPital EXpenditure (CAPEX), high OPerating EXpenditure (OPEX), low capacity factors and low reliability of devices. Due to these issues the electricity production from this source is still very low globally. The policy in lots of countries in Europe generally is supporting the ocean energy technology with a market support system. An example is the use of feed-in-tariff and feed-in premium with rates range between 30 €/MWh and 300 €/MWh (see Table 2.5). UK offers support to wave energy through the Contract for Difference programme

providing financial support to the generators when the wholesale electricity prices are lower than a strike price [110]. Table 2.5 show the main organizations and projects for European countries with a more developed policy towards ocean energy. Some of the projects involve different countries such as DTOcean+ [111], MARINERG-i [112] and Foresea [113]. UK has a strong investment in marine energy sector with his own organizations such as Wave Energy Scotland [114] and ORE Catapult [42].

Table 2.5: Pull mechanisms for ocean energy in the EU in 2019 [9, 115, 116, 117].

Country	**Tariff**	**Main projects and organizations**
Denmark	Premium tariff. Maximum subsidy of 170 €/MWh.	MaRINET2, DTOcean+, MARINERG-i, OES Task 10, Aalborg wave energy research group.
France	Feed in tariff. Maximum tariff of € 182/MWh.	WEAMEC, Foresea, MaRINET2, THeo-Rem, MARINERG-i.
Germany	Feed-in Tariff for ocean energy between 35 and 125 €/MWh depending on installed capacity.	TidalPower, SCHOTTEL HYDRO, NEMOS.
Ireland	Feed in tariff. 260/MWh up to 30 MW from 2016.	MaREI, NOTF, OPERA, FloTEC, MaRINET2, MARINERG-i, Foresea, INTERREG, MEA.
Italy	Feed in tariff. For projects until 5 MW 300 €/MWh For projects >5 MW 194 €/MWh.	PELAGOS, MAESTRALE Interreg Projects, Blue Energy Cluster Web Platform.
The Netherlands	Feed in premium. Maximum subsidy of 130 €/MWh.	SeaQurrent, Redstack, Tocardo, Tidal Technology Centre.
United Kingdom	Contracts for Difference (CfDs). Draft strike price of 281 £/MWh for wave technology for 2023/24.	Wave Energy Scotland, Foresea, Supergen, ORE Catapult, Innovate UK, UKRI.
Portugal	Feed in tariff. Maximum tariff of 260 €/MWh.	MaRINET2, DTOcean+, MARINERG-i, SEA-TITAN, MEGAROLLER.

The current LCOE of wave energy is between 60 c€/kWh and 110 c€/kWh for an average resource [9]. The reference value that is obtained as average between these 2 values is 85 c€/kWh. The 2025 target of 20 c€/kWh will be reached only when the installation of cumulative capacity will reach 10 GW as can be seen in Figure 2.15. As regards to the capacity factor the reference value is estimated of 25%.

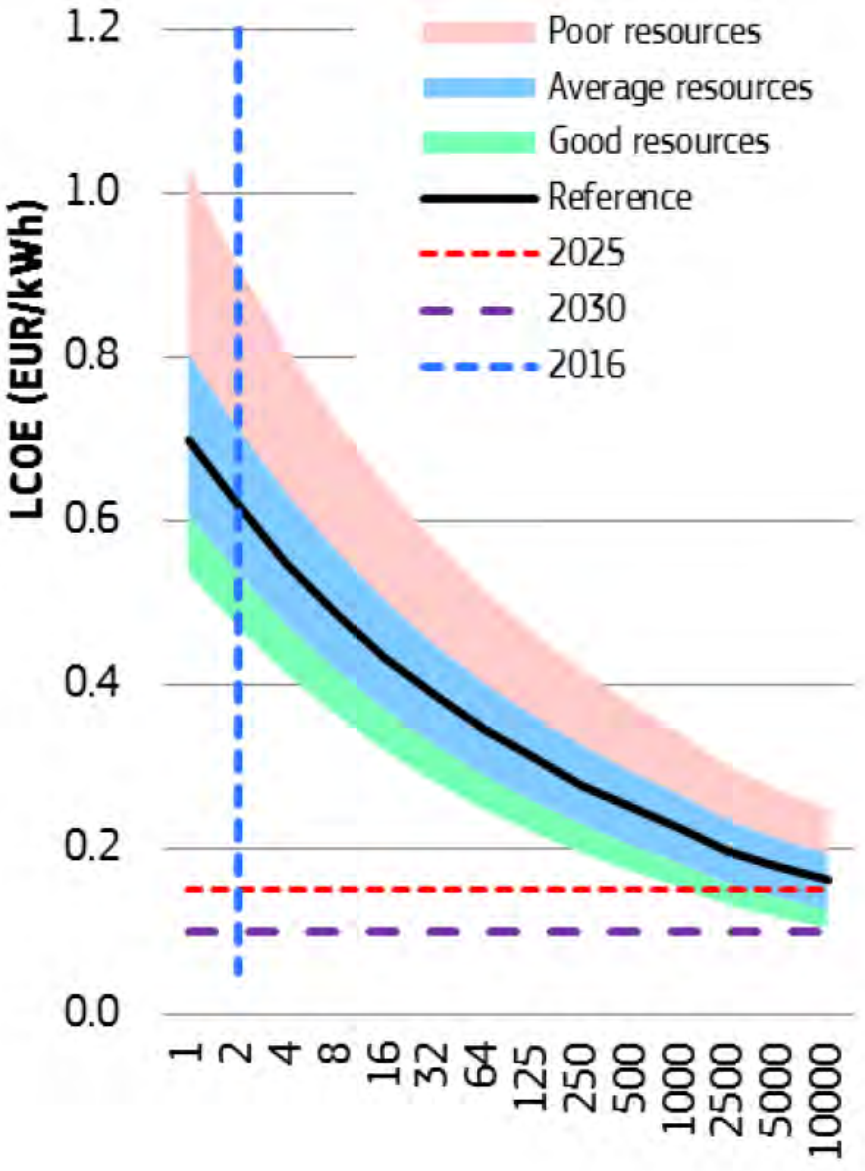

Figure 2.15: LCOE predictions for wave arrays [9].

2.4.3 Nearshore vs. Offshore

Near-shore devices are more subjected to breaking wave loads. So a careful design of the structural requirements should be taken in account. Off-shore technologies instead are more difficult to reach for maintenance and to connect with the electrical grid. For these reasons the off-shore WECs have still costs too high despite the higher wave resource.
A simple cost model was implemented in a Carbon Trust project to identify the areas with a lower cost of energy [118]. The cost of energy was determined as a function of the water depth and of the distance from the shore using a generic floating device. Figure 2.16 shows that the LCOE decreases until the sea bottom changes sharply. In fact, the mooring costs begin to predominate after this area.

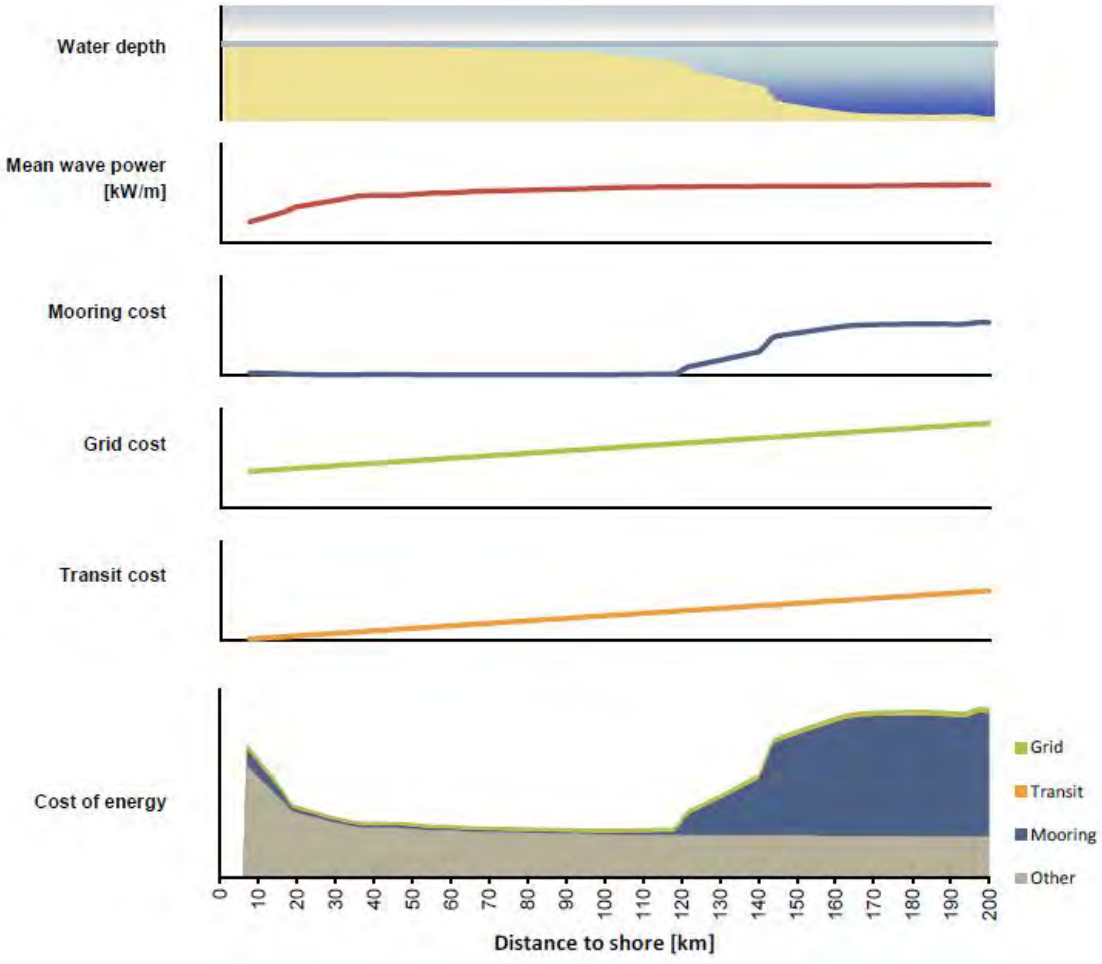

Figure 2.16: Illustration of the trade-off between cost of energy and distance to shore [118].

The cost of energy was calculated in the UK coasts with the aim to find the best areas for the setting of WECs devices (see Figure 2.17). In particular the considered near-shore technology was the Aquamarine's Oyster while the off-shore technology was described by a frequency-dependent capture width of a candidate floating WEC.

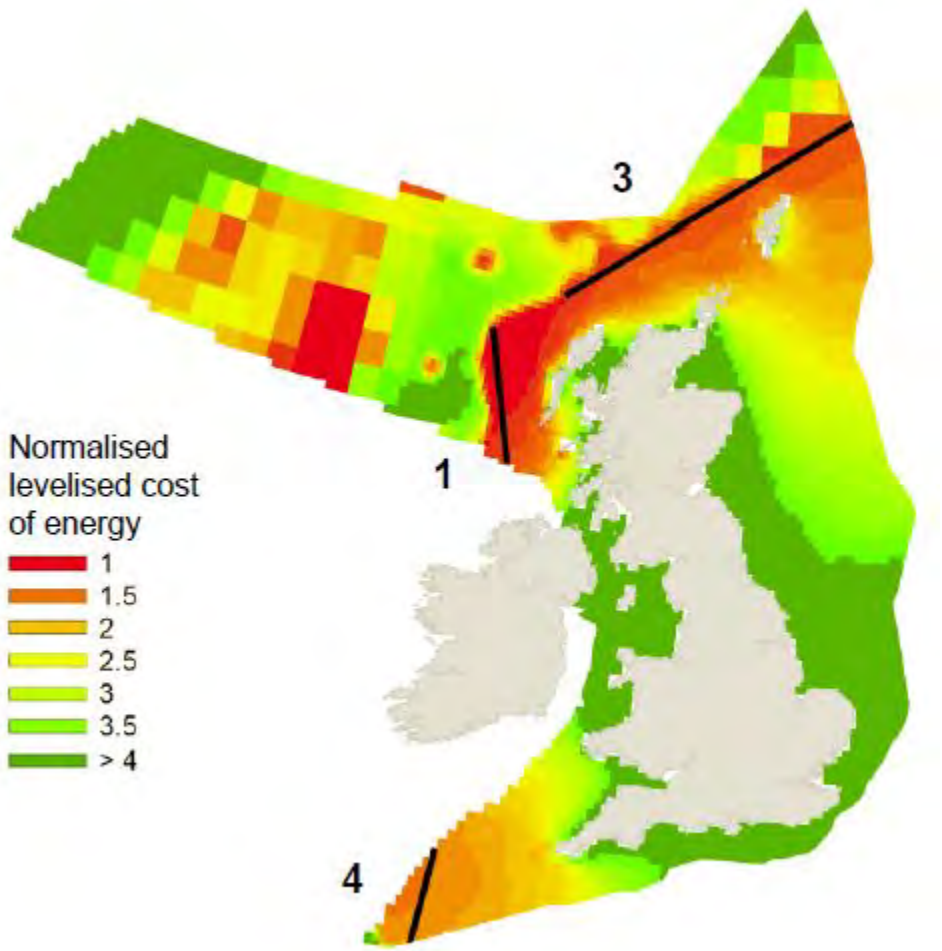

Figure 2.17: Cost of energy analysis in the UK coast [118].

2.4.4 Cost reduction opportunities

The LCOE can be reduced significantly acting on the CAPEX and on the OPEX. Two different cases of cost reduction are shown in Figure 2.18. In particular a reduction of 85% is obtained combining all the measures together. The best options of reduction opportunities are from the mechanical equipment and installation and from the OPEX. In fact, they determine a significant reduction of the LCOE with only 20% cost reduction. There are

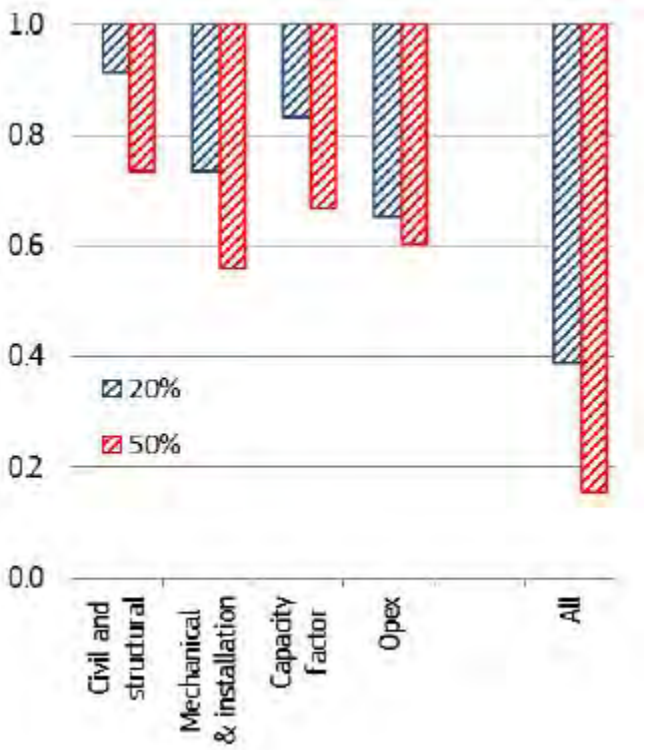

Figure 2.18: Reduction of 20% in blue and of 50% in red for each cost component. The capacity factor is shown instead with an improvement of 20% in blue and of 50% in red [9].

different ways to reduce the cost of a particular device [103, 119]. These are related mainly to:

- The scale and number of devices. A bigger scale decrease generally the LCOE because the installation cost doesn't increase proportionally. Moreover a larger number of similar devices reduces the cost of each individual device because of the serial production.

- Learning by doing. This can improve the efficiency of the device production reducing the cost. Moreover O&M strategies can be improved to reduce the OPEX costs.
- Innovation. This involves every aspect of the device from the installation techniques to the device components.
- Cost of Capital. The maturity of the technology will determine a decrease of this rate of return.

Figure 2.19 shows the time-line of the LCOE reductions. The increased installed capacity will determine mainly these reductions.

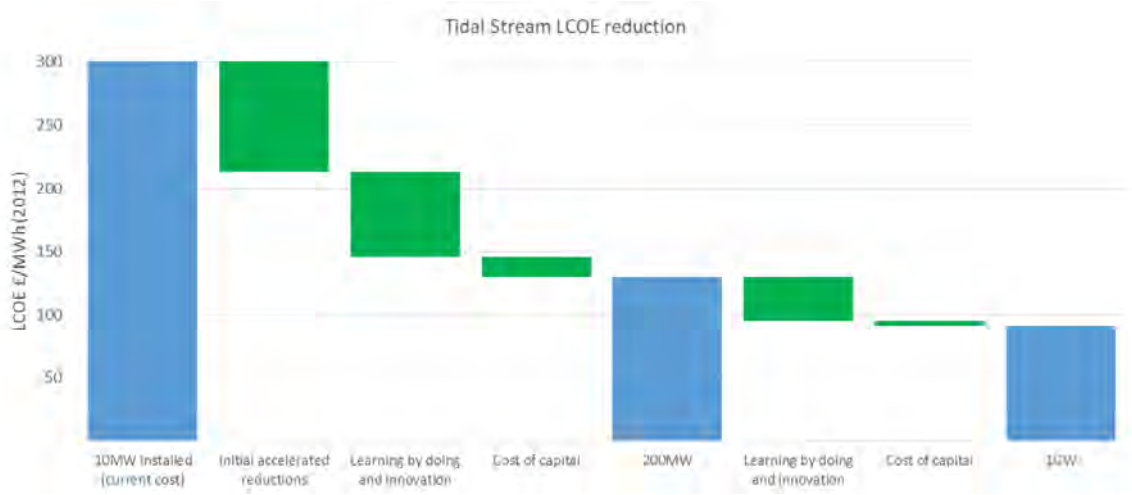

Figure 2.19: LCOE reduction [119].

The innovation and the optimization are the main factors that the developers must face in the design of the WECs. There are different components of the WEC that should be considered in the optimization:

- The structure. This component must respect the survivability condition. The cost of this component could be reduced by using a better design. The structure should also consider hydrodynamic design performance if it is foreseen to be tuned with the waves.
- The Power Take Off (PTO). Some significant cost reduction are foreseen for the future especially in relation with a control system that changes the PTO parameters as a function of the coming wave.

- The mooring and foundations. The possibility to reduce cost of this component are quite limited because there has been significant research in the off-shore wind industry. However there is still some on-going research [82].
- The electrical connection or grid connection. There are limited cost reduction possibility also for this due to the offshore wind industry optimization.
- Installation. This cost can be reduced using more efficient installation techniques especially for the foundation.
- The Operating and Maintenance (O&M). There are 2 ways to reduce this cost: to build a very robust and reliable device and to design a device that is simple to recover and maintain.

2.5 The theory of multi-directional wave fields

2.5.1 Introduction

Wave Energy Converters (WECs) are very often simulated in bi-dimensional waves but a more accurate simulation that represents a more realistic sea state should account for multi-directional waves. Variations are associated with modifications of the significant height, energy period and directional characteristics. Generally, WECs have a reduction of their performance when the wave directional spread is larger. Consequently, the estimation of the influence of the wave direction on a particular WEC should be considered carefully.
The assumption of this analysis is linear potential flow (see Section 2.1.2). The theory is given for multi-directional waves and irregular waves but it is also valid for single wave direction and regular waves just considering one wave direction and frequency.
The theory of the wave fields calculation is obtained with the help of a tool developed by Cruz Atcheson Consulting Engineering [120]. Then the calculation of the excitation force generated on a certain WEC has been presented for multi-directional waves using the superposition principle of the linear wave theory.

2.5.2 Theory

Use of a probabilistic distribution of wave direction is assumed to be sufficiently accurate to describe the characteristics of a multi-directional sea state in a temporal sense. More specifically, it is proposed that the frequency-directional spectrum ($S(f)D(\beta)$) is the product of the frequency spectrum ($S(f)$) and the directional distribution [121]:

$$S(f,\beta) = S(f)D(\beta) \tag{2.61}$$

Where f is the wave frequency and β is the angle relative to the mean wave direction. The directional distribution (D(β)) is assumed to be independent of the frequency. This result will give just an approximation. In fact, a more accurate directional distribution should be a function also of the frequency. Examples of directional spreading dependent also on the frequency are Mitsuyasu [122], Hasselmann [123], Donelan [124] and Donelan-Banner [125]. A general approach is shown in [126]. In particular, each climate location will have a different directional distribution. The directional distribution model has been chosen as a

Gaussian one but also a “cosine2s” form could be also used [121]:

$$D(\beta) = \frac{1}{\sigma\sqrt{2\pi}} \exp\left(-\frac{\beta^2}{2\sigma^2}\right) \tag{2.62}$$

where σ is the wave directional spread and β is the wave direction. The directional distribution fulfils the requirement:

$$\int D(\beta, \omega) d\beta = 1 \tag{2.63}$$

The sea surface elevation dependent also on the wave directions can be expressed as following:

$$\eta_I(x, y, t) = \sum_{n=1}^{N_f} \sum_{m=1}^{N_d} A_{I,nm} cos(k_n \cdot (x \cdot cos(\beta_m) + y \cdot sin(\beta_m)) - 2\pi f_n t + \phi_{I,nm}) \tag{2.64}$$

Where $A_{I,nm}$, f_n, k_n, $\phi_{I,nm}$ are respectively the amplitude, frequency, wave number and phase for each incident directional wave evaluated for a specific point of the wave field (x,y). N_d and N_f are the number of wave directions and frequencies. A visualisation of the various directional components of the surface elevation is shown in Figure 2.20.

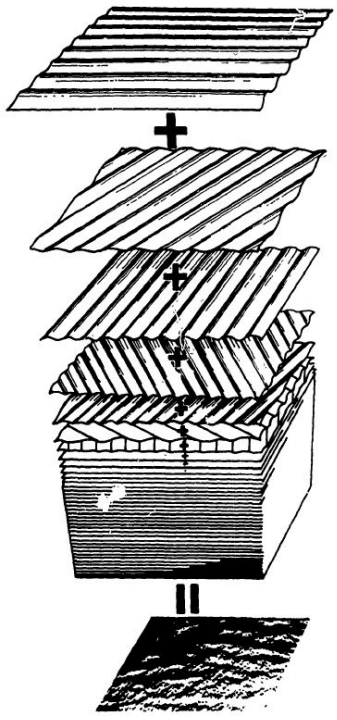

Figure 2.20: The sum of many simple sine waves make a sea [127].

Sea surface elevation can be then expressed as a function of the wave frequency spectrum thanks to the relation between the wave amplitudes and the wave spectrum. The relation is expressed for a discretized frequency step (Δf) as [7]:

$$A_{I,nm} = \sqrt{2S(f_n)D_m\Delta f} \tag{2.65}$$

There are different wave spectrum that describe the ocean wave. The most used are the Darbyshire spectrum, the Bretschneider spectrum, the Pierson-Moskowitz spectrum and the Joint North Sea Wave Observation Project (JONSWAP). In particular the JONSWAP spectrum was developed from the Pierson-Moskowitz spectrum adding a peak enhancement factor (γ).
The significant height can be obtained from the spectrum through the introduction of the spectral moments (m_n). The spectral moment and the significant height are expressed as following [128]:

$$m_n = \int_0^\infty f^n S(f)df \tag{2.66}$$

$$H_s = 4\sqrt{m_0} \tag{2.67}$$

The mean energy period can be also defined [128]:

$$T_e = \frac{m_{-1}}{m_0} \tag{2.68}$$

The mean incident power for an irregular wave is equal to [7]:

$$\overline{P}_I = \int_0^\infty E(f)v_g(f)df = \int_0^\infty \rho_w g S(f)v_g(f)df = \rho_w g \int_0^\infty S(f)v_g(f)df \tag{2.69}$$

The mean incident power in deep water is found substituting the expression of the group velocity (Table 2.1) and of the spectral moments (Equation (2.66)):

$$\overline{P}_i = \frac{\rho_w g^2}{64\pi} \cong 0.49 H_s^2 T_e [kW/m] \tag{2.70}$$

Wave fields are summarized in the incident, diffracted, radiated and perturbed fields [120]. After that the time domain wave fields are determined considering the real part for each point P(x_P, y_P) of the wave field [120]:

$$\eta_{IP}(t) = Re(\sum_{n=1}^{N_f}\sum_{m=1}^{N_d} A_{I,nm} e^{-2\pi f_n t + K_{nmP} + \Phi_{I,nm}}) \tag{2.71}$$

$$K_{nmP} = k_{nP} \cdot (x_P \cdot cos(\beta_m) + y_P \cdot sin(\beta_m)) \tag{2.72}$$

$$\eta_{DP}(t) = Re(\sum_{n=1}^{N_f} \sum_{m=1}^{N_d} A_{I,nm} A_{DP,nm} e^{-2\pi f_n t + \Phi_{I,nm} + \Phi_{DP,nm}}) \tag{2.73}$$

$$\eta_{RP}(t) = Re(\sum_{n=1}^{N_f} \sum_{m=1}^{N_d} \upsilon_{nm} A_{RP,nm} e^{-2\pi f_n t + \Phi_{\upsilon,nm} + \Phi_{RP,nm}}) \tag{2.74}$$

Where $A_{DP,nm}$ and $\Phi_{DP,nm}$ are the amplitude and phase of the diffracted field, $A_{RP,nm}$ and $\Phi_{RP,nm}$ are the amplitude and phase of the radiated field, υ_{nm} and $\Phi_{\upsilon,nm}$ are the amplitude and phase of the bodies velocities. η_{IP}, η_{DP}, η_{RP} are respectively the incident, diffracted and radiated wave fields. A summary of the amplitude and phase obtained from Nemoh and WEC-Sim is shown in the following Table 2.6:

Table 2.6: Summary of the wave field parameters.

	Nemoh	**WEC-Sim**
Incident wave field	β,f	A_I,k,β,f,Φ_I
Diffracted wave field	A_D,Φ_D	A_I, f,Φ_I
Radiated wave field	A_R,Φ_R	v,Φ_υ

Finally the total perturbed wave field can be calculated as the sum of the incident, diffracted and radiated fields:

$$\eta_{PP}(t) = \eta_{IP}(t) + \eta_{DP}(t) + \eta_{RP}(t) \tag{2.75}$$

Wave fields in the frequency domain are obtained using Equations 2.71, 2.73, 2.74, 2.75 but without accounting the time term $2\pi f_n t$ of the exponential term. The frequency wave field considers the complex results and not the real one because it gives information both of the amplitude and of the phase. The significant height can be used to describe the frequency wave fields and can be expressed as following [7] for each point P(x_P, y_P) of the wave field:

$$H_{sP} = 4\sqrt{\sum_{n=1}^{N_f} \frac{abs(\eta_{IPn}(f))^2}{2}} \tag{2.76}$$

The significant height for multi-directional waves can be obtained from the surface

elevation in the frequency domain through the summation for all the wave directions [128].

$$\eta_P(f) = \sum_{m=1}^{N_d} \eta_P(f, \beta) \tag{2.77}$$

The wave generates on the WEC following the linear potential flow theory (see Section 2.1.2) mainly the excitation force. The radiation force is then generated because of the motion of the WEC. The time domain excitation force can be expressed as following for multi-directional waves and considering the superposition principle of the linear wave theory:

$$\begin{aligned} \mathbf{F_{ex}}(\mathbf{t}) = \sum_{n=1}^{N_f} \sum_{m=1}^{N_d} \sqrt{2S(f_n) D_m \Delta f} \cdot \\ Re(\mathbf{F_{ex,n}} \cdot exp(i2\pi f_n t + \Phi_{I,nm})) = \\ \sum_{n=1}^{N_f} \sum_{m=1}^{N_d} \sqrt{2S(f_n) D_m \Delta f} \cdot (Re(\mathbf{F_{ex,n}}) \cdot cos(i2\pi f_n t + \Phi_{I,nm}) \\ - Im(\mathbf{F_{ex,n}}) \cdot sin(i2\pi f_n t + \Phi_{I,nm})) \end{aligned} \tag{2.78}$$

Chapter 3

Design and modelling of the WaveSub device

3.1 Numerical modelling methodology

3.1.1 Introduction

A numerical modelling methodology to simulate a multi-float configuration of the WaveSub device is described in this chapter. The multi-float configuration will be investigated in a small number of floats and so, a frequency domain model has been selected as an appropriate numerical model. Frequency domain models are based on a linear potential flow that is used to obtain the hydrodynamic forces acting on the WaveSub device (see Section 2.1.2). There are several limitations between which an inviscid fluid that assumes small motion of the device compared to its characteristic dimension.
To overcome this limit, a time domain model has been coupled with the frequency model. In fact, it gives the possibility to add an estimated drag force to the device.
A time-domain simulation is carried out so that it is possible to account for the non-linearities coming from the hydrodynamics, the PTO and the mooring. The first non-linearity coming from the hydrodynamics is related to the memory term of the radiation force of Equation 2.31. The other non-linearity coming from the hydrodynamics is related to the viscous force that is usually modelled as a quadratic term as described in Equation 2.26. The PTO and mooring forces have been, instead, linearised for computational time reasons but there is the potential to expand the same model with more complexity. The Cummins Equation (see Equation (2.31)) is used to solve the time domain simulation accounting for the hydrodynamic forces, PTO and mooring forces.
The most important factors that have contributed to the choice of a time domain model instead of an only frequency domain model are related to more confidence of the results and to be able to simulate the non-linear response of the wave energy device. In fact, a time domain model gives the possibility to observe in real time the response of the device under sea states.

3.1.2 The design of the WaveSub device

The WaveSub is a wave device developed by the Marine Power Systems (MPS) company [129]. Different improvements were made during the last years to increase the energy efficiency of the device. Since the formation of the company in 2008, different collaborations between MPS and postgraduate students from Plymouth University have contributed to im-

prove the design of the device [101].
The device is a point absorber device and it is characterized by a reactor and a floater completely submerged. The floater is near the free surface, at a location where it can follow the more powerful and largest wave orbits. The floater will be mainly a combined heaving and surging device.
The energy comes from the relative motion between the floater and the reactor. In particular the PTO is on the reactor and it exploits the variation of the cable length between the reactor and the floater.
The device follows the waves orbit that is circular in deep water while it becomes elliptical in intermediate depth (see Fig: 3.1).

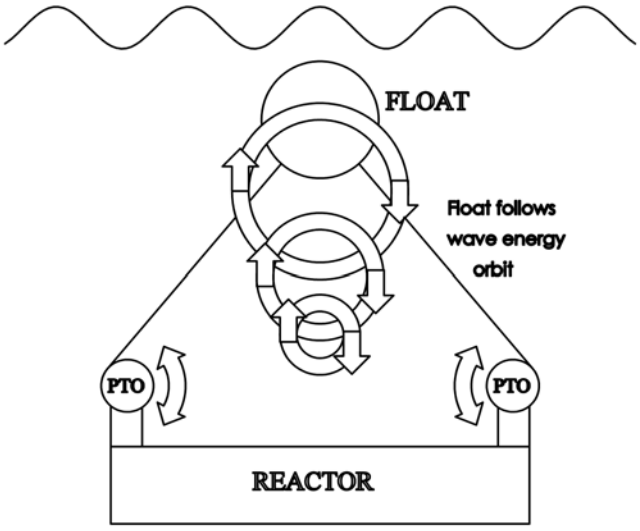

Figure 3.1: The motion of the floater.

There is a PTO on each corner of the reactor. The motion of the cables is converted in high hydraulic pressure in four sealed rams. The high pressure is stored in an accumulator and then turned into electricity through a hydraulic motor. There is also another central tether designed but it is not supposed to produce energy. The aim of this line is to reduce the pre-load on the corner cables.
The relative distance between the reactor and the floater can be changed with the aim to be tuned with the different sea states. In particular the reactor can be set at different sea depth including the survival option in which the device is deep enough to survive the storms.
The $1/4^{th}$ scale of the device was deployed at FaBTest [130] in Falmouth and recently the testing has been completed successfully. The reactor is 15 m long, 10 m wide and 2.5 m tall. At the time of writing, the full scale is expected to be 40 m long and will produce

around 1.5 MW at peak capacity.

A multi-float WaveSub is characterized by multiple floats connected by PTO lines to the same reactor (see Figure 3.2). The reactor is then connected to the seabed with mooring cables.

There has been some updates of the design of the device throughout the duration of the

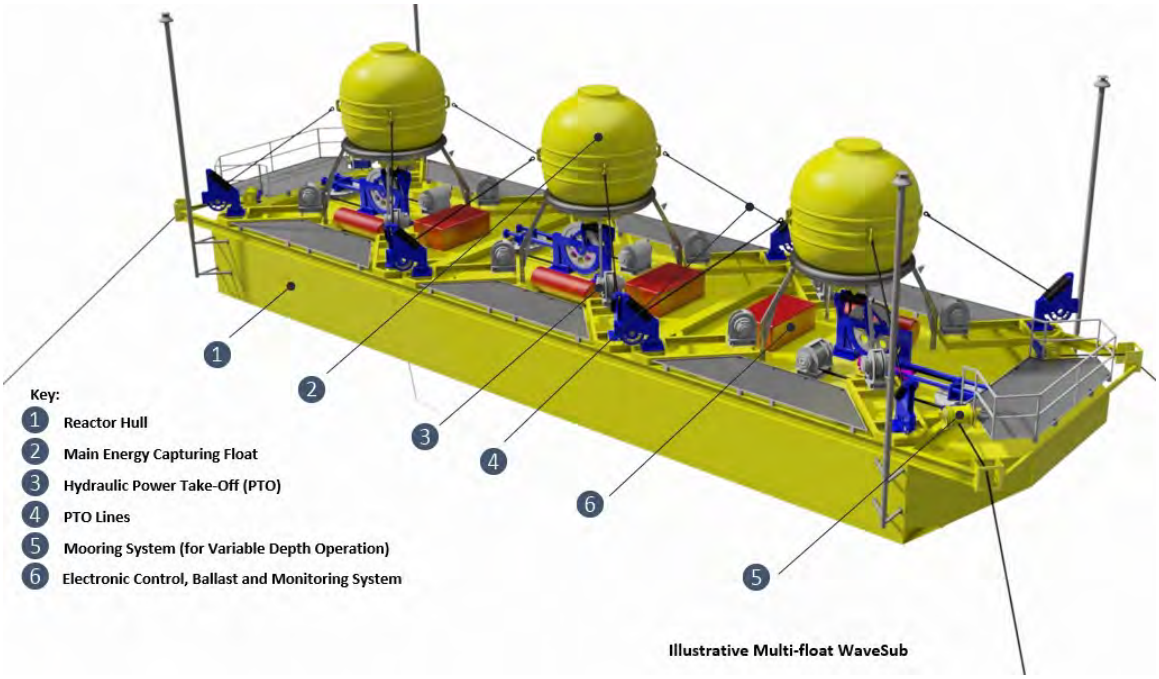

Figure 3.2: Illustrative multi-float of the WaveSub.

PhD project (see Table 3.1). These are mainly related to the reactor and float shape and net buoyancy and to the number of PTO and mooring lines.

Table 3.1: Summary of the differences between the two WaveSub design used.

	I Design	**II Design**
Mass float	7-8% of the displaced mass	80% of the displaced mass
Float shape	Capsule shape	Sphere
Reactor shape	It is simplified as a cuboid shape.	Framework of steel tubes connected to air filled tanks.
PTO lines per float	5	4
Mooring lines per reactor corner	1	2

The first numerical model has been based on the design of the tank testing conducted by MPS in March, June and July 2017 in Plymouth University's Ocean basin. This numerical

model is used for the benchmarking between the numerical model and the tank testing and for the optimisation of a linear multi-float design. The floats are designed to have a large buoyancy. The mass of each float is supposed to be around 7-8% of its displaced mass. The floats are characterized by a capsule shape with a cylinder in the middle and hemispheres in the sides. In previous work a frequency domain optimisation carried out by MPS suggested this geometry shape. The reactor is characterized by a metal frame and by big water tanks to have a larger inertia mass and inertia moments. The large net buoyancy of each float requires 5 PTO lines. Four of them are connected to the power generator while the central one is just a spring to reduce the loading to the corner PTO lines. As a result of this design the reactor shape could be simplified for the calculation of the hydrodynamic coefficients as a cuboid shape. A mooring line is connected from each corner of the reactor to the seabed.

The second numerical model has been based on updates of the design from MPS Ltd and has been used for the optimisation of different multi-float design. The net buoyancy on each float has been reduced despite a relationship that decreases the power produced. The mass of the float is obtained as 80% of the displaced mass. The decrease of the power produced has been considered negligible compared to the fact that the central PTO line was no longer necessary due to the decrease of the float buoyancy loading. The float shape in this case is simplified as a sphere. The optimisation of the float shape for a multi-float configuration is still not considered. The conceptual design of the reactor in this second phase is a framework of steel tubes that connect to the float PTO lines. These tubes are also connected to a number of air filled tanks which are designed to achieve the desired buoyancy. Two mooring cables are designed for each reactor corner (one vertical and the other describing a certain angle) to give more stability to the reactor.

The full scale device is considered in the numerical model. The numerical optimisation process enables the design team to investigate different multi-float configurations at a very low cost. However tank testing validation will be necessary to increase confidence in the numerical results.

3.1.3 The methodology

There are different steps to simulate a wave device numerically. Both commercial code or open-source code could be used. An open-source code is preferable in terms of research purpose because it is more easily accessible. Then it can be used and improved by a large

group of people.

Figure 3.3 shows a flow chart of the suggested numerical modelling for a wave energy device using different open-source software. A main MATLAB script is used to run both Nemoh (see Section 3.1.5) and WEC-Sim (see Section 3.1.6). The script contains the input simulation parameters input for Nemoh. Nemoh requires from the user the mesh .dat file for each hydrodynamic body obtained from Salome-Meca (see Section 3.1.4). WEC-Sim then needs the hydrodynamic coefficients from Nemoh, a geometry .stl file for each hydrodynamic body for the visualization of the time domain simulation in Mechanics Explorer (Simulink tool), a WEC-Sim input file for the definition of the input of the simulation and a Simulink file for the definition of the dynamic system. The most interesting results of the time domain simulation are the device motion and the power production. In fact, the power production is the most significant result that will be used for optimisation purposes. The different software used are described in more details in the following sections.

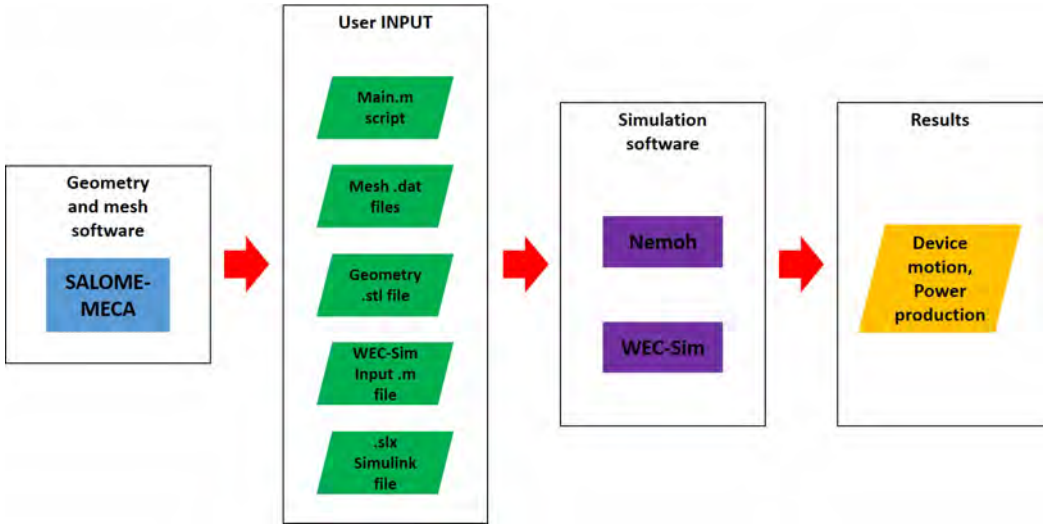

Figure 3.3: Flow chart of a wave device modelling.

3.1.4 Salome-Meca

First a CAD/mesh software is used for the mesh generation of the different hydrodynamic bodies that describe the wave energy device. Salome-Meca has been chosen because it is open-source and because a mesh converter from the Salome mesh format to the Nemoh mesh format was available. The mesh is created with triangular or quadrangular elements. The Netgen algorithm has been used for the generation of the mesh. It enables the user to

define a minimum and maximum size of the panels and to define local sizes. The minimum element size of the mesh panels has been generally chosen as a sub-multiple or equal to the minimum size of the device shape.
Salome-Meca [131] has advanced tools also to check the quality of the mesh. It is known that a good mesh quality control could improve the quality of the solution [132]. There are 4 types of quality control related to the node, edge, face and volume. The most common ones are the aspect ratio, the skew and the minimum angle and they are related to the face control [131]. The aspect ratio gives information about the degree of conformity of the mesh elements relative to the regular shape. The skew shows the greatest angle between the medians of a quadrangular or triangle element. This indicator is partly also related to the aspect ratio. Finally the minimum angle checks the minimum angle between 2 adjacent sides for each panel. There are some reference values for these mesh checking: these are for example an aspect ratio less than 1.8, a skew less than 38 degrees and a minimum angle more than 35 degrees [131].

3.1.5 Nemoh

The hydrodynamic coefficients are identified using a boundary element method implemented in Nemoh [27]. Nemoh has been developed by the Ecole Central de Nantes and it is an open-source software. It computes the first order wave loads on off-shore structures.
An important first step is to check the convergence of the hydrodynamic coefficients generated in Nemoh (added mass, radiation damping and excitation coefficients) for different mesh densities created in Salome. Three meshes could be used for this analysis, which are identified as coarse, moderate and fine with a spatial resolution that increases with a finer mesh. If convergence is not observed, more meshes will be necessary.
After obtaining a suitable mesh file (.dat file), Nemoh also requires some other inputs (obtained from the main MATLAB script described in Figure 3.3):

- ID.dat file necessary to identify the calculation.
- input.txt file necessary to identify the solver selection.
- Nemoh.cal file contains information necessary for the simulation. It gives details about environment quantities, bodies information, cases to solve and post-processing calculation.

The hydrodynamic coefficients then are calculated. The Nemoh solver can be described in 3 parts:

- a pre-processor to prepare the mesh and to generate the body conditions for the calculation of each radiation and diffraction case.
- a solver to solve the boundary value problem.
- a post-processor to give the results required in the Nemoh.cal.

Nemoh allows the user to simulate multiple bodies. In particular the different mesh files must be created in Salome-Meca and then converted in the Nemoh input file format (.dat files). The Nemoh.cal file needs to describe the details for each body.

3.1.6 WEC-Sim

WEC-Sim is an open-source tool for the simulation of wave energy converters [133]. It has been developed by the National Renewable Energy Laboratory (NREL) in collaboration with the Sandia National Laboratories (Sandia). The code is based on MATLAB and its Toolboxes (SIMULINK and SimMechanics) and it has the aim to simulate wave devices with their complexity of the PTO and mooring system.
WEC-Sim requires the following main INPUT for the simulation of the dynamic system:

- the hydrodynamics coefficients obtained from Nemoh in a HDF5 format [134]. The conversion between the Nemoh results and the HDF5 is obtained thanks to the BEMIO routine.
- the definition of the PTO, mooring and mechanical connections between the hydrodynamic bodies. The equation of motion of the device (see Equation (2.31)) is solved using a Multibody-solver developed in SimMechanics. A Simulink model is created to represent the device components and connectivities for this purpose while a MATLAB file describes the numerical INPUT of the model.

The Simulink model for a single float WaveSub has been obtained with the help of Cruz Atcheson Consulting Engineering [135]. The Simulink model is shown in Figure 3.4. It is possible to identify from the Figure the 2 hydrodynamic bodies, the PTO and mooring lines

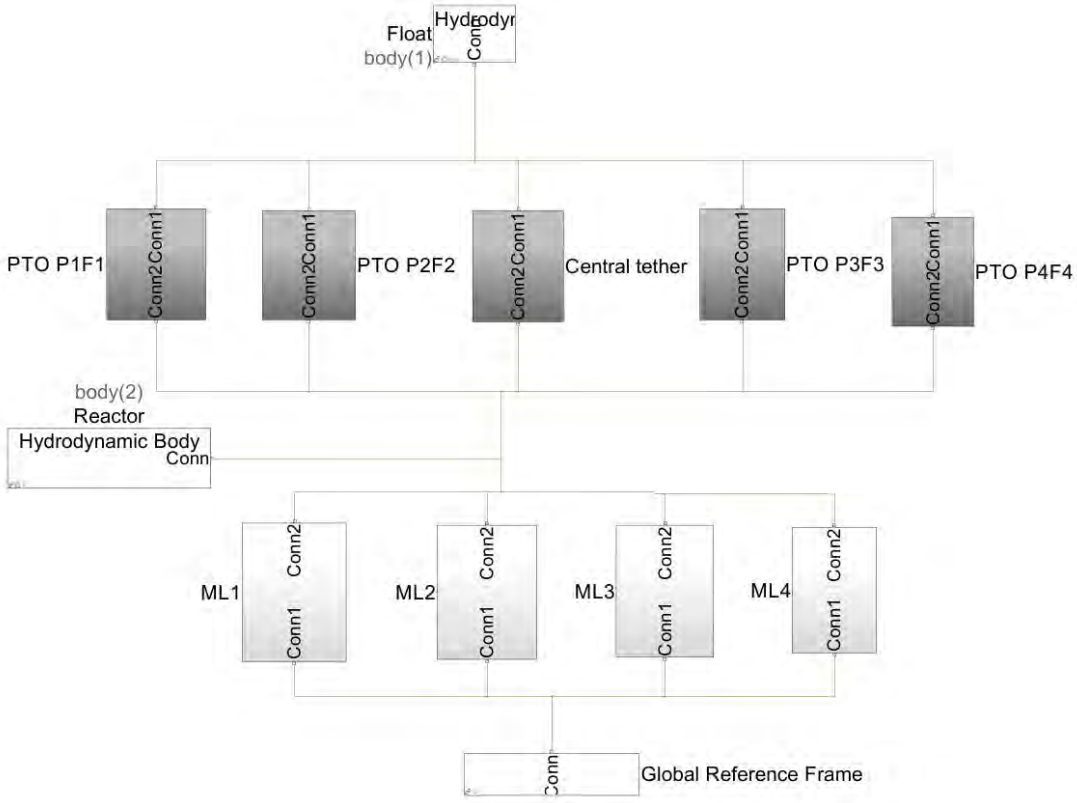

Figure 3.4: The Simulink model of the Wavesub device.

and the global reference frame. The PTO cables and mooring cables have been modelled in a similar way (see Figure 3.5). The PTO block is a translational PTO and it is modelled with a stiffness and a damping coefficient for the PTO corner lines while only with a stiffness coefficient for the central PTO line and for the mooring lines. A pre-load block has been applied on the PTO blocks to keep the full system in equilibrium with no waves. The constraints at the top and bottom of the cables were modelled as a gimbal and universal joint respectively. The difference between these 2 joints is that the universal gives 2 rotational degrees of freedom while the gimbal gives 3 rotational degrees of freedom. The WEC motion will determine a yaw constraint force on the universal joint that can be used to find the loading on the constraint. Finally a rigid transform has been applied to obtain the correct orientation of the lines while a visualization body for each line is used to check the correct setting.

WEC-Sim has been chosen because of its various capabilities to model complex scenarios. WEC-Sim has the capability of simulating an irregular wave field by using a wave spectrum as an input. Moreover, it is possible to take into account the fluid viscosity by adding

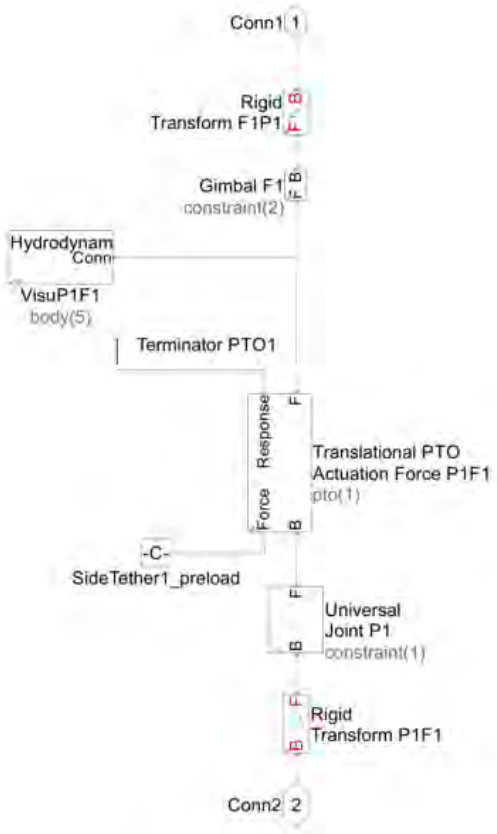

Figure 3.5: The Simulink model of the PTO and mooring cables.

a drag term. PTO original blocks of WEC-Sim are described as a simple linear spring-damper. However, the updated version can consider more accurate PTO models using the PTO-Sim module of Simulink that allows to simulate hydraulic and direct drive PTO [136]. An example of these PTOs already exist in the PTO-Sim library in Simulink. A more complex mooring can be also simulated using Moordyn [86]. It is an open-source lumped-mass mooring line model to simulate mooring of floating off-shore structures. Moordyn, in particular, can support different line interconnections including clump weights and floats and different line properties.

Different studies were carried out recently in order to improve the code and to verify and validate the results [137, 138, 136, 139, 140, 141, 142, 143, 144].

Two types of devices were simulated in WEC-Sim, comparing the results with other commercial numerical models (AQWA and WaveDyn) and with experimental datas [141, 137, 144]: a two-body point absorber (RM3) and a two oscillating surge devices (OSWEC).

Moreover a project called Wave Energy Converter Code Comparison (WEC3) was launched

to validate WEC-Sim comparing with different commercial codes (InWave, WaveDyn and ProteusDS) [140]. As a result there is a good agreement between them. The largest difference was due to the implementation of the viscous effects.
Another project was launched at the Center for Ocean Energy Research (COER) to model the response of a floating body and it compared WEC-Sim with another numerical tool called FAST [143]. This last numerical modelling was developed by NREL and it has the possibility to model floating devices. The results showed good agreement with the experimental results only in surge response while there was less agreement in heave response due to have a natural period of the device in heave very close to the peak period of the exciting wave field and so it was very sensitive to small discrepancies.
WEC-Sim was also improved taking in account nonlinear restoring forces for floating bodies and wave excitation forces [142]. The nonlinear restoring forces should be accounted for when there is a large motion of the device and when the wetted surface of the device can't be assumed constant.
All the hydrodynamic forces considered are modelled using only the first order wave theory and this could produce some error. In the future there will be the possibility to use also second or higher order wave theory.

3.1.7 Conclusions

Two different types of design of the WaveSub device have been described in this chapter. In fact, both of these will be used in this thesis. The last design derives from the progress and evolution of the device during the research project. Then, a numerical modelling methodology to simulate a wave energy converter has been presented. Different steps are necessary to obtain the main results of the device motion and power production. The main steps are the generation of the mesh, the hydrodynamic simulation and the dynamic system simulation. The hydrodynamic simulation is based on a linear potential flow theory that neglects viscosity saving computational time. An estimated drag force can be added in the dynamic system simulation but there is still uncertainty on the choice of the drag coefficient in the time domain equation (see Equation 2.31). More confidence can be obtained with a benchmarking between experimental and numerical results. This will be an important step in this thesis (See Chapter 4). The time domain simulation gives also the possibility to consider further non-linear forces such as the memory term of the radiation force and to check the simulation results also through the visualization. A great benefit of the methodology cho-

sen is that can be applied to a wide range of WEC devices. Moreover, it is based on free software that can be improved by users.
Further work will enhance the numerical model to consider a more detailed and realistic PTO and mooring.

3.2 Comparison between open-source and commercial codes

3.2.1 Introduction

A comparison between open-source software (Nemoh and WEC-Sim) and commercial ones (Wamit and WaveDyn) has been made to check their difference. The $1:4^{th}$ WaveSub device is considered in the comparison with a simplified first design described briefly in Section 3.1.2. The results of the commercial codes have been obtained from MPS Ltd.

3.2.2 The input settings

The input for the simulation are an approximation of the $1:4^{th}$scale WaveSub device. The float is approximated mainly as a short cylinder with two hemispherical ends. The reactor is simplified as a cuboid with a trapezoidal end on each longitudinal side.
The mass and the Center Of Gravity (COG) of the float and reactor are shown in Table 3.2 while the visualization of the device is reported in Figure 3.6:

Table 3.2: The input settings.

Float	**COG depth (m)**	2.2
	Mass (kg)	2126.9
Reactor	**COG depth (m)**	10.325
	Mass (kg)	145241.9

3.2.3 Nemoh vs. Wamit

Nemoh and Wamit use a panel method to solve the radiation/diffraction problem relative to the first order problem (see Section 2.1.2).
The mean drift force (from the second order response) can be calculated both in Nemoh and Wamit [19]. The drift forces calculation is available in Nemoh thanks to a MATLAB routine available on the website [27].
Wamit has more advanced features than Nemoh: for example it has the possibility to use a higher order method. This higher order method does not have exclusively flat panels but they could consider more generic surface with continuous curvature. In this way the shape of the body could be captured better [145] and also a lower number of panels would be

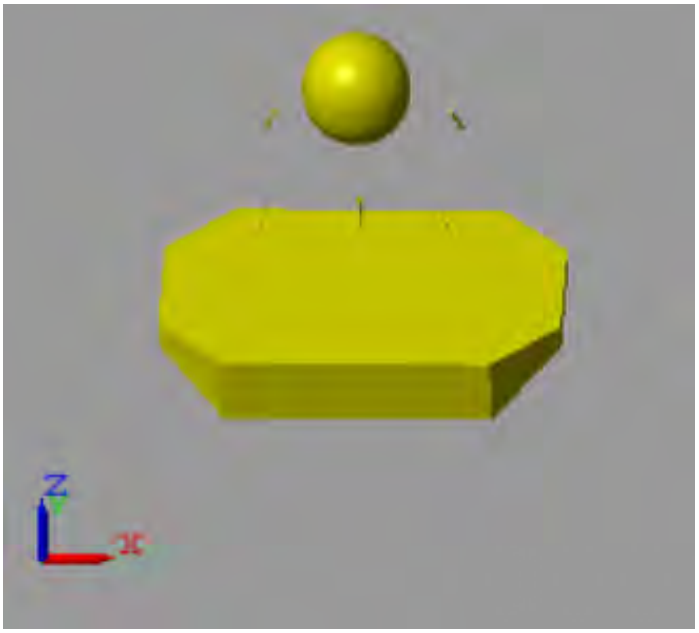

Figure 3.6: Visualization of the device in Mechanics Explorer.

necessary to have accurate results. Wamit also gives the possibility to remove irregular frequencies. The irregular frequencies are frequencies that lead to non-physical predictions of the hydrodynamic coefficients. This irregular solution comes from the free surface boundary condition and so it happens only for floating bodies.
Finally Wamit calculates the RAO (Response Amplitude Operator) based on the hydrodynamic forces (see Equation (2.30)) while Nemoh requires the calculation from the user.
There are some positive cases of this comparison that show a good agreement between the 2 codes ([146], [147]).
A good comparison has been found between the 2 software systems and so the open-source software Nemoh has been chosen for the computational modelling of the WaveSub device. These results have been obtained for a water depth of 100m while the frequency range investigated is from 0.05 rad/s to 5 rad/s. The excitation force of the float and of the reactor have demonstrated a good agreement as shown in Figure 3.7 and Figure 3.8. In particular, the main degrees of freedom of surge, heave and pitch have been checked. Wamit shows a smoother effect especially for the surge and pitch phases of the reactor because of the use of the higher order method.

The comparison of the added mass and of the radiation damping coefficients is also good (see Figure 3.9). The added mass can be calculated from the radiation damping and the added mass at infinite frequency (see Equations (2.34) and (2.36)). In particular, the

comparison of the most significant values of the added mass at infinite frequency is shown in Figure 3.9 with a relative error less than 20%.

There are some cases in which the behaviour of the radiation damping coefficient is less smooth in Nemoh in particular for the reactor (see Figure 3.10). The possibility that this could be due to irregular frequencies is excluded because the reactor is completely submerged [148]. Nemoh has some problems in calculating the hydrodynamic coefficients of thin elements and this could be the reason [149]. In fact, the thickness of the reactor is quite small compared to the other 2 dimensions (the depth is around 5 times less than the other 2 size dimensions). The problem is related, in particular, with the added mass and the radiation damping coefficient.

The choice between Nemoh and Wamit has been mainly decided based on the capabilities to calculate the hydrodynamic coefficients of the float. This will be the main component to determine the energy capture while the reactor will be described by small motion. Some discrepancies have been observed for some of the frequencies of the radiation damping coefficients of the reactor but there is generally still a reasonable agreement for the aims of this research work. More specifically, numerical instabilities of Nemoh could have played a certain significance and so a quality check will be necessary for future hydrodynamic coefficient calculations. Further work will investigate more deeply the reasons of these instabilities.

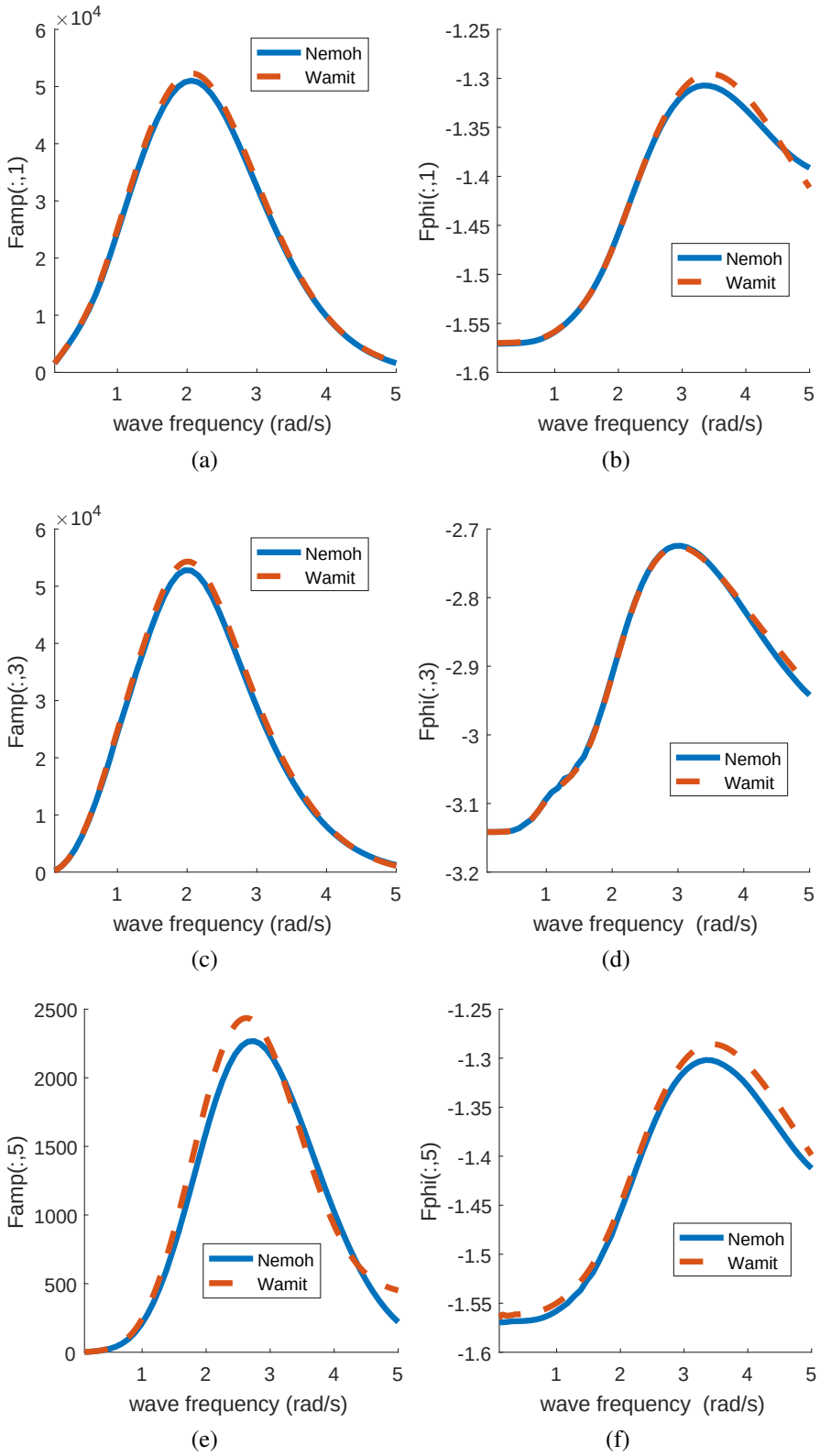

Figure 3.7: Excitation amplitude and phase (rad) of surge degree of freedom of float (a-b), of heave degree of freedom of float (c-d) and of pitch degree of freedom of float (e-f).

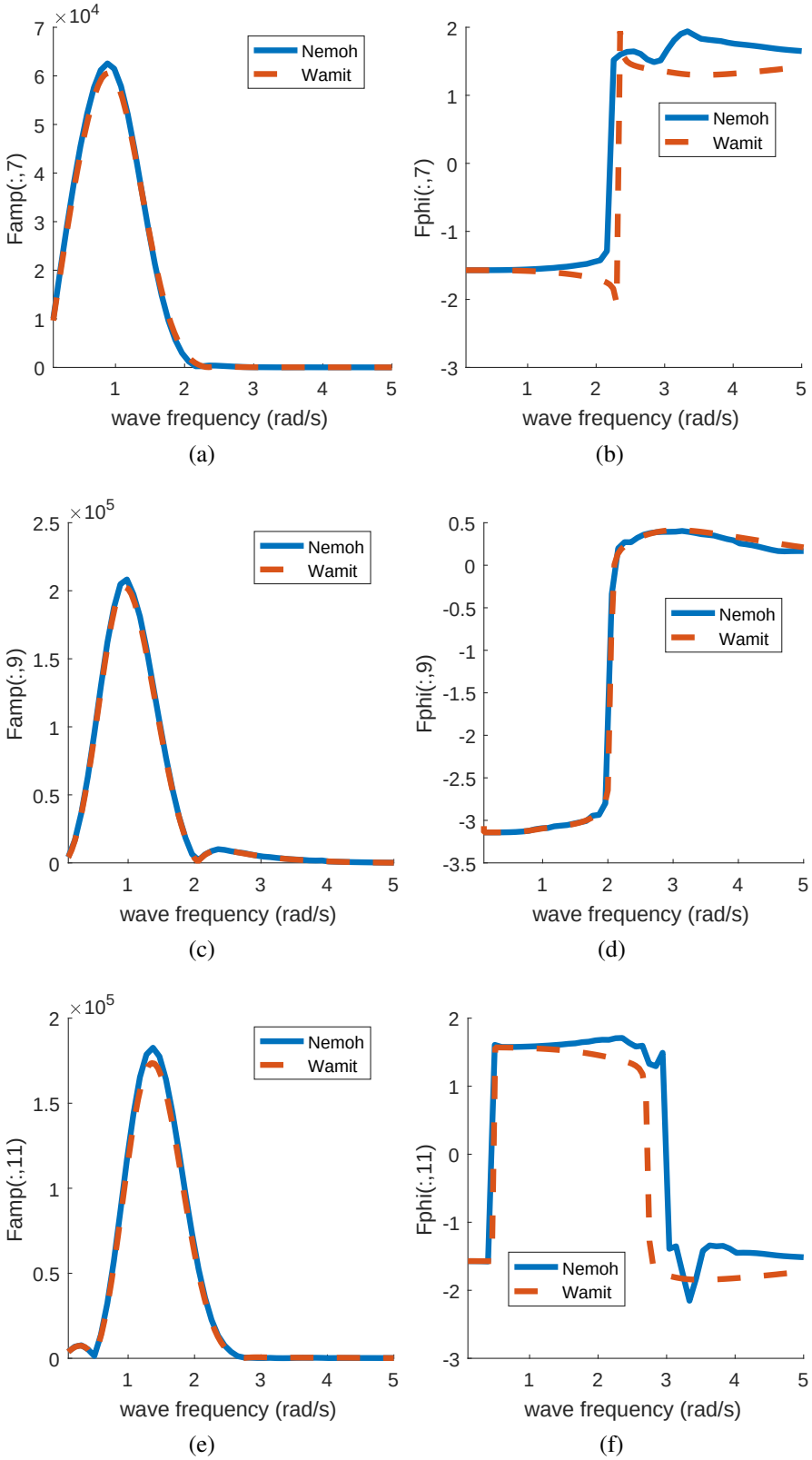

Figure 3.8: Excitation amplitude and phase (rad) of surge degree of freedom of reactor (a-b), of heave degree of freedom of reactor (c-d) and of pitch degree of freedom of reactor (e-f).

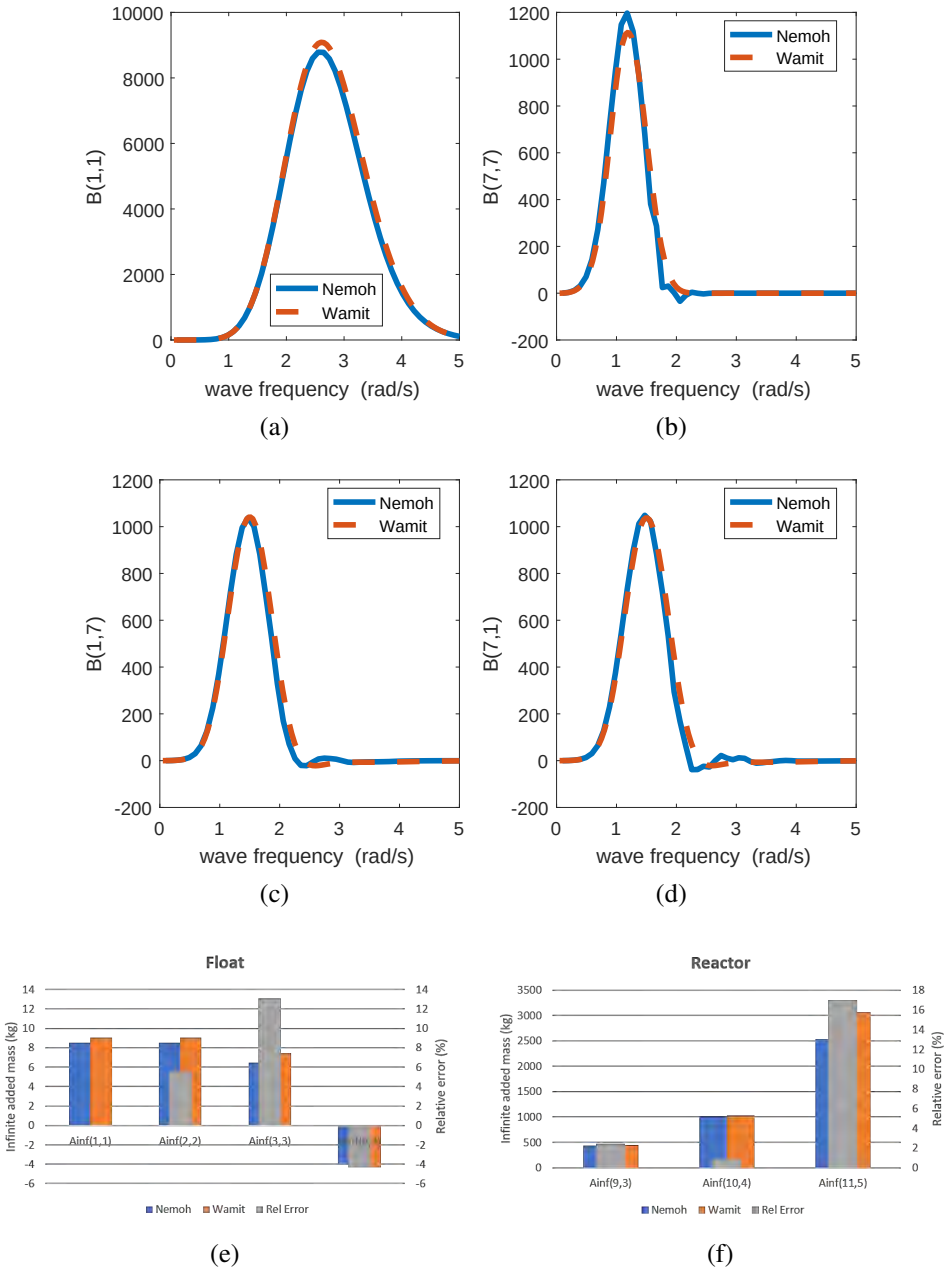

Figure 3.9: Radiation damping of surge of floater due to surge of floater and of surge of reactor due to surge of reactor (a-b), radiation damping of surge of floater due to surge of reactor and of surge of reactor due to surge of floater (c-d), relative error (%) between Nemoh and Wamit of the added mass at infinite frequency for the floater (e) and for the reactor (f).

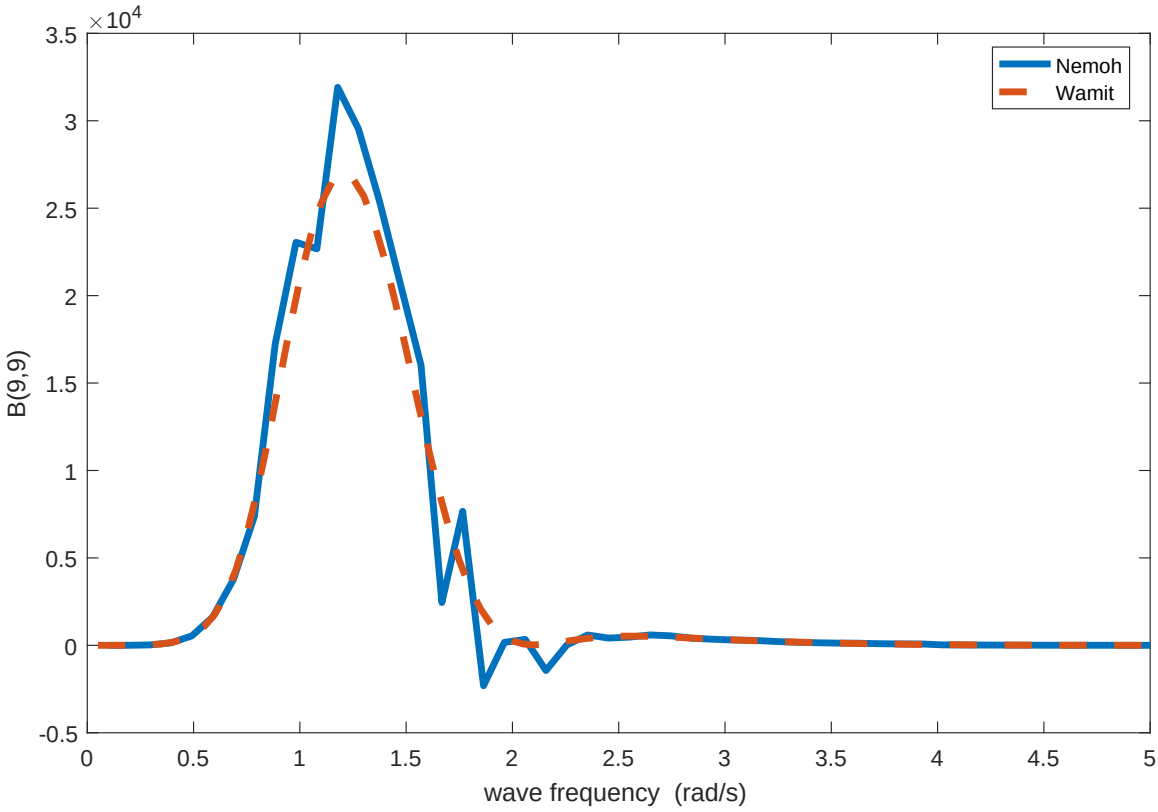

Figure 3.10: The heave radiation damping on the reactor due to the heave motion of the reactor.

3.2.4 WEC-Sim vs. WaveDyn

There are different codes that are able to simulate a wave energy dynamic system such as InWave, WaveDyn, ProteusDS and WEC-Sim. A comparison between them can be found in [140]. WEC-Sim and Wavedyn have more or less the same features: they can account for articulated multibody WECs, hydrodynamic interactions, Morison elements and quasi-static mooring. WEC-Sim is open-source but it needs external software such as MATLAB, Simulink and SimMechanics.

WEC-Sim and WaveDyn have been compared in this Section using the same Wamit hydrodynamic data to avoid possible differences due to the calculation of the hydrodynamic coefficients. Additionally the time domain simulation used in both software packages considers the same regular wave and the same simulation settings of the device. The WaveDyn simulation has been carried out by Annette Brask, a research and development engineer at MPS.

The main degrees of freedom are considered in the comparison (surge, heave and pitch), together with a comparison of the power produced in the 4 PTO corners.

First of all, a simulation with no waves is made to check the stability of the system. A preload force in each PTO and mooring line is important to reach this goal. WEC-Sim shows a larger numerical noise than Wavedyn but it has negligible effect on the power produced.

Then a regular wave of wave height 1m and period of 6s has been tested and the results are shown in Figure 3.11 and Figure 3.12. The two codes have an opposite convention for incident wave magnitude, which determines an opposite phase in surge and pitch. However Figure 3.11 shows the same phase convention results to notice more the differences between the two codes. Generally there is a good agreement in surge and pitch. The heave motion shows instead less agreement. The heave motion both for the float and for the reactor is characterized by 2 main amplitudes: one shorter and one larger. The shorter amplitude is more similar while the larger one shows some disagreement.

It is worth noticing that the device settings are not optimised and the device motion will be determined mainly by the float motion.

The relative and the absolute error have been also calculated (see Figure 3.13). Despite some differences in the double amplitude for the heave and pitch motion for the reactor, the mean power produced is very similar with a relative error less than 2%.

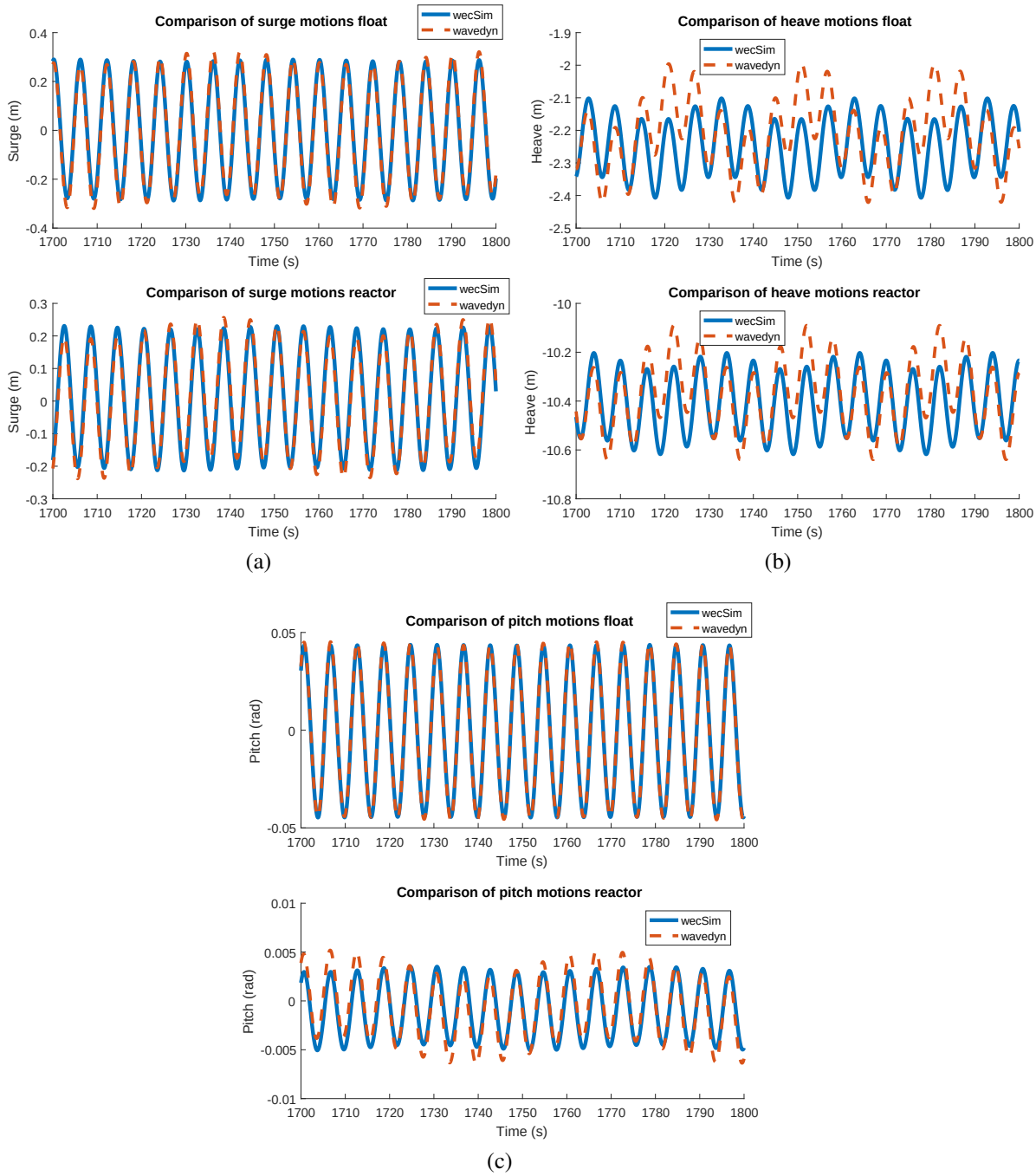

Figure 3.11: Surge (a), heave (b) and pitch (c) motion comparison between WEC-Sim and WaveDyn of the floater and reactor for a regular wave with H=1 m and T=6s.

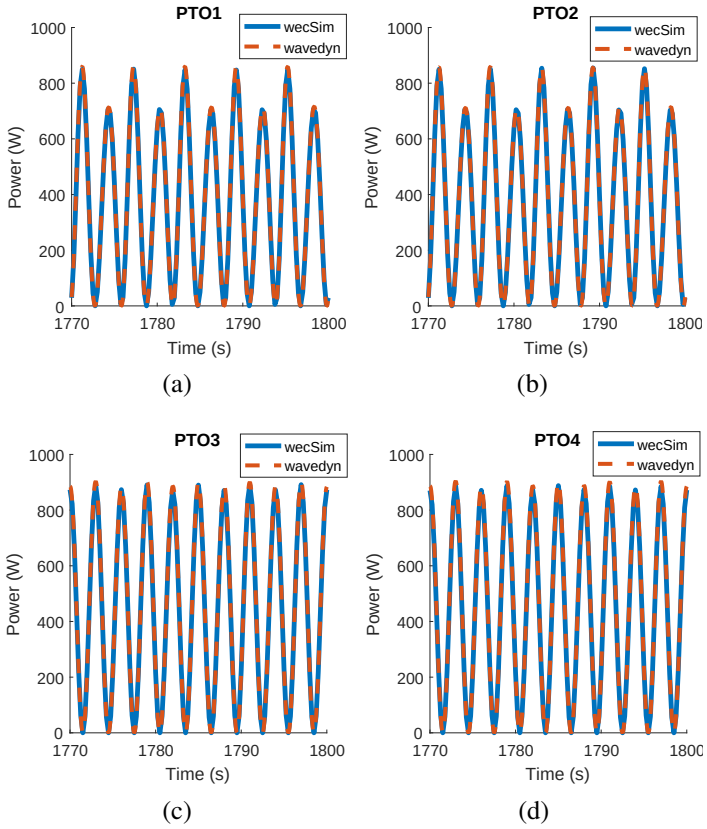

Figure 3.12: PTO power produced (a,b,c,d) for a regular wave with H=1 m and T=6s.

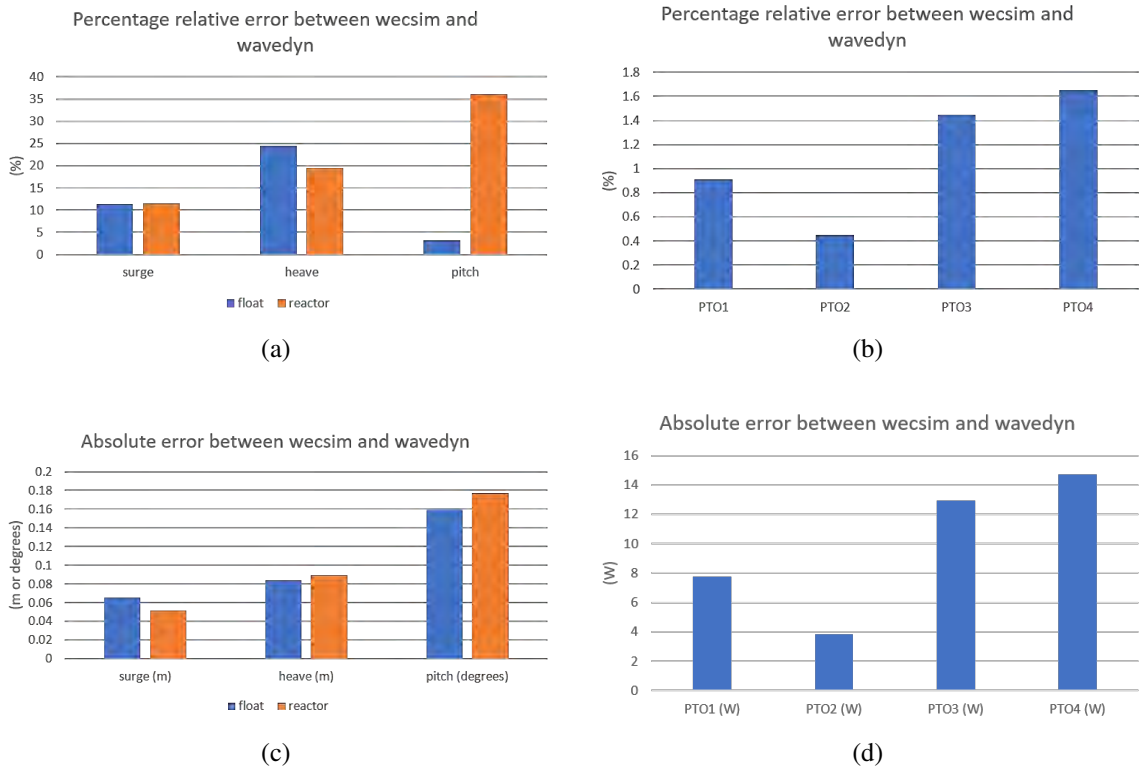

Figure 3.13: Relative error of the WEC motion and of the mean power produced of the PTO (a-b) and absolute error of the WEC motion and of the mean power produced of the PTO (c-d).

3.2.5 Conclusions

The comparison between open-source (Nemoh and WEC-Sim) and commercial codes (Wamit and WaveDyn) has been analysed in this chapter. Nemoh and Wamit are used for the calculation of the hydrodynamic coefficients and they are based on a linear potential flow theory. Afterwards, WEC-Sim and WaveDyn are used to simulate the dynamic system. As a result, open-source and commercial codes demonstrated a reasonable agreement. Nemoh and Wamit are very similar in the calculation of the excitation coefficients for both the float and the reactor while they show some differences in some of the added mass and radiation damping coefficients of the reactor. In particular, this could be related with the Nemoh calculation problem of thin elements with a poor aspect ratio [149]. WEC-Sim and WaveDyn have demonstrated similar results. There are, however, some discrepancies in the reactor heave and pitch motion. Finally the power produced shows a very small relative difference between them (less than 2%).

There are some limitations for both commercial and open-source codes. Both Nemoh and Wamit consider an inviscid, irrotational and incompressible fluid flow. The inviscid assumption determines, especially, inaccuracy in the calculation of the drag force associated to the float. Then, WEC-Sim and WaveDyn relies on the accuracy of the numerical solver of the time domain equation in 6 degrees of freedom (See Equation 2.31).

This comparison is necessary to check the simulation capabilities of the open-source software because they are the first choice in terms for research purposes because they are free to use and the source code is easily accessible to make improvements to it. Further work could consider a more extended comparison between the codes for a deeper analysis.

3.3 The investigation of the fluid resistance generated by the WaveSub device

3.3.1 Introduction

A single body at rest in a steady flow has 4 main forces: drag, lift, gravity and buoyancy. The first 2 forces are due to the shear stress and pressure generated by the flow on the body surface. Both the shear stress and the flow pressure on the body surface contribute to the drag and to the lift force. The drag force can be calculated generally as [150]:

$$F_V = \iint_{S_b} psin\theta dS_b + \iint_{S_b} \tau_0 cos\theta dS_b \tag{3.1}$$

where p is the local pressure around the body, τ is the local shear stress on the body, β is the relative angle between the local body profile and the flow direction and S_b is the surface area of the body. The first term represents the pressure drag while the second term the frictional drag.
The frictional drag force is dominant for elongated bodies while the pressure drag is dominant for bluff bodies [151]. In the first case the force is related to the area exposed to the flow. In the second case the force is related to the eddying motions of the fluid around the body. In particular the force is related in this case to the cross-sectional area of the body.
The relation between body shape and type of drag force is shown in Figure 3.14. In particular a sphere has the frictional drag that is of the same order of the pressure drag.

3.3.2 The drag coefficient

In an oscillatory flow the drag force is an important force that should be accounted especially when the characteristic diameter of the body is less than $1/5^{th}$ of the shortest wavelength and for large wave amplitude and body motion [16].
The drag force generally is expressed as a quadratic term (see Equation (2.26)) .
The distinction between frictional and pressure drag of an object immersed in the water flow is difficult to measure in a laboratory. Generally the total force is measured and then the drag coefficient is obtained with a Fourier averages [152].
An oscillatory flow can be expressed as:

$$u = -A_I cos\theta \tag{3.2}$$

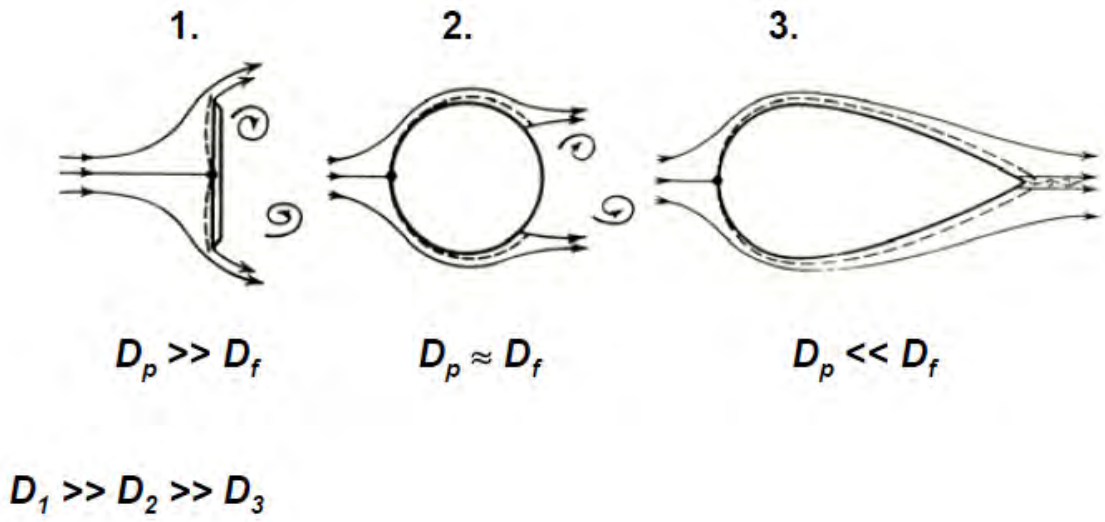

Figure 3.14: Examples of flow around different body shapes [150].

where θ is defined as following:

$$\theta = 2\pi t/T \tag{3.3}$$

Then the drag coefficient in an oscillatory flow for a cylinder perpendicular to the flow direction can be determined as following [152]:

$$C_D = -\frac{3}{4}\int_0^{2\pi} \frac{F_m cos\beta}{\rho_w D u_m^2} d\beta \tag{3.4}$$

where F_m represents the measured force for unit cylinder length, D is the cylinder diameter, u_m is the maximum flow velocity.

The drag coefficient should be characterized as accurate as possible to be used in the simulations and can be found experimentally. This coefficient is dependent on the Reynolds number (see Equation (2.55)), on the Keulegan-Carpenter number and on the surface roughness [153, 154].

The Keulegan-Carpenter number is defined as following in an oscillatory flow:

$$KC = \frac{uT}{l} \tag{3.5}$$

where l is the characteristic dimension of the body, T is the wave period and u is the flow velocity amplitude.

Some effects should be accounted for the calculation of the drag coefficients such as: orbital

motion, coexisting current, pile orientation, interference and wall proximity [155]. So the interaction between the different bodies should be taken in account for the calculation of the drag coefficients [156].

The most important non-dimensional number to be considered for the WaveSub floats drag coefficient characterization is the Keulegan-Carpenter number. In fact, a Reynolds number larger than 10^5 has a smaller influence in the drag coefficient variation especially for rough cylinders [157]. The Reynolds number for the floats of the full scale device is generally larger than this value and so it can be neglected. The drag coefficient for smooth and rough cylinders at high Reynolds number can be represented as a function only of the Keulegan-Carpenter number (see Figure 3.15). This relation was found experimentally by Sarpkaya [157]. It is observed that the drag coefficient becomes larger for small KC number. The parameter β_S is used by Sarpkaya that is defined as following:

$$\beta_S = \frac{Re}{KC} \tag{3.6}$$

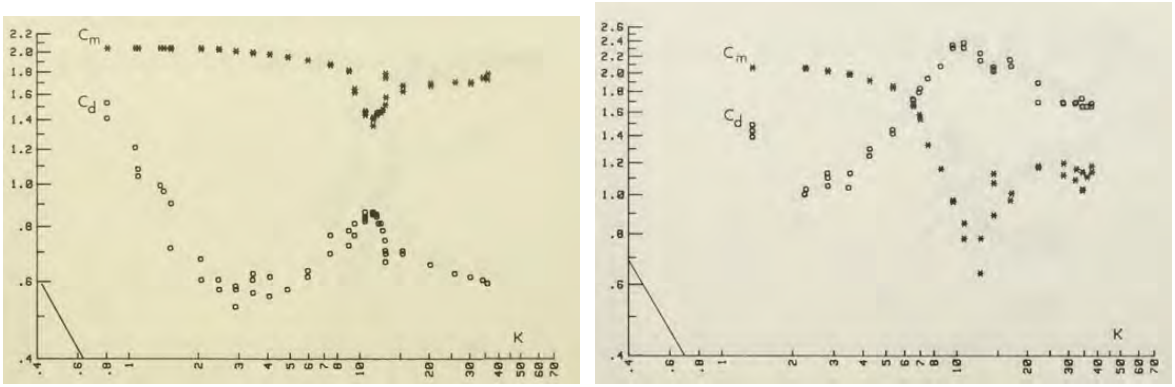

(a) (b)

Figure 3.15: The inertia and drag coefficient as a function of the KC number for smooth cylinders for $\beta_S = 9{,}354$ (a) and rough cylinders with Ra/D = 1/50 for $\beta_S = 11{,}525$ (b) [157].

If the Reynolds number is less than 10^5 the Reynolds number should be accounted as analysed by Sarpkaya [153] for smooth cylinders. The drag coefficient for lower Reynolds number reaches higher values as can be observed from Figure 3.16.

Surface roughness has an important influence on the drag force, in particular on the frictional drag. The surface roughness of a body is accounting the material and the marine

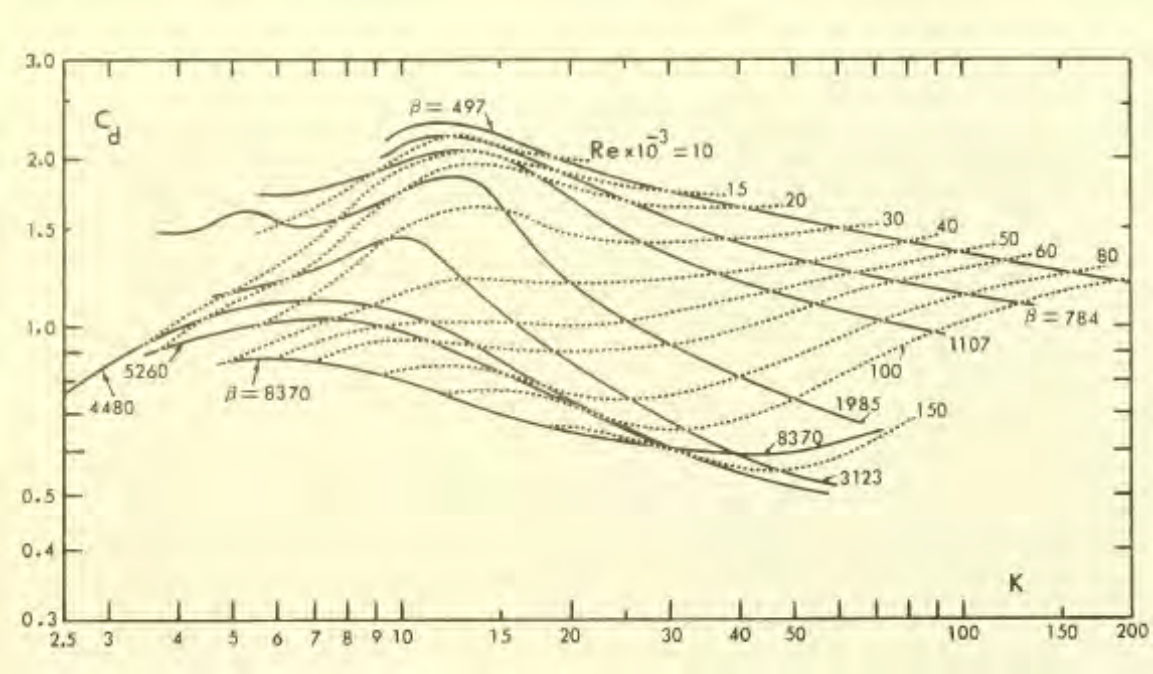

Figure 3.16: The drag coefficient of smooth cylinder as a function of the KC, Re and β [153].

growth. The marine growth is assumed to have minimal effects on the WaveSub response considering also that the floats are constantly in motion. However a more complex analysis should account this effect [158]. The roughness can be expressed in a first approximation as a function only on the material of the floats. The relative roughness (Ra/D) for the WaveSub is low because the characteristic diameter for the full scale is large compared to a possible absolute roughness (more than 1000 times smaller than the cylinder diameter). The relative roughness accounted in the Sarpkaya experiments on cylinders [157] was from 50 to 800 times smaller than the cylinder diameter and so in a first approximation the WaveSub can be considered smooth. Moreover the frictional drag is considered less significant compared to the pressure drag for the float and reactor of the WaveSub.
Generally each geometry shape has a very different drag coefficient curve as a function of the KC number. The drag force has been analysed experimentally in an oscillatory flow but mainly for simple geometries (spheres, cylinders and plates) and when these bodies were fixed ([159],[160],[161]). The drag coefficient of plates as a function of the KC number was investigated by Keulegan and Carpenter (see Figure 3.17). The drag coefficient reaches very high values for low KC.

The drag coefficient has been mainly characterized for regular waves. However it is

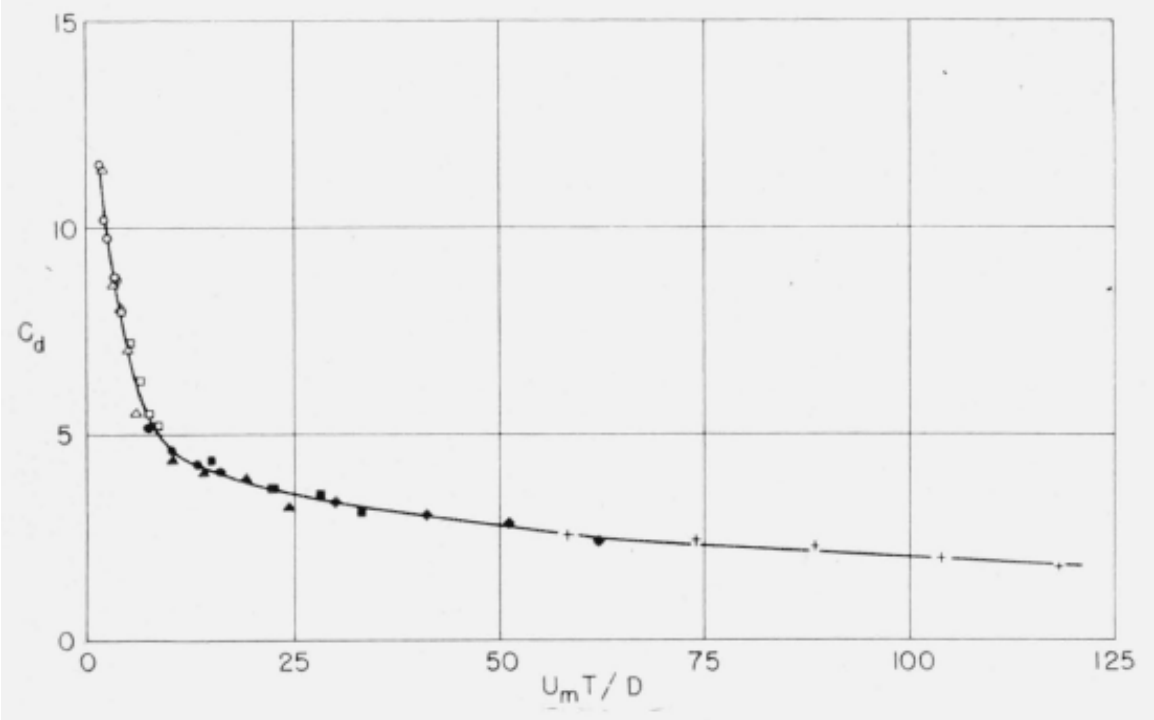

Figure 3.17: The drag coefficient as a function of the KC number for smooth plates [159].

possible to find also some research related to the characterization of the drag coefficient for random waves ([162], [163]). Similar values of the rms force coefficients are obtained in [163] between regular and random waves as a function of the Keulegan-Carpenter number. A CFD model could be used to assess the drag coefficient but experimental data will be necessary to validate it. In particular free oscillations and decay tests could be conducted to validate the numerical model. A comparison of the motion of a heaving point absorber between a CFD model and the experimental data can be found in [164]. Generally the drag coefficient characterization of an oscillating wave energy device with 6 degrees of freedom in an oscillatory flow is more much complex also for an experimental test.
Another factor of complexity is that the drag coefficient is not constant in a wave cycle but it is changing periodically [159] (see Figure 3.18).

The viscous force or drag force for a moving body in an oscillatory flow could be expressed as the Equation (2.26). The drag force is applied to a single point (the center of pressure) and expressed as a function of the undisturbed flow velocity. However the geometry of the float and reactor of the WaveSub can not be considered as slender bodies and so this equation is quite limited. In fact, the flow velocities around each body are modified by the diffraction and radiation wave fields.

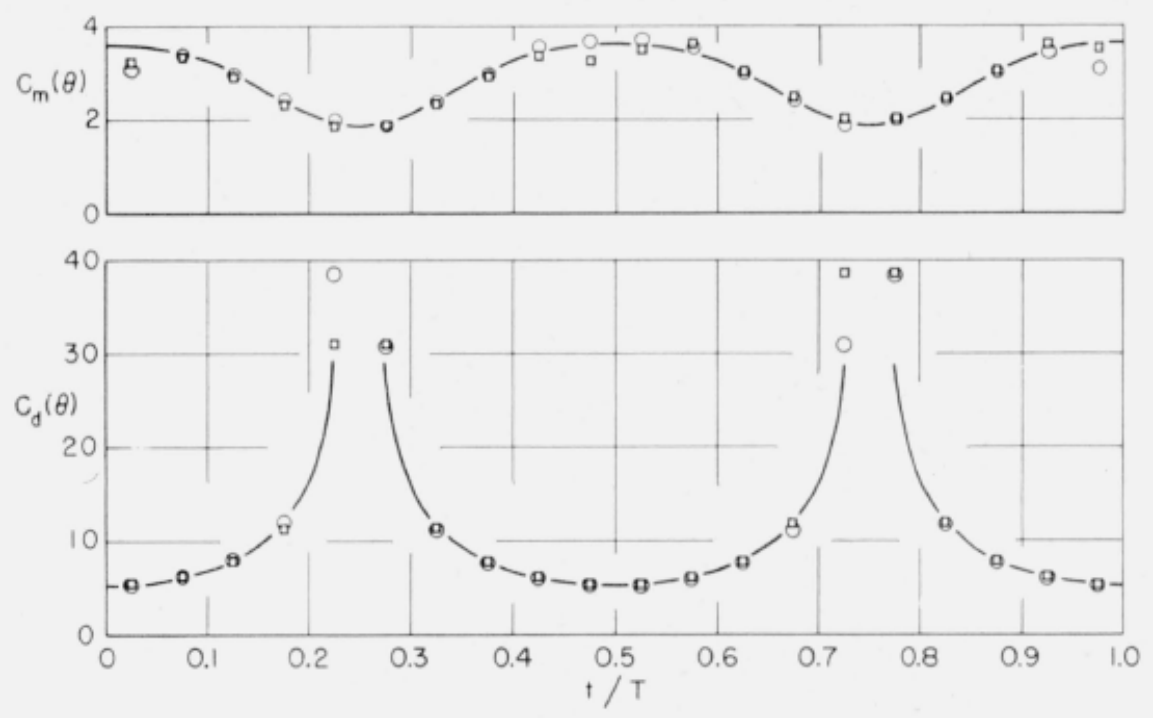

Figure 3.18: An example of variation of the inertia and drag coefficients of a plate during a wave cycle with $KC = 6.6$, $C_m = 2.42$ and $C_D = 6.31$ [159].

An analysis of the relationship between the motion of the float and the undisturbed flow velocity will be carried out here. The undisturbed flow velocity for a regular (only 1 frequency) or irregular waves is defined as following using the linear potential flow [165]:

$$u_x = \sum_{i=1}^{N_f} A_I(i) \cdot \omega(i) \cdot \frac{cosh(2\pi(z+d)/\lambda(i))}{sinh(2\pi d/\lambda(i))} \cdot cos(\omega(i)t - k(i)(x \cdot cos\beta + y \cdot sin\beta) + \phi_{Ii}) \cdot cos(\beta) \tag{3.7}$$

$$u_y = \sum_{i=1}^{N_f} A_I(i) \cdot \omega(i) \cdot \frac{cosh(2\pi(z+d)/\lambda(i))}{sinh(2\pi d/\lambda(i))} \cdot cos(\omega(i)t - k(i)(x \cdot cos\beta + y \cdot sin\beta) + \phi_{Ii}) \cdot sin(\beta) \tag{3.8}$$

$$u_z = \sum_{i=1}^{N_f} A_I(i) \cdot \omega(i) \cdot \frac{sinh(2\pi(z+d)/\lambda(i))}{sinh(2\pi d/\lambda(i))} \cdot sin(\omega(i)t - k(i)(x \cdot cos\beta + y \cdot sin\beta) + \phi_{Ii}) \tag{3.9}$$

where (x, y, z) is the particle position.

An example of surge and heave relative velocity of the float for a single float WaveSub configuration for regular and irregular wave is shown in Figure 3.19. The flow velocity has been calculated at the dynamic center of gravity of the float.

The body velocity and the flow velocity are not completely in phase and there is generally a certain delay between them (see Figure 3.19). A cross-correlation was undertaken to estimate their similarities (see Figure 3.19). There is a good agreement for a regular wave (both regular) but less for an irregular wave. For this case differences could be due to the modification of the incident wave field due to the float and the reactor. PTO forces could also have determined some influence on the motion of the float. A certain variation of the orbital velocity is expected along the body surface because the dimensions of the full scale bodies are pretty large. So the calculation of the drag force using the Morrison element is not very accurate if the number of Morrison elements that are approximating the body is not larger enough. Moreover, the size of the float and of the reactor are interfering significantly with the wave field and so the flow velocity will be influenced by their presence. In fact, they can not be considered slender bodies. In a first approximation, the drag force will be represented in the next chapters as a viscous term dependent on the square of the body velocity. This option is also possible from WEC-Sim [166]. The relationship between the drag coefficient and the KC number could be used in the numerical simulation in WEC-Sim. The main problem is that the KC number is known only after the simulation to know the body velocity amplitude. An iterative process could be used to match the Cd/KC of the simulation with the experimental curve. However this is not really practical for this research project and the best solution is to guess the range of KC of the simulations to estimate a drag coefficient. In fact, the optimisation of the WaveSub will require many simulations and furthermore, the relationship between the KC number and the drag coefficient will not be known very accurately.

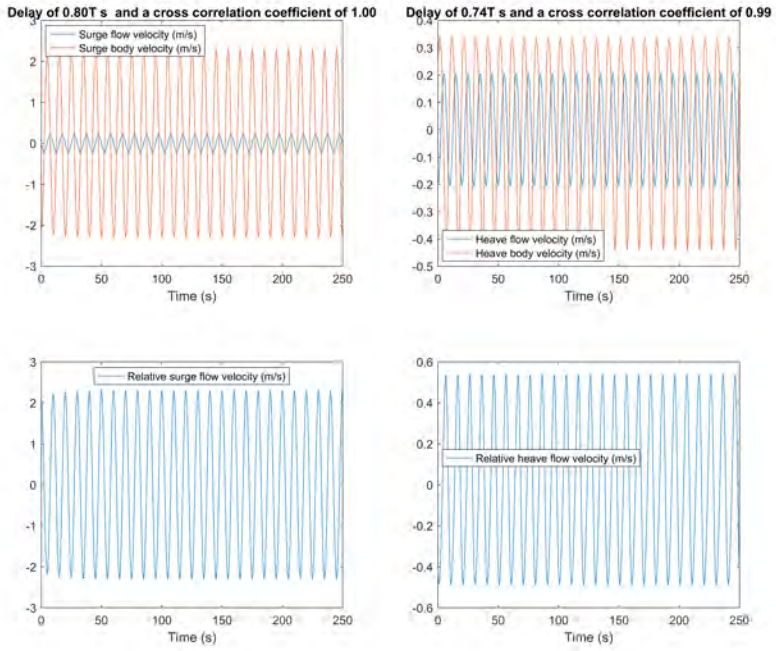

(a)

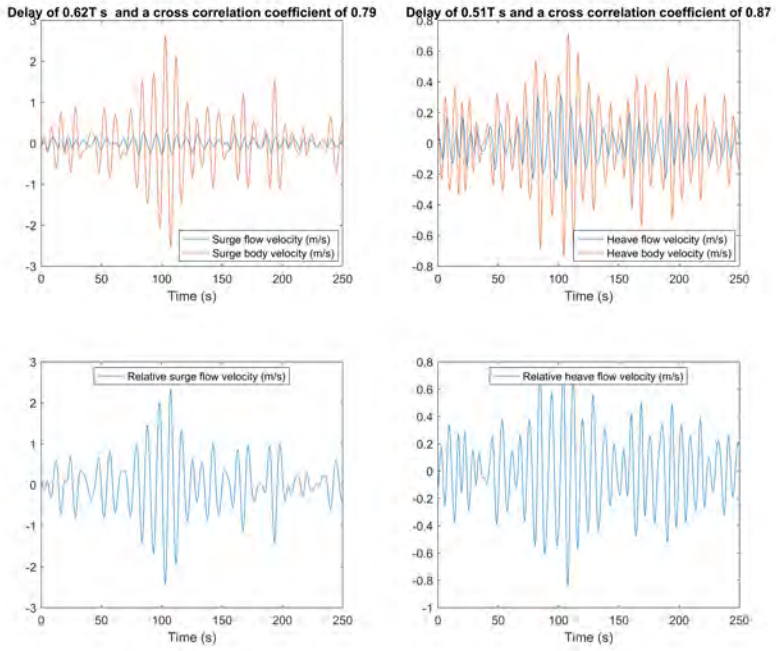

(b)

Figure 3.19: Relative surge and heave flow velocity of the float1 for a 3 float configuration for a regular wave (a) and for an irregular wave (b).

3.3.3 The drag coefficient estimation of the WaveSub

There are 2 main design considered in this thesis as explained in Section 3.1.2.
The main type of drag will be the pressure drag as this will be the most dominant for the typical high Reynolds numbers (lower frictional drag) of the full scale and for the geometries considered [167]. So the reference area will be the cross-sectional area.
The first design considers a float made by a cylinder in the middle and 2 hemispheres in the sides (See Figure 3.20). In a first approximation the experimental curve for smooth cylinders in Figure 3.15 could be used to evaluate the drag coefficient relative to a particular KC of each float. A drag coefficient of 0.7 for the floats is suggested considering the results of the benchmark between the numerical model and the tank testing of Chapter 4. The reactor is simplified as a cuboid shape and it is very large compared to the wavelength and so a small drag coefficient could be considered in a first approximation (0.5).
The second design considers the floats as spheres and the reactor simplified mainly with the air tanks for the drag force estimation (See Figure 3.20). A drag coefficient of 0.4 has been used for the floats considering Figure 3.21 and [167]. Figure 3.21 shows very low drag coefficients for a sphere for low KC number while in [167] it is suggested that a value of 0.4 for a laminar steady flow. This last value has been considered reasonable when compared with the Figure 3.21 and so it has been chosen.
The air tanks of the reactor have a shape similar to the floats of the first design. The KC for this case will be lower due to the lower velocity of the reactor. Figure 3.15 shows an increase of the drag coefficient for lower KC number and so a first estimation value of 2 has been chosen.
Rotational drag is accounted for the tanks of the reactor while it is supposed negligible on the floats (spheres). The drag momentum for each degree of freedom is calculated considering a simplified rectangle cross-sectional area of the tanks and calculating the integral as following for each tank:

$$M_{drag} = \frac{1}{2}\rho_w C_D \int_{l_{min}}^{l_{max}} v|v| \cdot l L_{Tank-ts} dl = \frac{1}{2}\rho_w C_D \omega^2 L_{Tank-ts} \int_{l_{min}}^{l_{max}} l^3 dl = \frac{1}{2}\rho_w C_D \omega^2 L_{Tank-ts} \cdot \frac{(l_{max}^4 - l_{min}^4)}{4} \tag{3.10}$$

where l_{min} and l_{max} are the minimum and the maximum distance between the rectangle cross-sectional area and the rotational axis, $L_{Tank-ts}$ is the transversal size of the cross-sectional area of the tanks.

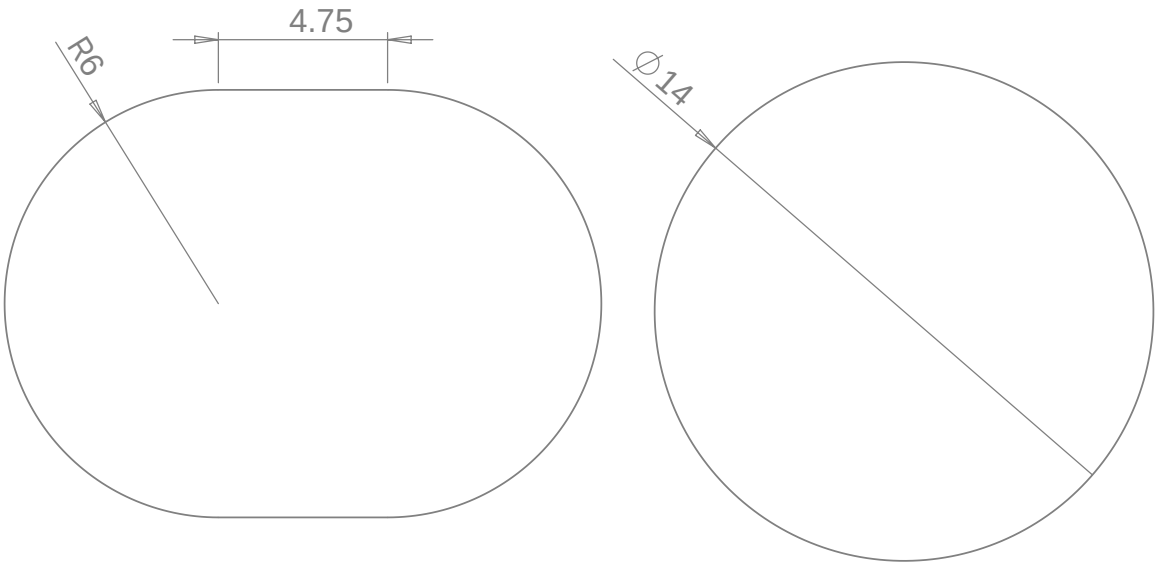

Figure 3.20: The first float design on the left and the second float design on the right.

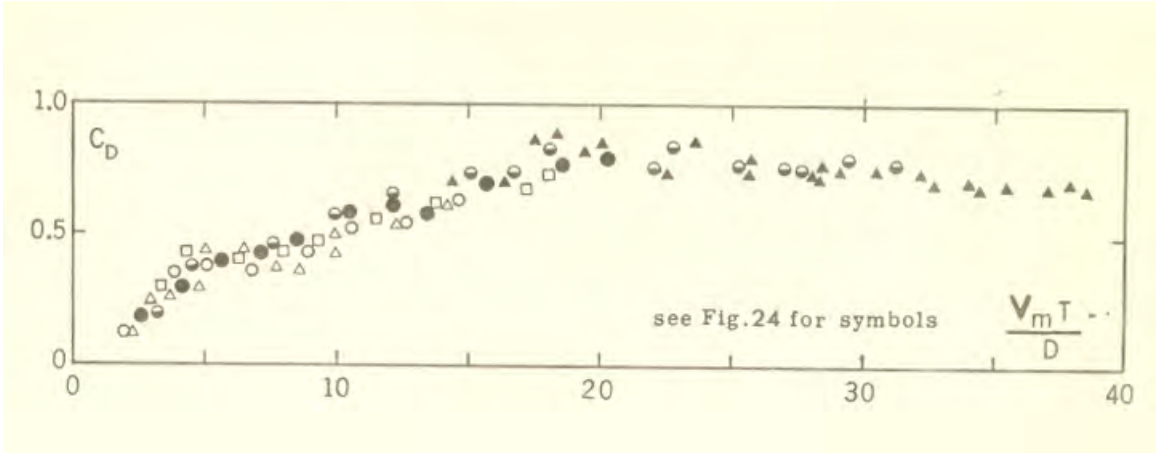

Figure 3.21: The drag coefficient versus the KC number for spheres [161].

3.3.4 Conclusions

The drag force has been investigated in this chapter to identify an appropriate drag coefficient for the simulations. In particular, the floats represent a critical part of this topic because their drag will influence more significantly the power produced. A possible drag coefficient related to the KC number could be accounted in the numerical simulations but the iterative way of this solution could determine a long solving process. Moreover, an accurate experimental curve is necessary for this approach. So a simplified constant drag coefficient value has been decided. The first WaveSub design considers an approximate drag coefficient value for the floats, obtained from the results of the experimental and numerical benchmarking discussed in Chapter 4. The second WaveSub design simplifies the drag coefficient of the floats with a constant value from literature regarding drag coefficients of spheres dependent on Reynolds and Keulegan-Carpenter numbers (See Figure 3.21 and [167]).

Main achievement of this chapter has been the definition of the drag force associated to the WaveSub device. In fact, most of the uncertainty could come from the setting of the drag coefficient value. However, these considerations could be just applied to the WaveSub device or to devices with a similar geometry.

There are some uncertainties in the choice of the drag coefficient of the WaveSub device. The tank testing benchmarking described in Chapter 4, from which the drag coefficient of the first design of the WaveSub considered in this thesis has been evaluated, has been limited to regular waves. However, the optimisation of Chapter 5 will consider irregular sea states. Furthermore, most of the previous research (see Section 3.3.2) is limited to some basic geometry shape of the objects (sphere, cylinders and plates) and only for a body at rest in a unidirectional oscillating flow or for an object oscillating in a fluid at rest. The WaveSub under sea states creates a more complex situation because it considers both an oscillating flow and an oscillating body and so the conclusions are quite limited. The relative velocity approach considered in this chapter is quite limited for slender cylinders and so the drag force is simplified to a viscous term dependent on the body velocity as implemented also in WEC-Sim [166].

Future work could include an implementation of the Cd-KC curve in the WEC-Sim code. This expansion of the code could be really useful if an experimental curve of the drag coefficient dependent on the Keulegan-Carpenter number for the geometry considered is available.

3.4 The perturbed wave field visualization

3.4.1 Introduction

The perturbed wave field allows observation of the interaction between the WEC and the wave field. In particular it is possible to visualize separately the incident, scattered, radiated and the perturbed wave field.
Results have been elaborated from material obtained from Cruz Atcheson Consulting Engineering [120]. The tool has been modified for a better performance of the calculation of the Fourier coefficients and extended to the time domain visualisation.
Finally multi-directional waves have been modelled in WEC-Sim based on the theory presented in Section 2.5 and adopted also in the official version of the software. The main update of the WEC-Sim code is related to the excitation force (see Equation (2.78)).
Results have been presented during the EWTEC 2019 conference [168].

3.4.2 Methodology

The core of the numerical simulation is the combination of Nemoh and WEC-Sim as described already previously in Section 3.1. The first computes hydrodynamic coefficients and the second the time domain simulation of the device and shown in Figure 3.22.
WEC-Sim source code has been modified accounting the influence of the wave directional distribution on the excitation force. This modification has been applied to the WEC-Sim linear model but could be theoretically extended to the weak non-linear model considering the non-linear Froude-Krylov force based on the dynamic pressure over each panel of the wetted body surface. Nemoh and WEC-Sim have an opposite notation of the incoming incident wave direction. The wave fields are expressed using the Equations 2.71, 2.72, 2.73 and 2.74 of Section 2.5 obtained using the Nemoh notation [27].
Nemoh needs to be simulated using the free surface elevation option. In particular, the size of the domain and the number of points in x and y dimensions are defined. This option increases significantly the computational time of Nemoh. A free surface elevation file is created for each frequency, wave direction and degree of freedom considered. Wave direction is related with the diffracted field while the number of degrees of freedom with the radiated field. The number of files generated follows

$$N_{total} = N_{Diffracted} + N_{Radiated} = N_f \cdot (N_d + N_{DOF}) \tag{3.11}$$

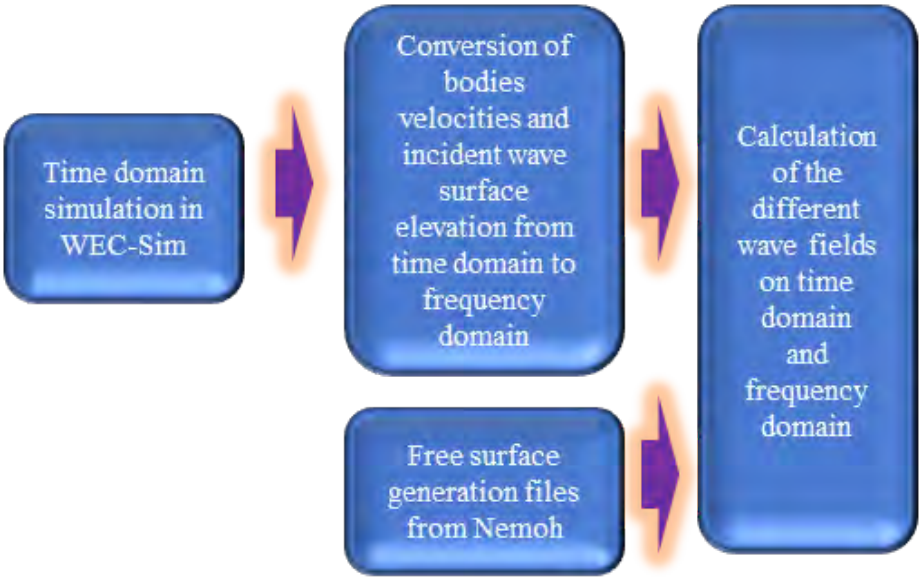

Figure 3.22: The overview of the calculation of the wave fields.

The incident wave elevation and the bodies velocities from WEC-Sim have been converted into the frequency domain using the Fourier transform. The same hydrodynamic Nemoh frequencies have been used in this conversion to match the free surface generation files generated by Nemoh. The hydrodynamic frequency step and the WEC-Sim simulation time step have been related using the reciprocity relation to have a good description of the bodies velocities and the incident wave elevation through the Fourier coefficients. The Fourier coefficients are considered well captured when they can be used to generate accurately the time domain results. The reciprocity relation can be expressed as [169]:

$$\Delta f \cdot \Delta t = \frac{1}{L_{ts}} \tag{3.12}$$

Where Δf is the hydrodynamic frequency step, Δt is the WEC-Sim simulation time step and L_{ts} is the length of the time series. The Fourier transform is used to find the amplitude and phases of the incident wave and of the bodies velocities as shown in

$$F(\omega) = \frac{2}{T_{sim}} \int \sum_{n=1}^{N_f} (f(t) \cdot e^{i2\pi f_n t}) dt \tag{3.13}$$

Where T_{sim} is the duration of the simulation and $f(t)$ is the value of the signal at the time t.

The wave directional distribution has been based on the average wave directional standard

deviation (28.95 degrees) of the Berth A wave buoy in the Belmullet site [170]. Wave directions between the main direction and 2 times the wave direction spread can be simulated to give a probability of 95.45% of the real incoming directional wave (see Figure 3.23). The normal distribution has been discretized in 7 wave directions, each with a related probability of occurrence.

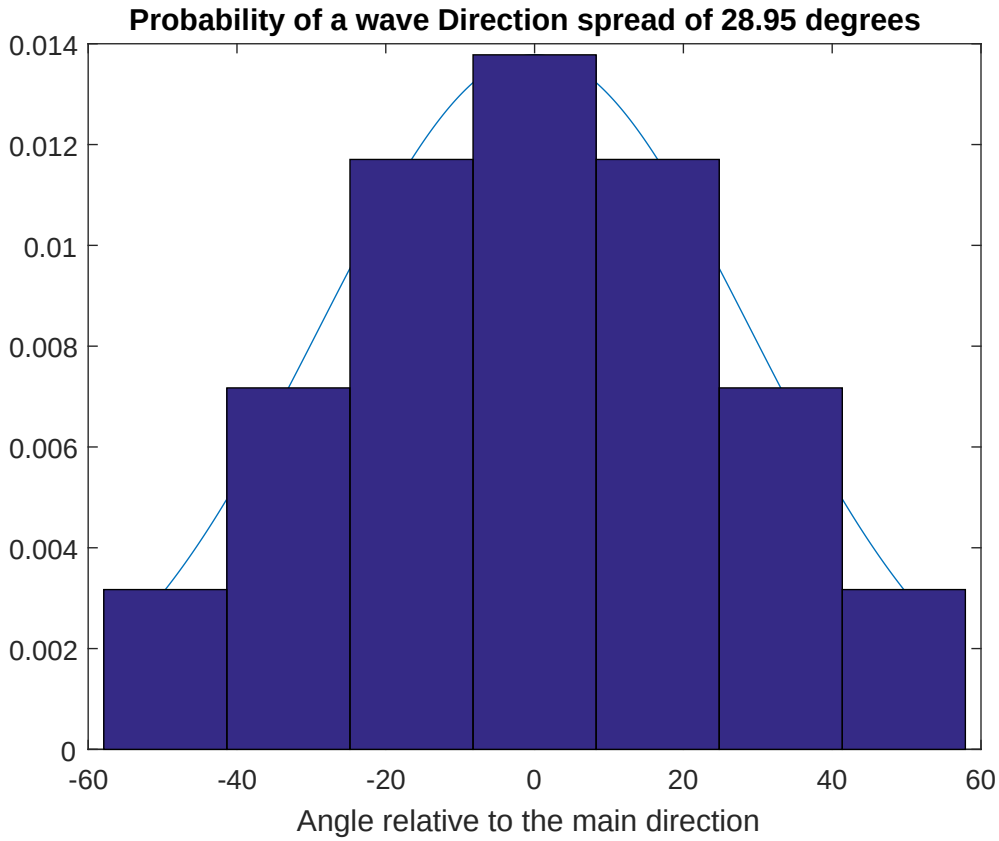

Figure 3.23: The discretization of the directional distribution.

3.4.3 Computational model set-up

The main inputs for the numerical model are described in Table 3.3. An irregular wave described by a Pierson-Moskowitz Spectrum with a significant height of 3m and a peak period of 10s is considered. Pierson-Moskowitz is expressed as a function of the peak period and the significant height following [133] and [171]. Two different main wave configurations have been used: a single wave direction and a multi-wave direction.
A reasonable number of frequencies (952) have been used for the hydrodynamic simulation

between 0.02 and 5 rad/s. The number of field points used is 50 points in x and y while the field area covers 100m in each dimension. So each point covers an area of $4m^2$. If local effects are targeted, this could require an increase in the resolution. Equation (3.12) shows a relation between the frequency step and the time step. The simulation time for WEC-Sim is determined from the frequency step of the Nemoh frequencies. In particular a simulation time of 1202s has shown a good approximation of the time domain incident wave field and of the bodies velocities through the Fourier transform.
A single float WaveSub configuration has been used for the simulations. The inertia properties and the hydrodynamic coefficients are based on the simplified version of the WaveSub (a cuboid shape for the reactor and a cylinder and 2 hemispheres for the float). Size and measurements come from the full scale representation of the tank testing conducted at the University of Plymouth Ocean basin in 2016 [172]. The reactor is simplified as a cuboid shape with length, width and height respectively of 51.55, 50 and 10.5m. The float is described by a central cylinder with a length of 4.75m and 2 hemispheres in the sides with a diameter of 12m. The float depth is 10.55m while the reactor depth is arbitrarily chosen and in this configuration a value of 33m has been used as an example. A mesh independence study has been undertaken to make sure that the hydrodynamic results were not dependent on the mesh resolution. The main direction (0 degrees relative to the x axis) has been chosen in this analysis (See Figure 3.24).

The mesh of the bodies has been created in Salome-Meca [131]. Panels can be created

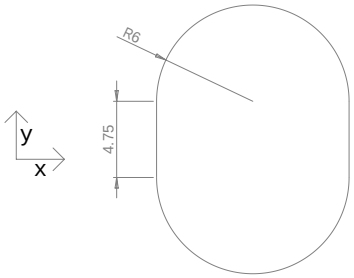

Figure 3.24: The reference system relative to the float position.

mainly triangular or quadrangular. Three types of mesh have been considered: a coarse (201 panels for the float and 200 for the reactor), a moderate (547 panels for the float and 877 for the reactor) and a fine mesh (868 panels for the float and 1501 for the reactor).
A good mesh convergence can be observed especially from Figures 3.24c, 3.24d, 3.24h, 3.24i, 3.24j, 3.24k and 3.24l. Main motion for a main single wave direction is expected to be in surge, heave and pitch due to the symmetry of the device relative to the wave di-

rection. It is expected that the excitation coefficients in the others degrees of freedom are negligible. In fact, it is found that excitation force in roll and yaw is around 100 times smaller than in surge and heave (see Figures 3.24a, 3.24b, 3.24c, 3.24d). It is converging to zero with an increasingly fine mesh. By contrast, radiation coefficients are significant in all the degrees of freedom but the force is only present in some directions because it is dependent on the velocity and acceleration of the device in each degree of freedom (radiation damping and added mass force respectively). Added mass force and radiation damping force will be more significant in the degrees of freedom where the excitation force is determining a more significant velocity and acceleration of the body. Added mass and radiation damping of the reactor show the problem of Nemoh related to thin elements (see Figures 3.24j, 3.24k, 3.24r, 3.24s, 3.24t). The behaviour of these coefficients are irregular for some frequencies and it is a known limitation of Nemoh. Nemoh is based on a source distribution and the computation of thin elements could have created this irregularity. In fact, the shape of the reactor has the height 5 times smaller than the other 2 dimensions. Finally, the fine mesh has been used because of the higher accuracy. Computational time in this case was around 20 times the coarser mesh.

Table 3.3: The main parameters of the model set-up.

Type of wave	Pierson Moskowitz wave spectrum
H (m)	3
T (s)	10
w (rad/s)	[0.05 5]
Number of frequencies	952
Number of field points in x and y	50
Field area (m^2)	100
Simulation time (s)	1202

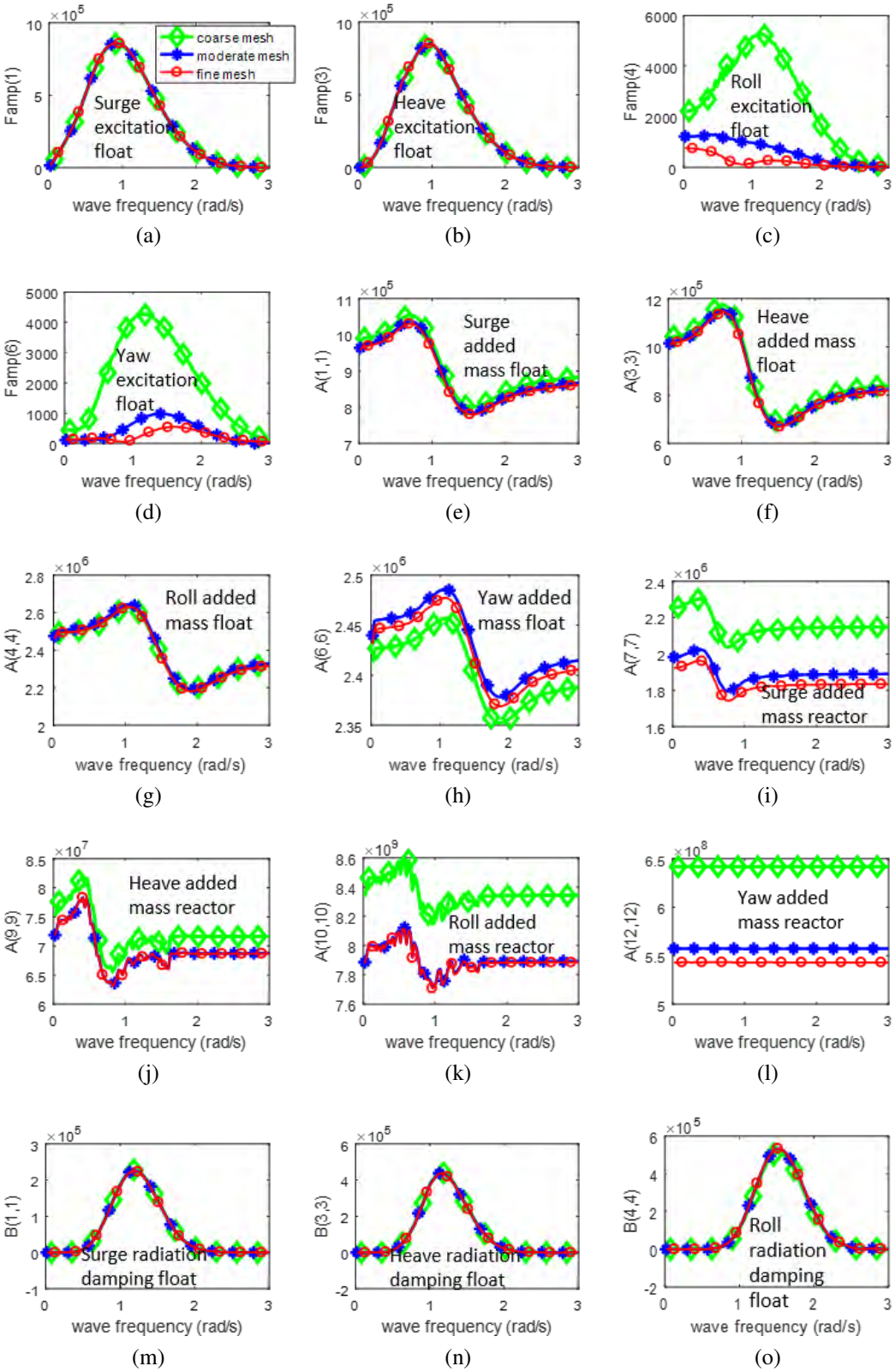
coarse mesh
moderate mesh
fine mesh
Surge excitation float
Heave excitation float
Roll excitation float
Yaw excitation float
Surge added mass float
Heave added mass float
Roll added mass float
Yaw added mass float
Surge added mass reactor
Heave added mass reactor
Roll added mass reactor
Yaw added mass reactor
Surge radiation damping float
Heave radiation damping float
Roll radiation damping float
wave frequency (rad/s)
(a)
(b)
(c)
(d)
(e)
(f)
(g)
(h)
(i)
(j)
(k)
(l)
(m)
(n)
(o)

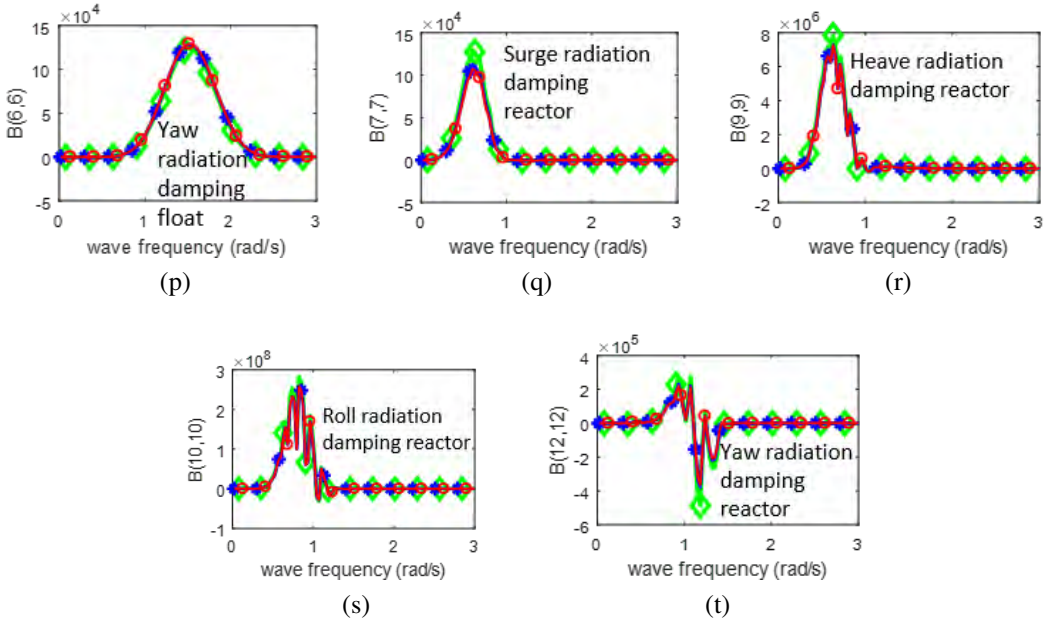

Figure 3.24: Surge, heave, roll and yaw excitation coefficients of float (a,b,c,d), surge, heave excitation coefficients of reactor (e,f), surge, heave, roll and yaw added mass coefficients of float (g,h,i,j), surge, heave, roll and yaw added mass coefficients of reactor (k,l,m,n), surge, heave, roll and yaw radiation damping coefficients of float (o,p,q,r), surge, heave, roll and yaw radiation damping coefficients of reactor (s,t,u,v).

3.4.4 Results

Results are presented in terms of a single wave direction and a multi-wave direction. A multi-wave direction simulation is more computationally demanding because it requires the hydrodynamic simulation for all the wave directions used for the approximation of the directional distribution. Then the time domain simulation is also longer because the excitation force is computed considering all the wave directions. Figure 3.25 shows the significant motion amplitudes for the float and the reactor in all the degrees of freedom. Main motion for the 1 incident wave direction case is in surge, heave and pitch. This conclusion was already observed in the mesh convergence due to the largest excitation coefficients in these degrees of freedom. Overall, the motion in these degrees modes decreases for the float considering the directional wave distribution while sway, roll and yaw become more important. The reactor shows also a similar motion behaviour. However, the wave directional distribution case shows a slight increase in the surge and heave motion. Figure 3.26 and Figure 3.27 show the frequency and time domain results for the different wave fields for a single wave direction. The significant height of the incident field is not shown because this is constant and equal to 2.91 m. A better accuracy of the chosen significant height equal to 3 m can be reached with a longer simulation time that however, corresponds to a larger number of hydrodynamic frequencies considered in the simulation. The diffracted field generates an increase of the significant height behind the device while the radiated field shows an increase in the front and in the back of the device. The relative difference between the total significant height and the incident wave height is shown in Figure 3.26 c to observe more clearly the influence of the radiation and diffraction wave fields on the total significant height and the positive increases. The total significant height has mainly an increase in the front while behind the device there is an increase further from the float. This different behaviour of the total wave field compared to the diffracted and radiated wave fields is due to the total wave field considering the phases of each wave field. So, the perturbed wave field shows generally a smaller significant height behind the device compared to the incident wave height. A larger value of the significant height follows more or less a parabolic curve centered on the float. Figure 3.27 shows a screenshot of the time domain of the incident and perturbed wave fields. In particular, it is possible to observe an expected increase of the perturbed wave field behind the float. The time domain visualization is valuable in a commercial context, because it shows in a very direct way if the results are reasonable or if they are the results of numerical errors. It is a first step to understand the numerical model that is to be used in parallel to a more formal validation process.

Figure 3.28 shows the significant height of the incident wave field with a different value in each point of the wave field due to the dependence on the wave direction for multi-directional waves. The random phase related to the wave direction and wave frequency and the different location of the wave field are determining this variation (Refer to Equation (2.64)). However, it is expected that there will be convergence of the incident significant height for all the grid points to the incident wave height (3m) for a very long simulation time. The significant wave height of the diffracted field shows a similar behaviour of the single wave direction but it is decreased. The radiated significant wave height reaches larger values not anymore along the main wave direction but along a certain relative angle to the main wave direction due to the different motion of the device (also in sway). The total significant height shows a narrower shading behind the device compared to a single wave direction. Figure 3.29 shows a snapshot of the time domain simulation. In particular it is shown when the incident field has a wave direction different from mean. It is possible to observe the wave field with different local peaks dependent on both the coordinates of the grid. The float is observed during a yaw motion due to a wave directional component coming from south-west.

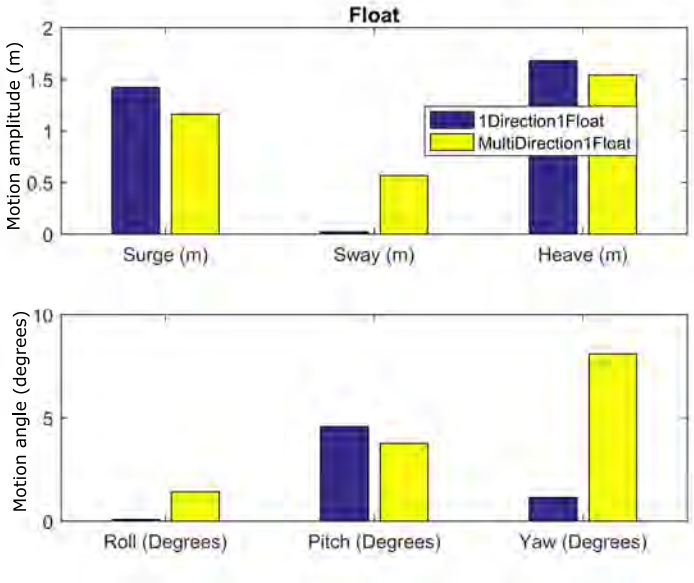

(a)

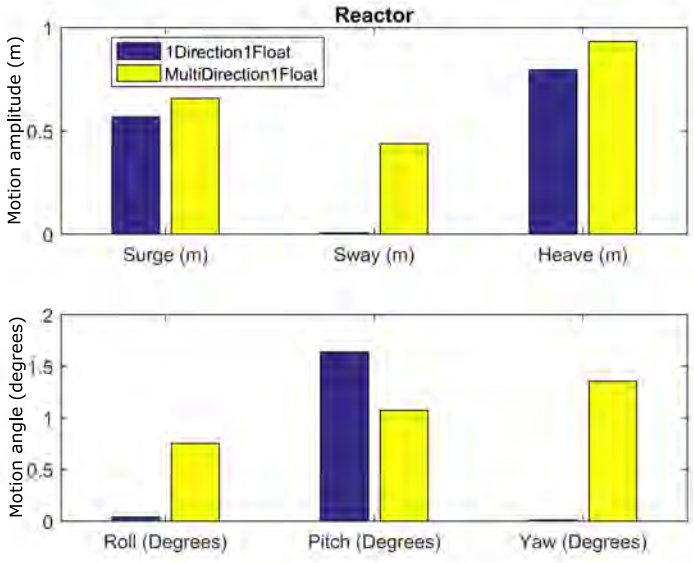

(b)

Figure 3.25: Significant motion amplitudes of the float (a) and of the reactor (b) in all the degrees of freedom. A comparison between the 1 direction and the directional distribution is shown.

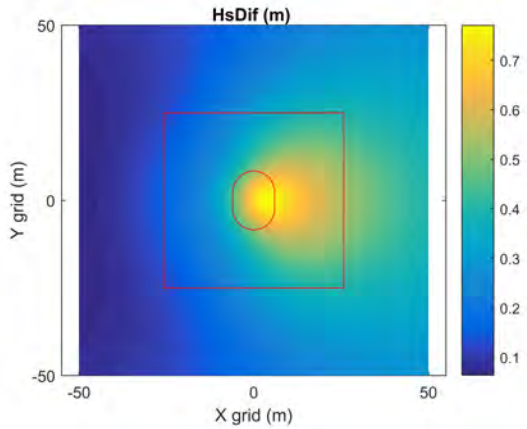

(a)

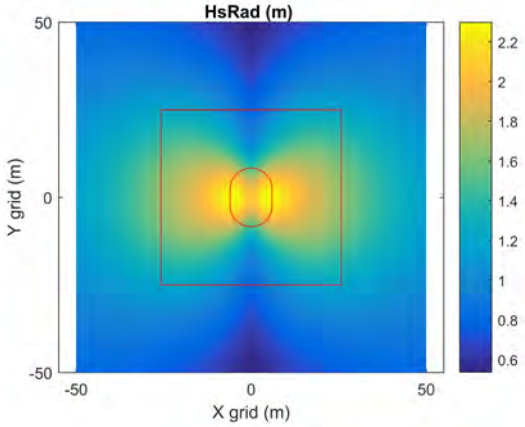

(b)

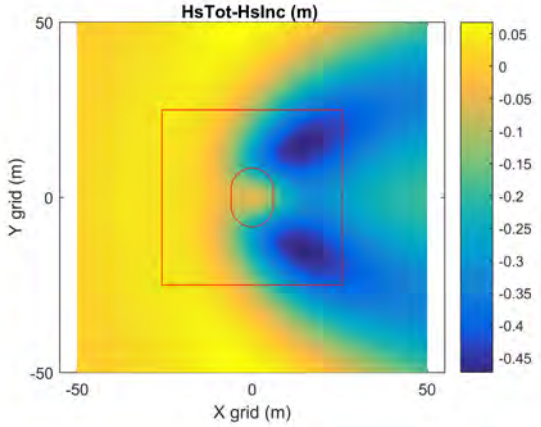

(c)

Figure 3.26: Significant heights (m) created by the diffraction (a), radiation (b) and perturbed (c) fields for a single wave direction case.

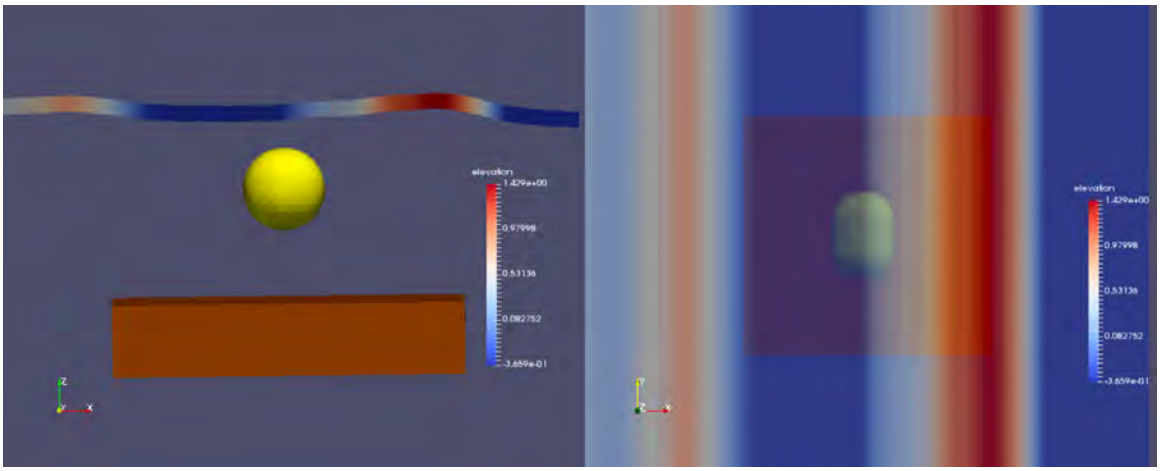

(a)

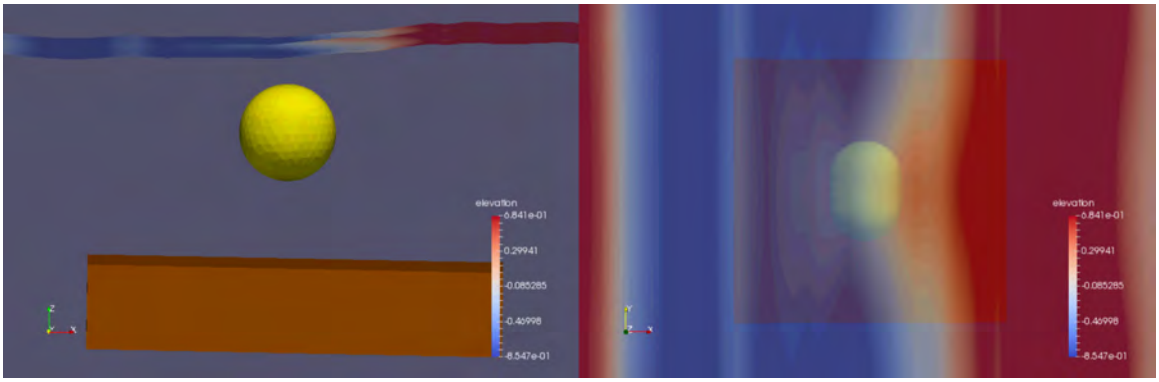

(b)

Figure 3.27: Screenshot of the time domain simulation created in Paraview [173] showing the incident (a) and the perturbed (b) fields for a single wave direction case. View angle are from the side on the left and from the top on the right. Only float and reactor are shown while PTO lines and mooring lines are omitted.

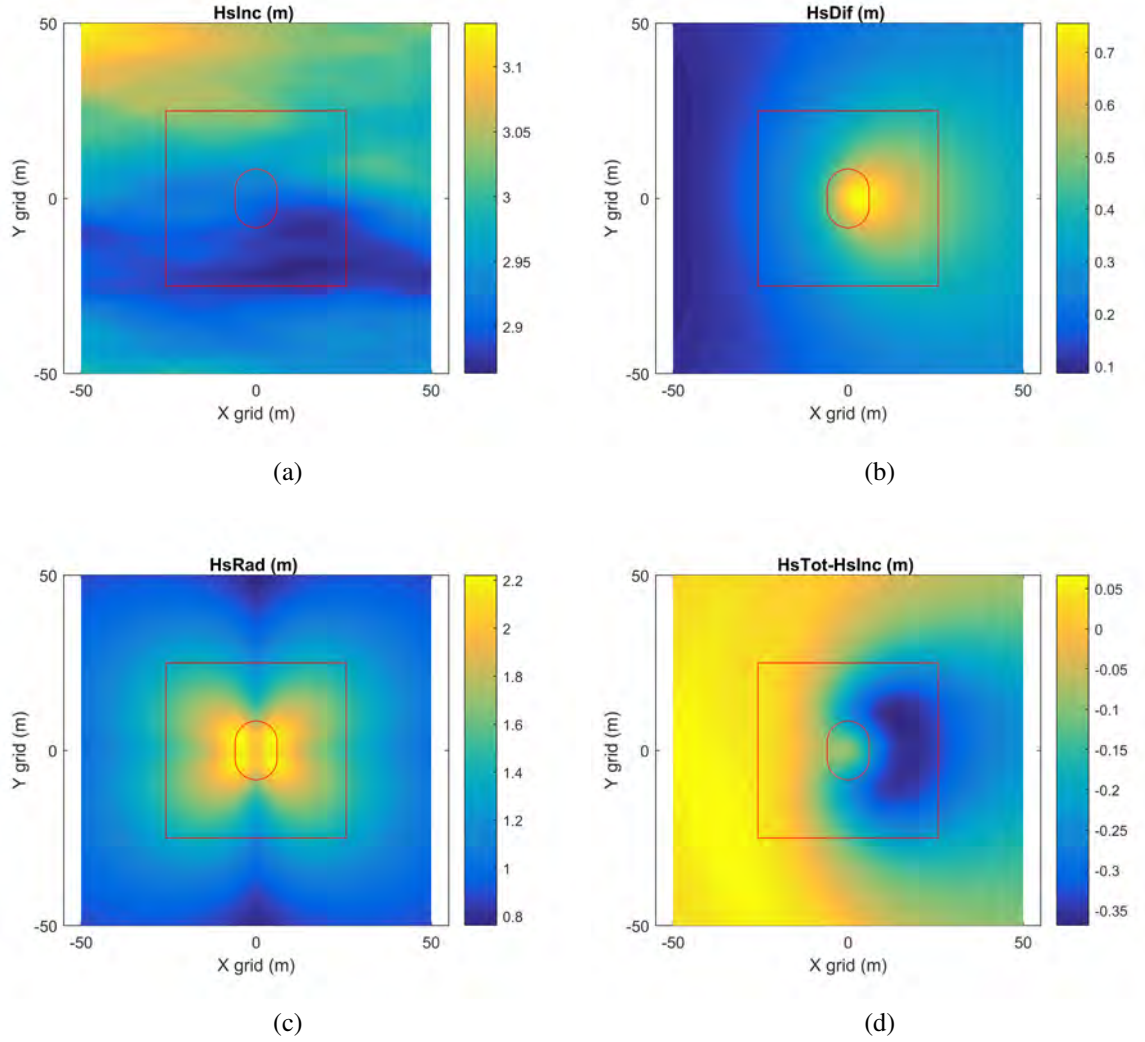

(a) (b)

(c) (d)

Figure 3.28: Significant heights (m) created by the incident (a), diffraction (b), radiation (c) and perturbed (d) fields for a multi-wave direction case.

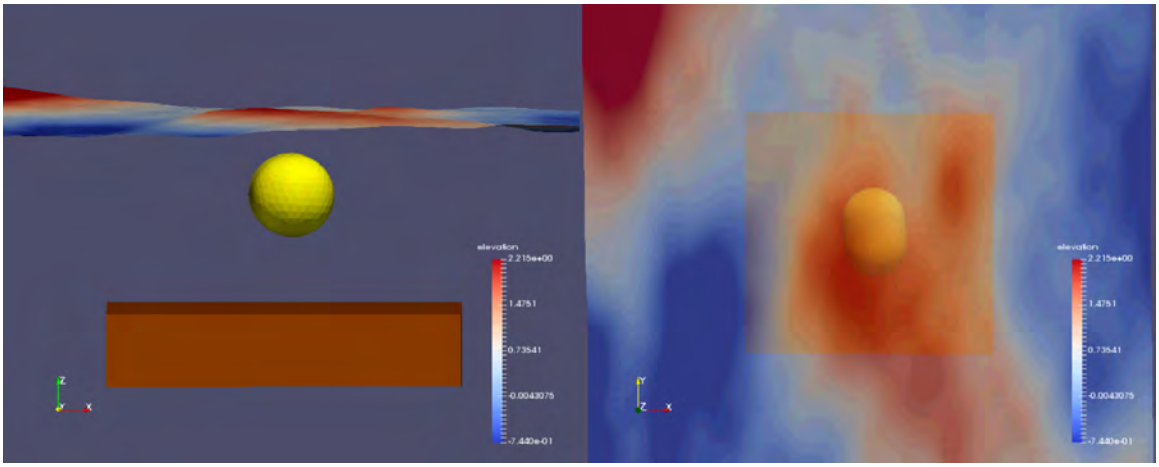

(a)

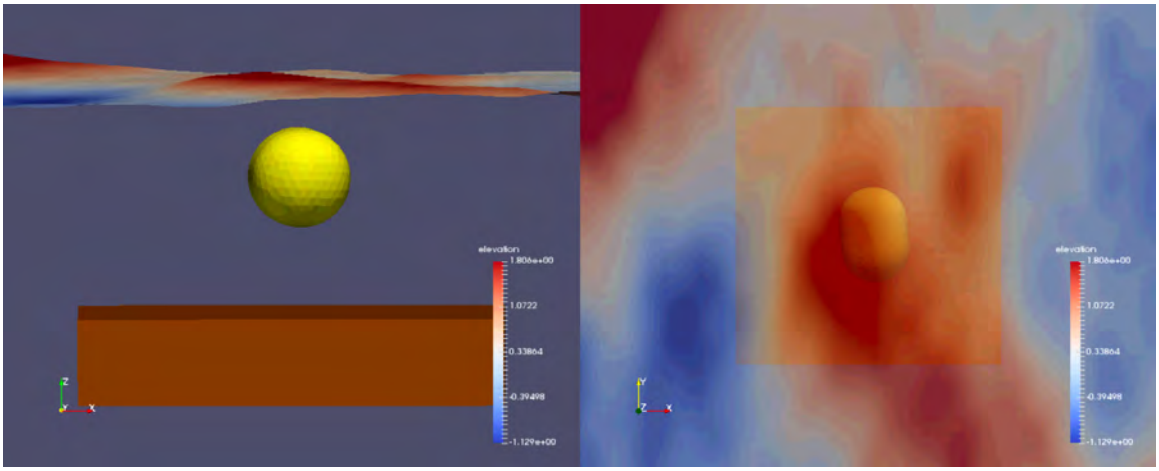

(b)

Figure 3.29: Screenshot of the time domain simulation created in Paraview [173] showing the incident (a) and the perturbed (b) fields for a multi-wave direction case. Only float and reactor are shown while PTO lines and mooring lines are omitted.

3.4.5 Conclusions

Multi-directional waves and wave fields have been modelled and analysed in this chapter. The WaveSub device has been considered as a reference for this purpose. The results show the influence of the device on the wave fields. These are the incident, the diffracted, the radiated and the perturbed wave fields. Then a time domain visualization of the wave fields is also presented. A comparison between a single wave direction case and a multi-directional waves case is described. The WaveSub device moves mainly in surge, heave and pitch for a single wave direction due to the symmetry of the device relative to the wave direction. As expected the device starts moving also in the others degrees of freedom when subjected to multi-directional waves. Finally, the total significant wave height is mainly reduced behind the device while an increase of it follows a parabolic shape for a single wave direction. Diffracted significant wave height has an increase behind the device while the radiated significant wave height has an increase in the front and behind the WaveSub device.

The implementation of multi-directional waves in the WEC-Sim numerical code is a good success for this research. The code is now available to several users [133]. The modelling of the wave fields is very useful to understand the influence of the device on the incident wave field. Furthermore, visualization of the frequency and time domain of the wave fields are great tools to give more confidence of the results obtained from the time domain simulation.

Further work will include a comparison and validation with results coming from tank testing. Additionally, the directional distribution that has been assumed independent on the frequency, could be still investigated for a more realistic relationship with the frequency.

Chapter 4

Experimental and numerical benchmarking

4.1 Introduction

Benchmarking against different regular wave cases tested in the tank will allow confidence in the numerical model and to understand more clearly its limitations. Results of this investigation have been accepted by the Renewable Energy journal [174].
The testing was conducted in three different sessions in March, June and July 2017 in Plymouth University's Ocean basin (see Figure 2.11). The device was tested in $1:25^{th}$ Froude scale. In particular this testing was related with the concept validation phase (TRL 1-3) investigating the variation of design variables (see chapter 2.3). The main aim of the tank testing was to compare the power produced by a single float device and by a 3 float device configuration. This project was funded by Innovate UK under the Energy Catalyst Round 3 Early Stage competition. MPS and the University of Bath as an academic partner involved in the control system, were in particular conducting the testing.
The benchmark was done relative to a three float configuration (see Figure 4.1). The three float configuration was tested changing the float to float spacing and the reactor depth. Different spring stiffness and damping values of the PTO were also applied, testing active and passive PTO modes. The specific configuration parameters used in the experimental test were taken into account in the setup of the numerical simulation.
When comparing physical and numerical models, it is important to decide the scale of each of the tests. To assist the design team for the WaveSub device, the numerical model was based upon the dimensions of the full scale design. Moreover, the hydrodynamic

calculation in Nemoh shows a better computational stability for the full scale than the tank scale. In order to compare with the tank test, the experimental results have been scaled from the testing scale using Froude scaling. This choice has been demonstrated enough accurate for the comparison between the numerical model and the tank testing because the hydrodynamic forces from Nemoh, PTO and mooring forces can be directly Froude scaled [89]. In fact, hydrodynamic forces from Nemoh depend only on the geometry shape and wave frequencies and so they can be Froude scaled. Then PTO and mooring forces are linearized and so they can be also Froude scaled. To improve the match between numerical and experimental models, drag forces have been implemented using the WEC-Sim option of viscous drag as discussed in Section 3.3. In particular, these drag forces are more realistic for a tank testing scale while they will be probably different for a full scale. A more realistic numerical model of the full scale device should account also the influence of the Reynolds number on the drag together with scaling effects of realistic PTO and mooring forces.

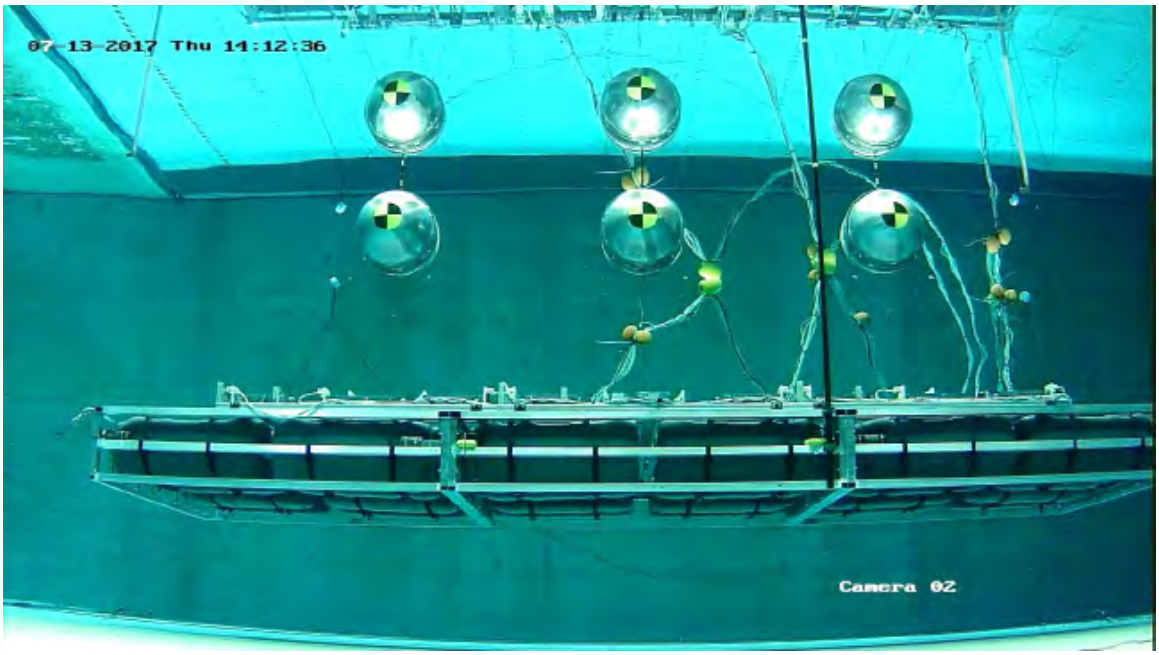

Figure 4.1: Multi-float model shown in its static position at a medium reactor depth and 2.25D float spacing.

4.2 Experimental set-up

Figure 4.2 shows the experimental test in the Ocean Basin. It is raised out of the water on an adjustable floor. This shows three floats in a "parked" condition above the reactor. Inertia ballast is given by the black 100L water tanks. Overall the model was 6.19m long at $1:25^{th}$ scale. Motion data has been obtained using the Qualisys system [92] while the wave elevation was measured using 6 wave probes (3 in the front and 3 in the back of the device). Rotational speed and position of PTO line drum have been found using non-contact Renishaw RM44 encoders. Load cells are used to measure the tension in each PTO and mooring line. The components are constructed as follows (measurements are referred to $1:25^{th}$ scale):
The floats were characterized by a central cylinder and two hemispheres on the ends. They were manufactured from 2mm thick aluminium. Flange rings welded externally to the central cylinder were designed with different holes to allow the testing of different PTO line attachment angles. Three different horizontal float spacings were tested and they were selected based on multiples of the diameter of the float. The spacings chosen were 2.25, 3 and 4 times the diameter of the float between the outer surfaces. The results here report on the 2.25 diameter spacing tests.

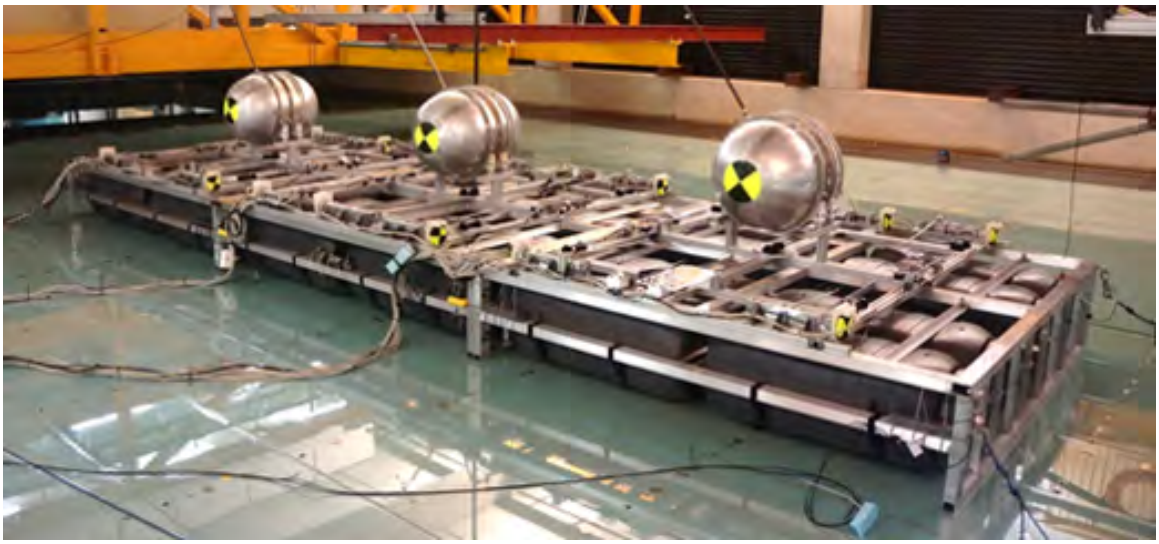

Figure 4.2: Multi-float device shown here in 3D horizontal float spacing before tank floor lowered for testing. Taken during May/June 2017 testing period.

The reactor contained a number of different parts: the reactor frame, the reactor ballast tanks, the reactor ballast and the PTO frame. The reactor frame was designed and

manufactured from aluminium box section welded together to form an individual module, three of these modules were then bolted together to form a single structure. The ballast tanks were 100 L water butts and there were 8 for each reactor module. These ballast tanks were flooded with water during testing and used to increase the inertia properties of the reactor. Other lead ballast on the top of the reactor was attached to decrease the mooring line tensions to more suitable values. Finally, the PTO frames were designed to be adapted to different float spacing configurations and were bolted to the top surface of each reactor frame in different positions accordingly.

The PTO system was based around an electrical system to minimise friction and to provide precise control. The key components consisted of Maxon EC90 flat [175] 48V, with RM44 encoders from RLS [176]. The motors could be driven by float motion as generators when connected to a variable resistance load bank, in the form of Ohmite rheostats [177]. This allowed passive testing with variable damping rates. The PTO motors could also be actively controlled in four quadrants to enable the testing of advanced control strategies. For the tests described here they were driven to provide an ideal damping characteristic described by a linear relationship between the PTO line drum rotational speed and motor torque. Real time control and data logging of sensor and actuator signals was achieved using SIMULINK RealTime with a NI PCI-6225 Multifunction DAQ. The control loop executed at a sampling rate of 2kHz and logging at a rate of 100Hz.

Five float tethers connect each float to the reactor: 4 in the corners (spring/damping PTO) and one in the centre (spring only). The central tether was designed to provide float buoyancy resistance therefore reducing the tensions on the corner tethers. A target buoyancy distribution of 90% on the central line and 10% shared between the corners was designed. The stiffness value of each PTO was related to the specific spring attached to that line, the four corner lines were identical and the centre line was different. The spring of the central PTO line used rubber bands normally used for spearfishing, 1x Omer 20mm band and 2x SFS 18.5mm band in combination. The corner springs were 1x Theraband silver tube [178], as used in therapeutic exercise. The mooring connected the reactor to the seabed with 4 taut, diagonal mooring lines in the corners with a spread of 3500 mm in x and 8000 mm in y.

4.3 Computational model set-up

The multi-float model which was tested in the tank in July 2017 was chosen for the comparison with the numerical model. Different regular waves of 4 m of wave height and a wave period between 7.5 and 10.5 s have been considered at full scale. In particular the regular wave of 4 m of wave height and 7.5 s wave period has been used for a detailed analysis. A carefully selected 20 second analysis window for each load bank settings was used (equivalent to 100s at full scale), when the start-up is ignored, half of this duration (50s at full scale) is shown in the results to more clearly see the differences between the models in the graphs. Generally, default regular wave simulation in WEC-Sim generates a different phase compared to the tank generated wave because the relative position between the wave maker and the device is not accounted. Moreover, there is a small slightly positive error in the tank mean wave elevation (Relative error less than 0.4 %). For a better comparison with tank testing results, tank wave elevation has been simulated in WEC-Sim thanks to an existing simulation wave class option, userDefined waves. Then the tank motion and power data have been compared to match the same time within the WEC-Sim simulation. In particular, a time difference due to the relative location of the wave probe and the device position has been observed and accounted in the analysis. The inertia properties of the floats and of the reactor were calculated based on their simplified geometry (A hollow cylinder and 2 hemispheres for the float and a cuboid for the reactor). In this calculation the wall thickness of the float was adjusted so that the mass was correctly scaled from the tank model to full scale. The reactor has been considered as a solid shape and its inertia properties were similar to the ones found by comparison to the 3D model properties in Autodesk Inventor of the CAD model of the test device (Relative error of inertia moments less than 5 %). The height of the reactor was obtained from its simplified volume (Cuboid shape) equal to the real reactor physical volume characterized by the frame, ballast tanks and the PTO system. The float spacing has been set up to 2.25 times the diameter in the numerical simulation giving a relative error of less than 4 % compared to the tank measured float spacing between the floats. Finally, the float depth has been set to an average of the experimental values of each float (Relative error less than 3 %). The mesh of the geometry was built in Salome-Meca [131] using triangle panels. A mesh independence study has been undertaken to make sure that the hydrodynamic results were not dependent on the mesh resolution. In particular, 3 types of mesh have been considered: a coarse (172 panels for the float and 826 for the reactor), a moderate (1672 panels for the float and 1932 for the reactor) and a fine mesh (2916 panels for the float and 2830 for the reactor). Furthermore,

a final comparison with the open-source OpenWarp [179] has been made keeping the same fine mesh. This software improves Nemoh capability, includes parallel computing and irregular frequency removal. The code has been also improved to fix the problem of the switch between finite/infinite water depth. In fact, Nemoh has some numerical issues when the product between the wavenumber (k) and the water depth (d) is around 20 and when an intermediate water depth is considered. It was found that the fine mesh with an increased number of panels was required to solve a problem in the results related to an overestimate of the roll and yaw motion in the time domain simulation. In particular, roll and yaw excitation coefficients of the floats (see Figure 4.2) are expected to be negligible due to the symmetry of the case. If this is not the case, some large motion in these degrees of freedom could happen which is increased by an amplification of the radiation coefficients in these modes. An example of radiation damping, added mass and excitation coefficients for the surge and heave motion relative to the float1 and to the reactor are shown in Figure 4.2. A good mesh independence can be observed from the graphs where the 3 different mesh size give similar result. Moreover reactor heave radiation damping and especially the added mass related to the heave motion of the reactor show the problem of Nemoh related to thin elements (see Figures 4.2d-4.2h). The behaviour of this coefficient is irregular for some frequencies and it is for now a limitation of Nemoh. Figure 4.2h shows there is a reduction of the heave added mass of the reactor for frequencies above 1.6 rad/s for Nemoh but not for OpenWARP. This is because OpenWARP addresses the problem of the switching between intermediate and deep water. Small differences probably can be obtained between Nemoh and OpenWARP in the calculation of the radiation impulse response function used in the time domain simulation. However this verification is left as a future work. Finally, the fine mesh has been considered for the WEC-Sim simulations because a better accuracy of the hydrodynamic coefficients is expected. Nemoh hydrodynamic coefficients has been used for the results of this chapter but improvements of the hydrodynamic coefficients could be in future be addressed using OpenWARP.

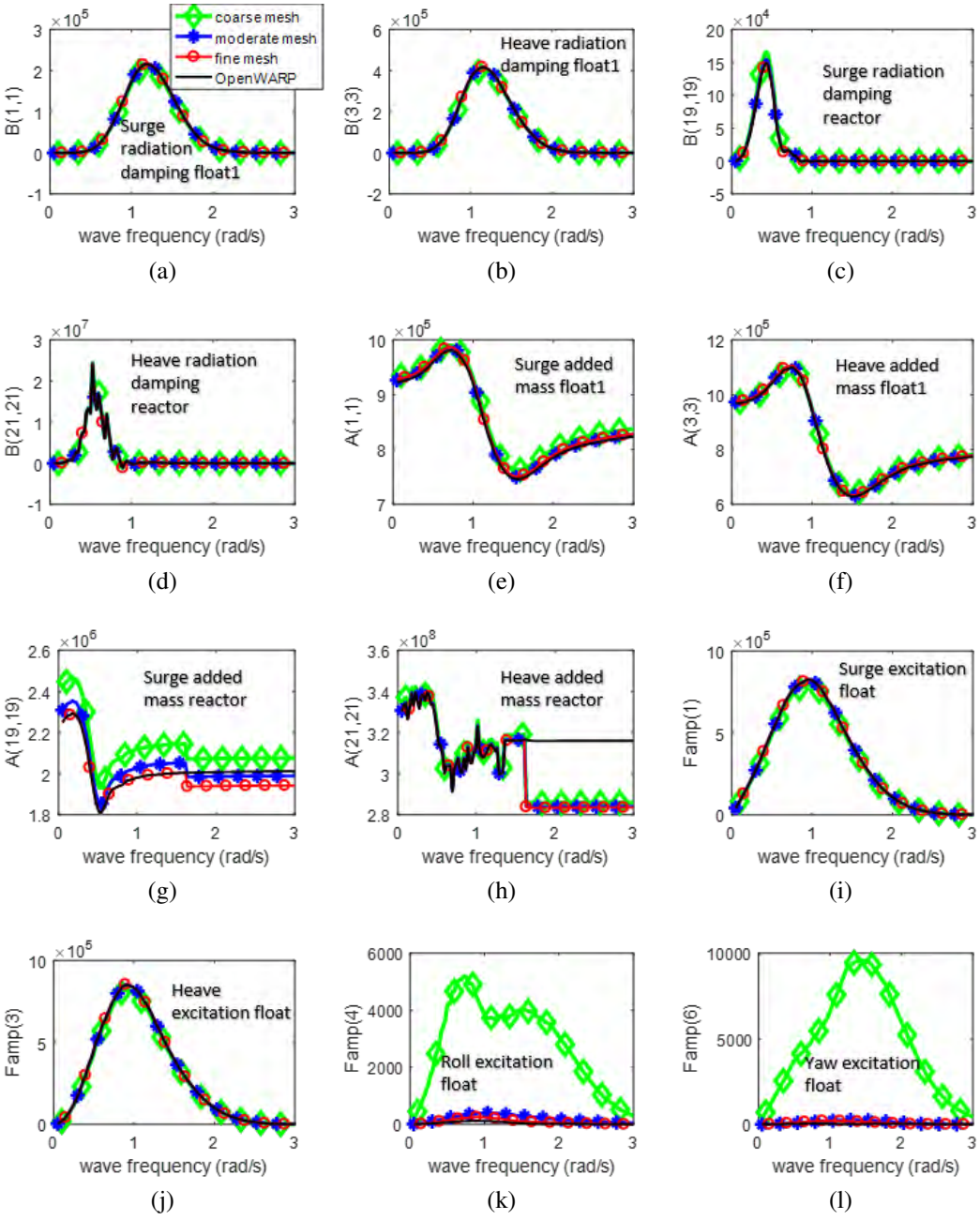
coarse mesh
moderate mesh
fine mesh
OpenWARP
Surge radiation damping float1
Heave radiation damping float1
Surge radiation damping reactor
Heave radiation damping reactor
Surge added mass float1
Heave added mass float1
Surge added mass reactor
Heave added mass reactor
Surge excitation float
Heave excitation float
Roll excitation float
Yaw excitation float
wave frequency (rad/s)
(a)
(b)
(c)
(d)
(e)
(f)
(g)
(h)
(i)
(j)
(k)
(l)

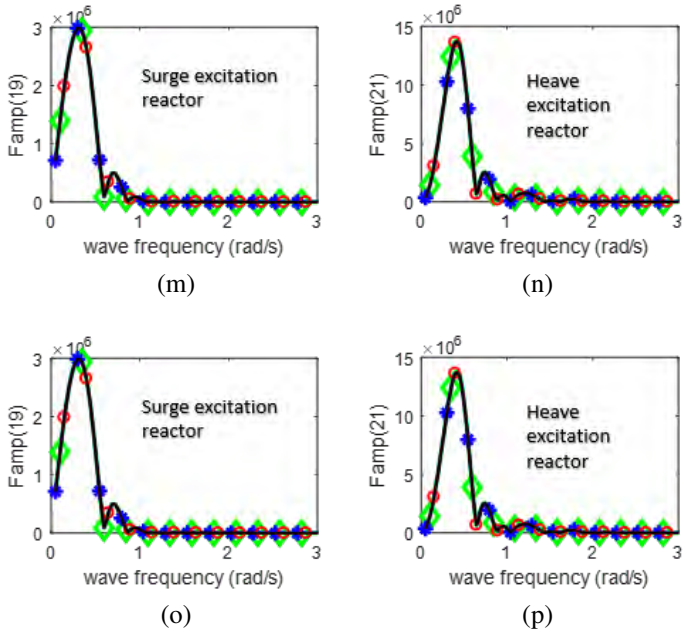

Figure 4.2: Surge and heave radiation damping coefficients of float1 (a,b), surge and heave radiation damping coefficients of reactor (c,d), surge and heave added mass coefficients of float1 (e,f), surge and heave added mass coefficients of reactor (g,h), surge, heave, roll and yaw excitation coefficients of float1 (j,k,l,m), surge and heave excitation coefficients of reactor (n,o).

The PTO system was simplified to a linear spring and damper with a constant stiffness and damping, while the mooring was simplified to a constant stiffness spring. This is not entirely accurate because the strain-load relationship for the elastic materials used for the spring in the tank is not linear. This relationship has been approximated as a polynomial equation and finally the stiffness-load relationship has been obtained. The stiffness is related to the gradient of the load-strain relationship and it can be expressed as follow:

$$k = \frac{d(L_{Spring})}{d(\epsilon \cdot SFL)} \tag{4.1}$$

where L_{Spring}, ϵ and SFL are respectively the load expressed in N, the strain and the free length of the spring.

The static line tension of the central spring in the tank model was approximately 77 kg while it was approximately 3 kg for the corner spring (see Figure 4.3). The stiffness values for the numerical model were obtained as an average of the values between 1-5 kg for the corner spring and 50-100 kg for the central spring. The damping value used in the

numerical model was obtained from the relation between PTO line speed and the driving torque relationship (see Figure 4.4). There is an initial torque necessary to apply to the PTO to overcome friction before it starts moving (Constant term of the linear equation shown in Figure 4.4). For this regular wave case the presumption is that it does not have a significant influence on the dynamic system because the floats are constantly moving but it could have some effects for an irregular wave case. This scaled data uses a linear line of best fit and so the PTO damping is approximated with a constant value. It is obtained using the following Equation:

$$C_{PTO} = \frac{T_{PTO}}{v_{PTOline} \cdot \frac{D_{PTO}}{2}} \tag{4.2}$$

where linear damping is C_{PTO}, torque is T_{PTO}, linear velocity is $v_{PTOline}$ and diameter of the PTO motor is D_{PTO}. The mooring was a taut mooring. A Liros Magic Speed 5mm line in polyester was used with a working stretch less than 8% defined as the elongation of a rope at 30% of its breaking load. The designed breaking load was 6800 N. The load-strain diagram of the mooring line provided by Liros [180] was used to find an approximation of the mooring stiffness to be used in the numerical model. The load-strain relationship of the mooring line is almost linear and so the approximation with a constant stiffness value is quite good (see Figure 4.5). However, there could be different factors influencing this relation such as effects of the mean load, load range and cyclic period [181]. Moreover the initial mooring line length was not the same for each corner of the reactor and this has introduced some non-linearity in the reactor motion. In the numerical set-up these different initial lengths have given a different spring value for each mooring line. The main factor that was difficult to define in the numerical model was the drag force on each float. A first estimation of the drag coefficient of 1.5 was used in the simulation based on previous research by Marine Power Systems Ltd [182]. This has been selected through a comparison of drag coefficients from spheres and cylinders found in the literature for example in [155]. After that, a process for tuning the estimate of the drag coefficient for each float was undertaken based on the comparison with the motion results of the tank testing. A drag coefficient has only been applied to the floats and not for the reactor because it is expected that drag force has a more significant importance relative to the inertia force when the characteristic dimension is less than 1/5th of the shortest wavelength [16] and the size of the reactor is significantly bigger than the float. Drag coefficient depends mainly on the geometry, Keulegan-Carpenter number, Reynolds number and surface roughness [155]. However due to lack of data relative to the shape of the float, an accurate result cannot be

obtained from the literature. The relation between drag coefficient (C_D) and drag force ($\mathbf{F_V}$) used in the model is shown in Equation (2.26). However the viscous force is referred only to the body velocity and not to the relative velocity between fluid and body. In fact, the approximation of the fluid velocity with the incident fluid orbital velocity is a quite rough estimation due to the presence of the body. So the viscous term referred only to the body velocity will show a similar accuracy. This formulation of the viscous term is available in WEC-Sim [166].

The drag coefficients for the floats of the single wave comparison described in the results section are shown in Table 4.1. The hydrodynamic heave drag coefficient was modelled as the default value (1.5) because heave float motion was also found to be related to the mechanical friction of the central float tether pulley system. In fact, another experiment with a spring directly connected vertically to the float improved the matching of the heave motion with the numerical model. Most of the mechanical friction is supposed to be concentrated in the central PTO line because there was most of the load (around 87%). Measurement of the torque and of the line speed on the PTO spindle has been used to calculate the mechanical power produced and are influenced by mechanical losses such as bearing friction, bending work of the PTO lines and hysteresis losses (see Figure 4.6). This is very complex to understand fully and further investigation should be still carried out.

Table 4.1: The hydrodynamic drag coefficient used in the single wave comparison.

	Surge hydrodynamic drag	**Heave hydrodynamic drag**
Float1	2.5	1.5
Float2	2	1.5
Float3	1.3	1.5

The mechanical friction of the central float tether pulley system was considered to match better the heave motion of the floats and modelled as a damping force. The mechanical friction has been set-up dependent on the float tether velocity and modelled as follows:

$$\mathbf{F_{MF}} = c \cdot \mathbf{v_{PTOline}} \tag{4.3}$$

A damping coefficient of 1000 kNs/m has been used in the full scale numerical model. The surge motion was not influenced significantly by the mechanical friction. In fact, the tuned hydrodynamic drag coefficients have sensible values compared to values that can be found in literature [155]. An interesting observation is that the tuned drag coefficient is different for each float. This is determined by the interference effects created by the hydrodynamic interactions between the floats. This phenomena is described in [155].

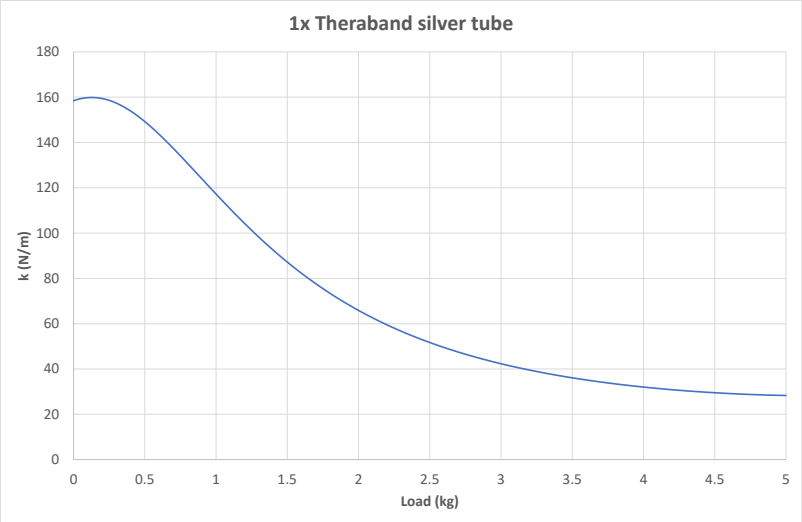

(a)

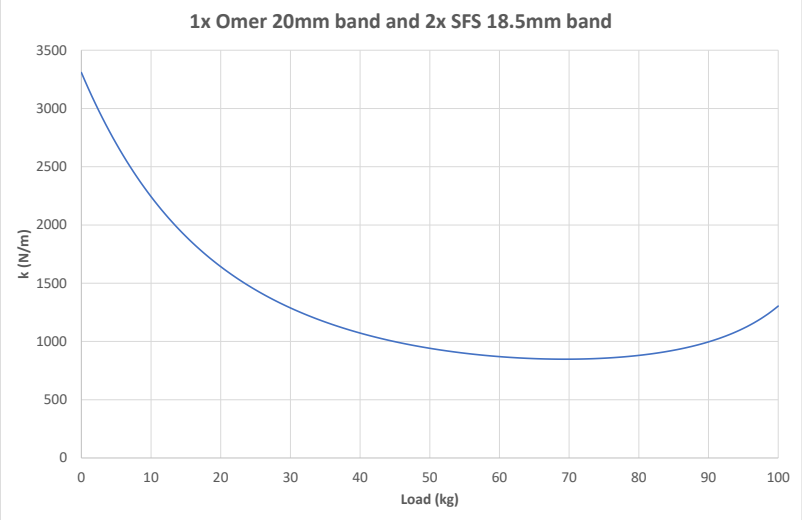

(b)

Figure 4.3: Stiffness as a function of the load of the 1x Theraband silver Tube (a) and of the 1x Omer 20 mm band and 2x SFS 18.5 mm band (b).

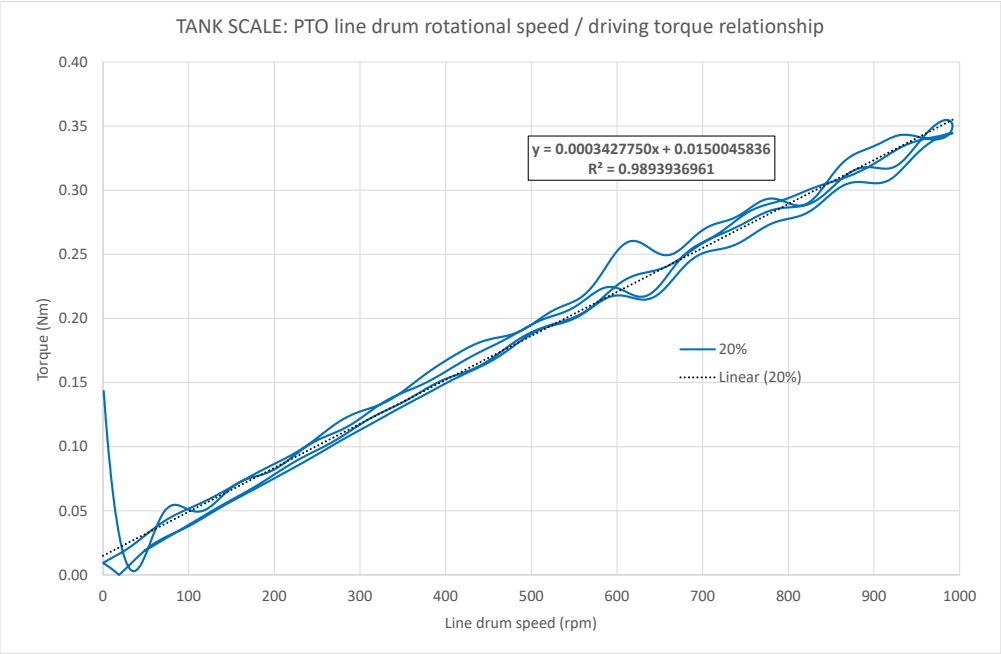

Figure 4.4: The tank scale PTO line speed / driving torque relationship. The percentage in the legend shows one particular setting of load / damping on the load bank.

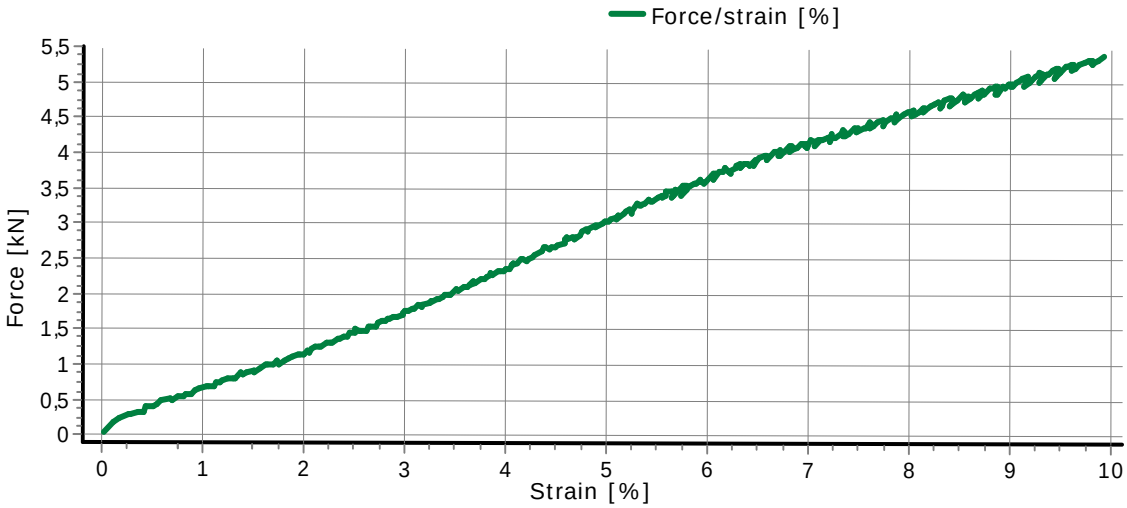

Figure 4.5: The stress-strain diagram of the model-tank mooring line.

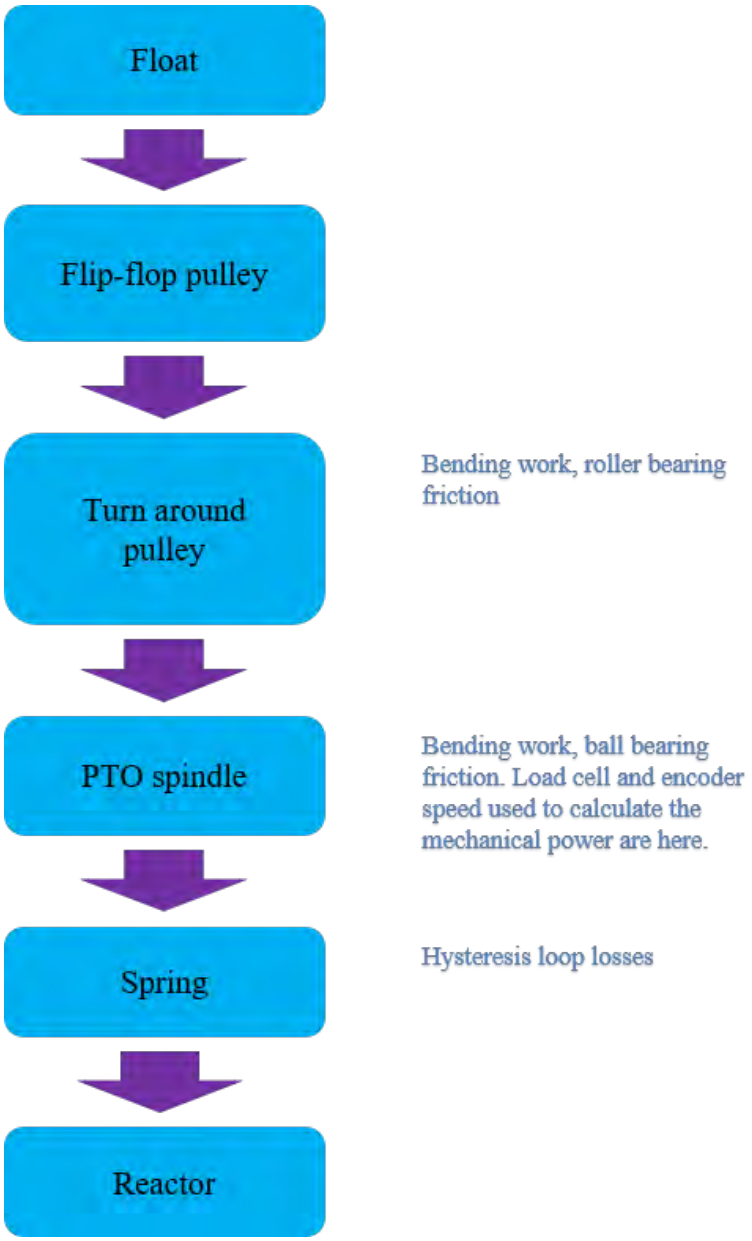

Figure 4.6: Scheme of the mechanical friction of the central float tether pulley system.

4.4 The results of the model-tank testing comparison

4.4.1 A detailed single wave case comparison

This section describes the results from both the numerical and experimental tests relative to the regular wave of 4 m wave height and 7.5 wave period in full scale measurement. The tank testing data are compared with three different versions of the numerical model: a model that includes both hydrodynamic drag and mechanical friction, a model that takes into account only hydrodynamic drag and a model without drag. Results are described using the same simulation time period for the tank and numerical models. Hydrodynamic drag is tuned to match the surge motion amplitude between the numerical model and the tank (Relative difference less than 10%). The basis of this tuning is to obtain the unknown physical drag force associated with the floats. Comparison with literature drag coefficient values will show if they are sensible. Mechanical friction is also tuned (Relative difference less than 20%) but the accuracy is decreased because same friction damping values are used for all the floats.

The parameters chosen for the numerical-physical comparison are the motion of the floats and reactor, forces and the power produced. Figure 4.7 shows the comparison of the reactor and floats motion in the main degrees of freedom. Main motions are the surge, heave and pitch motion due to the symmetry of the device relative to the vertical-longitudinal plane of the wave direction. However small motions in sway, roll and yaw are expected in the tank due to setup uncertainties and in the numerical model due to numerical errors. Numerical errors are expected to decrease with an increase of the number of panels of the mesh. Tank reactor response is characterized by higher frequencies that could be explained by the out of phases of the three floats, mooring settings and by tank wall reflection effects. The small motion of the reactor are more difficult to match correctly but it is still negligible compared to float motion. The results show the motions based on their average position without accounting for any offset values. Consistency between initial and final values has been checked for any error measurements.

Overall there is a good comparison for the main degrees of freedom (Surge, Heave and Pitch) especially for the model including drag and mechanical friction. Amplitudes are reduced in surge and heave due to the drag effect. Drag in the pitch mode has not been accounted for in this comparison because it has less important influence than surge and heave (see Table 4.2) but could be considered in further research. Floats orbit mainly in the surge-heave plane and become elliptical along the surge mode because the heave mode

is reduced by mechanical friction (see Figure 4.7). A good matching of the phases for the main degrees of motion is obtained in this case considering that the same tank wave elevation and simulation time has been used.

Table 4.2 shows the relative error of the body motion amplitude in the different model predictions. Relative error has been obtained as following:

$$RE(\%) = \frac{M_T - M_m}{M_T} \cdot 100 \tag{4.4}$$

Where RE is the relative error, M_T is the tank motion amplitude and M_m is the numerical model motion amplitude. The double amplitude or peak-to-peak has been used and obtained as a wave period average of the difference between the maximum and minimum excursions for a simulation time of fifteen times the wave period. Heave amplitude of the floats is not estimated well for models not including mechanical friction, while good agreement is found for the surge amplitude predicted by models accounting for hydrodynamic drag. Finally pitch motion is predicted with a good accuracy by all the numerical models for float2 and float3 but not for float1. However, the introduction of surge and heave drag provides a better match to this degree of freedom. Reactor tank amplitudes are more difficult to estimate correctly due to the small values. In a first approximation relative error based on the average double amplitude has been determined.

Table 4.2: Relative error (%) on the amplitude of motion of the floats and the reactor between the numerical models and the tank.

		Surge	**Heave**	**Pitch**
Float1	**Drag+DampMF**	4.4	-13.1	15.4
	Drag	0.2	-104.5	11.3
	No Drag	-52.3	-171.8	-35.3
Float2	**Drag+DampMF**	1.9	-1.5	11.3
	Drag	3.7	-80.3	12.7
	No Drag	-19.7	-105.7	-8.1
Float3	**Drag+DampMF**	-1.2	-16.5	10.8
	Drag	7.5	-108.6	18.3
	No Drag	-4.8	-114.8	7.3
Reactor	**Drag+DampMF**	8.0	-33.1	46.8
	Drag	8.7	-1.3	40.1
	No Drag	-23.9	-51.4	18.8

To show data obtained from the numerical models that is representative of the whole system, Figure 4.8 shows the main forces of float1 and the mooring forces. Most of the forces have a regular response; the mooring forces are more irregular due to the different

spring values set-up in each corner cable. The excitation force (as expected) is not dependent on the model because it depends only on the wave and hydrodynamic coefficients. Added mass and radiation damping are dependent on the response of the system (acceleration and velocity of the body respectively) and so their values change with the model used. In particular, the most significant values are obtained for the surge and heave mode. PTO forces and drag forces of float1 show a clear dependence on the drag coefficient. PTO forces are reduced by an increase of the drag coefficient. Drag forces are larger in surge than in heave because velocities reach higher values in this degree mode as shown also from the main motion in surge in Figure 4.7. A reduced heave drag force is obtained for the model accounting for drag and mechanical friction than the model accounting only drag because of the mechanical friction that decreases the heave motion and velocities.

The PTO torque is shown in next Figure 4.9. There is a good comparison for the torque of PTO3-4 while there is an overestimation for PTO1-2. This behaviour is related with the PTO lines velocities because the damping coefficient is a constant of the numerical model. So, the peaks of the PTO velocities for PTO1-2 are smaller for the tank testing. However, there is the same behavior of larger PTO line velocities of PTO3-4 than PTO1-2. In particular, mechanical friction plays an important role for the determination of the tank torque.

Finally, the mechanical power has been compared for the same time period as the motion comparison (see Figure 4.10). The mechanical power from the tank testing results has been obtained as following:

$$P_{tank} = \frac{T_{PTO}}{\frac{D_{PTO}}{2}} \cdot v_{PTO} \tag{4.5}$$

As expected the numerical model without accounting for drag and mechanical friction in the heave motion overestimates the mean total power by more than 150% compared to the tank testing. There is a good agreement between the tank test result and the model accounting for drag and mechanical friction. In particular, the relative difference on the mean total power for this model is less than 1%. There is also a good matching in the phase of the power for all models, but the amplitude is highly influenced by the drag and mechanical friction. Finally, the normalized power produced by the models is reported in Table 4.3.

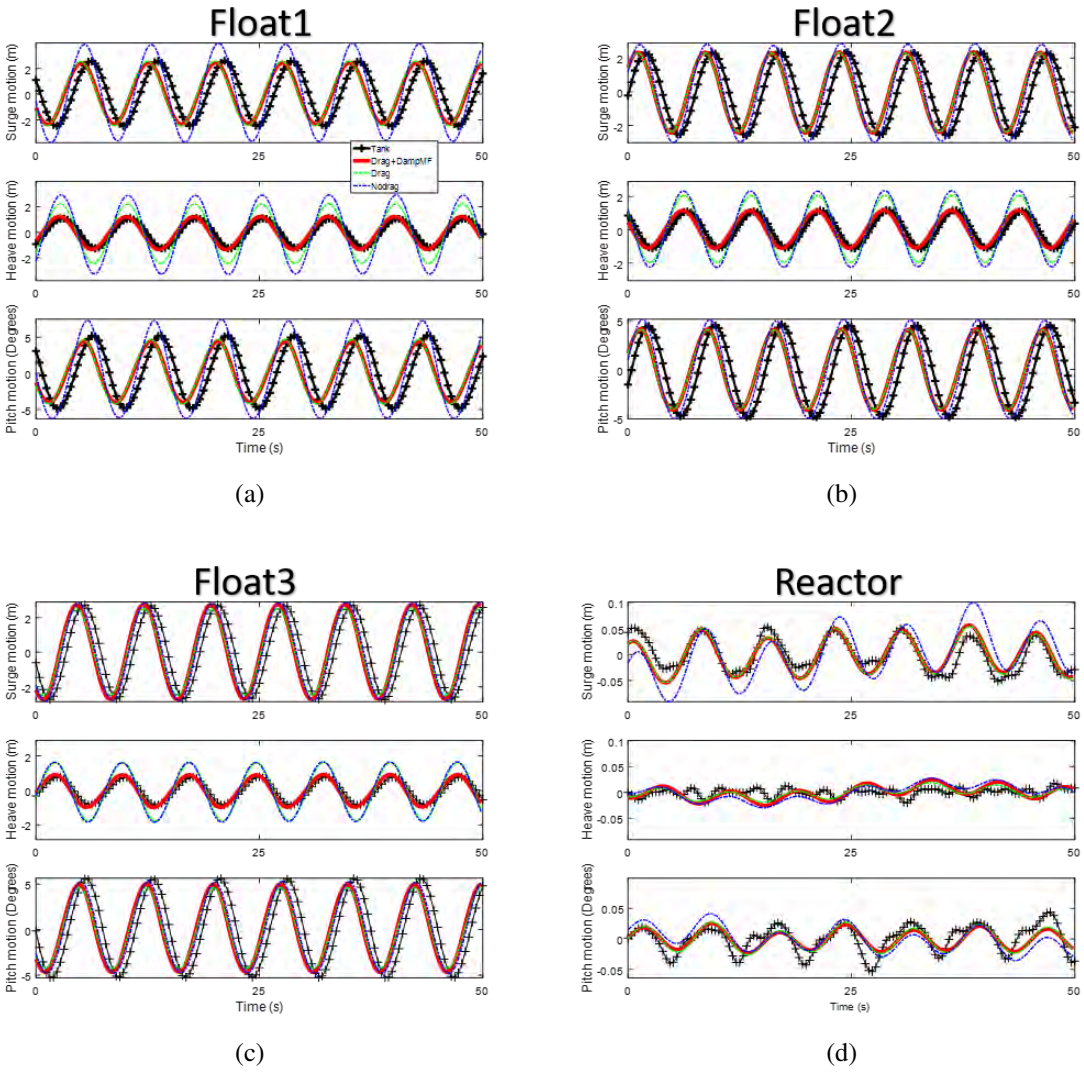

Figure 4.7: Float1 motion (a), float2 motion (b), float3 motion (c) and reactor motion (d) at a full scale of the tank testing and the 3 numerical models: the drag + mechanical friction, the drag and the no-drag model.

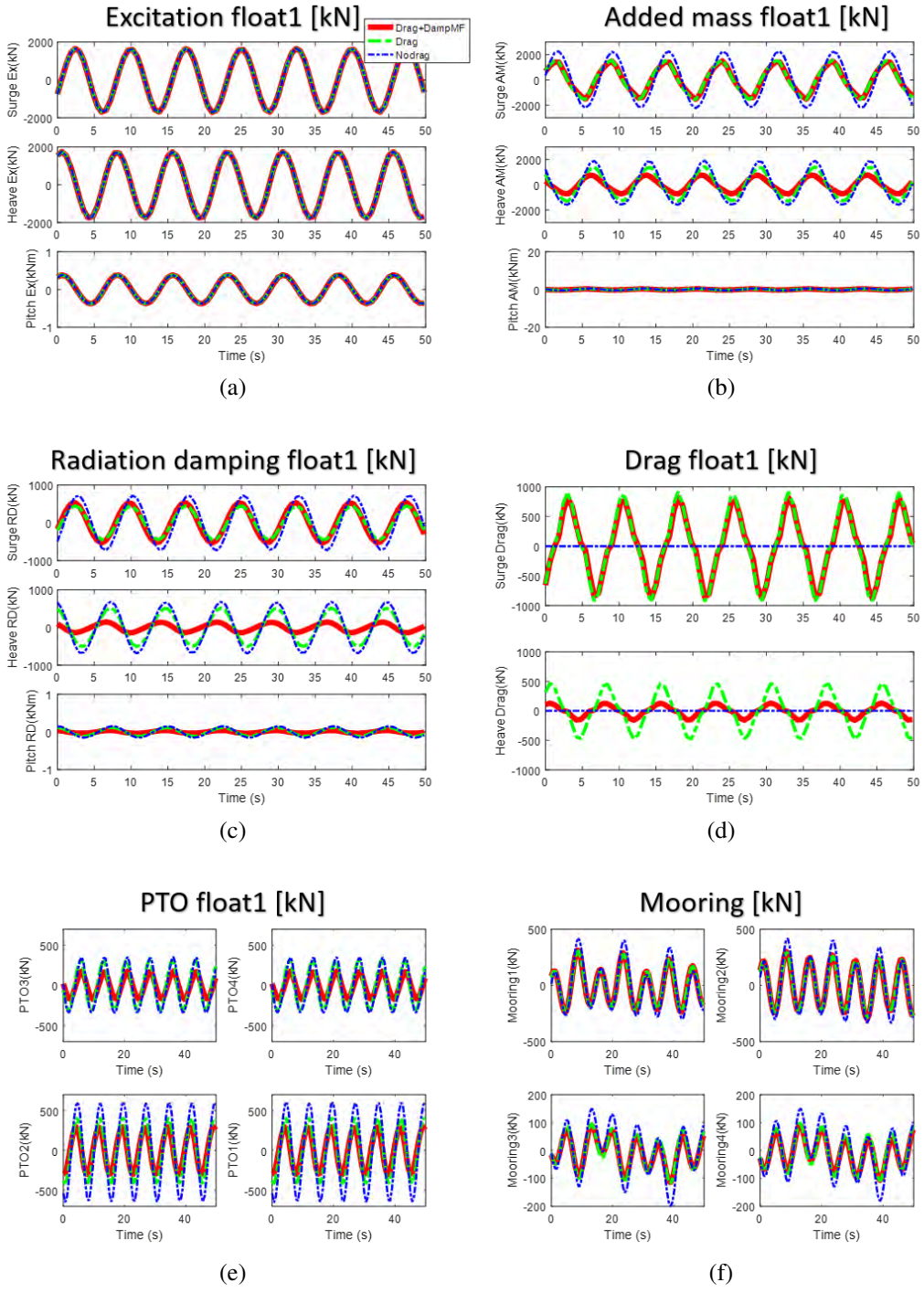

Figure 4.8: Forces acting on the WEC: the excitation force of float1 (a), the added mass force of float1 (b), the radiation damping force of float1 (c), the drag force of float1 (d), the PTO forces of float1 (e) and the mooring forces for each corner mooring cable (f). 3 numerical models are compared: the drag + mechanical friction, the drag and the no-drag model.

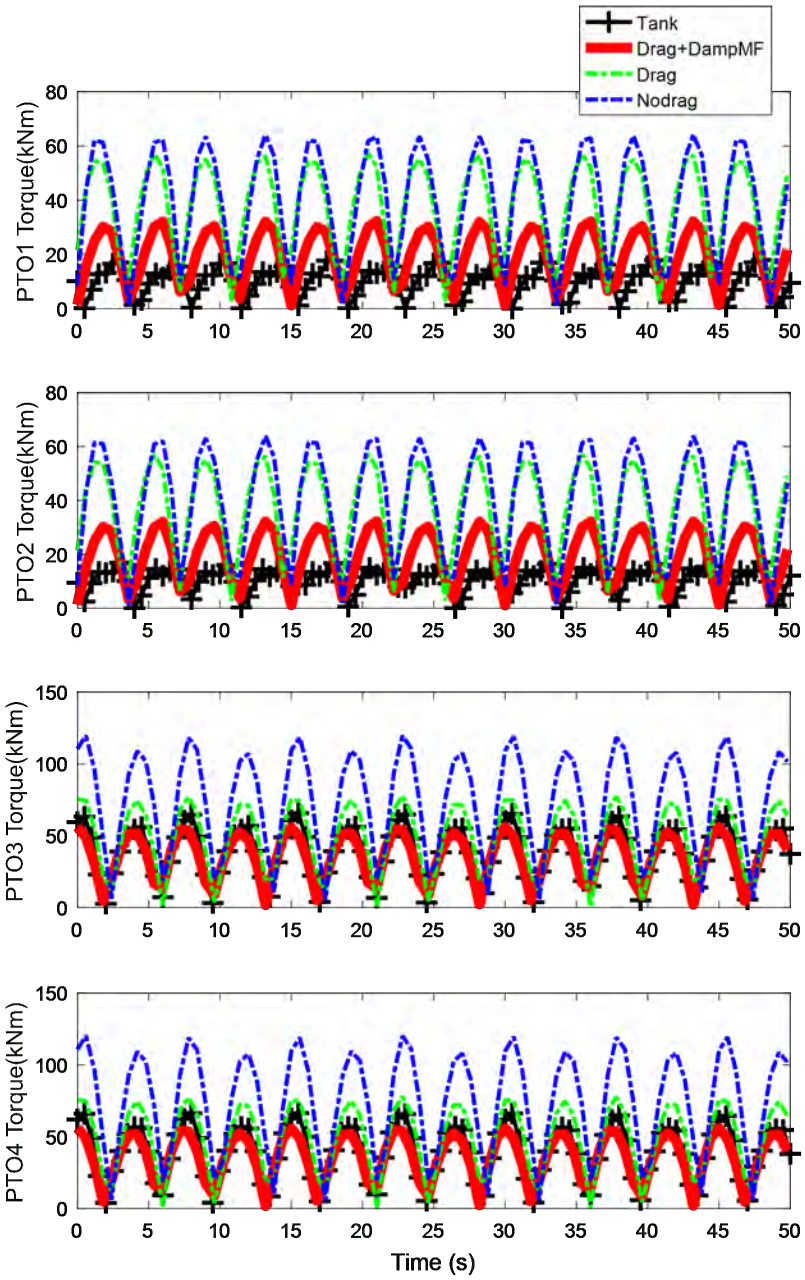

Figure 4.9: PTO Torque of float1 for each PTO line.

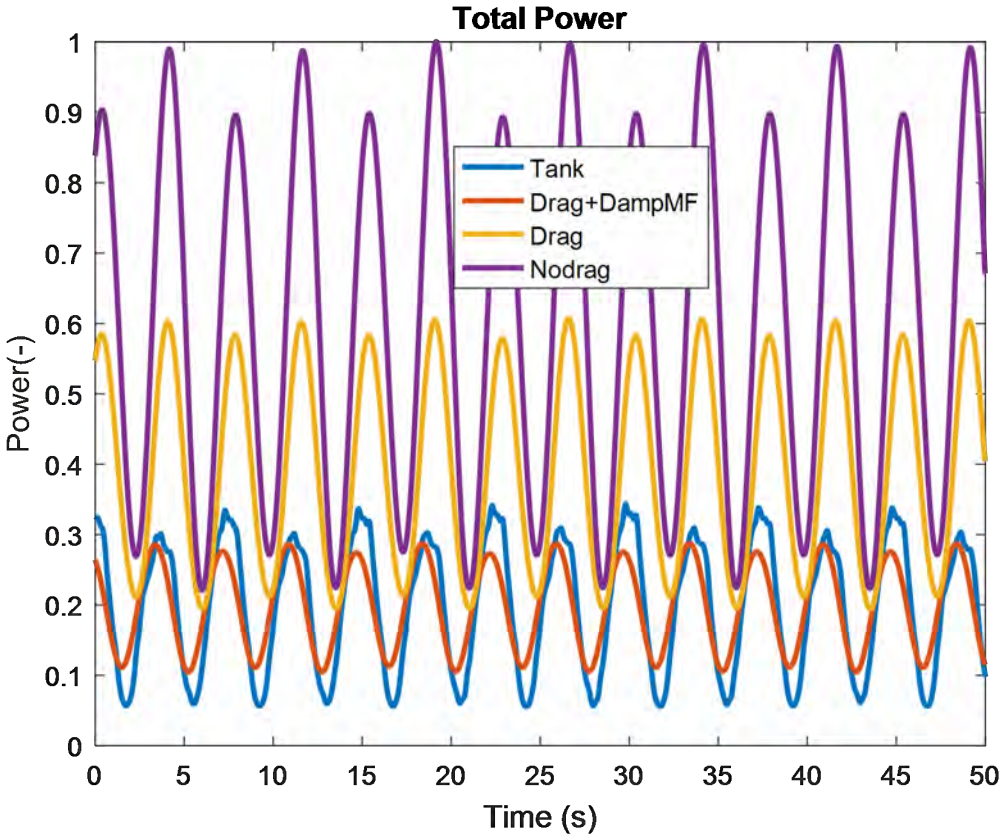

Figure 4.10: Total normalized power at a full scale of the tank testing and the 3 numerical models: the drag + mechanical friction, the drag and the no-drag model.

Table 4.3: The normalized power double amplitudes and normalized mean values of the power produced in the tank and in the numerical models at a full scale.

		Double amplitude (-)	**Mean (-)**
Float1	**Drag+DampMF**	0.10	0.12
	Drag	0.27	0.27
	No Drag	0.65	0.51
	Tank	0.20	0.13
Float2	**Drag+DampMF**	0.09	0.10
	Drag	0.20	0.21
	No Drag	0.34	0.28
	Tank	0.14	0.12
Float3	**Drag+DampMF**	0.11	0.11
	Drag	0.15	0.18
	No Drag	0.23	0.20
	Tank	0.15	0.12
Reactor	**Drag+DampMF**	0.23	0.33
	Drag	0.53	0.66
	No Drag	1.00	1.00
	Tank	0.37	0.36

4.4.2 Regular wave cases

Different regular waves have been tested and compared with the numerical model. Two main numerical model have been tested for the comparison with the tank testing results: a tuned drag model and a default one. The tuned drag model considers a tuned surge drag coefficient for each float, a default heave drag coefficient of 1.5 and a tuned damping coefficient to represent the mechanical friction on the central PTO line. Tuned surge drag coefficient are obtained after a process to match similar surge motion amplitude results between the numerical and the tank model (Relative difference in surge less than 10% and less than 30% in heave). Heave motion is tuned through a central PTO line damping coefficient but the accuracy is limited because the same value has been used for each float (see Figure 4.13). The default model instead considers a drag coefficient of 1.5 in surge and heave and a damping coefficient of 1000 kNs/m. Preliminary drag coefficient comes from a previous research of Marine Power Systems Ltd [182]. The default damping coefficient has been set up equal to the first case considered in previous section. The accuracy of the numerical model depends on the estimation of the tuned drag coefficient and so it is important to find any relation with simulation results or parameters. However a large amount of experimental data is necessary to investigate the drag coefficient for each specific conditions. More specifically the numerical model need to be tested and validated for different PTO settings and irregular waves. A huge amount of work is necessary for this and here is shown only a comparison for regular waves with the same wave height (4 m) and different wave periods (From 7.5 to 10.5 s). A good relation between the tuned drag coefficients and the Keulegan Carpenter number (KC) has been found (see Figure 4.11). The Keulegan-Carpenter number is expressed in Equation (3.5) but it is referred to the body velocity while the characteristic length is the diameter of the floats.

There is an increase of the tuned drag coefficient for smaller KC values. This behavior can be found also in experimental results of Sarpkaya [157]. In this work the drag coefficients has been determined as a function of the KC number for cylinders that could be used in a first approximation for a comparison with the tuned drag coefficients of the floats. Tuned drag coefficients for each float are not the same because of the interference effects explained by Sarpkaya [155]. However most of these are in a similar range between 0.5 and 1 giving an average around 0.7 for most of the wave periods. This average could be used to have a good approximation of the drag for most of the wave regular cases.

Figure 4.12 shows the tuned damping coefficients for the mechanical friction on the central PTO line. In particular there is an increase with the wave period. This behavior is difficult

to explain because the mechanical friction is very difficult to characterize correctly (see Figure 4.6). Figure 4.13 shows the heave amplitudes of the 3 floats that are significantly reduced compared to the surge amplitudes and reach very low values for higher wave periods. Surge amplitudes are instead increasing as a function of the wave period and reach a peak for a wave period between 9.5 and 10 s. This different behavior is due to the mechanical friction of the PTO lines because hydrodynamic coefficients show instead a similar resonance frequency (see Figure 4.2). The default model shows an overestimation of the heave motion and an underestimation in surge. While the first behavior is related to an underestimation of mechanical friction forces, the second is due to the large default drag coefficient in surge used. It can be seen from Figure 4.13 that float 1 has the largest surge amplitude and this reduces from float 1 to float 3. Finally the normalized power of each float and the normalised total power is shown in Figure 4.14. The numerical models are underestimating the mean power with a relative error in average around 10% for each float and around 6% for the total average power. Relative error is calculated as following:

$$RE(\%) = \frac{\overline{P}_T - \overline{P}_m}{\overline{P}_T} \cdot 100 \tag{4.6}$$

Where RE is the relative error, $\overline{P}_T$ is the tank mean power and $\overline{P}_m$ is the numerical model mean power. Float1 is the float that produces more power as expected because it shows the largest amplitude motion compared to the other 2 floats. Peak of the mean power is obtained around 9.5s. Float3 shows a more non-linear behaviour with a double peak around 9 and 10s, probably influenced by hydrodynamic interaction effects.

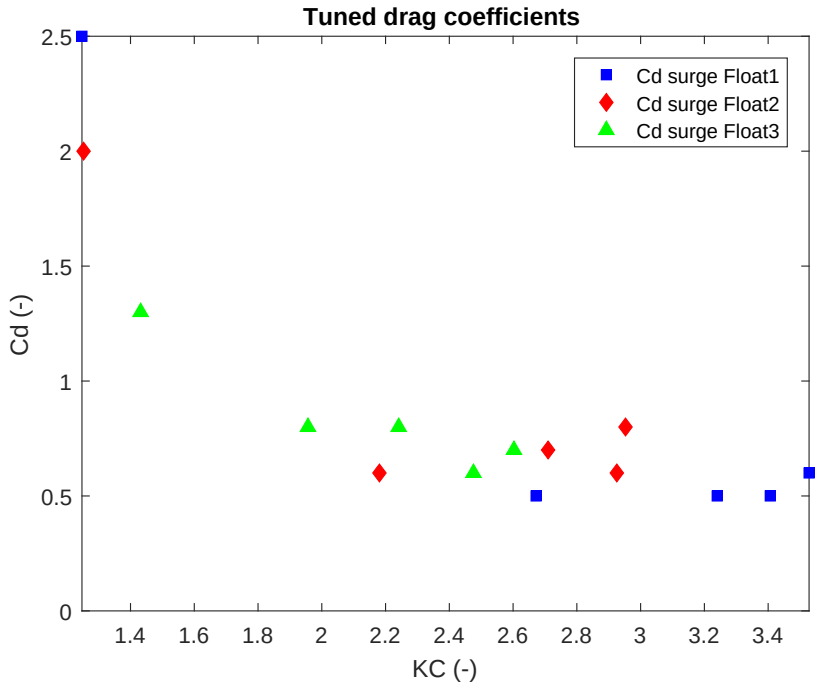

Figure 4.11: Tuned surge drag coefficients of the 3 floats as a function of the Keulegan-Carpenter number for 6 different regular waves.

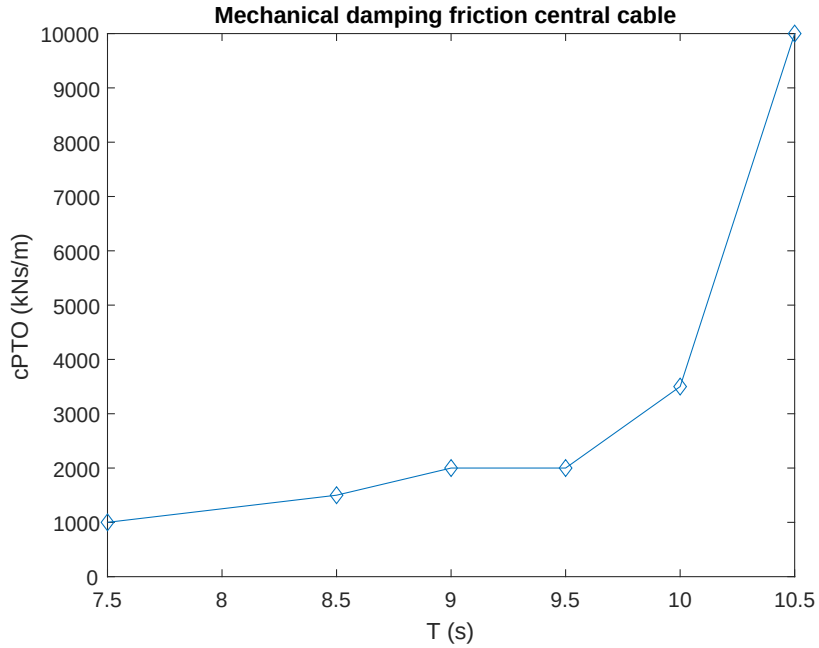

Figure 4.12: Tuned damping coefficients to represent mechanical friction on the central PTO line for 6 different regular waves.

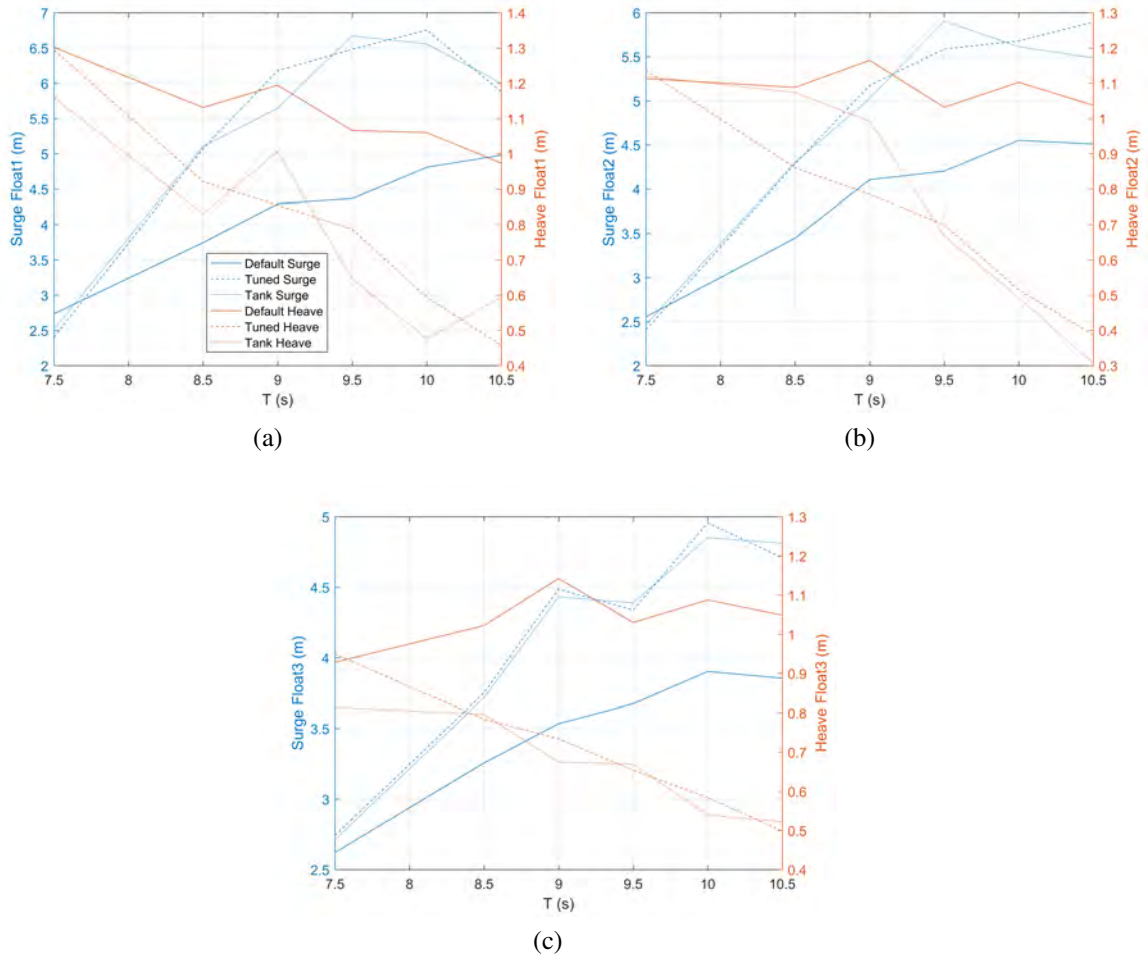

Figure 4.13: Surge and heave float amplitude of each float (a-c) for the default and tuned numerical models and for the tank testing.

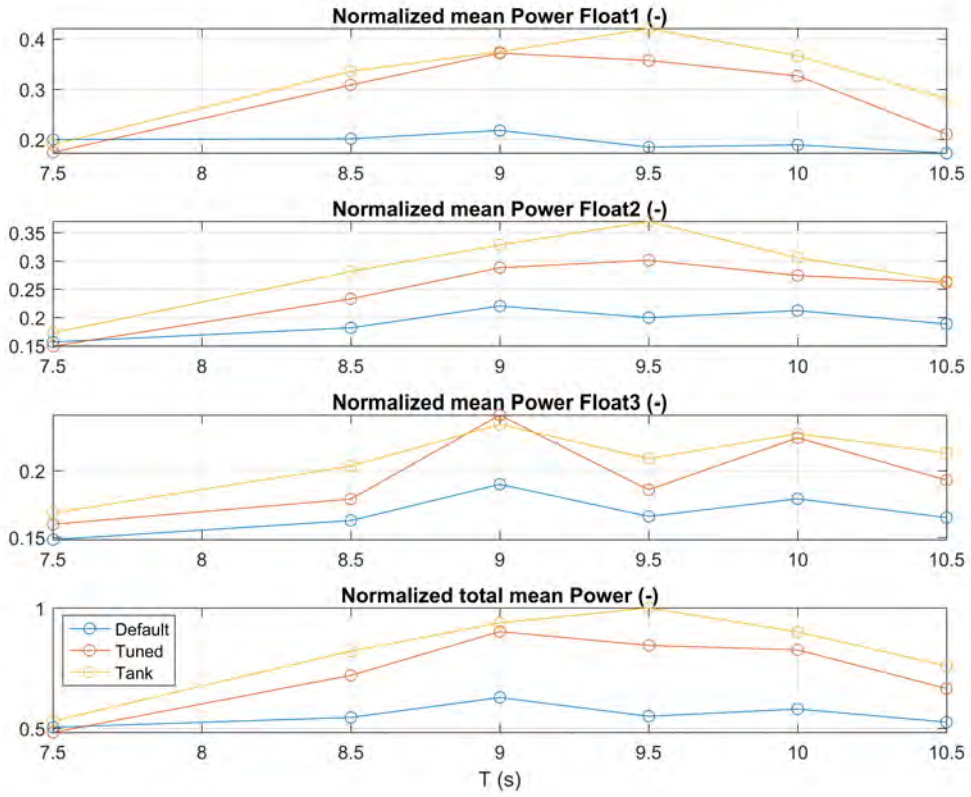

Figure 4.14: Normalized mean power of each float and of the total system for the default and tuned numerical models and for the tank testing.

4.5 Investigation of the reduced heave motion

The results of Section 4.4 has shown a reduced heave motion in the tank testing. This was investigated and recognised from some video of the tank testing. In particular a situation with a vertical central spring directly connected to the reactor was improving a lot the heave motion than a situation with the central spring mounted horizontally on the reactor and operated via a pulley system.

A numerical simulation of a single float with a simple vertical central spring was run to confirm this observation and to match better the numerical and tank result of the heave motion. This tank test was conducted in March 2017 in Plymouth University's Ocean basin.

Two numerical models were compared with the tank model: a drag model considering a hydrodynamic drag coefficient of 1.5 in the surge and heave float motion and a no drag model. This time the mechanical friction was not taken into account because it was supposed that this was caused mainly by the central spring pulley system.

The model was set up with the same procedure of Section 4.3. An offset value due to the initial position was considered in the display of the motion of the float and reactor.

The results show a reasonable agreement in the heave motion of the float with a relative difference less than 25% between the drag model and the tank while a very good agreement has been reached in the surge motion with less than 6% difference (see Table 4.4). Equation 4.4 has been used for the calculation of the relative error.

Finally the normalized power is shown in Figure 4.15 while the normalized double amplitude and mean power are shown in Table 4.5. Figure 4.15 has been normalized to the largest value of the time domain simulation while each column of Table 4.5 has been normalized to the largest value of the column. There is a reasonable agreement between the numerical model that consider drag and the tank testing with a relative difference in the mean power less than 25% while the no drag model overestimates the mean power produced by 77%. Equation 4.6 has been used for the calculation of the relative error. The power produced shows two main amplitudes due mainly to the different phases between the power generated from the PTOs in the front and the ones in the back of the float. There is a good agreement especially for the larger amplitude between the drag model and the tank.

A limitation to this comparison is an accurate evaluation of the mooring stiffness coefficients because of the manual mooring setting in the tank. Moreover the reactor was simplified with a cuboid shape reducing the possibility for a better matching. Another source of difference is that float and reactor could not have been completely aligned with the wave direction.

Table 4.4: Relative error (%) of the numerical models on the bodies motion for a single float case tank test at a full scale.

		Surge	Heave	Pitch
Float	**Drag**	-5.48	-22.70	23.93
	No Drag	-31.27	-48.94	5.55
Reactor	**Drag**	-97.25	69.56	-30.61
	No Drag	-149.69	66.90	-64.70

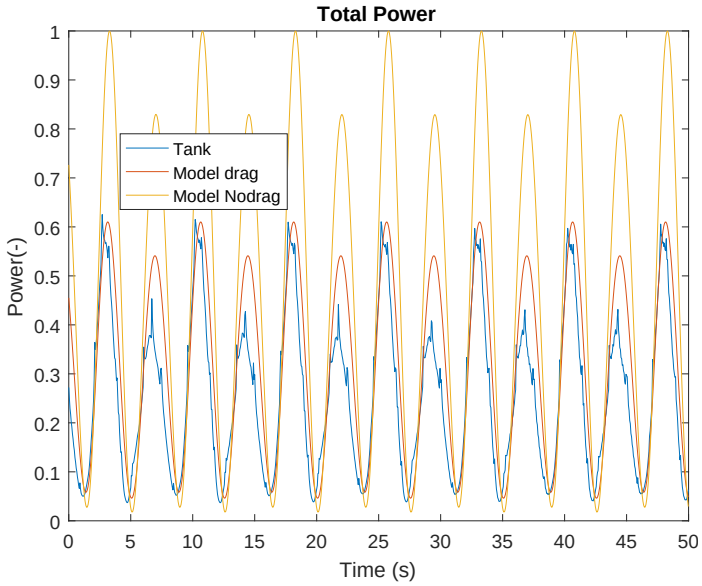

Figure 4.15: Total normalized power at a full scale of the single float case tank test and the 2 numerical models: the drag and the no-drag model.

Table 4.5: The normalized power double amplitudes and normalized mean values of the power produced in the tank and in the numerical models at a full scale for a single float WaveSub.

		Double amplitude (-)	**Mean (-)**
Total Power	**Drag**	0.57	0.67
	No Drag	1	1
	Tank	0.60	0.54

4.6 Conclusions

A comparison between the tank testing of a multi float 1/25th scale model of the WaveSub and various numerical models has been made. It is demonstrated that a numerical model that accounts for both hydrodynamic drag and mechanical friction could estimate accurately the motion and the power produced from the tank testing. Numerical models that, instead, don't account for these 2 effects are overpredicting the power produced. A limitation of this approach is that a process of tuning of the drag coefficient is necessary to determine a realistic drag associated with the motion of the floats. However, these results are a first step towards a process of validation of the numerical model associated to the WaveSub device.

The benchmark has been analysed in full scale using a Froude scaling because the hydrodynamic software is more computationally stable at full scale. Hydrodynamic forces can be Froude scaled because viscosity is not accounted for in the computation. Then PTO forces and mooring forces have been linearized and so they can also be Froude scaled. The main purpose of this paper section was not to obtain the most realistic full scale representation, but to compare the numerical model and the tank data. A more realistic representation of the full scale should take in account scaling effects for PTO, mooring and drag forces.

Historically, the main assumption of the hydrodynamic computation has been to neglect viscous effects. However, a realistic hydrodynamic drag force has been introduced in the time-domain simulation to match better the experimental results. Different tuned drag coefficients have been identified especially for the surge motion of the float and this will require further investigation to understand the influence of the particular geometric configuration. It is demonstrated that a tuned surge drag coefficient of 0.7 could approximate quite well the drag force in surge. It is clear that there is a trend relating to the KC number and this should be the starting point for further work. A further damping force has been added to account for the reduced heave motion of the floats probably due to mechanical friction in the pulleys. In particular, this friction was found to be mainly related to the pulley of the central cable where there was the majority of the load (90%). Future investigation to reduce the mechanical friction is related to a reduction of the total load on the PTO lines and understanding the relation between load and the amount of power produced.

Finally, a good benchmarking has been achieved for the model accounting for both drag and mechanical friction. A comparison of results has been reported for the motion amplitudes and for the power produced by the device for a specific regular wave case. Then different regular waves have been tested and tuned for a specific drag coefficient and mechanical

damping. Power in particular has been matched well with the damping and friction values chosen, reaching a relative mean total power difference around 10%.

Further work will include an investigation of different PTO settings and irregular waves. Tank testing results from different load bank settings can be compared with the numerical model which corresponds to different PTO damping coefficient. Then irregular waves and multi-directional waves [168] can be also considered to represent a more realistic sea state and power capture. Relationship between Keulegan-Carpenter number and drag coefficient can be then verified for these new cases. Additionally, mechanical friction of the central float tether pulley assembly is still also a topic of further research.

Chapter 5

The optimisation of a linear design concept of the multi-float WaveSub

5.1 Introduction

An optimised linear multi-float configuration of the WaveSub device has been investigated in this chapter. Results of this investigation have been submitted to the Ocean Engineering journal [183].
The optimal configuration is the one that gives the owner of the installed device the maximum profit at the end of the life time of the device. Profit is directly correlated with the energy produced and the costs required to create that energy. LCOE has been chosen as the parameter to be optimised because it takes into account both cost and energy (see Section 2.4). The estimation of the energy produced is based on a scatter matrix that describes the wave resource of a particular site. The scatter matrix gives the probability of occurrence of each sea state. The incident energy per metre of wavefront can be obtained from the scatter matrix and it is used to design the WEC for the most energetic sea states. The Incident Energy per metre of wavefront (IE) for each sea state can be approximated as follows for deep sea water (Refer to 2.70):

$$IE_{i,j} = O_{i,j} \cdot 8760 \cdot 0.49 \cdot H_{s,i}^2 * T_{e,j} \tag{5.1}$$

where O_i, j is the occurrence for a particular sea state. To add further detail, where a device has directional properties, the wave directional spread could be considered to account for the wave direction.

The second part of the LCOE calculation is the CAPEX and OPEX of the wave farm 2.4. A wave farm is more cost effective than a single unit because mainly of the shared installation and grid connection costs. A set of design optimisation parameters have been used to build the wave farm cost calculation in collaboration with MPS Ltd.

5.2 The calculation of the Levelized Cost Of Energy

The calculation of the Levelized Cost Of Energy (LCOE) is one of the most critical issues of the optimisation process (see Section 2.4). A cost estimation is very difficult for Wave Energy Converters because there isn't enough experience in this sector to use known costs from existing farms. However an existing cost calculation given by MPS Ltd was used in this work. It was based on the experience of the company and on information given by different manufacturers and components suppliers.
A WEC farm of 400 MW is considered in the cost calculation. The fixed farm costs per device are estimated to decrease with a larger number of devices due to the cost per device reduction of the grid connection and installation costs.
Design parameters that determine the cost of the device are the float spacing, the number of floats and the rated power. The float spacing influences cost because it requires a different size and mass of the reactor. This relationship depends mainly on the multi-float configuration. A linear relationship between the cost and the number of floats is considered while the rated power is influencing the cost of the PTO as explained later.
The costs considered in the CAPEX are dependent on the number of devices:

- The cost of the structure is dependent on the mass of the floater and of the reactor and on the specific cost of the material (fabricated steel). A fixed cost value of on-board mooring system components is also added to this cost component.

- The Power Take Off (PTO) is hydraulic and a cost related to the primary transmission and to the secondary transmission and energy storage is considered. The cost of the secondary transmission and energy storage is calculated dependent on the rated power (P_{Rated}) and on the specific cost of it. A preliminary fixed proportion between the secondary transmission/energy storage and the primary transmission cost is based on a cost breakdown of the Pelamis device [184]. This can be shown in the following Equation:

$$\begin{aligned} Cost_{PTO} = Cost_{Primary} + Cost_{Secondary/Storage} = \\ Cost_{Secondary/Storage} \cdot \left(\frac{64}{36} + 1\right) = \\ P_{Rated} * Cost_{SpecificRatedPower} \cdot \left(\frac{64}{36} + 1\right) \end{aligned} \tag{5.2}$$

- Control and instrumentation per device are based on a constant value.

- The installation and grid connection per device are dependent mainly on the number of devices, the distance between the devices and the shore, the distance between the devices, the number of days of installation and the vessel hire per day. As expected, increasing the number of devices causes a decrease in these costs.

- The mooring cost per device is a constant cost determined by the cost of the anchors, shackles, wire ropes, mooring springs, work-boat rate and time of installation.

The OPEX (OPerating EXpenditure) is also calculated: planned minor serving; farm major overhaul; unplanned maintenance; grid fees; insurance and lease. These costs are also dependent on the number of devices. The first 3 costs of the OPEX are based mainly on the possible costs of the new component parts, on the occurrence and on the work-boat rate. The insurance cost is considered as a fraction of these 3 costs while the grid fees and the lease are respectively proportional to the annual average device power and to the annual energy produced. Finally, decommissioning costs are included and considered equal to the installation costs relative to the transportation on site. More specific details about these costs are considered confidential with MPS.
The LCOE is calculated considering the CAPEX, the OPEX and the energy produced by the WEC farm (EP) ([105]). Then a nominal discount rate (NDR) and maintenance inflation rate (MIR) are considered. In particular these 2 rates have an opposite effect on the present value of a future cash flow. A mathematical shortcut was finally applied to obtain the present value of an ordinary annuity.
The expression of the LCOE is shown as below:

$$LCOE = \frac{(CAPEX + OPEX \cdot PVF_{OP} + DECOM \cdot PVF_D)}{(PVF_E \cdot E_{year})} \tag{5.3}$$

where PVF represents the present value factor and $DECOM$ is the decommissioning cost. The energy produced in an year (E_{year}) is calculated considering an availability factor, a conversion and a transmission efficiency. The present value factor is calculated in a different way if related to the OPEX, decommissioning and the energy produced. In particular they can be expressed as following considering a project lifetime (PLT) of 20 years:

$$PVF_{OP} = \frac{(1+\frac{NDR-MIR}{1+MIR})^{PLT}-1}{(1+\frac{NDR-MIR}{1+MIR})^{PLT} \cdot \frac{NDR-MIR}{1+MIR}} \tag{5.4}$$

$$PVF_D = \frac{(1+MIR)^{PLT}}{(1+NDR)^{PLT}} \tag{5.5}$$

$$PVF_E = \frac{(1+NDR)^{PLT}-1}{(1+NDR)^{PLT} \cdot NDR} \tag{5.6}$$

The optimisation considers a nominal discount rate of 12.5 % and a maintenance rate of 3 %. The nominal discount rate is the bank interest rate for lending money without considering inflation. This is relatively high to take into account the financial risk because of the early stage of the technology. The maintenance rate has been obtained from MPS Ltd.

5.3 The optimisation procedure

Hydrodynamic independence between the different devices is assumed for the optimisation study of the WaveSub farm. This is a reasonable assumption for small to medium sized arrays if the distance between WECs is large enough (600m for this optimisation). However, hydrodynamic interactions between the components of the multi-float configuration of each device are taken in account.
The design parameters considered in the optimisation are the float spacing and number of floats, the float-reactor separation, PTO stiffness, PTO damping and rated power of the PTOs. Some of them require a simulation in Nemoh for every variation (float spacing, float-reactor separation and number of floats) while for others, only a WEC-Sim simulation is necessary. During the optimisation the parameters are considered in the following range:

- Float Spacing: $[35 - 150]$ m
- Float number: $[1 - 6]$
- Float-reactor separation: $[20 - 84.6]$ m
- k PTO: $[5 - 1000]$ kN/m
- c PTO: $[50 - 1000]$ kN/(sm)
- Rated Power: $[0 - 100]$ MW

The float spacing is considered from center to center between the floats. The range chosen is from the minimum feasible distance to around four times this mimimum.
The float number has been limited to 6 due to the significant increase in the computational cost with increasing number of floats. An initial optimisation considering the number of floats as a design variable resulted in a measurable increase in simulation time and the optimisation always converged up to the 6 floats limit.
The float-reactor separation is the distance between the centre of gravity of the float and of the reactor.
The PTOs are simplified with a simple translational PTO but a more complex PTO model will be necessary in a future further analysis to follow more accurately a designed hydraulic PTO. The optimal PTO damping coefficient is supposed to be larger than the PTO stiffness based on the experience of MPS and so the minimum allowed values of each parameter are

set accordingly.

Finally the rated power is considered in the optimisation which does not need to be calculated as part of the time domain simulation but can be calculated in a post-processing step. The rated power determines both the amount of energy captured from the power matrix obtained from the simulations and the cost of the PTO. In particular, the rated power limits the power produced for each sea state. A larger rated power will increase the power produced for the most energetic sea states but the cost of the PTO will be also higher.

A coupling between an optimisation algorithm and a parallel simulation has been chosen (see Figure 5.1 and Figure 5.2). The design parameters are changed at each generation to values that minimize the LCOE. The LCOE calculation is given by the solver that involves the use both of Nemoh and WEC-Sim. The OPT block shows the second optimisation used to optimise the rated power and the LCOE for each time domain simulation.

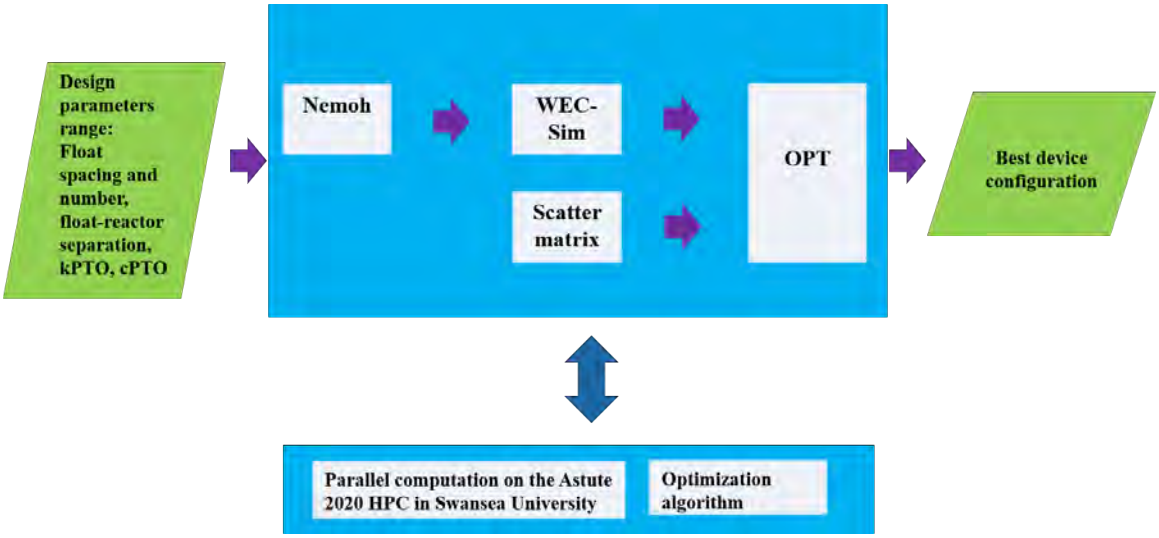

Figure 5.1: The optimisation scheme for a WaveSub array.

Two different Design of Experiment (DOE) approaches have been used for a first stage exploration of the domain. The Taguchi method has been used to estimate the average response of each design variable on the response [185]. A latin hypercube DOE has been then used for the better equidistribution of the sample points.

Various metaheuristic algorithms have been then tested to check their efficiency to find the minimum LCOE. Only free gradient methods have been considered because the information of the gradient of the objective function is not easily available. Two algorithms inspired by nature are chosen in the optimisation: a particle swarm algorithm and a genetic algorithm.

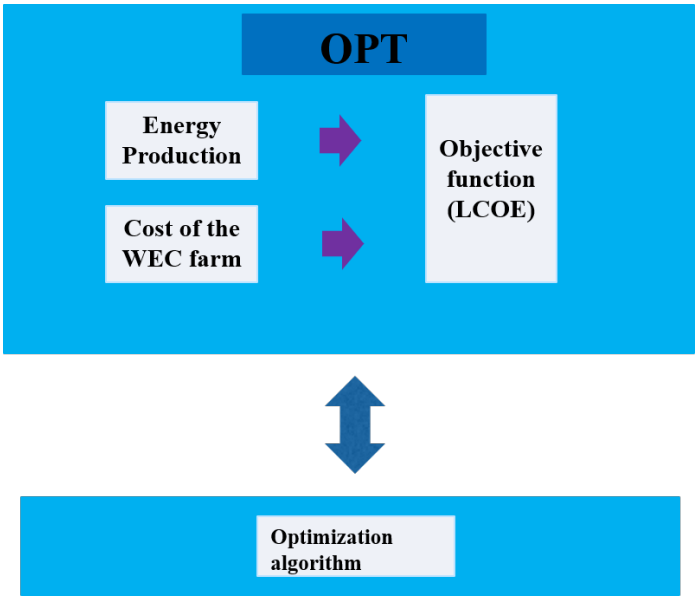

Figure 5.2: The OPT block in detail.

The particle swarm algorithm (PSO) and the genetic algorithm have some similarities but the particle swarm also considers memory [186]. PSO is a swarm intelligence technique, inspired by social behavior of bird flocking or fish schooling as described by [186]. Each particle in this method is related with a certain randomized velocity that move them in hyperspace of the optimizing variables. The best fitness reached by each particle (P_{Best}) is memorized as well as the best global fitness of all the particles (G_{Best}). In particular at each time step the particle is moved with a certain algorithm towards these best fitness ([186]):

$$V_{p-New} = w_{inertia} * V_{p-Old} + c_1 \cdot rand \cdot (P_{Best} - P_{Old}) + c_2 \cdot rand \cdot (G_{Best} - P_{Old}) \tag{5.7}$$

where V_p is the velocity of the particle, $w_{inertia}$ is the inertia weight of the particle, c_1 and c_2 are the personal and global learning coefficients, $rand$ is a random number and P is the position of the particle described by the different design parameters. Constriction coefficients ($\Phi 1$ and $\Phi 2$) are used to find the inertia weight and the personal and global learning coefficients as following [187]:

$$\Phi = \Phi 1 + \Phi 2 \tag{5.8}$$

$$\chi = \frac{2}{(\Phi - 2 + \sqrt{\Phi^2 - 4 \cdot \Phi})} \tag{5.9}$$

$$c1 = \chi \cdot \Phi 1 \tag{5.10}$$

$$c2 = \chi \cdot \Phi 2 \tag{5.11}$$

The position of the particle is then updated with the new one ([186]):

$$P_{New} = P_{Old} + V_{p-New} \tag{5.12}$$

An open source implementation of ([187]) is used.
The genetic algorithm is one of the most famous evolutionary algorithms. It uses different operators such as selection, crossover and mutation that will enable to improve the global fitness at each generation. A more detailed description of the different phases is given here:

- The selection operator is used considering a Stochastic Universal Sampling (SUS).
- A uniform cross-over operator is used. The new population is generated by linear recombination of the previous generation.
- The mutation operator considers a real coded mutation.

Two versions of the genetic algorithm are used. The first is based on an open-source code implemented in MATLAB ([188]). The second implements the genetic algorithm MATLAB function using the adaptive mutation option to have a better convergence of the algorithm.
There are a significant number of optimization iterations and each requires a transient analysis of a WEC in a realistic sea state, consequently a parallel implementation is necessary using HPC facilities. All these algorithms were made suitable for parallel computing thanks to the use of the MATLAB function "parfor" [189]. This function enables to execute in parallel for cycles in a parallel pool. It is possible to set-up the number of workers that the user wants to use giving the possibility to be used in a cluster. The "parfor" loop is mainly different from the "for" loop because each cycle must be independent and consecutive with an increasing integer number. In particular the codes were adapted to be executable with this type of loop.

5.4 Computational model set-up

The device considered in the optimisation is obtained by scaling the $1:25^{th}$ prototype to the full scale (see Section 4). The floats have the same geometrical shape as the tank testing benchmarking with a central cylinder and 2 hemispheres in the sides (see Section 4). The reactor is simplified to a cuboid shape.
A linear multi-float design is characterized by a long reactor and a series of floats aligned along the wave direction. Figure 5.3 shows the scheme of the design. The mooring connects the reactor and the seabed. The attachment points on the reactor are placed on the corner while the attachment points on the seabed describe the x and y spacing as follows:

$$x_{MSpac} = \frac{4}{3}RL \tag{5.13}$$

$$y_{MSpac} = \frac{7}{4}RW \tag{5.14}$$

where RL and RW are the length and width dimensions of the reactor.

The main simulation parameters for Nemoh and WEC-Sim are shown in Table 5.1:

Table 5.1: Main simulation parameters for Nemoh and WEC-Sim.

Simulation parameters	
Water depth (m)	100
Density sea water (kg/m^3)	1026
Minimum frequency (Hz)	0.05
Maximum frequency (Hz)	5
Number of frequencies	51
Simulation time (s)	1300
Ramp time (s)	100
Solver WEC-Sim	ode45
Timestep (s)	0.02

From previous experience, the number of wave frequencies and the duration of the simulation time are assumed to give a reasonable accuracy on the results. Interpolation of the hydrodynamic coefficients from Nemoh is used to obtain their values for further frequencies. The time simulation is between 15-30 minutes, the typical record length suggested for irregular waves [128].
The length of the reactor is related to the float spacing following this linear relationship:

$$RL = RLb + FS \cdot (nfloats - 1) \tag{5.15}$$

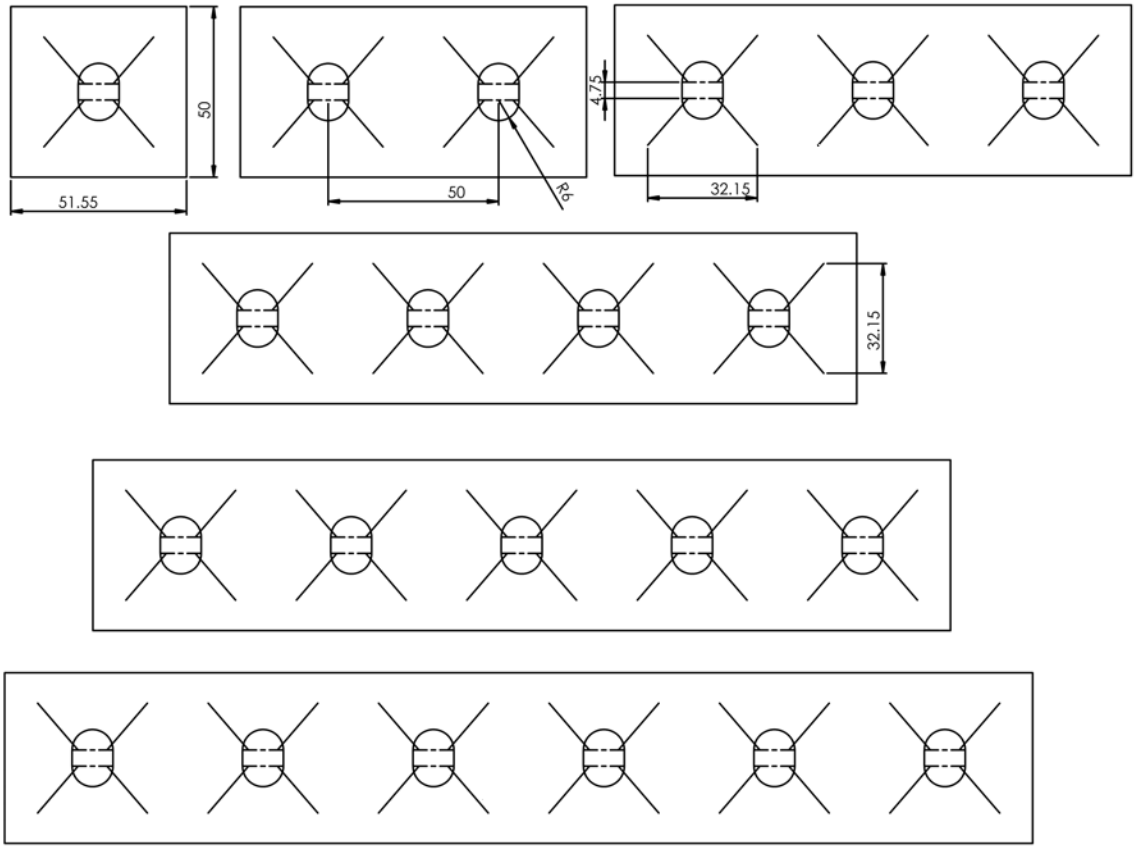

Figure 5.3: Schematic of the linear float configuration for a float spacing of 50 m. Configurations are shown from a single float to a six floats multi-float device.

where RL is the reactor length, RLb is the baseline reactor length, FS is the float spacing and $nfloats$ is the number of floats.

The system net buoyancy has been designed dependent on the number of floats while the designed displaced mass of the reactor has been obtained using a linear relationship with reactor length. So the mass of the reactor is obtained as follows:

$$M_R = \frac{SNB_b}{g} \cdot nfloats + M_{Rdb} \cdot \frac{RL}{RLb} + nfloats \cdot (M_{Fd} - M_F) \tag{5.16}$$

where M_R is the reactor mass, SNB_b is the baseline system net buoyancy, M_{Rdb} is the baseline displaced mass of the reactor, RL and RLb are the reactor length and the baseline reactor length respectively, M_{Fd} is the displaced mass of the float and M_F is the mass of the float.

5.5 Mesh sensitivity

The mesh of the float and of the reactor has been obtained considering a balance between two main factors: the computational time and the accuracy of the results. The optimisation requires the minimum number as possible of panels of the mesh to have a larger number of simulations. By contrast accuracy requires a fine mesh. Chapter 4 shows the mesh independence from a coarser mesh to a finer mesh. The hydrodynamic coefficients in the main degrees of freedom (surge, heave and pitch) are almost identical between the different meshes. So a coarse mesh could be used for the optimisation to obtain a reasonable accuracy. Specifically a quadrangular mesh has been used for the float and the reactor. The mesh of the float used a similar amount of nodes as the tank testing case (80). The mesh considers quadrangular elements with 81 panels. The mesh of the reactor has been obtained for a length equal to the tank testing size of 51.55m (98 panels). Mesh of the reactor with a different length have been obtained using a linear scaling of this mesh. The linear scaling of the mesh of the reactor probably will not create a good aspect ratio. However the main motion is expected to come from the floats and so the accuracy of the hydrodynamics of the reactor is of secondary importance. The mesh convergence of the reactor for a 6 floats device and a float spacing of 50m is shown in Figure 5.4. The coarse mesh (96 panels) is obtained applying the scaling for the reactor length while the moderate (165 panels) and the fine mesh (335 panels) are obtained directly from Salome [131] for the exact length of the reactor. The main motions of the reactor are in surge and heave and generally the coarse mesh approximates quite well compared to the fine mesh results.

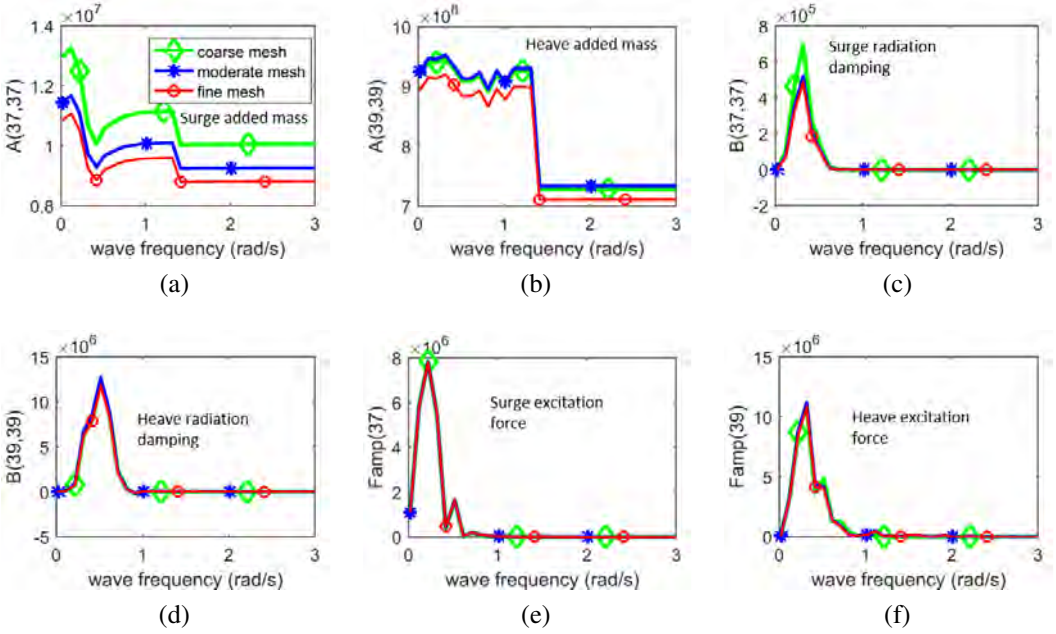

Figure 5.4: Surge and heave added mass coefficients of the reactor (a,b), surge and heave radiation damping coefficients of the reactor (c,d), surge and heave excitation coefficients of the reactor (e,f). The simulation is made for a 6 float configuration and a float spacing of 50 m.

5.6 The wave site location

A specific wave farm location has been identified for the optimisation. This was the Berth A wave buoy in Belmullet, the Atlantic Marine Energy Test Site (AMETS), Ireland [170]. This area has a water depth of 100 m which matches the designed depth of the WaveSub device. A wave data analysis for the years from 2013 to 2017 has been used to obtain information about the scatter matrix and the raw spectra. The Incident Energy matrix has been obtained from the scatter matrix using Equation 5.1.

Figure 5.5 shows the full scatter matrix for significant heights between 0.25m and 15.5m and for energy periods between 4s and 22s. The spacing considered in the significant height is 0.25m while the spacing considered in the energy period is 0.5s.

A reduced scatter matrix that considered three main range of energy periods have been used (see Figure 5.6). There is a range of energy periods under 9s, between 9s and 11s and over 11s. The total sum of the occurrences of the scatter matrix is 1 and so the reduced scatter matrix approximates mostly in the lower and upper energy period range. In particular, a sea state in the reduced scatter matrix considers the sum of the occurrences of the various energy periods considered in the full scatter matrix. The power produced by the device can be estimated in a first approximation to be dependent on the square of the significant height and so the simulated sea states are dependent only on the energy period (see Table 5.2). In fact, the increase of the motion of the device with the wave height will be approximately linear because of the linear potential flow theory. The efficiency of the device will be the same and will be not dependent on the wave height. As a consequence that the power content of the waves increases with the square of the significant wave height (Equation 5.1) then also the power produced will increase in a similar way.

The spectra for each of the simulated sea states have been obtained as an average of the spectra in each energy period range (see Figure 5.7). The lower and upper range of the energy periods have been reduced to account only the spectra of the most energetic sea states for this calculation (87% of the total energy of the full scatter matrix). The most energetic sea states are considered in the optimization. Peak period and energy period properties for each sea state simulated are reported in Table 5.2. A comparison between the raw spectra and the theoretical spectra that minimizes the standard deviation between them is made. In particular a narrower spectra for higher peak periods has been observed. Finally the spectra used in the simulations has been normalized for a significant height of 1m.

Table 5.2: The sea states used in the optimisation.

Approximated theoretical spectra	**Bretschneider**	**JONSWAP (Gamma=1.1)**	**JONSWAP (Gamma=1.3)**
Approximated range of Te (s)	7<=Te<=9	9<=Te<=11	11<=Te<=13
Hs (m)	1	1	1
Te (s)	8.32	10.03	11.83
Tp (s)	10	11.76	14.29
Tp/Te	1.20	1.17	1.21

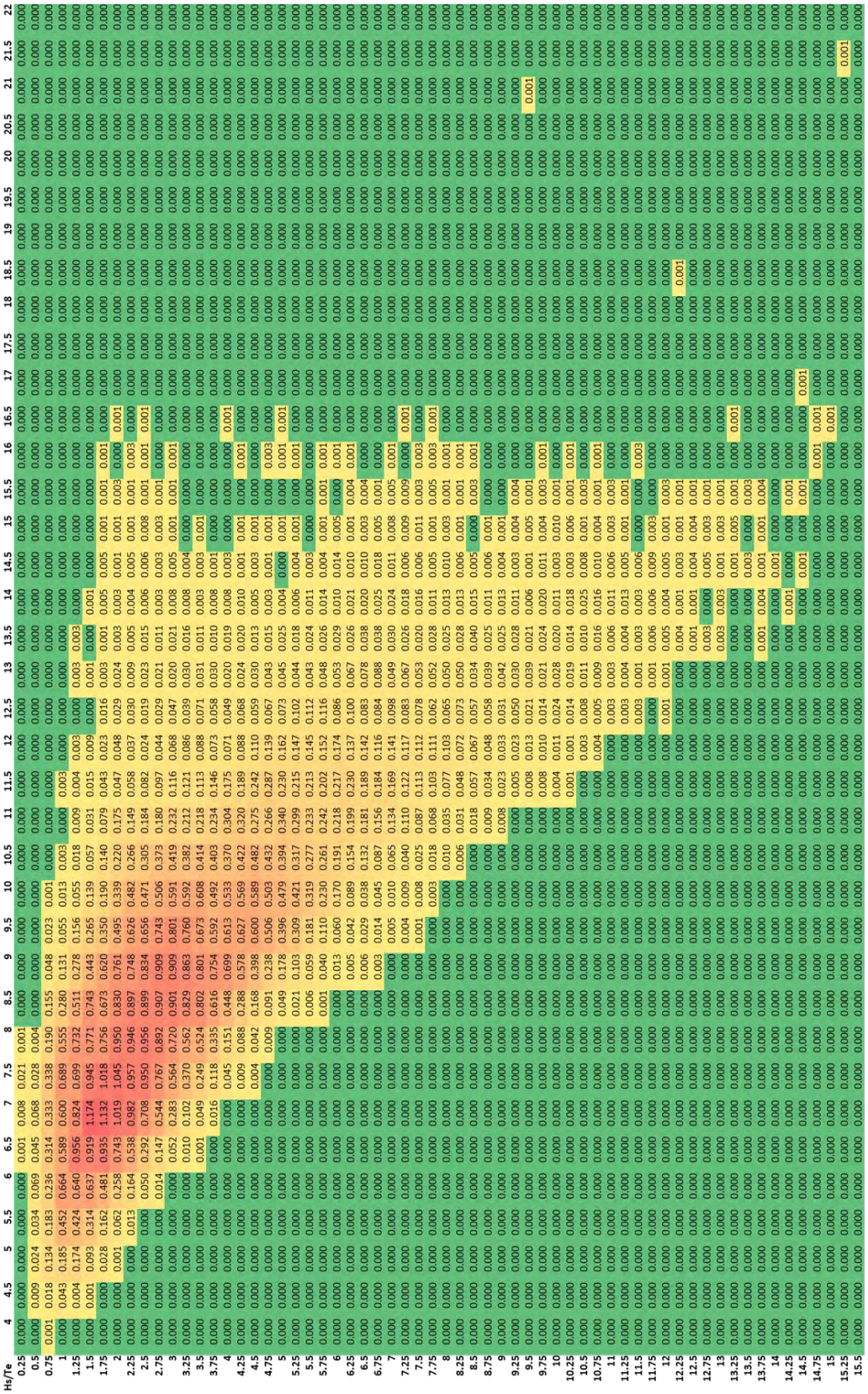

Figure 5.5: The full scatter matrix of the Belmullet site in percentage.

Hs/Te	<9	9-11	>11
0.25	0.03	0.00	0.00
0.5	0.28	0.00	0.00
0.75	1.92	0.05	0.00
1	4.12	0.14	0.00
1.25	5.10	0.37	0.02
1.5	5.82	0.70	0.04
1.75	5.49	1.03	0.14
2	5.29	1.52	0.25
2.25	4.87	1.82	0.23
2.5	4.27	1.94	0.28
2.75	3.73	2.17	0.30
3	2.98	2.38	0.40
3.25	2.30	2.27	0.41
3.5	2.03	2.20	0.43
3.75	1.46	1.98	0.44
4	0.99	2.02	0.50
4.25	0.67	2.07	0.56
4.5	0.41	2.01	0.60
4.75	0.22	1.69	0.69
5	0.14	1.53	0.71
5.25	0.07	1.25	0.69
5.5	0.04	0.92	0.67
5.75	0.02	0.74	0.69
6	0.01	0.54	0.70
6.25	0.00	0.39	0.70
6.5	0.00	0.29	0.66
6.75	0.00	0.23	0.64
7	0.00	0.15	0.60
7.25	0.00	0.11	0.51
7.5	0.00	0.08	0.46
7.75	0.00	0.05	0.42
8	0.00	0.03	0.37
8.25	0.00	0.02	0.31
8.5	0.00	0.01	0.29
8.75	0.00	0.00	0.23
9	0.00	0.00	0.18
9.25	0.00	0.00	0.16
9.5	0.00	0.00	0.12
9.75	0.00	0.00	0.12
10	0.00	0.00	0.11
10.25	0.00	0.00	0.08
10.5	0.00	0.00	0.07
10.75	0.00	0.00	0.07
11	0.00	0.00	0.03
11.25	0.00	0.00	0.03
11.5	0.00	0.00	0.02
11.75	0.00	0.00	0.03
12	0.00	0.00	0.02
12.25	0.00	0.00	0.01
12.5	0.00	0.00	0.01
12.75	0.00	0.00	0.01
13	0.00	0.00	0.01
13.25	0.00	0.00	0.01
13.5	0.00	0.00	0.01
13.75	0.00	0.00	0.01
14	0.00	0.00	0.00
14.25	0.00	0.00	0.00
14.5	0.00	0.00	0.00
14.75	0.00	0.00	0.00
15	0.00	0.00	0.00
15.25	0.00	0.00	0.00
15.5	0.00	0.00	0.00

(a)

Hs/Te	<9	9-11	>11
0.25	0.69	0.00	0.00
0.5	24.61	0.00	0.00
0.75	379.09	11.79	0.00
1	1444.53	59.58	1.32
1.25	2793.94	255.15	12.93
1.5	4587.82	687.06	49.90
1.75	5895.81	1381.20	224.03
2	7412.89	2666.85	517.70
2.25	8640.15	4041.34	603.27
2.5	9356.59	5313.42	914.42
2.75	9872.92	7178.14	1199.07
3	9382.19	9389.14	1912.58
3.25	8528.66	10503.50	2272.60
3.5	8699.09	11830.15	2769.49
3.75	7208.81	12207.34	3277.01
4	5575.12	14140.81	4178.69
4.25	4268.93	16357.26	5345.13
4.5	2922.50	17807.59	6381.24
4.75	1727.70	16729.32	8192.89
5	1208.19	16722.98	9384.18
5.25	705.55	15061.39	9971.99
5.5	380.50	12232.67	10603.87
5.75	248.07	10743.43	11929.04
6	79.44	8470.59	13191.47
6.25	34.48	6615.92	14326.59
6.5	46.62	5419.28	14600.59
6.75	20.11	4499.38	15262.69
7	0.00	3162.82	15538.34
7.25	0.00	2479.33	14180.02
7.5	0.00	1908.49	13573.54
7.75	0.00	1424.83	13121.71
8	0.00	776.77	12329.52
8.25	0.00	657.11	11061.97
8.5	0.00	279.02	10905.51
8.75	0.00	147.83	9148.85
9	0.00	134.06	7453.72
9.25	0.00	0.00	7080.54
9.5	0.00	0.00	5556.53
9.75	0.00	0.00	5789.89
10	0.00	0.00	5892.01
10.25	0.00	0.00	4312.34
10.5	0.00	0.00	3941.35
10.75	0.00	0.00	4054.77
11	0.00	0.00	2162.83
11.25	0.00	0.00	2010.90
11.5	0.00	0.00	1225.74
11.75	0.00	0.00	1828.01
12	0.00	0.00	1525.30
12.25	0.00	0.00	894.10
12.5	0.00	0.00	930.97
12.75	0.00	0.00	968.58
13	0.00	0.00	895.06
13.25	0.00	0.00	813.59
13.5	0.00	0.00	482.61
13.75	0.00	0.00	1126.47
14	0.00	0.00	129.76
14.25	0.00	0.00	268.86
14.5	0.00	0.00	417.57
14.75	0.00	0.00	288.06
15	0.00	0.00	148.96
15.25	0.00	0.00	153.96
15.5	0.00	0.00	0.00

(b)

Figure 5.6: The reduced scatter matrix in percentage (a) and the related Incident Energy matrix (b) for the Belmullet wave site between 2013-2017.

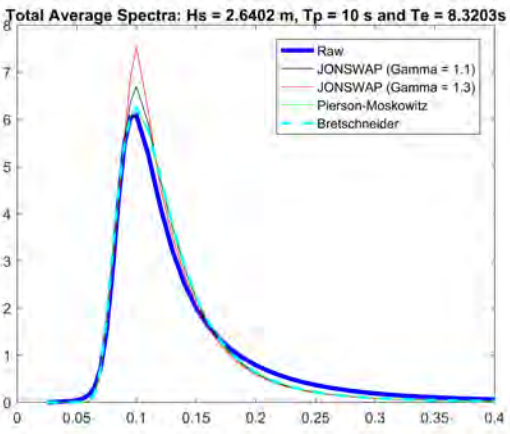

(a)

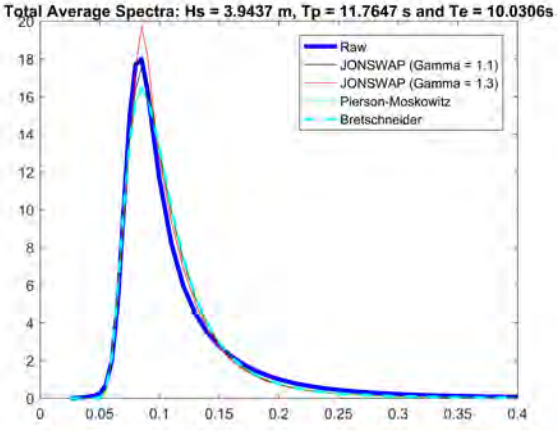

(b)

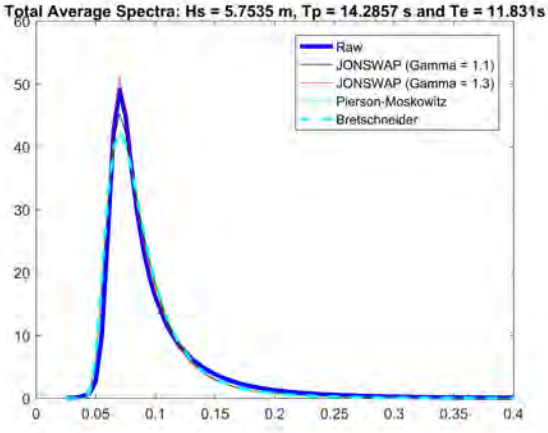

(c)

Figure 5.7: The average spectra between Te=7 and Te=9 (a), Te=9 and Te=11 (b), Te=11 and Te=13 (c) for the Belmullet wave site between 2013-2017.

5.7 Selection of an optimisation algorithm

5.7.1 Introduction

The choice of a nature inspired algorithm has been investigated with application to a single float configuration. This option becomes less suitable with an increase of the number of floats per device because of the increase of the computational time. The combination of the nature inspired algorithm with the surrogate model will be considered in the next Section 5.8 to overcome this limitation.
A sensitivity analysis is also investigated to test the influence of the design parameters on the LCOE.

5.7.2 Nature inspired algorithm

A genetic algorithm and a particle swarm have been tested to compare the relative efficiency of the search for an optimum (see Figure 5.8). The comparison between these 2 algorithm with application to the WaveSub device has been presented during the RENEW 2018 conference in Lisbon [190]. A single float WaveSub device is used for this comparison. The genetic algorithm is tested using two algorithms, an open-source code [188] and the built in MATLAB function. A better convergence is obtained for the open-source genetic algorithm and so this one has been chosen for further applications. Remembering that a complete WEC-Sim simulation is required for each realisation, this optimisation considers a short simulation time (300s) for the time domain wave analysis to reduce the computational time despite a decrease in the accuracy of the results. The simulation time is then extended to 1300s for the comparison between the multi float configurations (see Section 5.8). Drag is also not accounted in this Section to reduce the computational time of the simulations but it will be accounted in the next Section 5.8. So, it is expected that the results of this section will overestimate the power produced. However, this section mainly aimed to choose the optimisation algorithm and the accuracy of the results was of secondary importance. This optimisation used 4 design variables: the float reactor separation, the stiffness and damping of the PTOs and the rated power. The rated power is still a design variable in this section and will become part of a second optimisation, as described in Section 5.3, from Section 5.8. These algorithms are used with their default settings (see Table 5.3). The only common setting applied is the population number, fixed as 5 times the

number of variables and the generation number (50).

Table 5.3: Main default settings of the optimisation algorithm.

GA Open source	Cross-over probability=0.9, mutation probability=0.1
GA MATLAB	Adaptive mutation option
PSO	$\chi 1 = 2.05$, $\chi 2 = 2.05$

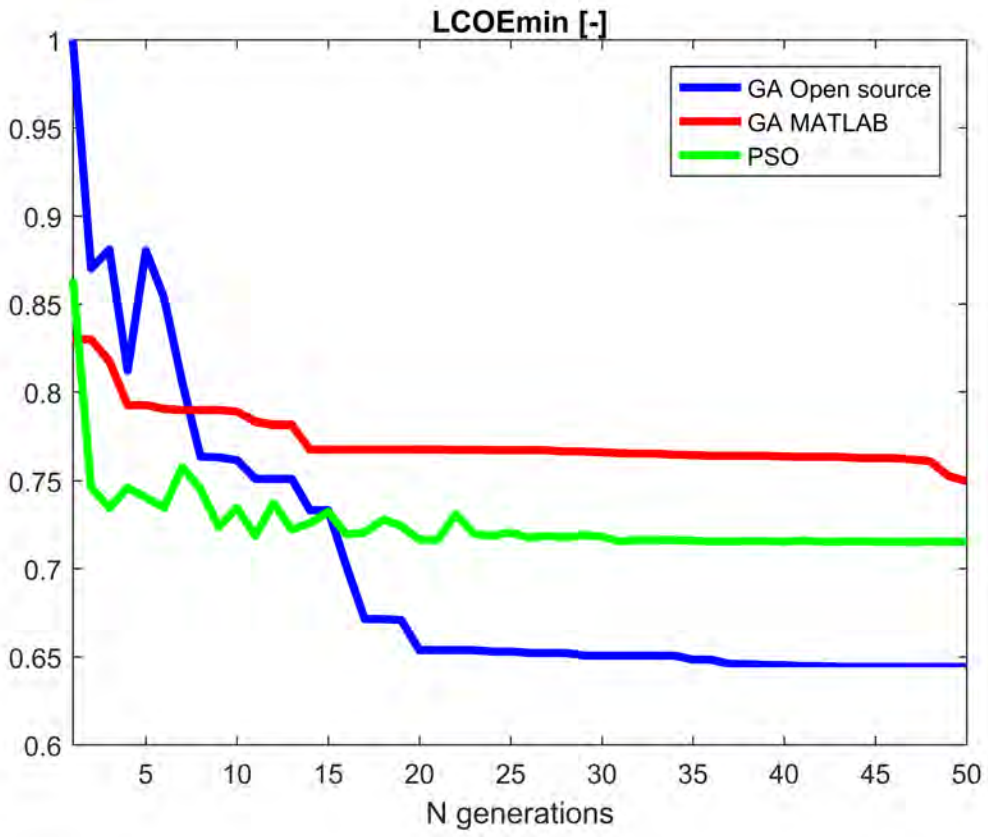

Figure 5.8: The comparison between optimisation algorithm for a single float configuration.

5.7.3 Improvements of the genetic algorithm

After having chosen the optimisation algorithm, some improvements have been investigated. The memory of the previous evaluations is accounted in the algorithm as well as the tuning of the mutation, cross-over coefficients and of the population. The sample points already evaluated have been changed with new ones near the global optimum obtained. In particular, the new points have been randomized around the global optimum and their distance from it has been decreased using a cubic relationship by generation in generation. This can be expressed as:

$$xd_{NewPoint} = xd_{min} + \frac{\frac{xd_{range}}{2} * rand}{gen^3} \tag{5.17}$$

where xd_{min} represents the combination of design parameters that minimize the objective function, xd_{range} is the search space of the design variables, $rand$ is a random vector with the same dimension of the design variables and gen is the number of generations. Finally if the evaluation of this new point is worse than the old one, then the old one will be restored. No specific references were used for this change.
The code has been improved also considering the tuning of the mutation, cross-over probability and of the population by generation in generation. This approach was inspired by the adaptive genetic algorithm that is possible to find also in literature [191]. The particle swarm approach has been considered for this purpose but applied to a single particle. The particle is described by 3 elements: the mutation probability, the cross-over probability and the population. The particle swarm methodology used is the same as described in Section 5.3 but with the best and the global position of the particle are considered coincident. The method is expressed as following:

- If the optimum found or the maximum of the generation relative to the previous one is decreased then the particle swarm algorithm is used.
- If the previous condition is not verified then the new particle is generated randomly.

The population keeps the best individuals if the population is reduced while it considers new random individuals if the population is increased.
The open-source genetic algorithm has been improved considering also the optimisation capability of the surrogate model. A Kriging surrogate model [192] has been adopted for its high efficiency for non-linear responses. This model is updated by generation in generation with the simulation carried out by the genetic algorithm. The surrogate model is

introduced in the genetic algorithm through the use of an elitism of 10% the number of population. The surrogate model is evaluated for new random points with a number of points equal to the same number of evaluations computed until that moment by the genetic algorithm. It is, in fact, supposed that the efficiency of the surrogate model will increase with the number of evaluations of the genetic algorithm. Then the best individuals evaluated by the surrogate model are added in the next generation. The huge advantage of the surrogate model is that enables the user to estimate results at a very low computational time compared to the real simulation. However the simulation time becomes more significant when the number of evaluations to fit is larger than 1000. Then probably a radial basis function could be replaced to have a more reasonable time required but with a lower efficiency for non-linear response (see Section 5.7.5). In fact, the surrogate model of the Kriging model requires a simulation time that increases as a cubic term ($R^2 = 0.9475$) as shown in Figure 5.9.

These changes have brought an improvement in the test function of the Schwefel Function example case with 2 variables (see Figure 5.10). This function has many local minima and so the convergence to the global minimum is more difficult. In Figure 5.10 (b) the objective has been obtained as average of 1000 different optimisations. The genetic algorithm without the tuning consider a cross-over coefficient of 0.9, mutation coefficient of 0.1 and a population of 100 individuals while the genetic algorithm with the on-time tuning considers a range of variation between 0-1 of the cross-over coefficient, 0-0.3 of the mutation coefficient and 50-150 of the number of individuals.

The algorithm that considers all the improvements shows the highest efficiency. The Kriging surrogate model shows an a cubical increase of the computational time with the number of simulations of the Schwefel function (see Figure 5.9). So the number of generations has been limited to 11 as shown in Figure 5.10.

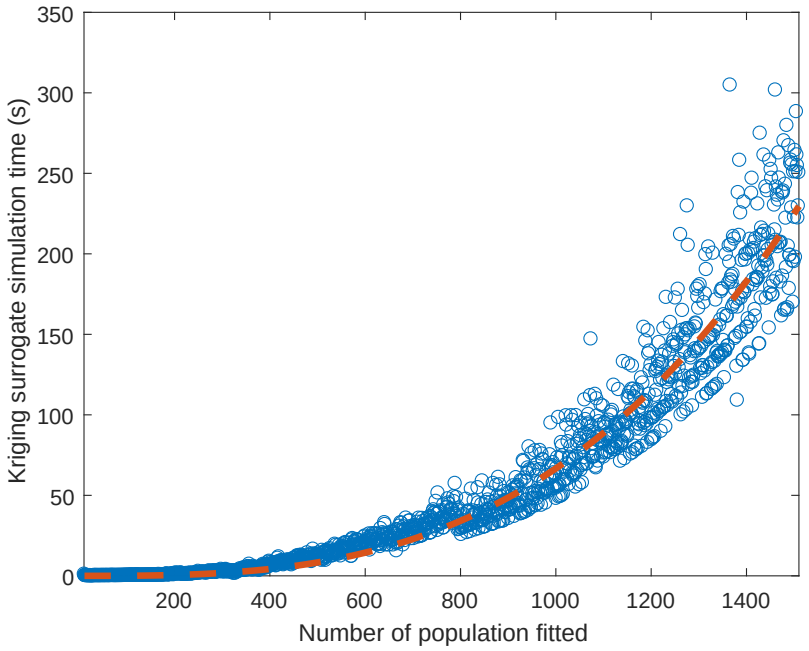

Figure 5.9: The simulation time required for the Kriging surrogate model.

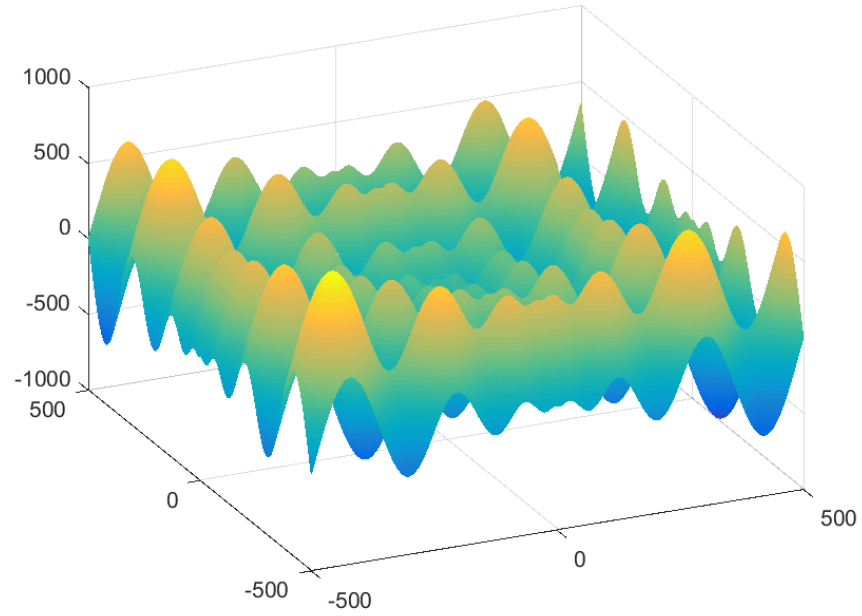

(a)

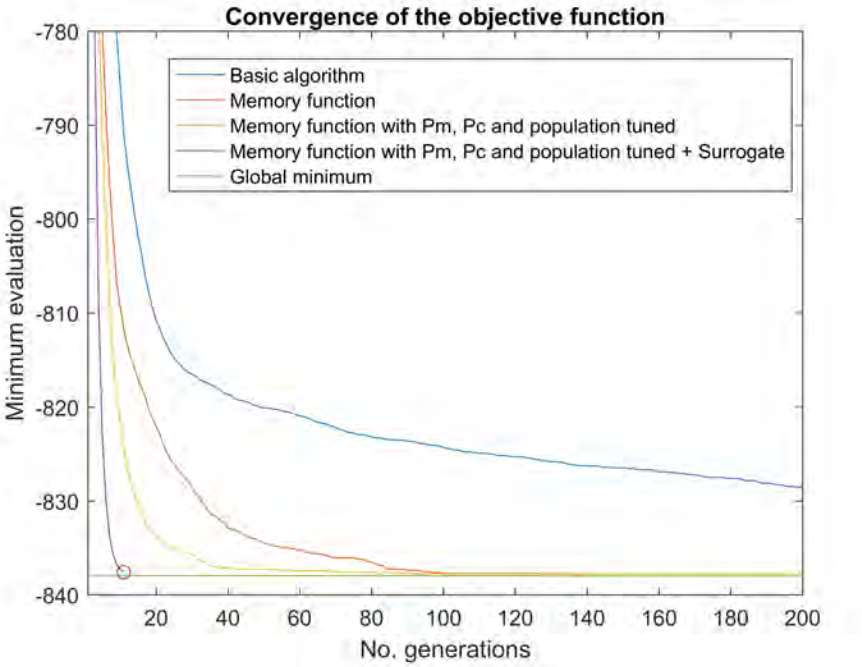

(b)

Figure 5.10: The Schwefel Function (a) and the average convergence of the genetic algorithm of 1000 different optimisations (b).

5.7.4 Results

Four different optimisations are investigated: a standard case (4 variables), the float-reactor separation sea state tuning (6 variables), the stiffness-damping PTO tuning (8 variables) and tuning of both the conditions (10 variables). The number of variables for each design variable and optimisation case can be summarized in the following Table 5.4:

Table 5.4: The number of variables for each optimisation case.

	Standard case	**FR sea state**	**kc sea state**	**FRkc sea state**
Float-reactor separation	1	3	1	3
kPTO	1	1	3	3
cPTO	1	1	3	3
Rated Power	1	1	1	1
Total design variables	4	6	8	10

The genetic algorithm is used considering the original code and the modifications described in the previous section 5.7.3. The surrogate model improvements is not considered in these results because it was introduced in a later version of the genetic algorithm. The original code is used for different mutation and cross-over values. The genetic algorithm after the modification made is called "Code Improvement". A fixed population equal to 10 times the number of variables is considered as a rule of thumb. The generations are limited to 50 for computational time reasons. The results are summarized in Figure 5.11 and Table 5.5. The results of these optimisations show that the convergence of the algorithm is very difficult especially for larger numbers of variables. The optimisation that considers both the k-c sea state tuning and the float reactor separation sea state tuning (10 variables) show a large range of the 60% evaluations in the last 5 generations (see Table 5.5). Some of the optimal values are outside the range because the algorithm is still not converged. It happens especially when the converged range is still large.

The convergence of the "Code Improvement" shows generally an average performance compared to the other cross-over and mutation coefficients curves. Its efficiency is very high for the optimisation that consider both the k-c PTO and float-reactor separation sea state tuning in which this algorithm shows the best performance. The "Code Improvement" can be used to compare the LCOE results of the various optimisations (see Table 5.6). In particular it can be seen that this method obtains an improvement in the minimum LCOE of around 12 % for both the float reactor separation and the k-c PTO sea state tuning doubling more or less the single way of tuning. The improvement of the tuning modes is expected

because the energy produced from these cases should be larger than the standard case. It's important to underline that all the optimisation carried out are still not converging completely as can be observed from the final optimum LCOE of the various optimisations of Figure 5.11. This is probably due to the fact that the influence of the variables on the response is strongly non-linear and generates lots of local minimum. In particular, the sensitivity of the mutation and cross-over coefficients on the optimisation convergence has been demonstrated to be quite important. For example Figure 5.11 (a) shows a difference around 20% between the minimum and the maximum LCOE in the last generation.

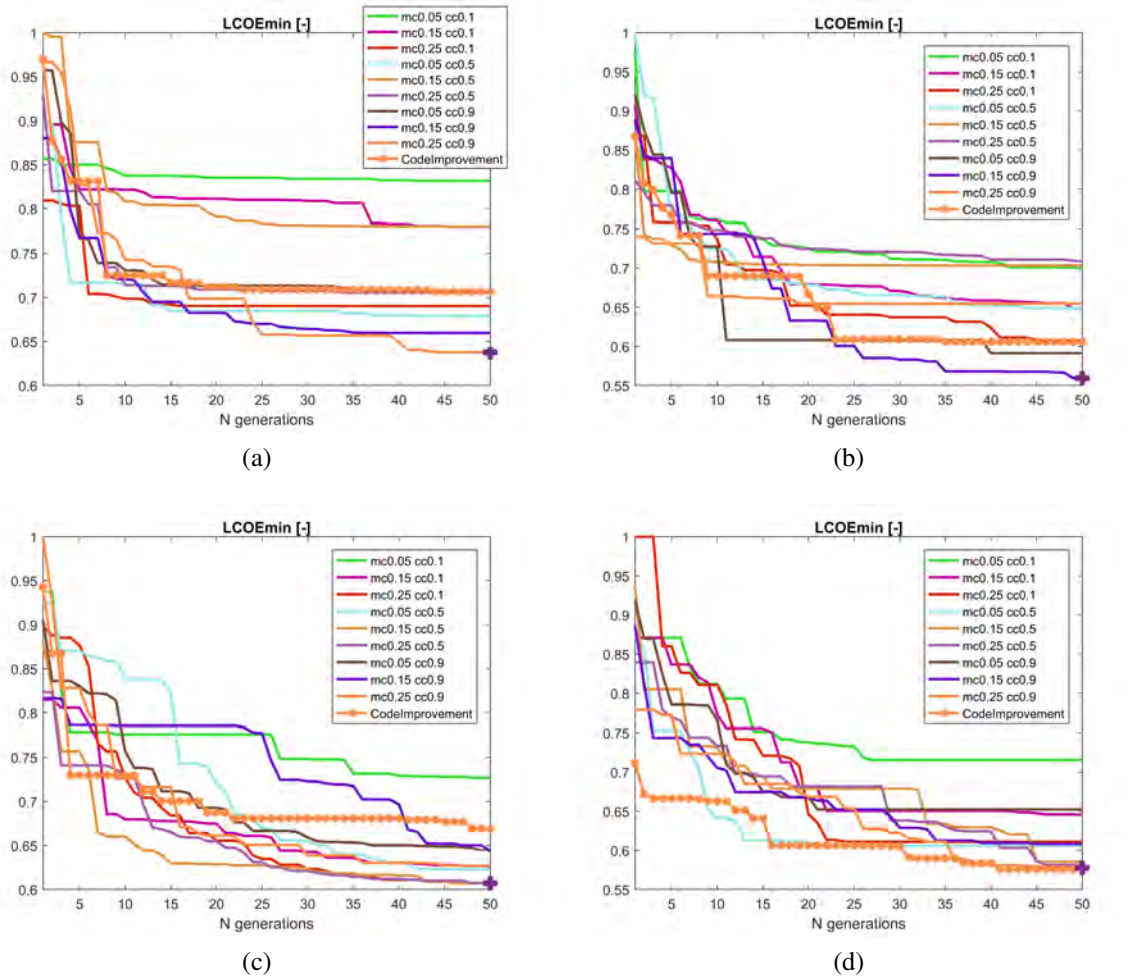

Figure 5.11: The normalized LCOE as a function of the number of generations for 4 different cases: the standard case (a), the float-reactor separation sea state tuning (b), the k-c PTO sea state tuning (c), the k-c PTO and float-reactor separation sea state tuning (d).

Table 5.5: The optimal design parameters and the range in which they are found to be for the 60 % of the last 5 generations.

	Standard case	**FR sea state**	**kc sea state**	**FRkc sea state**
Float-reactor separation1 (m)	53	50 [50.02 51.72]	57 [56.30 57]	52 [47.04 60.56]
Float-reactor separation2 (m)	-	55 [53.91 54.95]	-	57 [46.31 62.94]
Float-reactor separation3 (m)	-	65 [64.01 65.95]	-	54 [48.37 62.94]
kPTO1 (kNm^{-1})	777.17 [760.12 791.55]	983.18 [860.81 947.54]	904.9 [867.41 906.08]	867.20 [199.47 834.62]
kPTO2 (kNm^{-1})	-	-	690.62 [646.54 677.90]	787.61 [421.81 787.13]
kPTO3 (kNm^{-1})	-	-	921.87 [802.52 897.31]	656.67 [193.86 631.67]
cPTO1 ($kNsm^{-1}$)	921.33 [874.74 922.42]	761.09 [715.03 773.89]	970.03 [898.42 957.38]	805.84 [375.25 737.92]
cPTO2 ($kNsm^{-1}$)	-	-	979.46 [828.79 957.50]	136.58 [192.01 609.49]
cPTO3 ($kNsm^{-1}$)	-	-	555.84 [503.37 571.30]	484.78 [434.63 746.18]
Rated Power (MW)	1.45 [1.28 1.66]	1.92 [1.84 2.07]	1.81 [1.73 1.87]	1.56 [1.08 2.07]

Table 5.6: The relative difference of the minimum LCOE obtained with the "Code Improvement" algorithm between the standard and the different optimisation cases.

	Taguchi	**Standard case**	**FR sea state**	**kc sea state**	**FRkc sea state**
Relative error (%) referred to the Standard Case	21	0	-6	-7	-12

5.7.5 The sensitivity study of the WaveSub LCOE

A sensitivity study is very important in engineering design problems to understand better the relationship between output and input design variables. The model behaviour can be analysed considering the influence on the output of different parameter values. There are numerous statistical and probabilistic tools that aim to model an output variable dependent on design parameters [193]. An application of a graphical method can be found in [194]. It is used a screening technique called One At a Time (OAT) that enables to see the effect of the variation of each single variable keeping the other variable values at their nominal value. This approach is the most practical and common way to test the sensitivity of the model. However it is not fully exploring the searching area because it is not detecting the interactions between the design variables.
The sensitivity analysis can be obtained from a surrogate model or a meta-model that simulate the behaviour of the model. The main problem is to find a meta-model that is similar to the model.
There are two main steps to build a surrogate model [195]:

- The sampling of the model that involves the Design of Experiments (DOE) theory.
- The type of emulator or mathematical function to use (polynomial, radial basis function, Kriging).

Two common ways to sample a model are the Latin hypercube and the Sobol sequence [195]. These are near-random design that enable a low discrepancy and a good equidistribution of the sample points. In particular, these two methods obtain a better efficiency than a set of randomly positioned sample points. The Taguchi design can be also used to build orthogonal arrays that can help to understand the influence of each variable on the output [185]. It is a fractional factorial design and so the interaction effects between the parameters can't be understood completely. Especially a highly non-linear model is difficult to describe well using this kind of sampling. Ortoghonal arrays have been built based on a MATLAB file exchange [196]. The orthogonal array is built based on the paper [197] that establishes the following relation between the number of factors (NF) and levels (Ql):

$$NF = \frac{Ql^j - 1}{Ql - 1} \tag{5.18}$$

where j is an integer number. Radial Basis Function (RBF) is a real-valued function whose value depends on the distance from a certain point x_i called centre ($\Phi(x, x_i)$). The distance

is expressed by the Euclidian norm:

$$r_{RBF} = ||x - x_i|| \tag{5.19}$$

The RBF can be used to interpolate response surfaces:

$$f(x) = \sum_{i=1}^{N} \lambda_i \Phi(||x - x_i||) \tag{5.20}$$

where λ_i are the weights for each function evaluation and can be obtained through the least squares method.
There are different radial basis function that can be used: linear, cubic, thin plate splines, gaussian, multiquadric and inverse multiquadric.
Kriging is suitable for highly nonlinear responses and it belongs to the family of linear least squares algorithms. The open-source Oodace toolbox has been used for this purpose [192]. The estimation of the response variable of a point x is based on a linear combination of the results of the simulations:

$$f(x) = \sum_{i=1}^{N} \lambda_i(x) f(x_i) \tag{5.21}$$

where λ_i are the weights obtained through a regression analysis. Then a Gaussian process is built through the residuals.
The Normalised Root Mean Square Error (NRMSE) and the maximum error (MAX) are used to estimate the efficiency of the different emulators. They are evaluated for a certain number of testing points and are expressed as following:

$$NRMSE = \frac{\sqrt{\frac{1}{n_p}\sum_{i=1}^{n_p}(y_i - \hat{y}_i)^2}}{y_{max} - y_{min}} \tag{5.22}$$

$$MAX = max|y_i - \hat{y}_i| \tag{5.23}$$

where n_p is the number of points, y_i and $\hat{y}_i$ are the real and predicted value of the response.
A sensitivity study of the LCOE generated by a single WaveSub configuration has been investigated here. It is reported in particular the comparison between the application of 2 types of DOE (Taguchi and Latin hypercube) and 2 types of emulator (radial basis function and Kriging). The Taguchi DOE is considered with a number of levels between 10 and 50 with a spacing of 10 while the total number of evaluations is given in this case by the square of the number of levels. Then the linear RBF has been chosen for this comparison. The best

surrogate model for a single float configuration has been obtained using a Latin hypercube and the Kriging emulator because of the high non-linearity of the model (see Figure 5.12). NRMSE and the MAX error have been calculated for 20 testing points. In particular a NRMSE of 0.057 and a MAX error of 533 £/MWh have been reached. A NRMSE < 0.1 and NRMSE < 0.02 gives respectively a reasonable and excellent predictive capabilities as reported in [194]. So a reasonable predictive capability has been reached. However the MAX error is still too high and the surrogate model can't be used to find accurately the global minimum (see Figure 5.12). So metaheuristic algorithm remains still a better option to search the optimum.

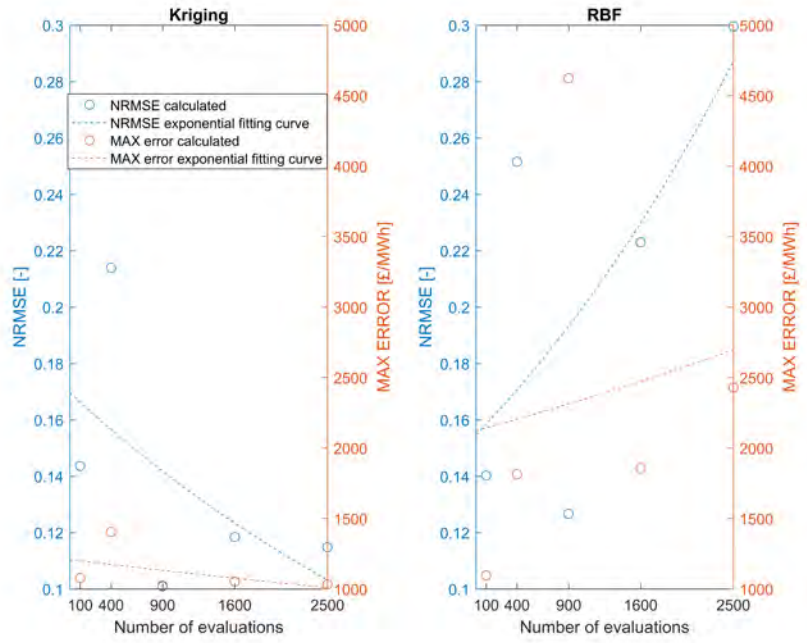

(a)

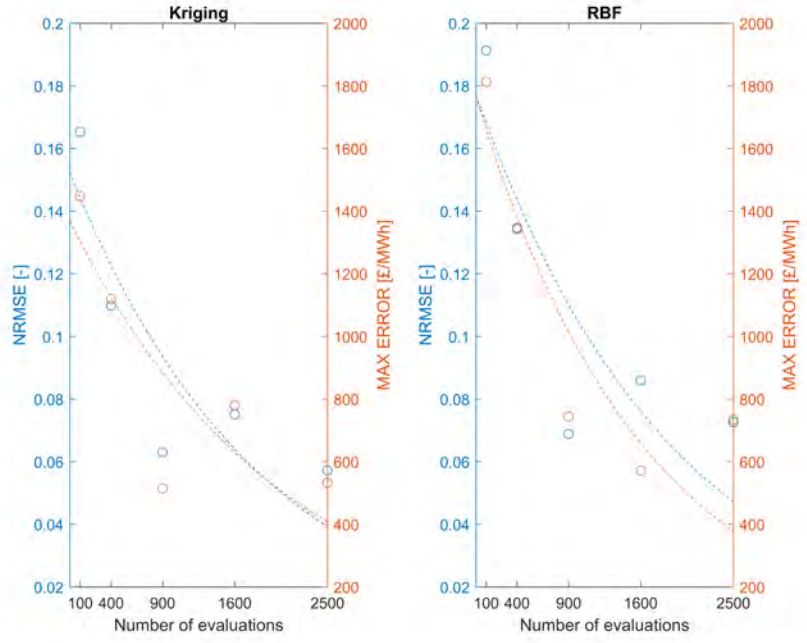

(b)

Figure 5.12: The NRMSE and the MAX error obtained using the Kriging and the RBF for a Taguchi (a) and Latin hypercube (b) DOE for a single float configuration.

5.8 The WaveSub optimization

5.8.1 Introduction

The optimisation of the design parameters for a single float WaveSub has been demonstrated to be difficult in terms of convergence of the parameters (see Section 5.7.4). A different approach will be used as explained in the optimisation procedure in Section 5.3. DOE such as the Taguchi and the latin hypercube are mainly used for sensitivity study purposes. Then the genetic algorithm is used to refine the optimum.

5.8.2 Taguchi and Latin DOE

The Taguchi optimisation is an efficient way to have a first estimate of the optimum with a lower number of simulation cases and can also be used for sensitivity analysis purposes. The Taguchi optimisation gives an estimation of the average influence of each parameter on the response but neglecting interaction effects between the variables. The latin hypercube can be used to have a better equidistribution of the sample points and to consider interaction effects. The latin hypercube is also used for a sensitivity study generating a surrogate Kriging model of the sample points simulated. The number of simulations is limited to 100 for computational reasons. The Taguchi DOE is obtained for a Taguchi ortoghonal array with 10 levels [185].
Figure 5.12 shows the results of the sensitivity analysis of the Taguchi DOE. The average LCOE and energy produced of the various design parameters is similar between the different multi-float configurations. So it is suggested that different multi configurations will have similar optimal design parameters. The float-reactor separation gives a minimum LCOE in the central range. The float spacing has the best optimum located along the border of the range considered but the lower values reached a better optimum. PTO stiffness and damping coefficients have a different influence on the minimum LCOE between each other. The best PTO stiffness coefficient is in the lower area of the range considered while the best PTO damping coefficient is in the higher area. The value of each parameter that gives the minimum LCOE from the Taguchi analysis for each WaveSub configuration are shown in Table 5.7. The model has been re-run with the suggested optimal values of each design parameter and as expected the multi-float configurations have given a better optimum compared with the runs in the original taguchi array. Similar optimal LCOE are obtained for

the 5 and 6 float configurations. In particular it is suggested that for larger multi-float configurations there should not be any improvement in the LCOE.
The LCOE and the energy average response show a very good correlation between each other as expected, this is demonstrated from the cross-correlation coefficients shown in Table 5.8. These coefficients have been obtained using the MATLAB function 'xcorr' [198]. The correlation is not total because of the influence also of the cost on the LCOE.
The capacity factor shows an increase for the multi-float configurations and it varies around 0.42 (see Figure 5.13). The energy produced from the device shows a proportional increase with the number of floats. The LCOE decreases mainly because of the decrease of the largest cost, CAPEX (see Figure 5.14). In fact, an increase of the number of floats per device determines mainly a decrease of the control and instrumentation, installation, grid connection, mooring and margin costs due to the the lower number of devices (see Table 5.7). Structure and PTO costs show instead a similar total cost for each float configuration. In particular structure costs are similar between the configurations because the float spacing is similar and the rated power is proportional to the number of floats per device. The total farm rated power is constant and so the total PTO cost is similar. Small differences in the total PTO costs are due to the finite number of devices with a total rated power sum that is not exactly 400 MW.
OPEX and decomissioning costs are instead decreasing with an increase of the number of floats per device due to a smaller number of devices. These last costs compared to the CAPEX are really small and so their influence on the LCOE is less significant.
Optimal results of the latin DOE are shown in Table 5.9. It is interesting to notice that the float spacing converges both towards lower values because of lower costs and for larger values such as for the 3 float configuration because the device produces more energy when the float spacing is going near the wavelength [66].
The capacity factor increases for the multi-float configurations and becomes very similar between 4 and 6 multi-float configurations as shown in Figure 5.13. Figure 5.14 shows again the decrease of the LCOE for the multi-float configurations mainly due to the decrease of the CAPEX reaching the minimum for the 6 float configuration.
The influence of the optimal design parameters on the LCOE for the 6 float configuration has been investigated in more detail in Figure 5.15 based on the latin DOE results. In fact, this multi-float configuration is considered one of the most promising between the ones analysed. Two parameters are investigated while the other two are fixed to the optimal values found by the latin hypercube. So Figure 5.15 shows a 2D surface representation of

the surrogate model. The darker blue of the plots shows where the optimal (lower) LCOE can be found. The NRMSE and the maximum error defined in Section 5.7.5 are calculated and shown at the bottom of Table 5.9. The NRMSE is always under 0.1 and so as reported in [194] the surrogate model has reasonable predictive capabilities. Similar conclusions of these graphs (Figure 5.15) agree with the Taguchi average response of the design parameters (Figure 5.12). Optimal values show the lower range for the float spacing and PTO stiffness, average range for the float-reactor separation and generally larger values for the PTO damping. In particular lower values of the PTO damping show a fast increase of the LCOE.

Table 5.7: The design parameters and main results for each multi-float WaveSub configuration derived for the optimum obtained from the Taguchi DOE.

	1 Float	**2 Floats**	**3 Floats**	**4 Floats**	**5 Floats**	**6 Floats**
Float Spacing (m)	-	35	35	35	35	35
Float-reactor Sep (m)	56	56	56	56	56	56
kPTO (kN/m)	116	116	5	5	116	5
cPTO (kNs/m)	1000	1000	1000	1000	1000	1000
RatedP (MW)	0.83	1.56	2.28	3.06	3.61	4.42
Energy device (MWh/y)	2749	5660	8178	10923	13649	16082
Ndevices	485	257	176	131	111	91
CF	0.38	0.42	0.41	0.41	0.43	0.42
CAPEX (M£)	1.000	0.873	0.831	0.798	0.810	0.790
CAPEX-Structure (-)	0.455	0.452	0.454	0.446	0.469	0.459
CAPEX-PTO (-)	0.278	0.277	0.278	0.278	0.278	0.279
CAPEX-Control (-)	0.055	0.029	0.02	0.015	0.013	0.01
CAPEX-Grid (-)	0.054	0.029	0.02	0.015	0.013	0.011
CAPEX-Mooring (-)	0.037	0.02	0.013	0.01	0.008	0.007
CAPEX-Installation (-)	0.012	0.007	0.005	0.004	0.004	0.004
CAPEX-Margin (-)	0.11	0.058	0.04	0.03	0.025	0.021
OPEX (y-1)	0.008	0.005	0.004	0.003	0.003	0.003
Decommissioning (-)	0.005	0.003	0.002	0.001	0.001	0.001
LCOE (-)	1.00	0.79	0.75	0.72	0.69	0.70

Table 5.8: The cross-correlation coefficients between the LCOE and the energy average response for each design variable.

	1 Float	**2 Floats**	**3 Floats**	**4 Floats**	**5 Floats**	**6 Floats**
Float Spacing (m)	-	0.97	0.97	0.97	0.97	0.96
Float-reactor Sep (m)	0.96	0.94	0.95	0.95	0.95	0.95
kPTO (kN/m)	0.86	0.89	0.89	0.89	0.89	0.88
cPTO (kNs/m)	0.84	0.81	0.81	0.80	0.80	0.81

Table 5.9: The design parameters and main results for each multi-float WaveSub configuration derived for the optimum obtained from the Latin DOE.

	1 Float	2 Floats	3 Floats	4 Floats	5 Floats	6 Floats
Float spacing (m)	-	40	101	40	40	40
Float-reactor sep (m)	42	35	21	35	35	35
kPTO (kN/m)	110	25	11	25	25	25
cPTO (kNs/m)	94	507	262	507	507	507
RatedP (MW)	0.95	1.68	2.80	3.13	4.00	4.79
Energy (MWh)	3586	6252	11418	12336	15631	18752
Ndevices	420	238	143	128	100	84
CF	0.43	0.42	0.47	0.45	0.45	0.45
CAPEX (-)	1	0.925	0.917	0.882	0.85	0.844
CAPEX-Structure (-)	0.436	0.471	0.52	0.494	0.48	0.482
CAPEX-PTO (-)	0.307	0.307	0.307	0.308	0.307	0.309
CAPEX-Control (-)	0.053	0.03	0.018	0.016	0.013	0.011
CAPEX-Grid (-)	0.052	0.03	0.018	0.017	0.013	0.011
CAPEX-Mooring (-)	0.035	0.02	0.012	0.011	0.008	0.007
CAPEX-Installation (-)	0.011	0.007	0.005	0.005	0.004	0.004
CAPEX-Margin (-)	0.106	0.06	0.036	0.032	0.025	0.021
OPEX (y-1)	0.008	0.005	0.004	0.004	0.004	0.004
Decommissioning (-)	0.005	0.003	0.002	0.002	0.001	0.001
LCOE (-)	1	0.92	0.82	0.82	0.79	0.78
NRMSE (-)	0.03	0.05	0.08	0.08	0.06	0.05
MAX (£/MWh)	65.10	50.00	76.16	88.87	49.34	49.96

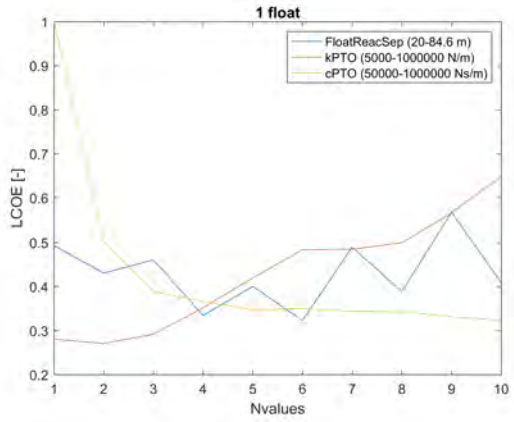
1 float
FloatReacSep (20-84.6 m)
kPTO (5000-1000000 N/m)
cPTO (50000-1000000 Ns/m)
LCOE [-]
Nvalues

(a)

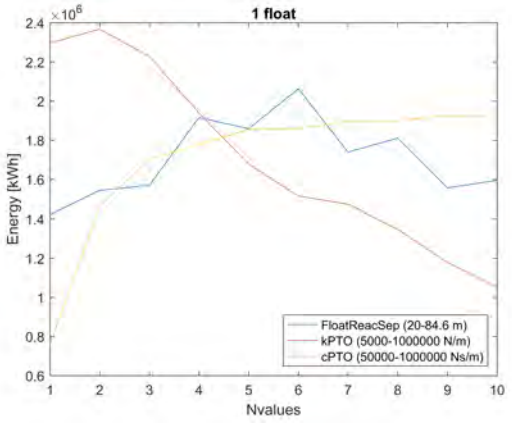
1 float
×10^6
FloatReacSep (20-84.6 m)
kPTO (5000-1000000 N/m)
cPTO (50000-1000000 Ns/m)
Energy [kWh]
Nvalues

(b)

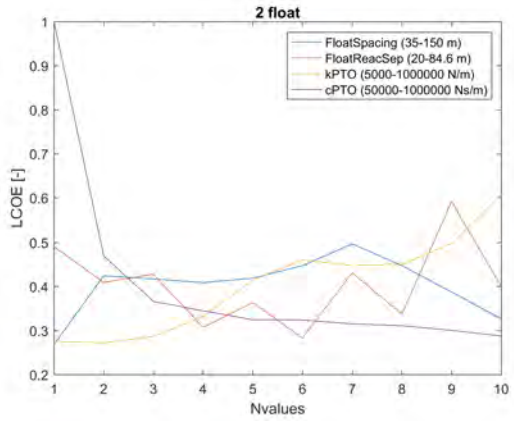
2 float
FloatSpacing (35-150 m)
FloatReacSep (20-84.6 m)
kPTO (5000-1000000 N/m)
cPTO (50000-1000000 Ns/m)
LCOE [-]
Nvalues

(c)

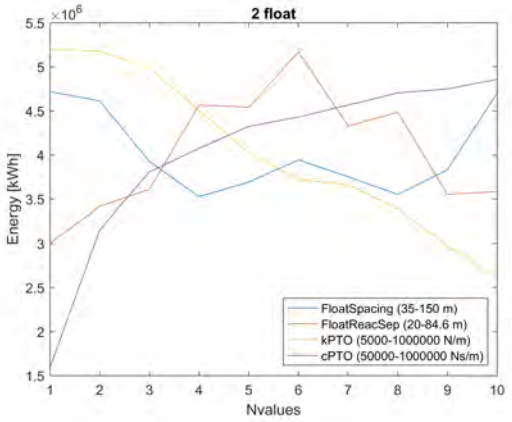
2 float
×10^6
FloatSpacing (35-150 m)
FloatReacSep (20-84.6 m)
kPTO (5000-1000000 N/m)
cPTO (50000-1000000 Ns/m)
Energy [kWh]
Nvalues

(d)

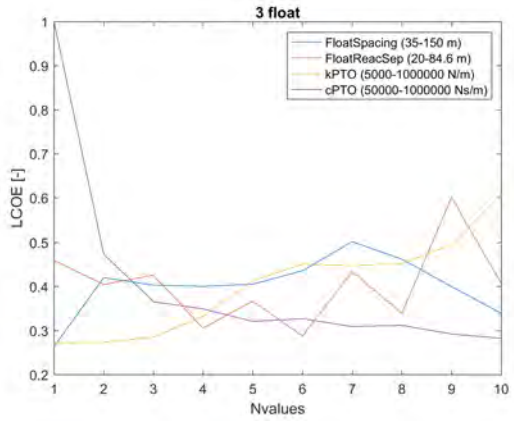
3 float
FloatSpacing (35-150 m)
FloatReacSep (20-84.6 m)
kPTO (5000-1000000 N/m)
cPTO (50000-1000000 Ns/m)
LCOE [-]
Nvalues

(e)

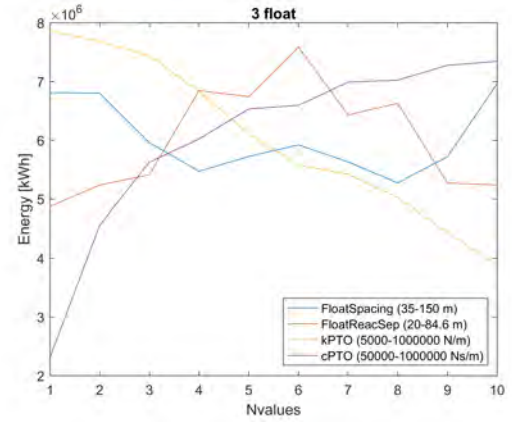
3 float
×10^6
FloatSpacing (35-150 m)
FloatReacSep (20-84.6 m)
kPTO (5000-1000000 N/m)
cPTO (50000-1000000 Ns/m)
Energy [kWh]
Nvalues

(f)

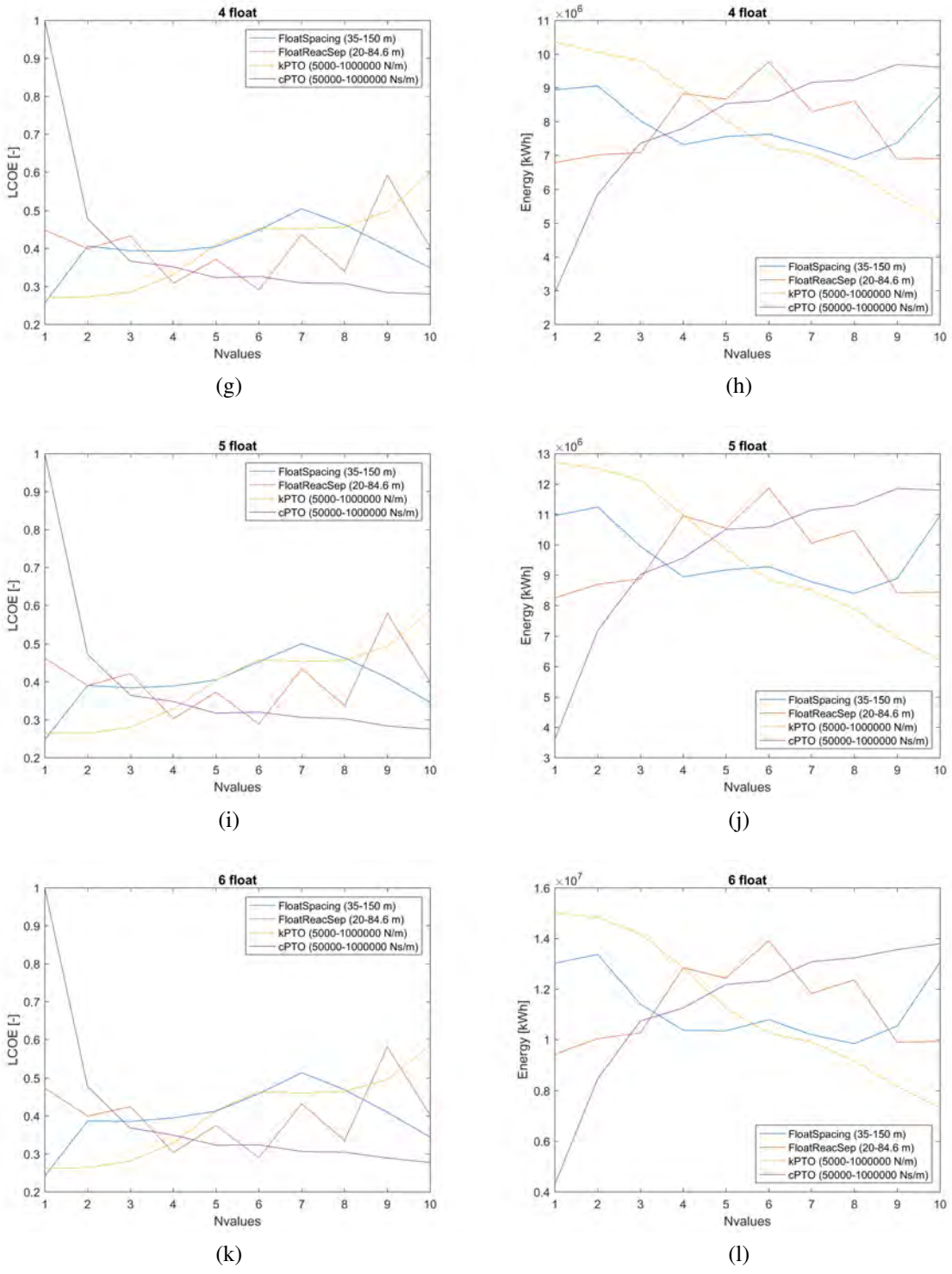

Figure 5.12: The LCOE and energy average response of the various design parameters from the Taguchi results for 1 float (a-b), for 2 float (c-d), for 3 float (e-f), for 4 float (g-h), for 5 float (i-j) and for 6 float (k-l) multi-float configurations.

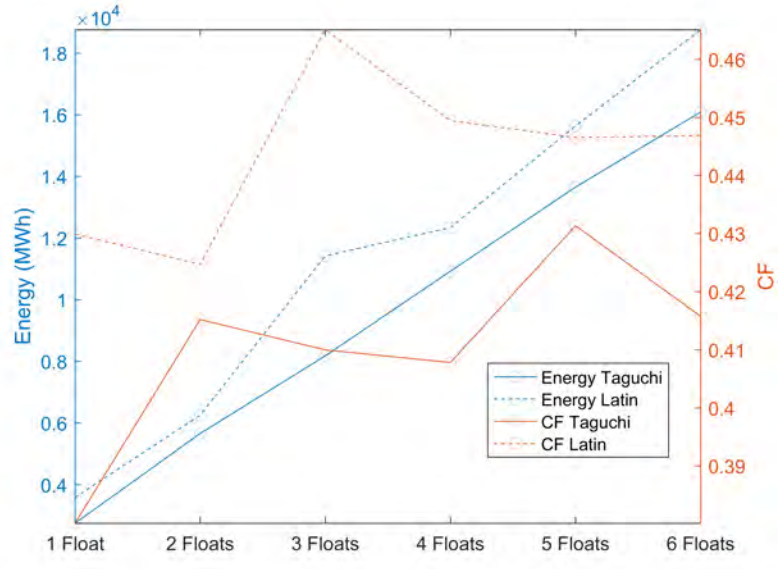

Figure 5.13: The energy produced and the capacity factor for the optimal cases given by the Taguchi and Latin DOE.

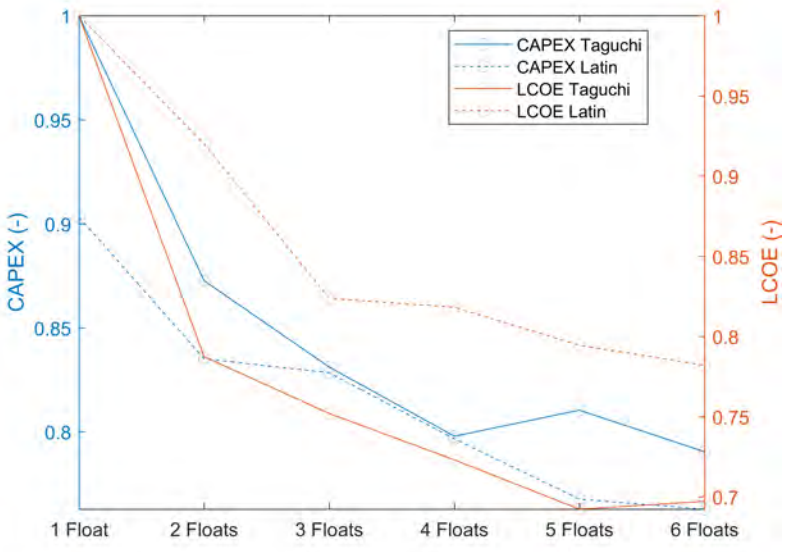

Figure 5.14: The CAPEX and the normalised LCOE for the optimal cases given by the Taguchi and Latin DOE.

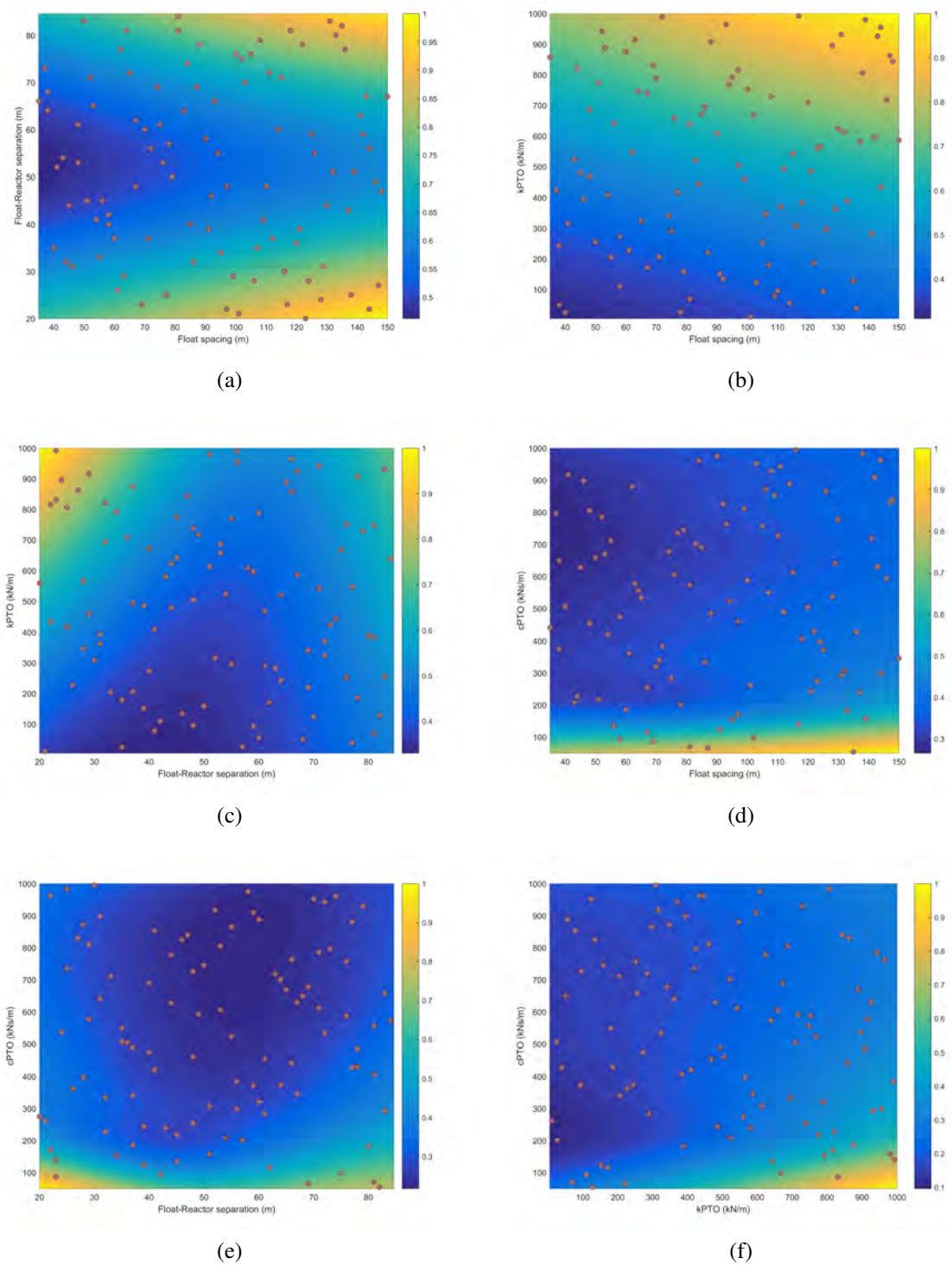

Figure 5.15: The surrogate model for the optimal case of the latin hypercube DOE for a 6 float configuration. 2 parameters are investigated while the other 2 are fixed to the optimal case. Darker blue shows where the optimal values of the LCOE are expected. LCOE is normalized in the Figure.

5.8.3 The genetic algorithm optimisation

The optimisation of the multi-float configurations consider the genetic algorithm with an elitism of 20% of the population. A more regular behaviour than the extremely non-linear Schwefel function is expected (see Section 5.7.3). The evaluation of the new points from the surrogate model is calculated using a latin hypercube DOE of the square of the number of simulations of the genetic algorithm until that generation.
The population number is fixed as 5 times the number of variables while the total number of generations is fixed to 5 due to computational time reasons. The total number of simulations is the same of the previous Taguchi and latin DOE analysis.
Table 5.10 shows the optimal results of the various configurations. Float spacing generally converges towards lower values but not for the 3 and 4 float configurations. Float-reactor separation converge in the lower range as well as the PTO stiffness and damping. Finally the LCOE is decreased from a single float configuration to a 6 float configuration by 21%.
Figure 5.16 shows the increase of the capacity factor with an increase of the number of floats per device. The decrease of the LCOE with an increase the number of floats per device is shown in Figure 5.17. In particular the 6 float configuration shows an increase of the CAPEX compared to the 5 float configuration but in the same time it shows also an increase of the capacity factor with the result to have a lower LCOE.
Figure 5.18 shows the sensitivity study of the LCOE for a 6 float configuration. Two parameters are investigated while the other two are fixed to the optimal values found by the genetic algorithm. So Figure 5.18 shows a 2D surface representation of the surrogate model. The darker blue of the plots shows where the optimal (lower) LCOE can be found. Similar conclusions of the latin DOE sensitivity study can be obtained. The evaluation points are more concentrated in this case around the optimal value because of the use of the genetic algorithm (see Figure 5.18). A complete convergence is not expected due to the limited number of evaluations but this method enables refinement of the optimum LCOE found compared to the Taguchi and latin DOE. The NRMSE and the MAX error are shown in Table 5.10 and they are calculated considering the predictability of the surrogate model on the last generation. The surrogate model is constructed for this calculation on the first 4 generations simulation cases.
A summary of the optimum LCOE obtained from the different methods is shown in Figure 5.19. The optimum found from the surrogate models of the latin DOE and the genetic algorithm has been also added in the comparison. In particular they don't obtain a better optimum because the surrogate model is not accurate enough. The optimum found by the

genetic algorithm is demonstrated to be the most efficient to find the minimum LCOE from all the methods used. It is also clear that configurations with a number of floats larger than 3 will have only a slight reduction of the minimum LCOE.
Finally Figure 5.20 shows the visualization of the optimal 6 float configuration for a regular wave. More specifically it is shown the screenshot of the time domain simulation and the total wave amplitude.

Table 5.10: The design parameters and main results for each multi-float WaveSub configuration derived for the optimum obtained from the GA optimisation.

	1 Float	**2 Floats**	**3 Floats**	**4 Floats**	**5 Floats**	**6 Floats**
Float spacing (m)	-	46	101	94	39	53
Float-reactor sep (m)	45	44	33	34	36	29
kPTO (kN/m)	58	74	10	14	10	10
cPTO (kNs/m)	203	370	177	251	337	206
RatedP (MW)	1.02	1.72	3.19	4.10	4.10	4.91
Energy (MWh)	3881	6751	12759	16503	16548	20605
Ndevices	393	232	126	98	98	82
CF	0.44	0.45	0.46	0.46	0.46	0.48
CAPEX (-)	1	0.96	0.885	0.882	0.877	0.903
CAPEX-Structure (-)	0.427	0.489	0.479	0.493	0.489	0.525
CAPEX-PTO (-)	0.321	0.321	0.323	0.323	0.323	0.323
CAPEX-Control (-)	0.052	0.031	0.017	0.013	0.013	0.011
CAPEX-Grid (-)	0.051	0.031	0.017	0.013	0.013	0.012
CAPEX-Mooring (-)	0.034	0.02	0.011	0.009	0.009	0.007
CAPEX-Installation (-)	0.011	0.007	0.005	0.004	0.004	0.004
CAPEX-Margin (-)	0.103	0.061	0.033	0.026	0.026	0.022
OPEX (y-1)	0.008	0.006	0.004	0.004	0.004	0.004
Decommissioning (-)	0.005	0.003	0.002	0.001	0.001	0.001
LCOE (-)	1	0.92	0.82	0.81	0.80	0.79
NRMSE (-)	0.15	0.03	0.04	0.10	0.02	0.11
MAX (£/MWh)	61.48	25.50	14.41	134.36	16.05	56.12

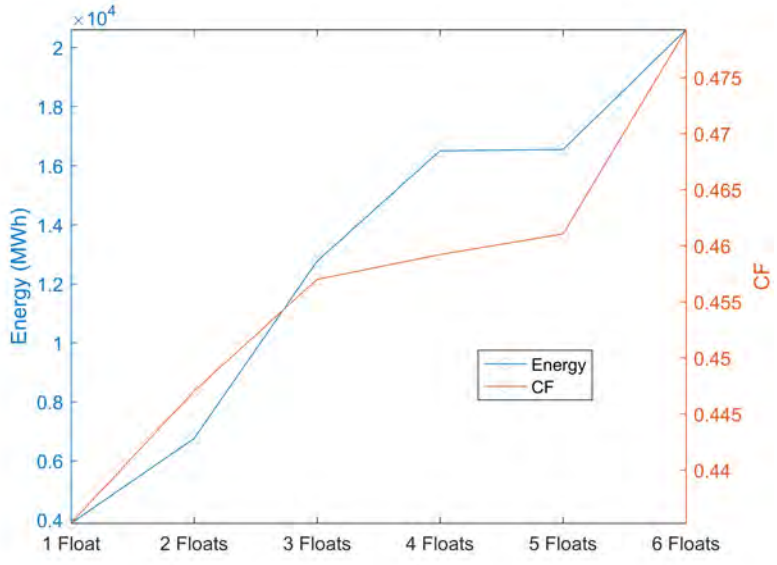

Figure 5.16: The energy produced and the capacity factor for the optimal cases given by the GA optimisation.

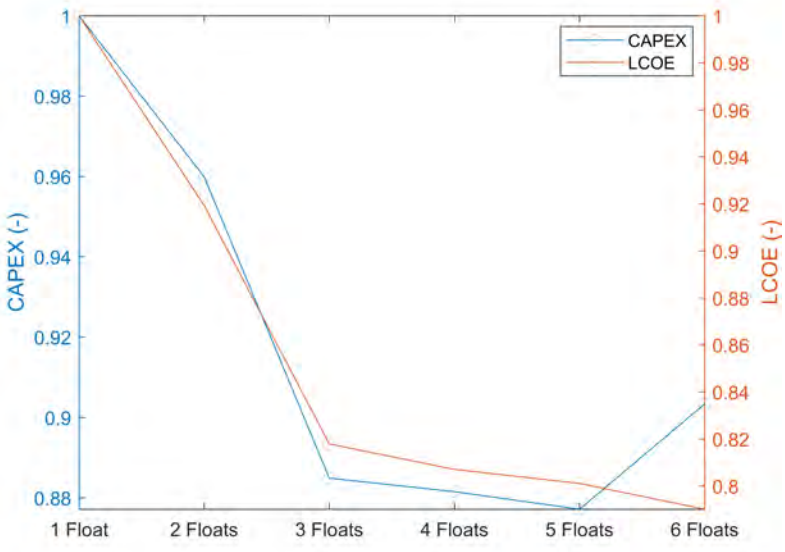

Figure 5.17: The CAPEX and the normalised LCOE for the optimal cases given by the GA optimisation.

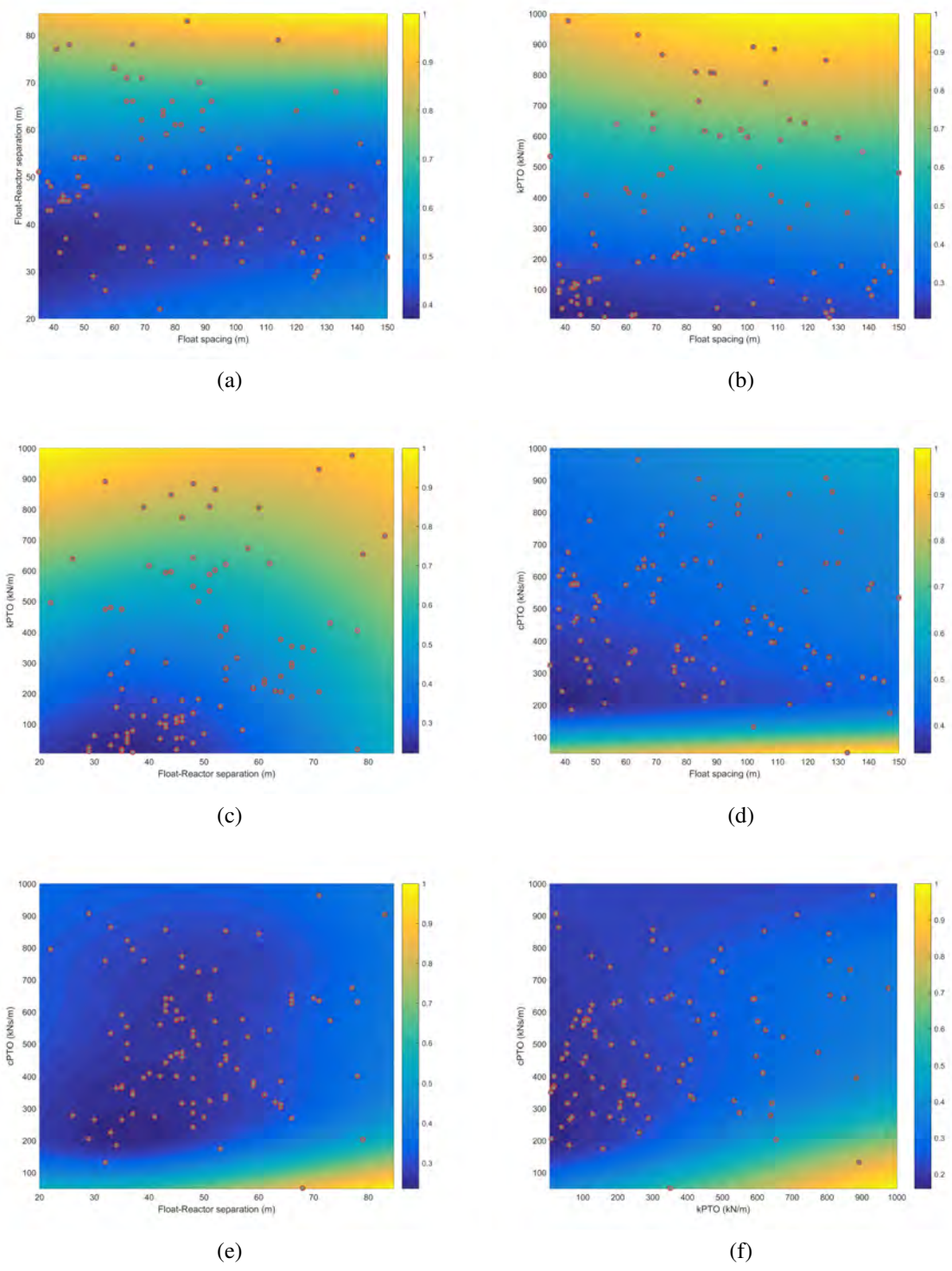

Figure 5.18: The surrogate model for the optimal case of the GA optimisation for a 6 float configuration. 2 parameters are investigated while the other 2 are fixed to the optimal case. Darker blue shows where the optimal values of the LCOE are expected. The LCOE is normalised in the Figure.

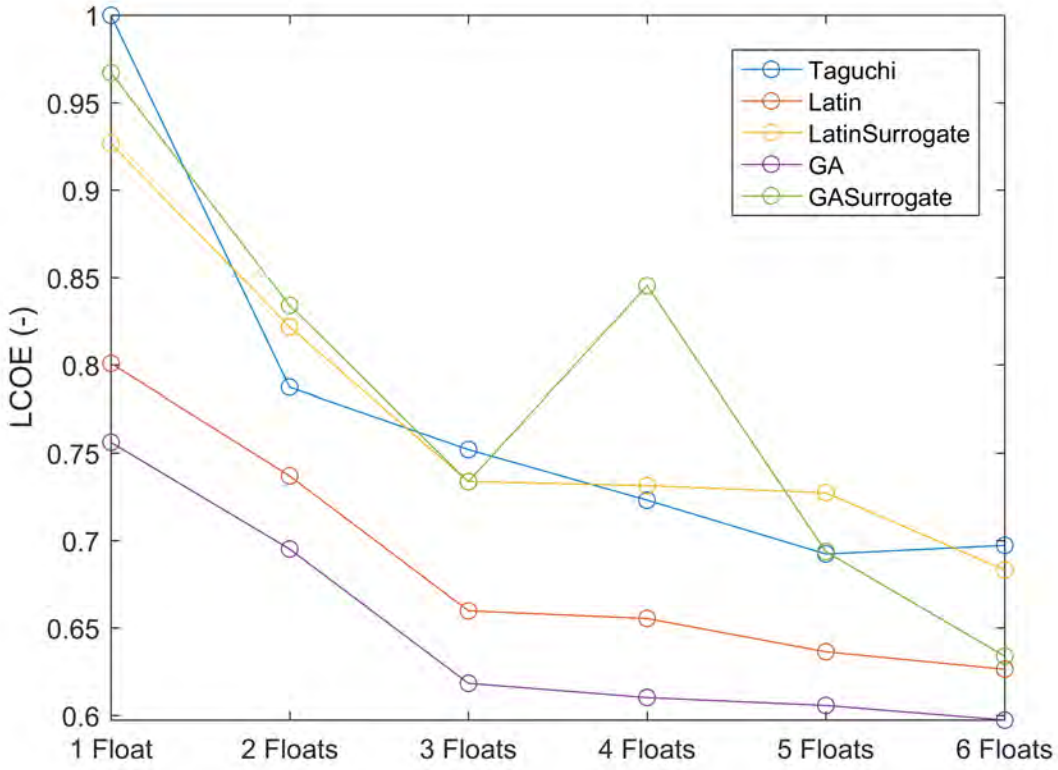

Figure 5.19: The optimum normalised LCOE summary for the Taguchi and latin DOE and for the genetic optimisation. The optimum is also given by the surrogate model of the latin DOE and of the genetic optimisation.

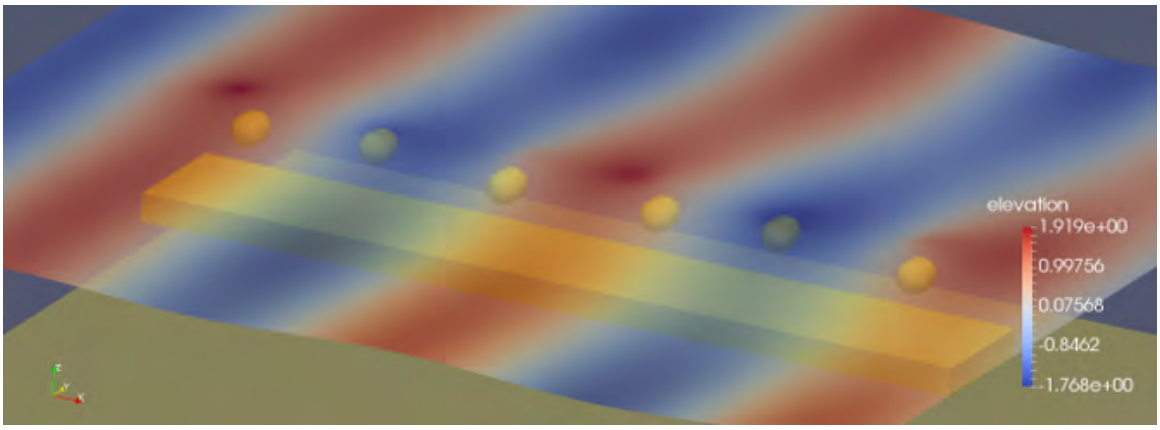

(a)

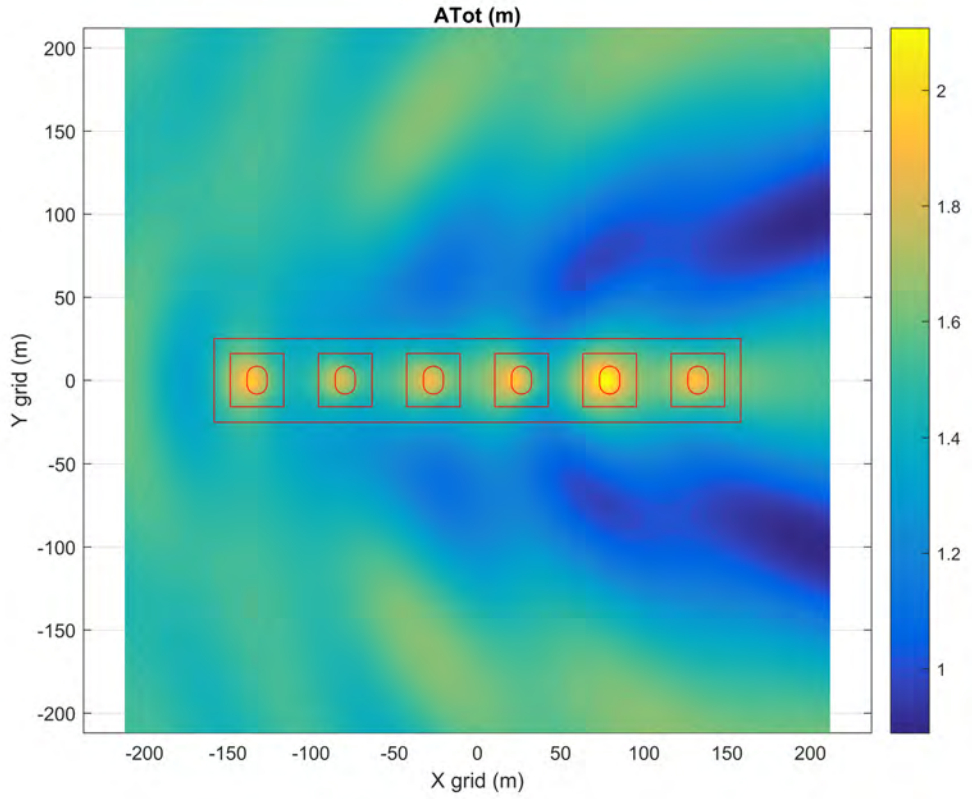

(b)

Figure 5.20: The visualization of the 6 float optimal configuration in Paraview (a) and the total wave amplitude generated (b). This results are referred to a regular wave with H=3m and T=10s. Wave amplitude is given in m.

5.9 Sensitivity analysis of key factors influencing the LCOE

The significant financial factors that influence the LCOE are the CAPEX, the OPEX and the interest rate. Figure 5.21 shows the sensitivity analysis on the LCOE of CAPEX, OPEX and interest rate for the optimal case found by the genetic algorithm of the 6 float configuration. The sensitivity was tested considering 3 different plots in which for each one of them, one factor was varied from 0 to the optimal case while the other ones were considered with 2 different values and 4 cases. The different cases determined by the factor values were the following:

- CAPEX of 50% and 100% of the optimal value of the genetic algorithm.
- OPEX of 50% and 100% of the optimal value of the genetic algorithm.
- Interest rate of 6% and 12%.

It is found that the LCOE is significantly dependent on the CAPEX and interest rate values. The OPEX, instead, determines only a slight variation on the LCOE. In fact, the OPEX is a lot smaller than the CAPEX (0.4%). There is overall a linear relationship between the LCOE and the CAPEX and OPEX while it is non-linear between the LCOE and the interest rate. For more details, Equation 5.3 gives a more insight between their relationship.
The accuracy of the calculation of the CAPEX and OPEX will determine the quality of the results of the optimisations carried on in this chapter, especially regarding the CAPEX due to the larger cost. So, it has been assumed that the method of the calculation of the CAPEX and OPEX is enough accurate to understand how it changes with the configuration. The definition of the interest rate, in the other side, will give the same answer when comparing the different multi-float layout. In fact, the LCOE for each configuration will increase or decrease proportionally based on this value.

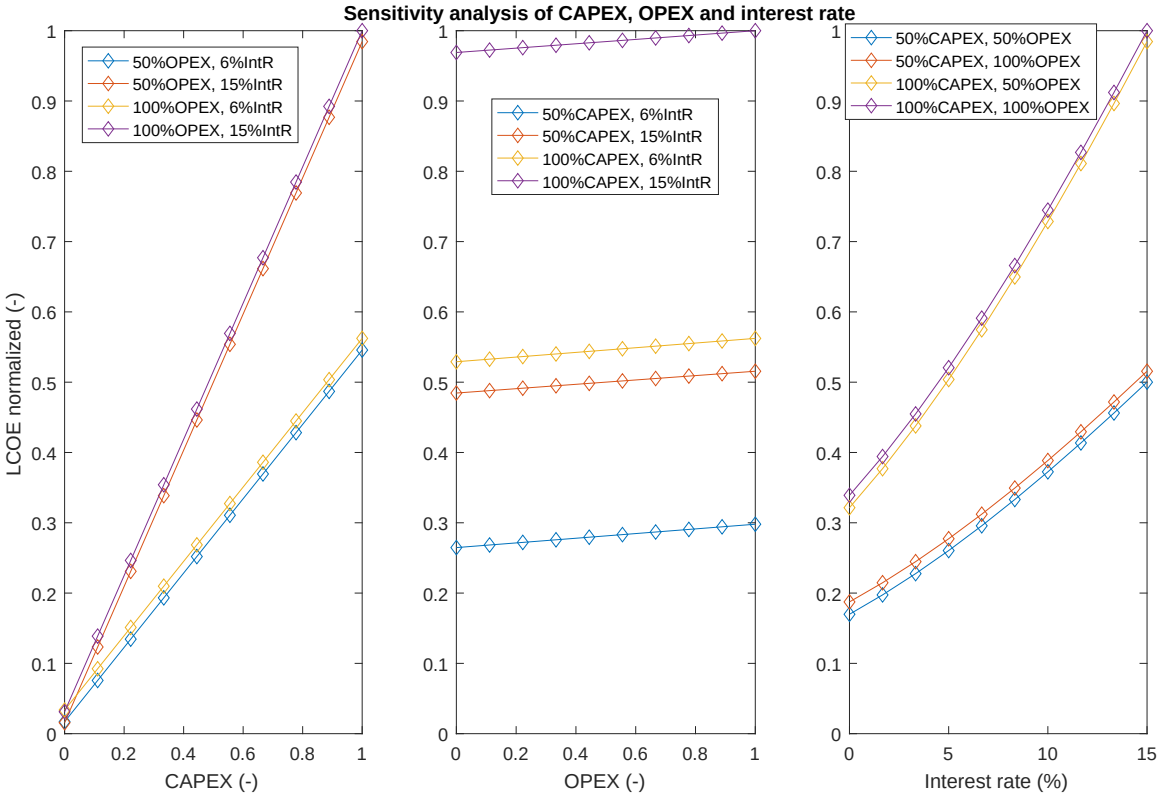

Figure 5.21: The influence of the key parameters influencing the LCOE for the optimal case of the genetic algorithm.

5.10 Conclusions

A linear multi-float configuration has been modelled and optimised using 3 main methods. A Taguchi and latin DOE are mainly used for sensitivity purposes while a genetic algorithm optimisation has been applied for a refinement of the optimal configuration obtained by the first 2 methods.

Sensitivity studies give similar conclusions regarding the optimal range of the design parameters. They agree all in the convergence of the PTO stiffness towards lower values. Float spacing generally converges towards lower values while the float-reactor separation converges towards the low-medium range. Finally the optimal PTO damping is generally in the medium range but it shows less convergence compared to the other ones. The Taguchi DOE shows that the average influence of each design parameter in the response is very similar between the multi-float configurations. The latin DOE is used mainly to build the Kriging surrogate model and to analyse the influence of design parameters combined together.

The genetic algorithm optimisation show the optimal design parameters for each multi-float configuration. There is clearly a reduction in optimal LCOE with an increase of the float number per device because mainly of a reduction of the CAPEX. The 6 float configuration has given the largest improvement compared to a single float configuration. However the reduction of the LCOE is small for multi-float configurations larger than 3. The reduction of the LCOE from the single float configuration to the 6 float configuration is around 21%. The results of this chapter are very significant in a commercial sense for MPS. In fact, the choice of a multi-float configuration is a key decision for the progress and evolution of the device. The improvements of the genetic algorithm could be also very interesting for the research community. The combination of the genetic algorithm with the surrogate model is a novel approach and is an additional optimisation strategy for the research community.

This work is based on a number of assumptions. There are first all the limitations of the numerical model described in chapter 3. In particular, the drag coefficient was estimated here but there is still uncertainty on it because of its possible dependence on the design parameters. After that, there is uncertainty on the cost model. The cost model is especially sensitive to the choice of the CAPEX and interest rate. Finally, the optimisation involves various design parameters and a large number of simulations is required. The optimisation was limited to 100 simulations for computational time reasons. As a consequence the results of the genetic algorithm may not converge. For this reason, 3 different optimisation approach have been used and compared.

Further work will include an extension of the optimization for different arrangements of the floats in addition to the linear shape considered here. Additionally, a calculation of the energy production of the wave farm that takes in account the hydrodynamic interactions between the WECs could be also considered.

Chapter 6

The optimisation of new design concepts of the multi-float WaveSub

6.1 Introduction

In this chapter various multi-float layouts have been investigated for a possible further reduction of the LCOE compared to a linear multi-float configuration. The number of floats considered is 6 because this multi-float configuration was demonstrated to be more efficient than lower numbers of floats (see Chapter 5). Larger multi-float configurations are not considered for computational time reasons. However, the results from chapter 5, show that for the optimal design of a WEC array, there is a small difference in LCOE for multi-float configurations larger than 3 floats (See Figure 5.19).
Four different layout designs have been investigated based mainly on regular geometry properties of each design:

- A 6 float linear layout
- A 6 float rectangular layout
- A 6 float triangular layout
- A 6 float circular layout

6.2 Improvements to the calculation of the Levelized Cost Of Energy

The LCOE is an important indicator of the performance of the technology and needs to be constantly updated with the increase of the experience of MPS. The accuracy of the calculation of the energy production and the cost of the wave farm is of primary importance to demonstrate the confidence to MPS. So the calculation of the LCOE has been updated for this main purpose.
The hydrodynamic coefficients and the simulation time are the main aspects that can be improved for the estimation of the energy produced. The hydrodynamic coefficients are mainly improved with an increase of the mesh panels of the different bodies. Then the simulation time is increased to half an hour for a more precise estimation of the energy produced by an irregular sea state. However, this increase in the accuracy of the results also increases the computational time required for the optimisation of the design parameters.
The calculation of the total cost used in the optimisation has been updated, based on the sharing of MPS confidential information. A WEC farm of 500 MW is considered in the cost calculation. The experience of the wind farm sector is used for this calculation [199] as well as detailed cost calculation of some device components. A detailed calculation can't be obtained in this stage due to the uncertainties of the new design concepts of the multi-float configurations that could determine a great influence on the results. So only the main significant cost components are considered.
The CAPEX is considered as the sum of: the structure, the PTO, the mooring, Balance of System and installation costs. All these costs are obtained proportional to the number of devices. The specific cost per device can be described as following:

- The structure cost is dependent on the specific cost of the material used and on the mass of the different bodies.
- The calculation of the hydraulic PTO cost has been updated since chapter 5 considering specific costs of the components of the primary transmission. Then the sum of the cost of the secondary transmission and energy storage is proportional to the rated power using a constant specific value.
- The mooring cost is based on the cost of the mooring lines, anchors and winches. The cost of the mooring lines is based on the number of them and the length of them. The cost of the anchors and winches depends on the number of them.

- The Balance of System cost is proportional to the rated power of the device.
- The installation cost per device is fixed.

Finally the OPEX cost is a fraction of the CAPEX while the decommissioning cost per device is a constant value. More details of the cost calculation are confidential with MPS.

6.3 The optimisation procedure

The optimisation procedure has been slightly changed because the design parameters to be optimised are reduced to the PTO related parameters which are the stiffness and the damping. The range of these coefficients are the same as used for the previous linear multi-float design (see Section 5.8). The float spacing and the float-reactor separation are not involved in the optimisation procedure. However 3 different values of float spacing have been tested in this chapter, each of them has an appropriately sized design of the reactor. Then each float spacing case corresponds to a different optimisation case. The float-reactor separation has not been considered because the new heavier design of the floats determined that this variable is less significant as reported by MPS (see Section 3.1.2).
The optimisation does not require the Nemoh simulation because the same hydrodynamic coefficients are used for each optimisation case. The optimisation scheme is updated after this modification as shown in Figure 6.1. The OPT block is described as previously in Figure 5.2. The number of simulations is limited to 50 for computational reasons. The genetic algorithm is considered with a very high elitism of 90% because the results have shown generally a single optimum and because there are only 2 design parameters in total to optimize.

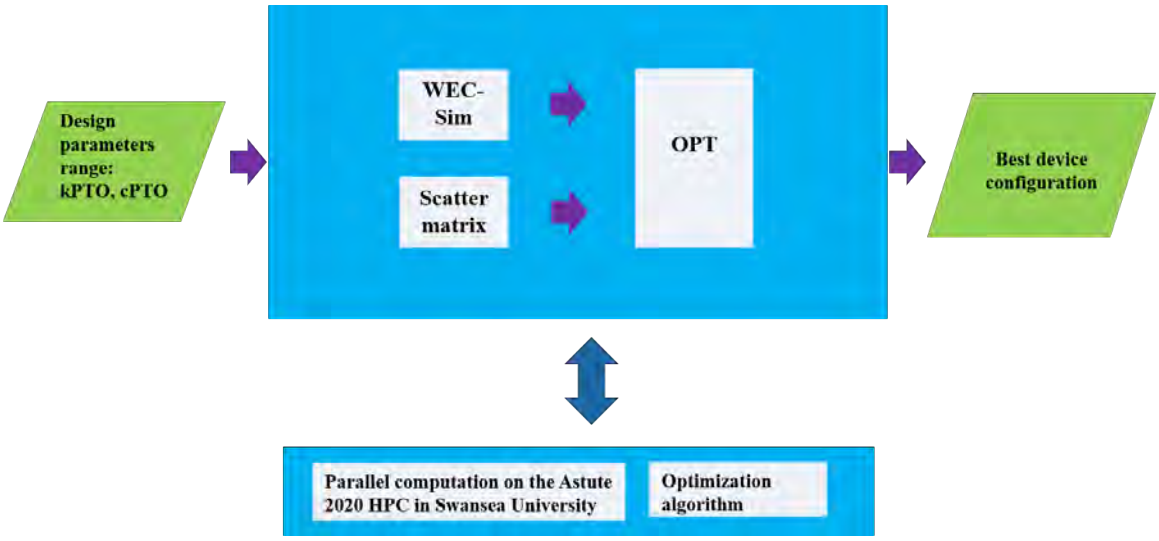

Figure 6.1: Updated optimisation scheme for a new concept WaveSub array.

6.4 Computational model set-up

In this chapter, the computational model for the float and reactor has used the most updated design suggested by MPS. The description of the design is given in Section 3.1.2 where it is referred as the second design. The main design parameters are detailed in Table 6.1.

Table 6.1: The design parameters for the float and the reactor.

Float	**Number of floats ($nfloat$)**	6	–
	Radius	7	m
	Depth to top	5	m
	Submerged mass	1179288.5	kg
	Dry mass	101000	kg
	Steel shell density	7700	$\frac{kg}{m^3}$
Reactor	**Radius of buoyancy tanks (R_{tank})**	2.5	m
	Number of buoyancy tanks ($Ntanks$)	3-4	–
	Depth to top	33	m
	Steel shell density	7700	$\frac{kg}{m^3}$
	Baseline Net buoyancy	500000	kg
	Baseline mass reactor frame	200000	kg
	Baseline mass subsystem	50000	kg

The net buoyancy and the frame mass of the reactor and the mass of the subsystem have been obtained dependent on the float spacing and the float number through the definition of multipliers. The multipliers are defined in the following Table 6.2:
The frame mass and net buoyancy of the reactor and the subsystem mass are calculated as

Table 6.2: The multipliers used for the design of the multi-float configurations.

Float Spacing Multiplier (FSM)	0.75
Float Number Multiplier (FNM)	0.75
Net Buoyancy Multiplier (NBM)	0.2
Sub-system Multiplier (SM)	0.6

following:

$$NetBuoyancyReactor = BaselineNetBuoyancyReactor \cdot (1 + NBM \cdot (nfloat - 1)) \tag{6.1}$$

$$MframeReactor_{dryMass} = BaselineMframeReactor \cdot (1 + FNM \cdot (nfloat - 1)) \cdot (1 + FSM \cdot (\frac{Areaxy}{AreaxyMin} - 1)) \tag{6.2}$$

$$Msubsystem_{dryMass} = BaselineMsubsystem \cdot (1 + SM \cdot (nfloat - 1)) \tag{6.3}$$

A rule of thumb that relates the frame mass of the reactor and the ratio between the area covered by the reactor $Areaxy$ relative to the minimum area covered by the minimum float spacing $AreaxyMin$ has been used.
The buoyancy tanks have been designed to obtain the designed net buoyancy of the reactor. In particular the following relationship has been used between the tank dry mass and the required net buoyancy for each tank:

$$Mtank_{dryMass}(kg) = 0.315 \cdot (Mtank_{Buoyancy} - Mtank_{dryMass}) + 8523 \tag{6.4}$$

The dry mass and the buoyancy mass of the tanks can be obtained considering a linear system of the previous equation and of the reactor net buoyancy balance expressed as following:

$$\begin{aligned} NetBuoyancyReactor = (&MframeReactor_{Buoyancy} + Msubsystem_{Buoyancy}) \\ -(&MframeReactor_{dryMass} + Msubsystem_{dryMass}) + Ntanks \\ &\cdot (Mtank_{Buoyancy} - Mtank_{dryMass}) \end{aligned} \tag{6.5}$$

The length of the tank is then obtained from the buoyancy mass of the tank considering a capsule shape with a predefined radius (R_{tank}):

$$L_{tank} = \frac{Mtank_{Buoyancy}}{\rho_w \pi R_{tank}^2} - \frac{4}{3} R_{tank} \tag{6.6}$$

The main simulation parameters are the same ones of the linear multi-float WaveSub optimisation (see Table 5.1) but the simulation time considered is increased to 1900s that includes the ramp time of 100s. The number of frequencies considered in Nemoh is 101 instead of 51. These improvements address the purpose to increase the accuracy in the calculation of the LCOE discussed in Section 6.2. Finally the same site location and number of sea states is used for the calculation of the energy production.

6.4.1 The linear 6 float design

The design of this multi-float concept is summarized in the following sketch of Figure 6.2. An important design feature is that the PTO and 4 of the mooring lines generate an angle of 45 degrees in the orthogonal views in the xz and yz planes. The other 4 mooring lines are

vertical and connect the attachment points placed on the corners of the reactor and on the seabed. The reactor has 4 tanks as the number of corners of the reactor to give the required buoyancy to the system.

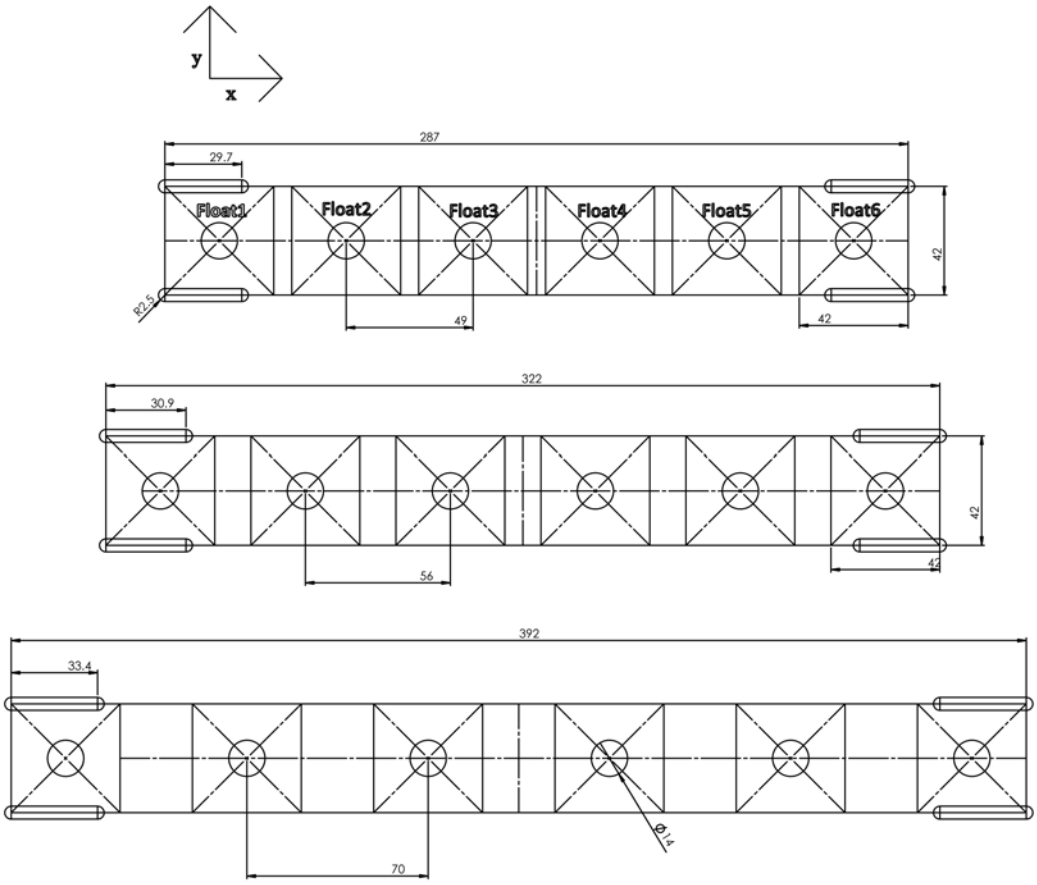

Figure 6.2: Schematic of the linear configuration for the 3 float spacing values.

6.4.2 The rectangular 6 float design

The design of this multi-float concept is summarized in the following sketch of Figure 6.3. The mooring lines and buoyancy tanks are set out in the same way and with the same purpose as the linear configuration.

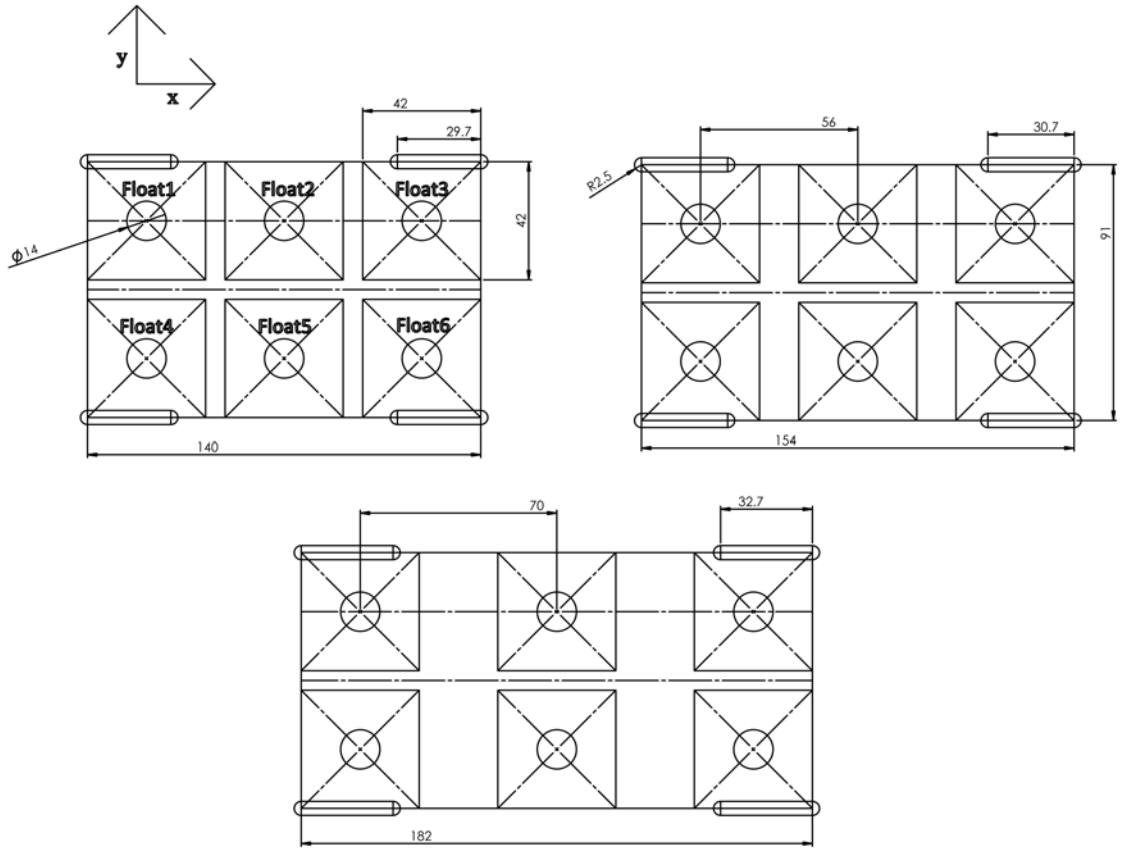

Figure 6.3: Schematic of the rectangular configuration for the 3 float spacing values.

6.4.3 The triangular 6 float design

The design of this multi-float concept is summarized in the following sketch of Figure 6.4. PTO lines generate an angle of 45 degrees in the orthogonal views in the xz and yz planes. 3 of the mooring lines generate an angle of 45 degrees in the planes described by the vertex of each triangle and the bisector of the corner angle. The reactor and seabed attachments of the mooring (R and S indexes of the next equation respectively) for the 2 corners of the back side of the device can be defined as following:

$$x_S - x_R = \frac{y_S - y_R}{\sqrt{3}} = \frac{z_R - z_S}{2} \tag{6.7}$$

The attachment points relative to the corner in the front of the device can be defined as

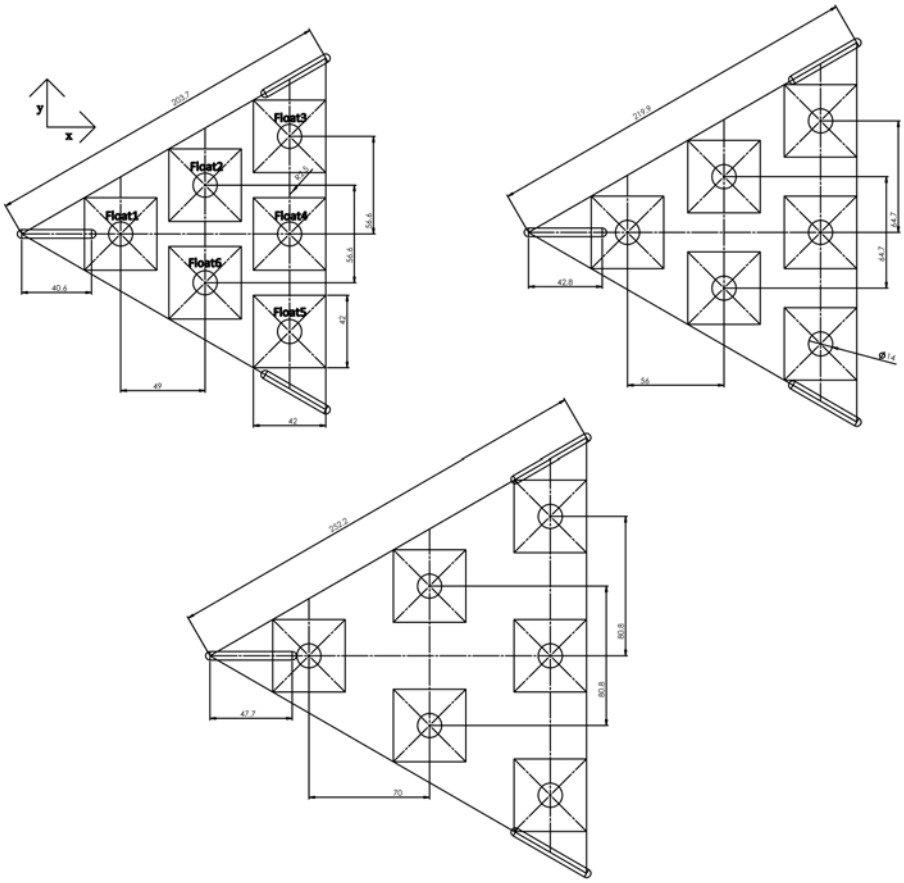

Figure 6.4: Schematic of the triangular configuration for the 3 float spacing values.

following:

$$\begin{cases} x_M - x_S = z_M - z_S \\ y_M = y_S = 0 \end{cases} \tag{6.8}$$

The other 3 mooring lines are vertical and connect the attachment points placed on the corners of the reactor and on the seabed.

The center of gravity of the reactor (defined as R in Figure 6.5) is uncertain because it depends on the position of the various components of the reactor. For simplicity, this has been chosen to be the point where the rotational moment due to the net buoyancy of the floats is 0. This condition gives the specific position of the reactor:

$$f = \frac{s}{3} \tag{6.9}$$

where f and s are defined in Figure 6.5. The definition of the vertical pre-load forces applied to the mooring attachment point in the front and to the 2 attachment points in the back of the device (T_1 and T_2 respectively) are also defined:

$$\begin{cases} T_1 = \frac{NetBuoyancyReactor}{1+\frac{a}{b}} \\ T_2 = \frac{NetBuoyancyReactor - T_1}{2} \\ T_{1l} = \frac{T_1}{2 \cdot sin(\pi/4)} \\ T_{1v} = \frac{T_1}{2} \\ T_{2l} = \frac{T_{1l}}{2sin(\pi/6)} \\ T_{2v} = T_2 - T_{2l} \cdot sin(\pi/4) \end{cases} \tag{6.10}$$

where $NetBuoyancyReactor$ is the total net buoyancy of the reactor and the indexes l and v represent the mooring line describing an angle and the vertical mooring line respectively. Finally the reactor has 3 tanks, as the number of corners of the reactor, to give the

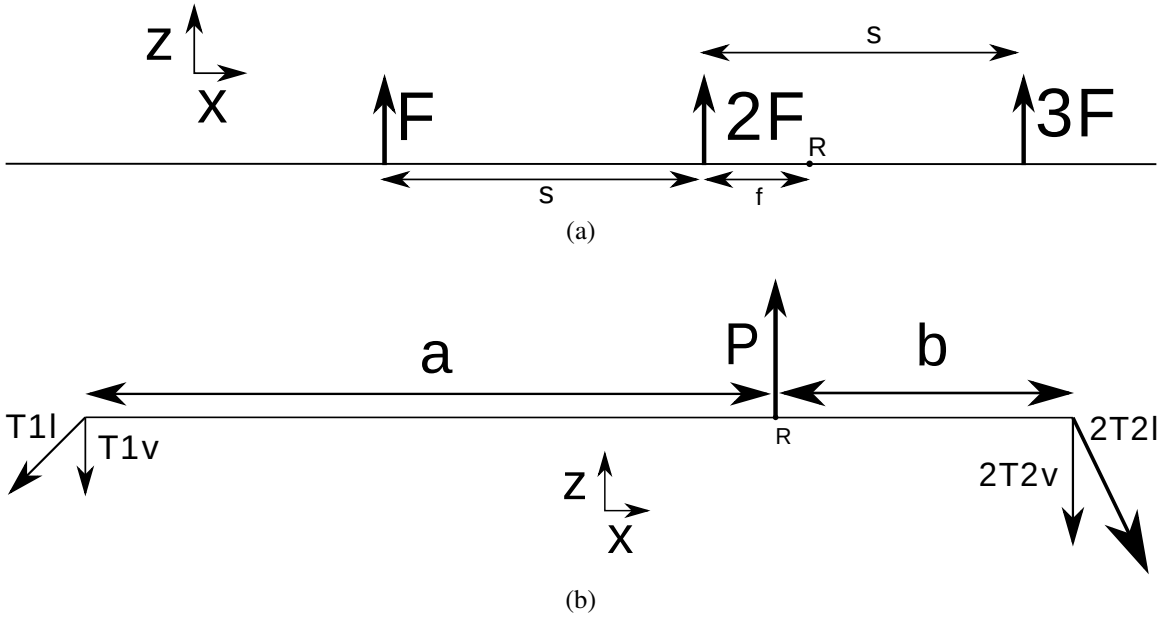

Figure 6.5: The sketch for the calculation of the forces on the mooring lines. The view is on the longitudinal plane xz. Figure (a) shows the net buoyancy forces due to the floats. Figure (b) shows the mooring pre-load forces due to the net buoyancy of the reactor. The P notation in Figure (b) represents the net buoyancy of the reactor.

required buoyancy to the system.

6.4.4 The circular 6 float design

The design of this multi-float concept is summarized in the following sketch of Figure 6.6. An important design feature is that the PTO lines generate an angle of 45 degrees in the vertical plane of the PTO lines. The attachment points of the PTO lines on the reactor are located along 2 circles as shown in Figure 6.6. The mooring attachment on the reactor are located in an imaginary inscribed square to the external circle and aligned to the x axis (see Figure 6.7). 4 of the mooring lines generate an angle of 45 degrees in the orthogonal views in the xz and yz planes while the other 4 mooring lines are vertical and connect the attachment points placed on the corners of the reactor and on the seabed. The reactor has 4 tanks as the number of corners of the reactor to give the required buoyancy to the system.

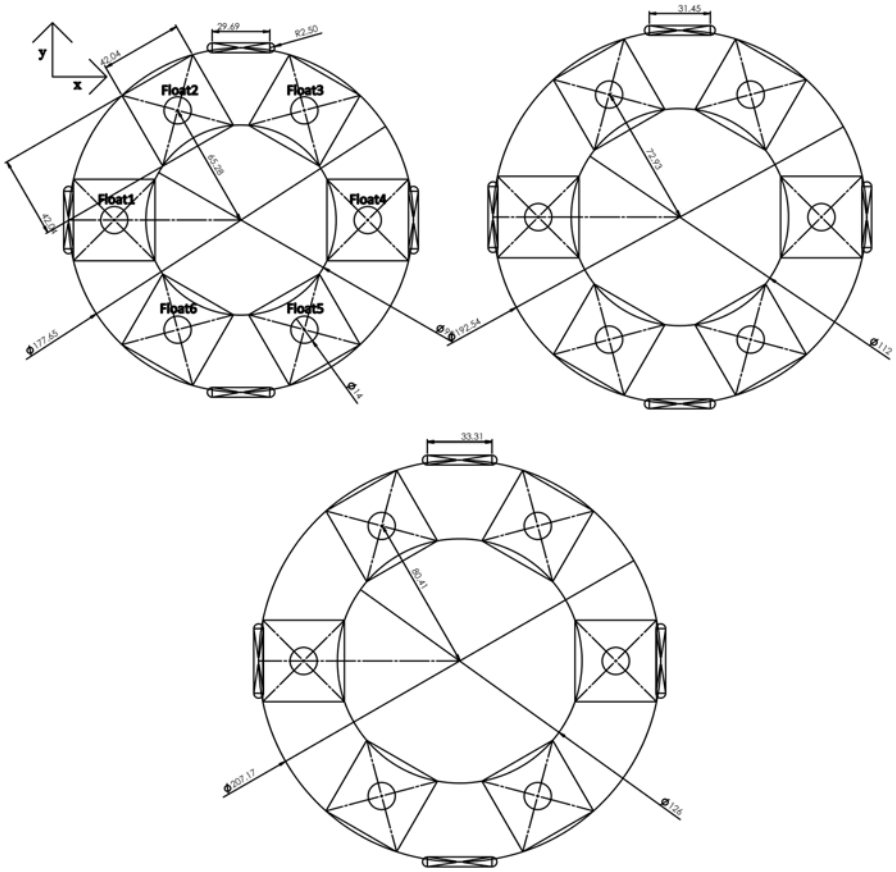

Figure 6.6: Schematic of the circular configuration for the 3 float spacing values.

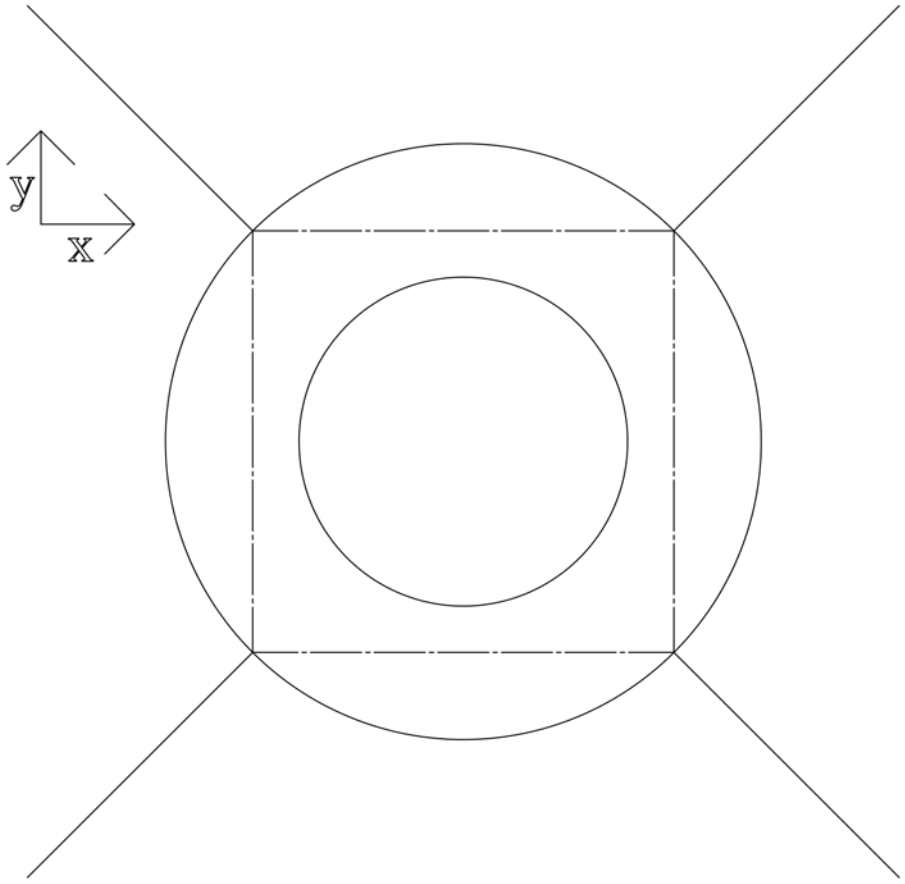

Figure 6.7: Sketch of the mooring attachment location.

6.5 Mesh sensitivity

The quality of the mesh is checked by considering the hydrodynamic independence of the lower float spacing of the various configurations. Then similar properties of the minimum and maximum size of the fine mesh elements have been used for the larger float spacing cases.

The ratio of number of panels between the different mesh for the floats is kept around 2 while for the reactor the ratio is more limited due to the thin tubes of the reactor frame (see Tables 6.3 and 6.4). A larger number of frequencies has been also tested (101 instead of 51) to check the increase of accuracy of the hydrodynamic coefficients. The simulation with 101 frequencies is labelled as FineNf.

Table 6.3: Mesh nodes and panels of the mesh files used for the Nemoh simulation for the reactor of the various configurations.

	Nodes	**Panels**
Linear-Coarse	3305	3376
Linear-Moderate	3967	4020
Linear-Fine	4760	4808
Rectangular-Coarse	2722	2792
Rectangular-Moderate	3350	3404
Rectangular-Fine	4134	4193
Triangular-Coarse	3917	3979
Triangular-Moderate	4491	4543
Triangular-Fine	5122	5184
Circular-Coarse	2338	2396
Circular-Moderate	4147	4266
Circular-Fine	5088	5208

Table 6.4: Mesh nodes and panels of the mesh files used for the Nemoh simulation for the float. The hydrodynamic coefficients for a larger number of frequencies (101 instead of 51) are shown as "FineNf".

	Nodes	**Panels**
Coarse	105	108
Moderate1	222	226
Moderate2	274	282
Fine	439	451
FineNf	439	451

The hydrodynamic coefficients of the float show generally a very good agreement between the different mesh sizes (see Figures 6.8, 6.9, 6.10 and 6.11). Figure 6.8g and Figure 6.8h show some discrepancies between the hydrodynamic coefficients of the different mesh. However, the overall behaviour with the frequency is very similar and the difference between them is very small (around 2%) and it could be related to numerical inaccuracies and not to the mesh. The most sensitive hydrodynamic coefficients are generally the surge, heave and pitch modes of motion because they will influence more significantly the energy production of the device. These main motion of the float is a consequence of the symmetry of the device with the main direction of the wave (see Section 3.1.2). Sway hydrodynamic coefficients will become more important for multi-directional waves but they will not as important as surge and heave ones because of the directional spread limited to the main direction. It is observed a good improvement in terms of convergence when the number of panels of the float changes from the moderate1 to the moderate2 mesh for the pitch excitation force of the float. Surge and heave excitation coefficients of the float agree generally very well between the different mesh size as well as the radiation damping and added mass of the float. Figure 6.9 j shows an example of excitation coefficient in the sway mode for the rectangular configuration. This mode of motion is expected to be more significant than the linear configuration because of the hydrodynamic interactions with the nearer float with the same x position. However it is still around 20 times smaller than the surge and heave excitation coefficients.

The hydrodynamic coefficients of the reactor show various number of peaks (For example in Figure 6.8 c). This behaviour could be explained by the resonance of the reactor for various wave frequencies due to the presence of the tanks and their separation distance. There is a good agreement for the number of peaks of the excitation force between the 51 and 101 number of frequencies simulation cases especially for the rectangular configuration. However there is some small disagreement in the heave radiation damping and added mass.

Finally the hydrodynamic coefficients from the finer mesh accounting 101 frequencies are the ones that will be used for the optimisation because of their more accuracy.

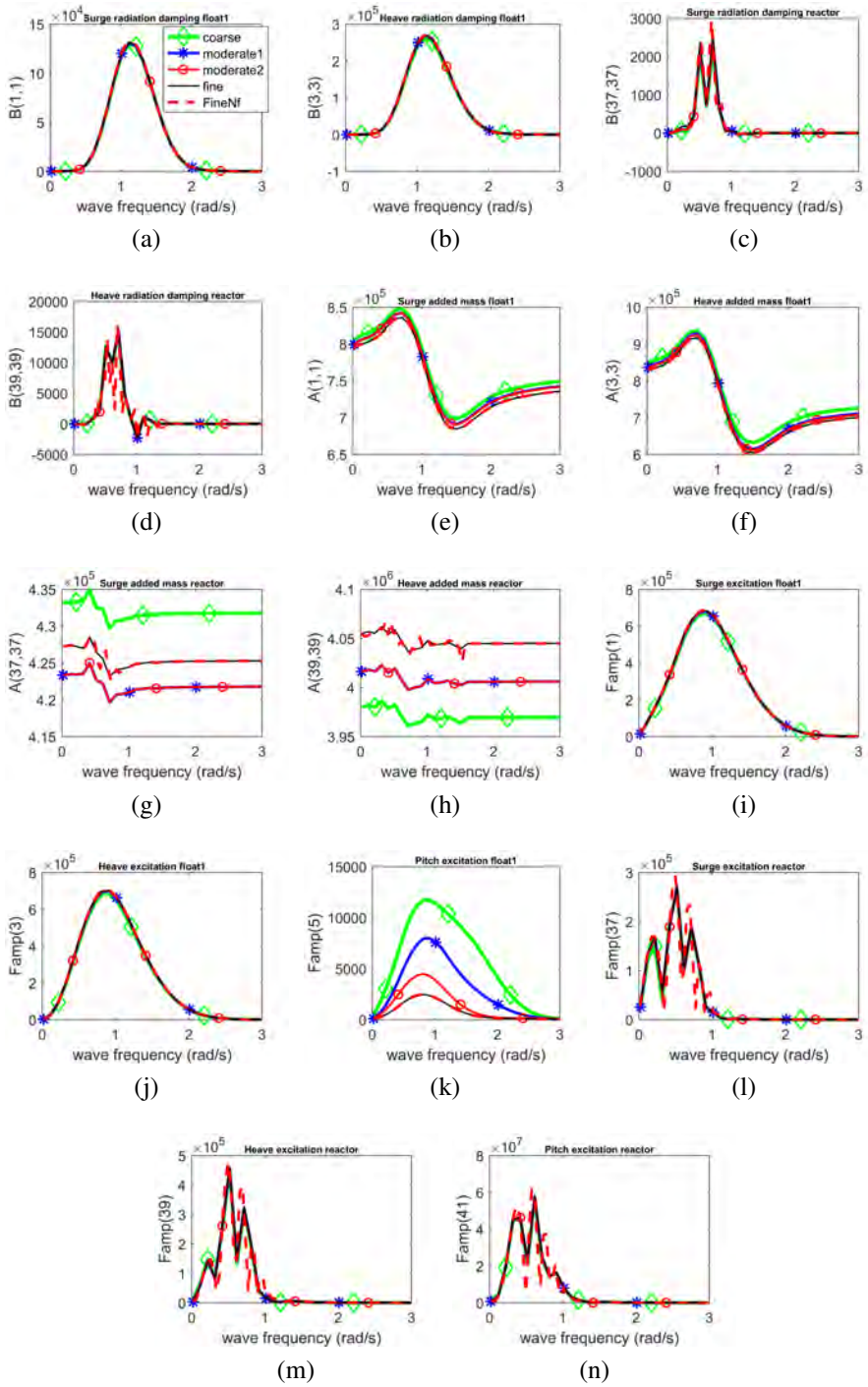

Figure 6.8: Mesh hydrodynamic convergence relative to the linear 6 float configuration. The float refers to the float1 of the schematic of the linear multi-float design shown in Figure 6.2.

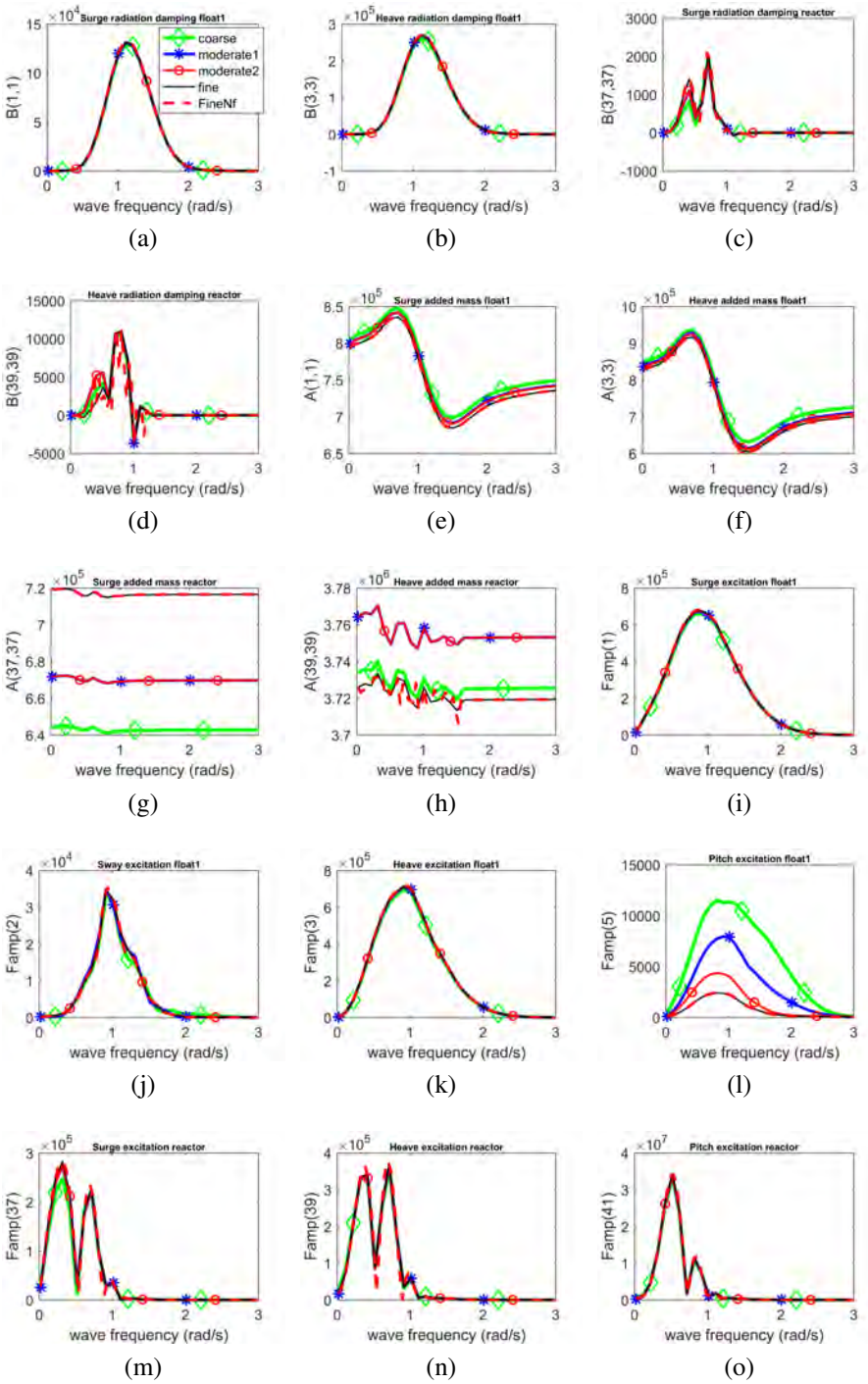

Figure 6.9: Mesh hydrodynamic convergence relative to the rectangular 6 float configuration. The float refers to the float1 of the schematic of the rectangular multi-float design shown in Figure 6.3.

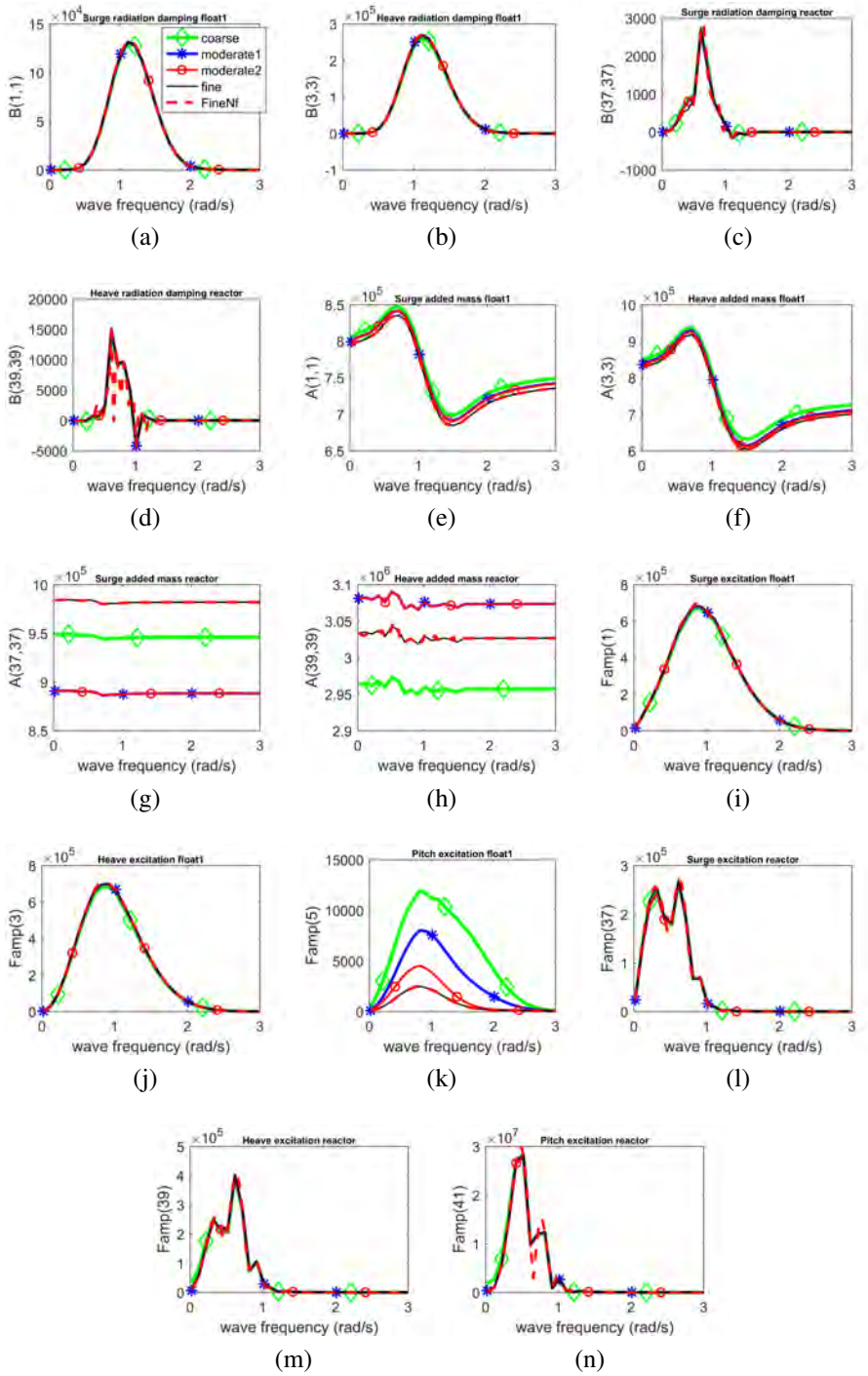

Figure 6.10: Mesh hydrodynamic convergence relative to the triangular 6 float configuration. The float refers to the float1 of the schematic of the triangular multi-float design shown in Figure 6.4.

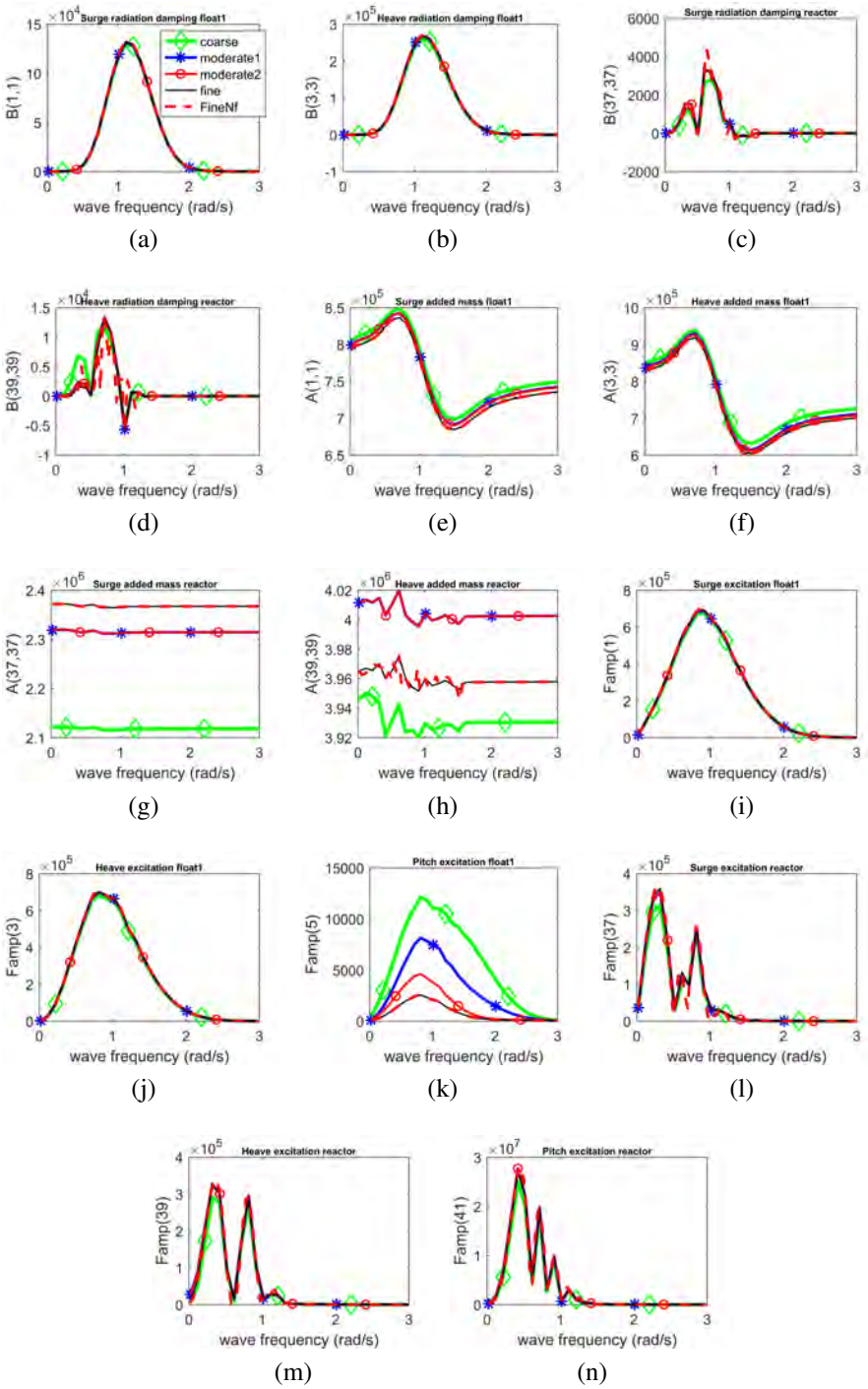

Figure 6.11: Mesh hydrodynamic convergence relative to the circular 6 float configuration. The float refers to the float1 of the schematic of the circular multi-float design shown in Figure 6.6.

6.6 The investigation of different multi-float concepts

6.6.1 The linear 6 float design

The surface plot of the surrogate model of the main results dependent on the design parameters is shown in Figure 6.12. Red data points represent the simulations of the model that are used to build the surrogate model. Each generation of the genetic algorithm converges the simulations towards the optimum. The results are mainly the LCOE, the average total power, the average power for each of the 3 sea states simulated, the rated power and the capacity factor. The average total power is calculated based on the rated power, the occurrence and the power matrix. The average power for each sea state is calculated from each wave spectra described in Section 5.6. Results show that there is generally a single optimum. The LCOE plot shows a very good convergence to the minimum found. The optimisation of the stiffness and damping of the PTO could bring to possible LCOE reductions of around 50% compared to the maximum value obtained. The genetic algorithm supported by the Kriging surrogate model has determined this fast convergence. The optimum given by the LCOE and the average power show a very similar optimum mainly because the stiffness and the damping of the PTO are not influencing the cost of the device. The optimum LCOE is influenced by the rated power and the capacity factor and it will need high values of both. A high rated power reduce the structure cost due to a lower number of devices while a high capacity factor increases the average power produced for that specific rated power. The power produced by the sea states shows that the optimum moves towards low stiffness for larger wave periods. The optimal design parameters are similar to the values of the second sea state.

The float spacing does not have a clear influence on the energy produced by the device (see Figure 6.13). In particular, the single wave direction and the multi-directional waves have an opposite effect on the total energy. The capacity factor is generally slightly increased with an increase of the float spacing. CAPEX and LCOE tends to increase with a larger float spacing for both the wave cases. The LCOE increases with the float spacing because of the increase of the CAPEX.

The optimal results are shown in Table 6.5. Optimal damping tends to decrease with an increase of the float spacing for both the single direction and multi-directional case. Optimal stiffness shows a slight decrease with the float spacing for the single direction case while it is less predictable for the multi-directional case. The main CAPEX component is the structure cost that is around 3 or more times each of the other ones. The OPEX and

the decommissioning costs are instead quite negligible compared to the CAPEX. They are each about 3% of the CAPEX. NRMSE and the MAX error are shown in Table 6.5 and they are calculated considering the predictability of the surrogate model, that is built on the first 4 generations, on the last generation. The NRMSE of the surrogate model shows a reasonable predictive capabilities as defined in [194] for most of the cases.
Figure 6.14 and Table 6.6 show the total wave amplitude generated by the perturbed wave field and the power produced by each float respectively for a regular wave with wave height of 3m and wave period of 10s. There is generally a decrease of the power produced from float1 to float6 due to the shadowing effects of the previous floats facing the incoming wave. In fact, each float, if interaction effects between the floats are not considered in a first approximation, generates a parabolic wave amplitude field (see Section 3.4) and so each float will be in the negative increase of the wave field generated by the previous float. A larger power produced by a float is also associated with a larger reduction of the total amplitude before and after the float as it is possible to notice for example comparing float1 and float5 of Figure 6.14.

Table 6.5: The optimal PTO parameters and main results of a linear multi-float configuration.

	SD: FS1	**SD: FS2**	**SD:FS3**	**MD: FS1**	**MD: FS2**	**MD: FS3**
kPTO (kN/m)	436.36	433.33	429.52	432.28	436.08	426.71
cPTO (kNs/m)	213.04	195.42	190.24	203.00	196.66	191.75
RatedP (MW)	6.41	6.42	6.55	6.85	6.69	6.63
Energy (MWh)	17748	17952	18297	18637	18551	18436
Ndevices	78	78	76	73	75	75
CF	0.316	0.319	0.319	0.310	0.317	0.318
CAPEX (-)	0.963	0.983	1.000	0.911	0.952	0.989
CAPEX-Structure (-)	0.398	0.418	0.446	0.373	0.402	0.440
CAPEX-PTO (-)	0.115	0.115	0.113	0.109	0.112	0.111
CAPEX-Mooring (-)	0.124	0.124	0.120	0.116	0.119	0.119
CAPEX-Anchors (-)	0.072	0.072	0.070	0.067	0.069	0.069
CAPEX-BoS (-)	0.135	0.135	0.134	0.135	0.135	0.134
CAPEX-Installation (-)	0.119	0.119	0.116	0.112	0.115	0.115
OPEX (-)	0.028	0.029	0.029	0.026	0.028	0.029
Decommissioning (-)	0.026	0.026	0.025	0.024	0.025	0.025
LCOE (-)	0.968	0.977	1	0.932	0.951	0.994
NRMSE (-)	0.06	0.19	0.35	0.07	0.10	0.01
MAX (£/MWh)	0.08	0.19	0.79	0.08	0.13	0.03

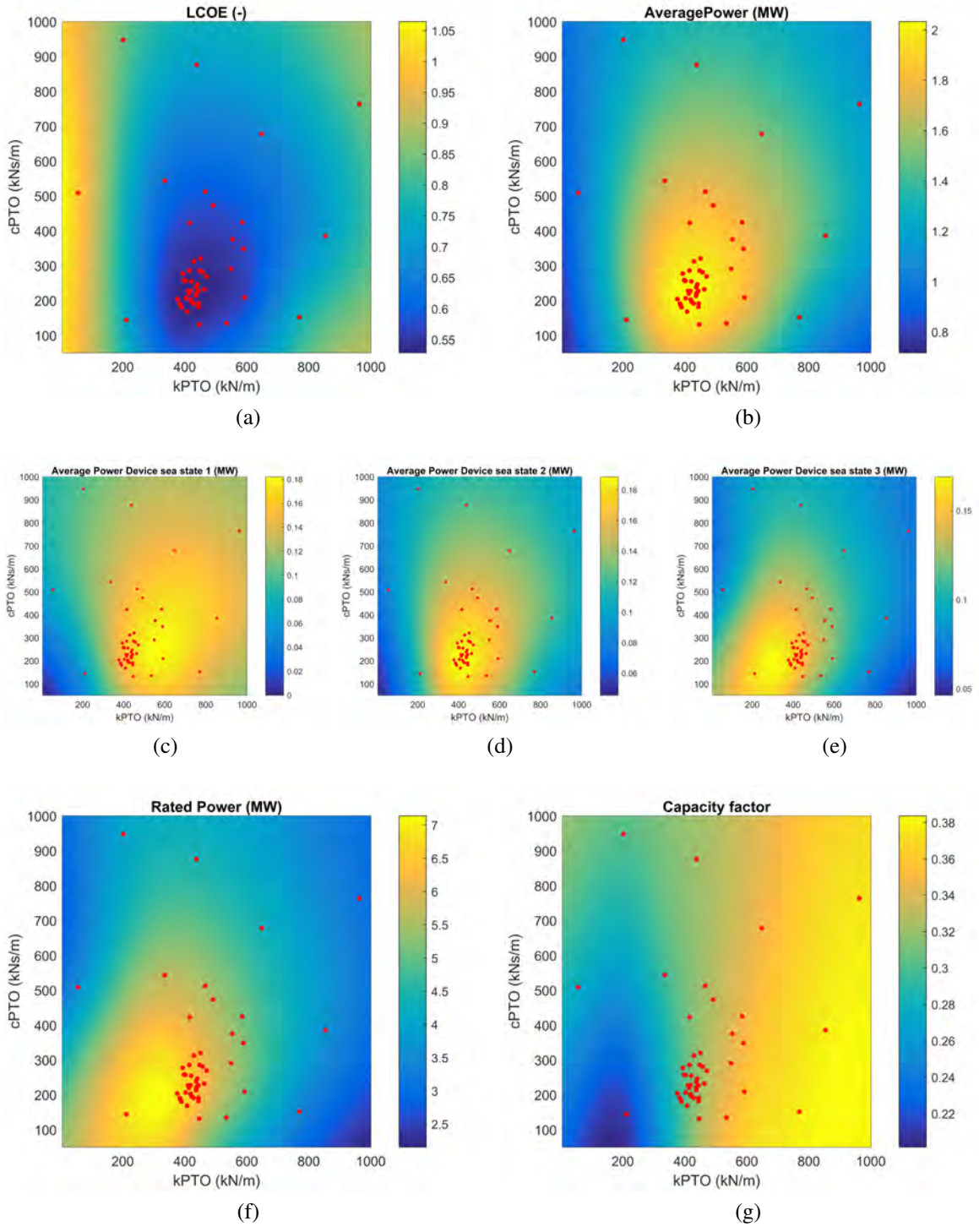

Figure 6.12: Kriging surrogate model of the main results of the linear multi-float configuration for the lowest float spacing considered. Red data points represent the simulation of the numerical model.

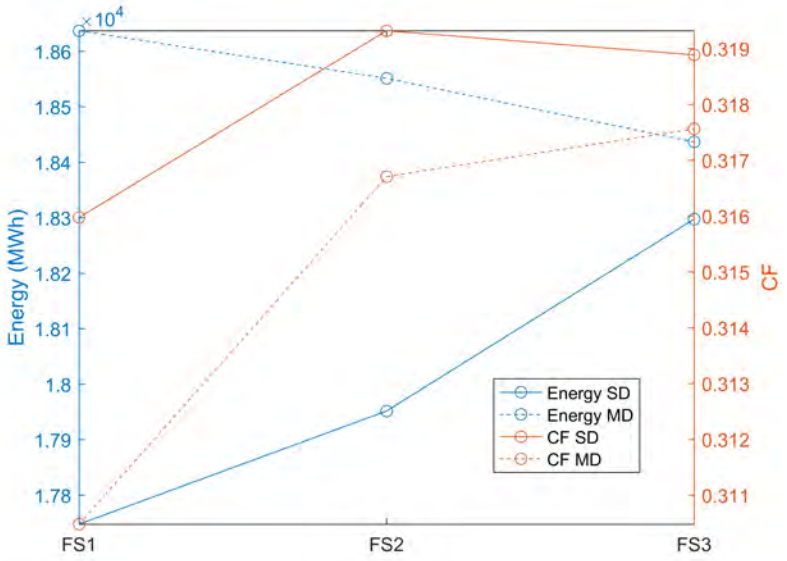

(a)

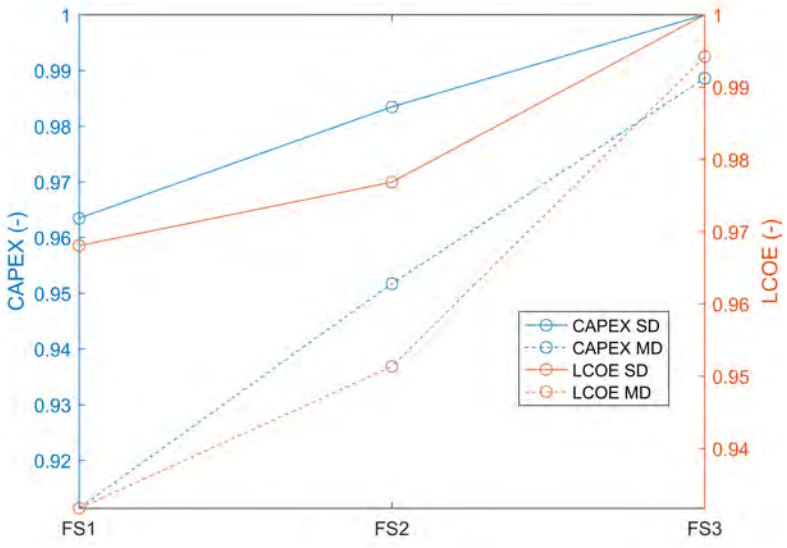

(b)

Figure 6.13: Comparison of the main results of a linear multi-float configuration between 3 different float spacing cases and between the single direction (SD) and the multi-directional (MD) cases.

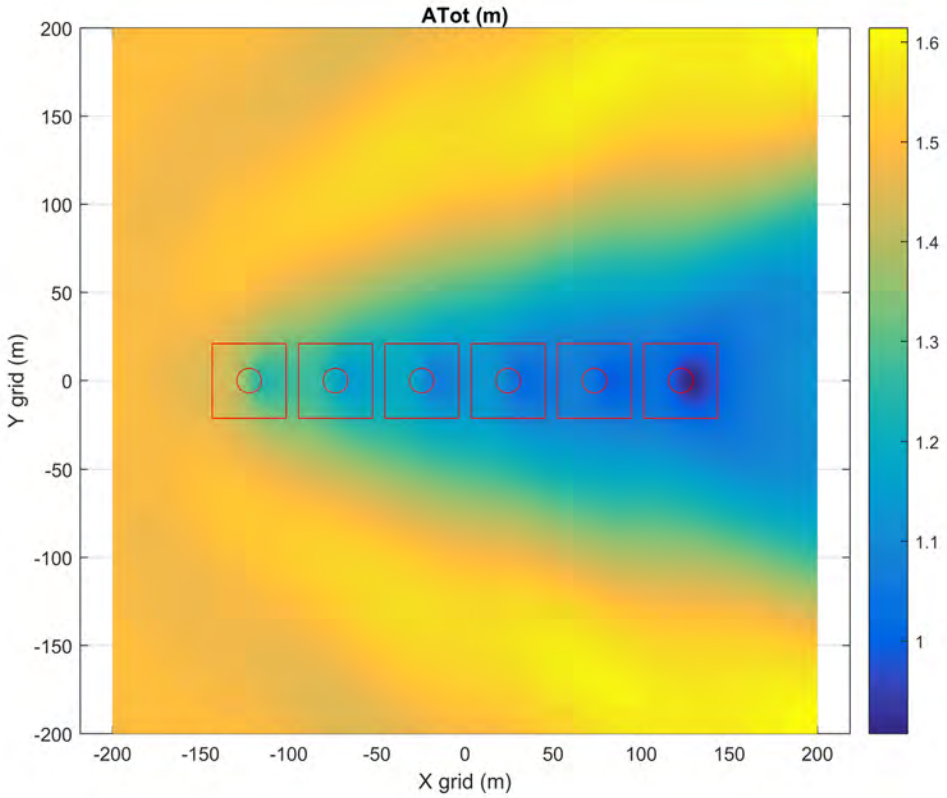

Figure 6.14: Total wave amplitude generated by the lowest float spacing of the linear configuration for a regular wave with H=3m and T=10s.

Table 6.6: Power produced (kW) by the lowest float spacing of the linear configuration for a regular wave with H=3m and T=10s.

Float1	**Float2**	**Float3**	**Float4**	**Float5**	**Float6**	**Total**
948	905	931	810	569	654	4818

6.6.2 The rectangular 6 float design

The energy produced for the single direction case decreases with the float spacing while it is oscillatory for the multi-directional case (see Figure 6.15). The single direction case shows an increase of the capacity factor with the float spacing while there is an opposite trend for the multi-directional case. CAPEX and LCOE are generally increasing with the float spacing but the second float spacing for the multi-directional case demonstrates a reduction of both of them.

Optimal stiffness and damping show generally a decrease with the float spacing (see Table 6.7). However the damping coefficient increases for the largest float spacing and the single direction case. Similar comments of the linear configuration regarding the cost components and the NRMSE can be made.

Figure 6.16 and Table 6.8 show the total wave amplitude generated by the perturbed wave field and the power produced by each float respectively for a regular wave with wave height of 3m and wave period of 10s. There is a similar power produced between floats 1 and 6, floats 2 and 5 and floats 3 and 4 because of the symmetrical position relative to the x axis. Floats 1 and 6 are the first floats to face the incoming wave and they are producing the largest power. Hydrodynamic interaction between the floats determine an increase of the power produced in the middle row (floats 3 and 4).

Table 6.7: The optimal PTO parameters and main results of a rectangular multi-float configuration.

	SD: FS1	**SD: FS2**	**SD:FS3**	**MD: FS1**	**MD: FS2**	**MD: FS3**
kPTO (kN/m)	469.63	460.89	453.39	580.99	476.75	436.77
cPTO (kNs/m)	235.57	219.56	252.61	311.77	216.75	195.54
RatedP (MW)	7.50	7.36	6.92	7.10	7.35	7.27
Energy (MWh)	19474	19280	18237	19227	19704	19303
Ndevices	67	68	72	70	68	69
CF	0.296	0.299	0.301	0.309	0.306	0.303
CAPEX (-)	0.899	0.924	1.000	0.930	0.924	0.966
CAPEX-Structure (-)	0.362	0.382	0.437	0.378	0.382	0.418
CAPEX-PTO (-)	0.107	0.109	0.114	0.111	0.109	0.110
CAPEX-Mooring (-)	0.112	0.114	0.121	0.117	0.114	0.116
CAPEX-Anchors (-)	0.065	0.066	0.070	0.068	0.066	0.067
CAPEX-BoS (-)	0.143	0.143	0.142	0.142	0.142	0.143
CAPEX-Installation (-)	0.109	0.110	0.117	0.113	0.110	0.112
OPEX (-)	0.026	0.027	0.029	0.027	0.027	0.028
Decommissioning (-)	0.024	0.024	0.025	0.025	0.024	0.024
LCOE (-)	0.904	0.926	1	0.907	0.905	0.952
NRMSE (-)	0.08	0.03	0.35	0.30	0.01	0.08
MAX (£/MWh)	0.11	0.06	1.77	0.71	0.02	0.10

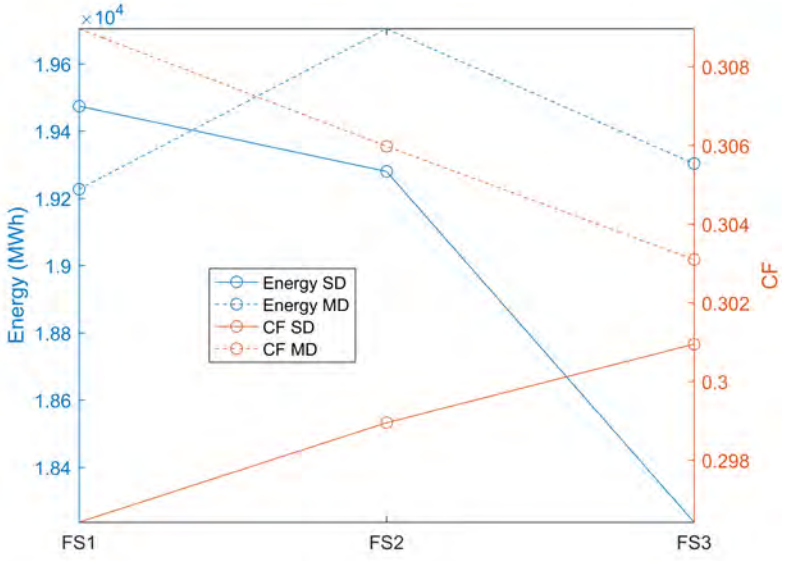

(a)

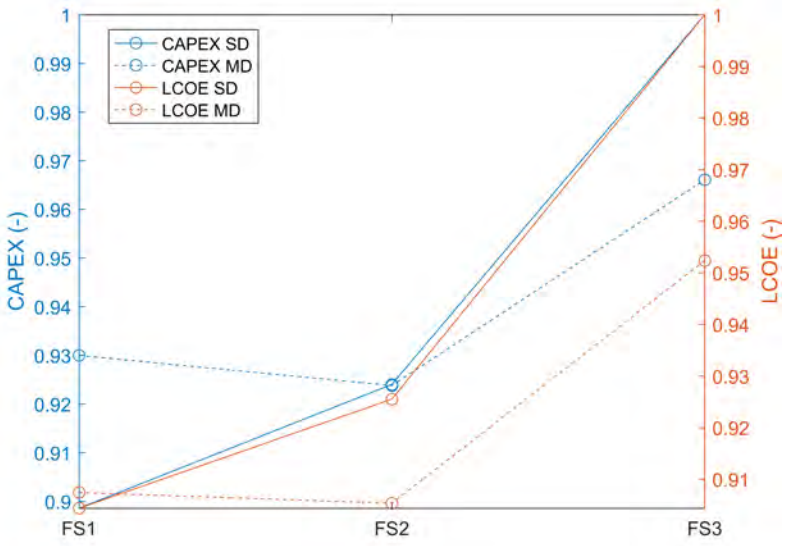

(b)

Figure 6.15: Comparison of the main results of a rectangular multi-float configuration between 3 different float spacing cases and between the single direction (SD) and the multi-directional (MD) cases.

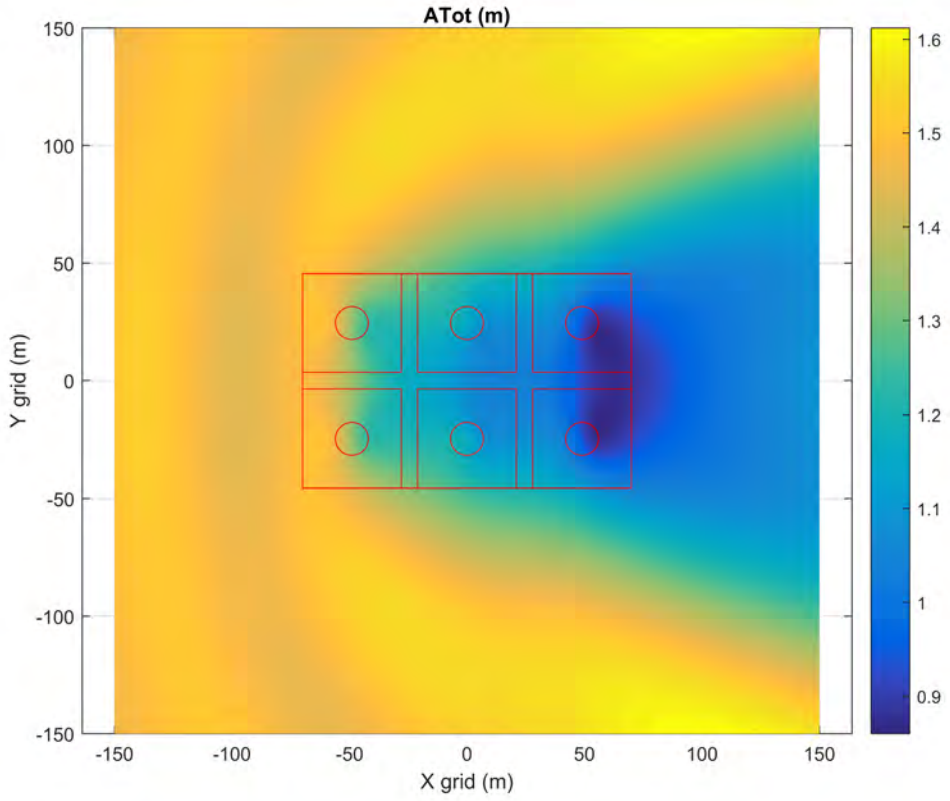

Figure 6.16: Total wave amplitude generated by the lowest float spacing of the rectangular configuration for a regular wave with H=3m and T=10s.

Table 6.8: Power produced (kW) by the lowest float spacing of the rectangular configuration for a regular wave with H=3m and T=10s.

Float1	**Float2**	**Float3**	**Float4**	**Float5**	**Float6**	**Total**
995	847	910	910	847	994	5502

6.6.3 The triangular 6 float design

The energy produced increases with the float spacing while the capacity factor decreases for both the wave configurations (see Figure 6.17). CAPEX and LCOE both increase with the float spacing.

Optimal stiffness and damping show generally a decrease with the float spacing (see Table 6.9). However the damping coefficient increases for the largest float spacing and the multi-directional case. Similar comments of the linear configuration regarding the cost components and the NRMSE can be made.

Figure 6.18 and Table 6.10 show the total wave amplitude generated by the perturbed wave field and the power produced by each float respectively for a regular wave with wave height of 3m and wave period of 10s. There is a similar power produced between floats 2 and 6 and between floats 3 and 5 because of the symmetrical position relative to the x axis. Float1 produce around the double amount of power compared to each other float and it is the main influence of the wave field of the total amplitude. The floats in the back of float1 are not in the positive increase of the parabolic shape created by the float1 (see Section 3.4 for reference to the parabolic wave field) and so they produce less energy (shadowing effect).

Table 6.9: The optimal PTO parameters and main results of a triangular multi-float configuration.

	SD: FS1	**SD: FS2**	**SD:FS3**	**MD: FS1**	**MD: FS2**	**MD: FS3**
kPTO (kN/m)	482.09	466.45	433.53	494.28	466.70	450.90
cPTO **(kNs/m)**	203.77	180.61	166.34	217.98	182.55	187.19
RatedP (MW)	6.30	6.46	6.71	6.21	6.43	6.53
Energy (MWh)	18103	18482	18666	18217	18598	18779
Ndevices	79	77	74	80	78	77
CF	0.328	0.327	0.317	0.335	0.330	0.328
CAPEX (-)	0.931	0.938	0.965	0.941	0.950	1.000
CAPEX-Structure (-)	0.409	0.426	0.467	0.414	0.431	0.486
CAPEX-PTO (-)	0.119	0.116	0.112	0.120	0.118	0.116
CAPEX-Mooring (-)	0.088	0.085	0.082	0.089	0.087	0.085
CAPEX-Anchors (-)	0.056	0.054	0.052	0.056	0.055	0.054
CAPEX-BoS (-)	0.136	0.136	0.136	0.136	0.137	0.138
CAPEX-Installation (-)	0.123	0.120	0.115	0.125	0.122	0.120
OPEX (-)	0.027	0.027	0.028	0.027	0.028	0.029
Decommissioning (-)	0.027	0.026	0.025	0.027	0.026	0.026
LCOE (-)	0.932	0.944	1	0.924	0.937	0.990
NRMSE (-)	0.15	0.09	0.09	0.14	0.02	0.02
MAX (£/MWh)	0.26	0.09	0.17	0.42	0.01	0.05

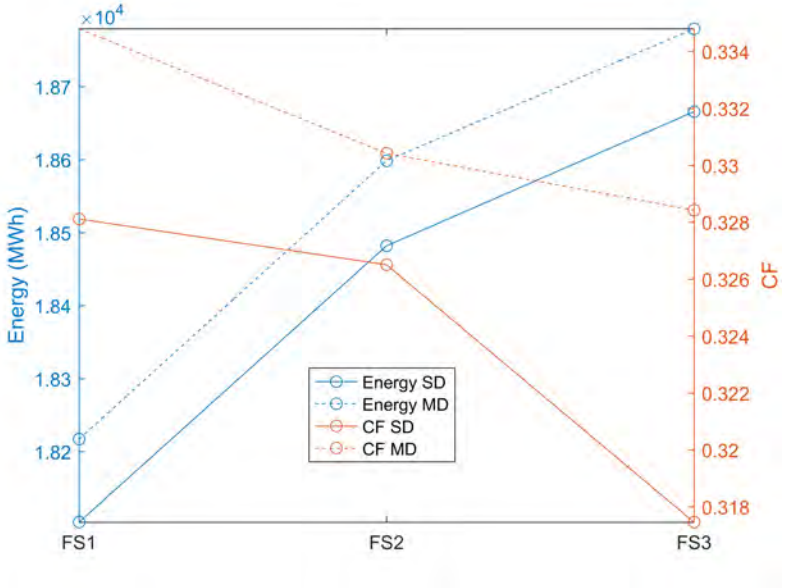

(a)

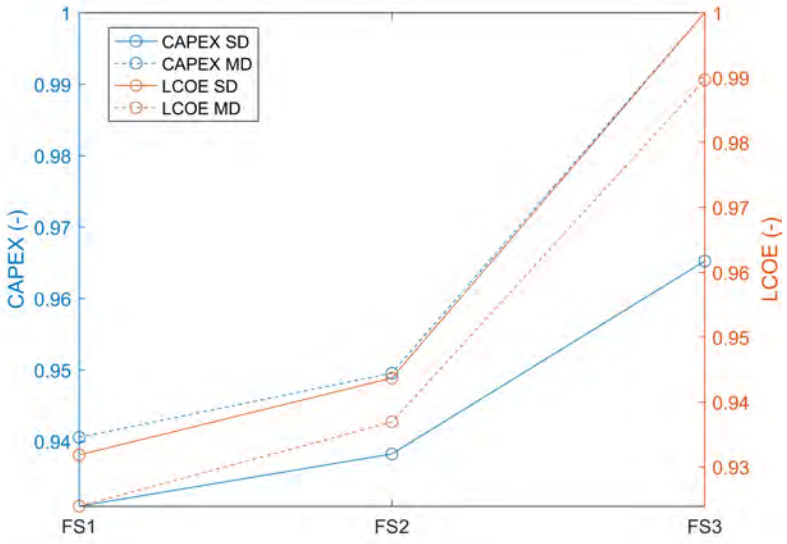

(b)

Figure 6.17: Comparison of the main results of a triangular multi-float configuration between 3 different float spacing cases and between the single direction (SD) and the multi-directional (MD) cases.

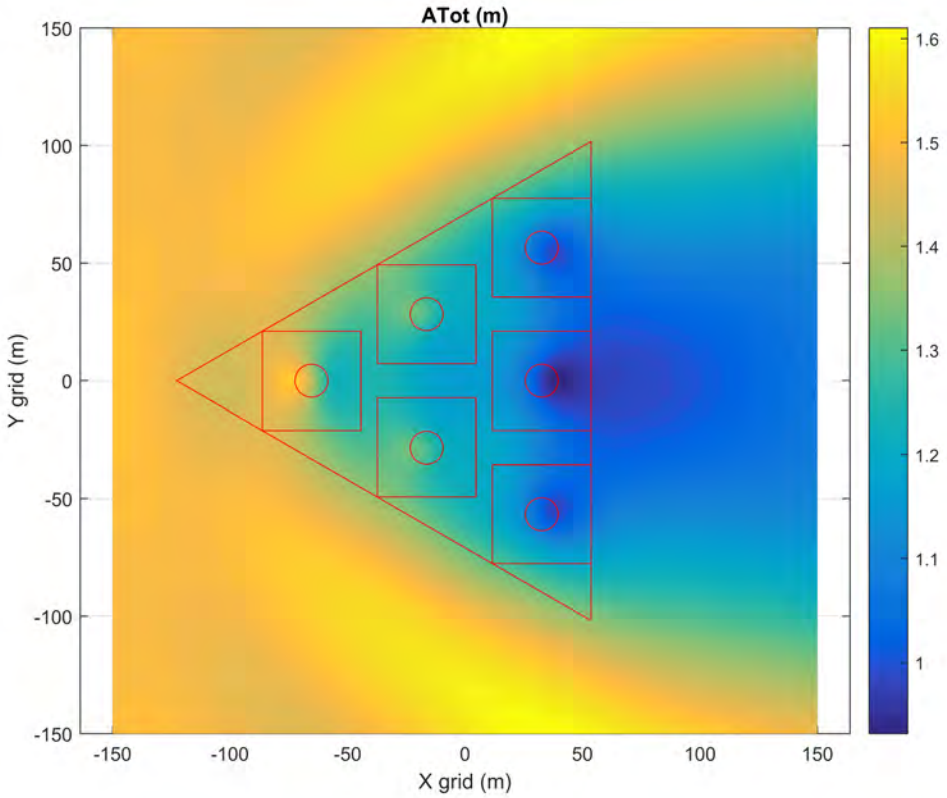

Figure 6.18: Total wave amplitude generated by the lowest float spacing of the triangular configuration for a regular wave with H=3m and T=10s.

Table 6.10: Power produced (kW) by the lowest float spacing of the triangular configuration for a regular wave with H=3m and T=10s.

Float1	**Float2**	**Float3**	**Float4**	**Float5**	**Float6**	**Total**
1663	894	785	735	790	891	5757

6.6.4 The circular 6 float design

The energy produced decreases with the float spacing while the capacity factor increases for the single direction case while it is oscillatory for the multi-directional case (see Figure 6.19). CAPEX and LCOE both increase with the float spacing.
Optimal stiffness and damping show a decrease from float spacing 1 to float spacing 2 (see Table 6.11). There is instead generally a slight increase of the design parameters between float spacing 2 and 3. Similar comments of the linear configuration regarding the cost components and the NRMSE can be made. Figure 6.18 and Table 6.10 show the total wave amplitude generated by the perturbed wave field and the power produced by each float respectively for a regular wave with wave height of 3m and wave period of 10s. There is a similar power produced between floats 2 and 6 and between floats 3 and 5 because of the symmetrical position relative to the x axis. Float2 and float6 are in the parabolic shape of the total amplitude created by the float1 (see Section 3.4 for reference to the parabolic wave field) and so they produce more power then the others. Floats 3 and 5 are not at the intersection of any parabolic shape and so their power is less than the other ones (shadowing effect from float 2 and 6). Finally float4 is at the intersection of the parabolic increases of float 3 and 5 and its power is slightly larger than them despite the reduction of the total amplitude reaching it.

Table 6.11: The optimal PTO parameters and main results of a circular multi-float configuration.

	SD: FS1	**SD: FS2**	**SD:FS3**	**MD: FS1**	**MD: FS2**	**MD: FS3**
kPTO (kN/m)	461.16	451.69	450.02	490.13	447.23	464.41
cPTO (kNs/m)	184.70	170.16	182.26	194.27	174.45	176.12
RatedP (MW)	7.51	7.40	7.31	7.25	7.28	6.94
Energy (MWh)	20116	19950	19768	20044	19731	19273
Ndevices	67	68	68	69	69	72
CF	0.306	0.308	0.309	0.316	0.310	0.317
CAPEX (-)	0.890	0.927	0.952	0.911	0.938	1.000
CAPEX-Structure (-)	0.358	0.390	0.417	0.369	0.395	0.442
CAPEX-PTO (-)	0.106	0.108	0.107	0.109	0.109	0.113
CAPEX-Mooring (-)	0.111	0.113	0.113	0.114	0.114	0.119
CAPEX-Anchors (-)	0.065	0.066	0.066	0.067	0.067	0.069
CAPEX-BoS (-)	0.142	0.142	0.140	0.141	0.142	0.141
CAPEX-Installation (-)	0.107	0.109	0.109	0.111	0.111	0.115
OPEX (-)	0.026	0.027	0.028	0.026	0.027	0.029
Decommissioning (-)	0.023	0.024	0.024	0.024	0.024	0.025
LCOE (-)	0.916	0.948	0.983	0.914	0.956	1
NRMSE (-)	0.21	0.05	0.02	0.04	0.08	0.38
MAX (£/MWh)	0.63	0.058	0.02	0.06	0.13	0.59

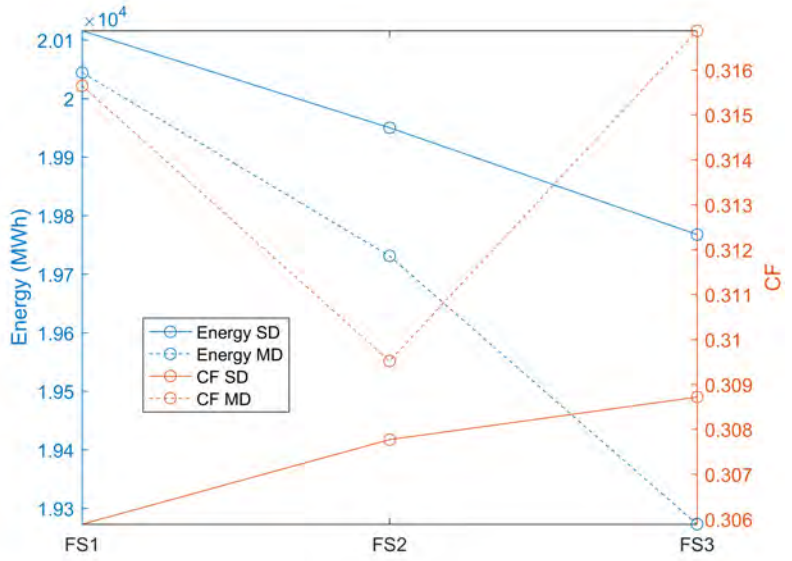

(a)

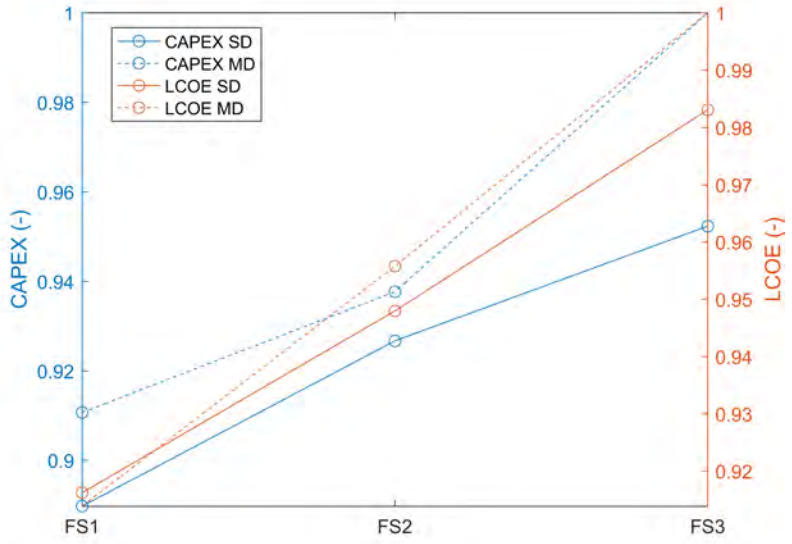

(b)

Figure 6.19: Comparison of the main results of a circular multi-float configuration between 3 different float spacing cases and between the single direction (SD) and the multi-directional (MD) cases.

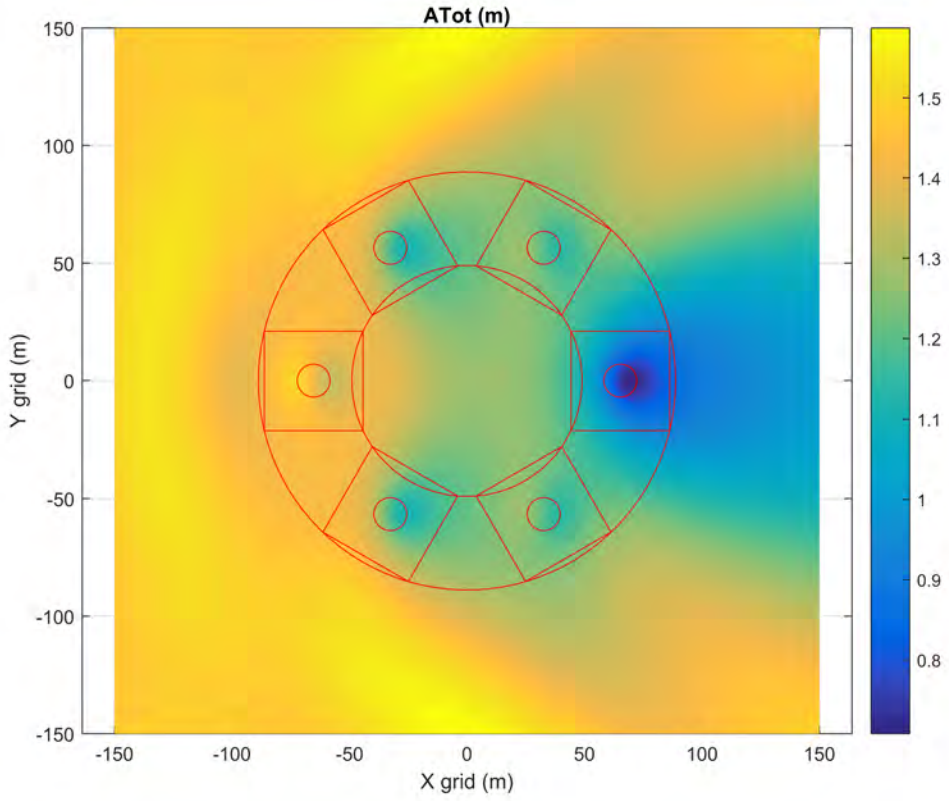

Figure 6.20: Total wave amplitude generated by the lowest float spacing of the circular configuration for a regular wave with H=3m and T=10s.

Table 6.12: Power produced (kW) by the lowest float spacing of the circular configuration for a regular wave with H=3m and T=10s.

Float1	**Float2**	**Float3**	**Float4**	**Float5**	**Float6**	**Total**
836	1173	856	893	858	1171	5786

6.6.5 Final comparison

Figure 6.21 shows the normalized LCOE relative to the maximum value against the rated power for the different multi-float configurations obtained by the single wave direction and multi-directional wave cases. The circular and the rectangular configurations show the largest rated power compared to the other ones (see Figure 6.21). The lowest LCOE is generally given by the lowest float spacing for each configuration. The linear configuration is outperformed by the other configurations. The lowest float spacing of the circular configuration shows the minimum LCOE (around 12% LCOE reduction compared to the worst configuration) followed by the lowest float spacing of the triangular configuration. The MAX error is generally very little. The float spacing 3 of the rectangular configuration for the single wave direction case shows the largest error but still reasonable for the comparison. The inclusion of multi-direction does not change the overall conclusion.
The optimum given by the surrogate model is generally slightly less than the optimum given by the genetic algorithm (see Figure 6.22). However it is outperformed by the genetic algorithm for the linear configuration and the single wave direction case. For this case the surrogate model will need more evaluation points for a more accurate surrogate model optimisation.

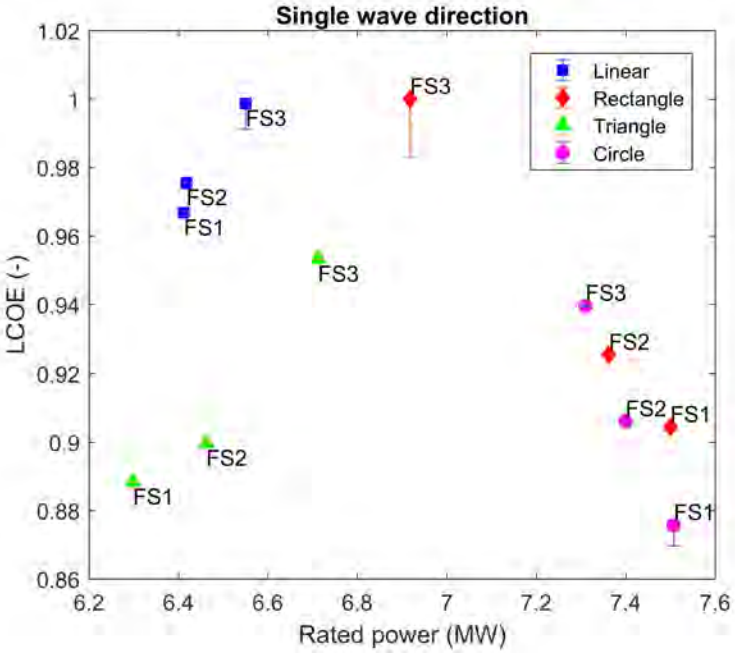

(a)

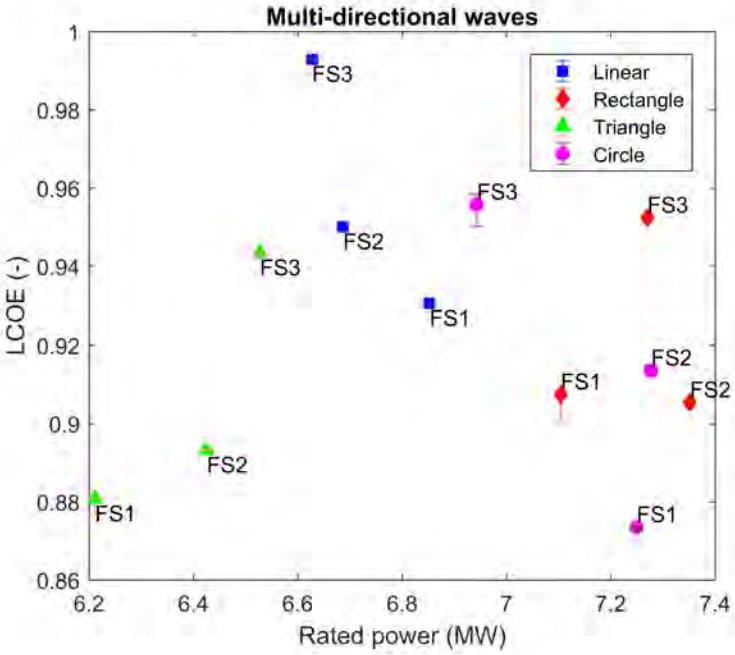

(b)

Figure 6.21: Comparison of the LCOE/power results between the different multi-float configurations and between the single direction (SD) and the multi-directional (MD) cases. The error bars refer to the MAX error (lower and upper bounds) of the surrogate model on the last generation.

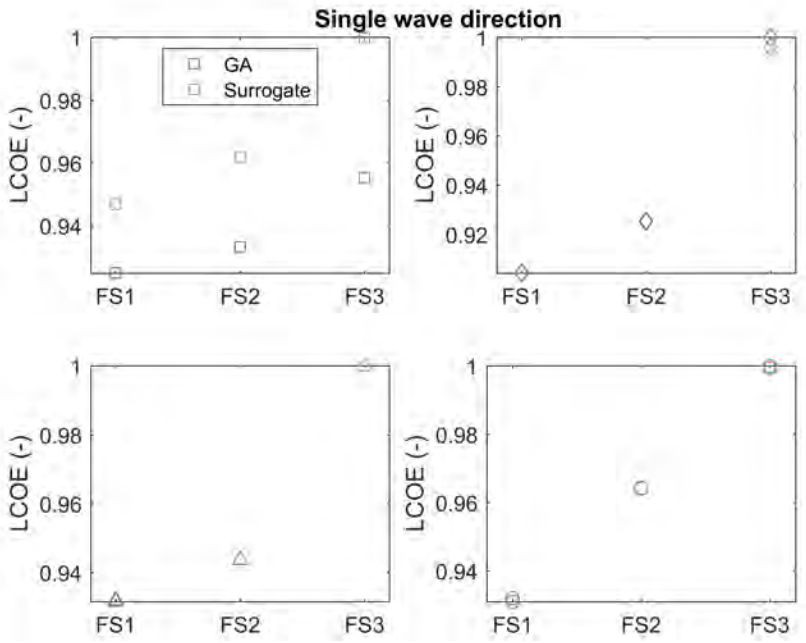

(a)

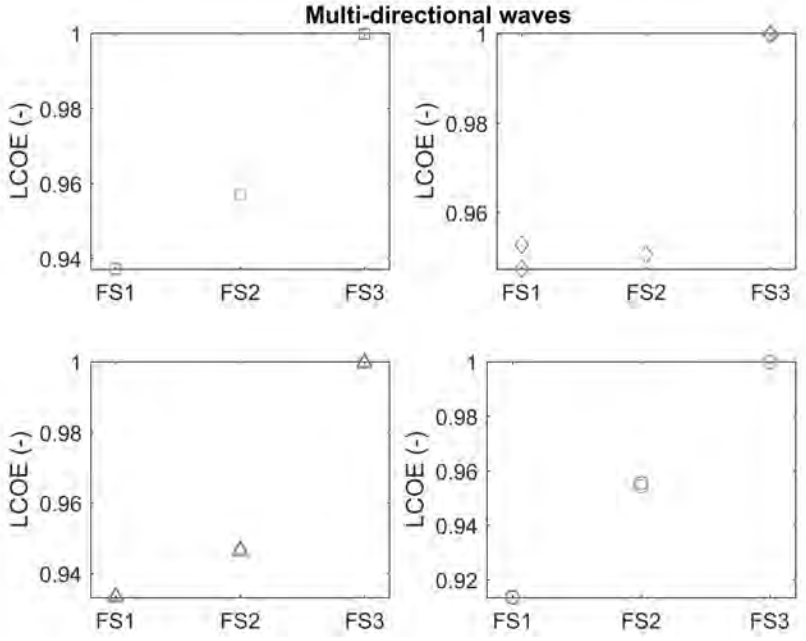

(b)

Figure 6.22: Comparison of the LCOE results between the GA (represented in blue) and the surrogate optimisation results (represented in red) and between the single direction (SD) and the multi-direction (MD) cases.

6.7 Sensitivity analysis of key factors influencing the LCOE

A similar sensitivity analysis of the cost model of section 5.9 has been undertaken here. Figure 6.23 shows the sensitivity analysis on the LCOE of CAPEX, OPEX and interest rate for the optimal 6 floats circular configuration.

Similar results to the previous cost model sensitivity are found; the LCOE is mainly dependent on the CAPEX and interest rate. However this time, the OPEX has a larger influence on the LCOE because the OPEX cost is more significant than before (2.9% of the CAPEX). The observations discussed in section 5.9 are also valid here.

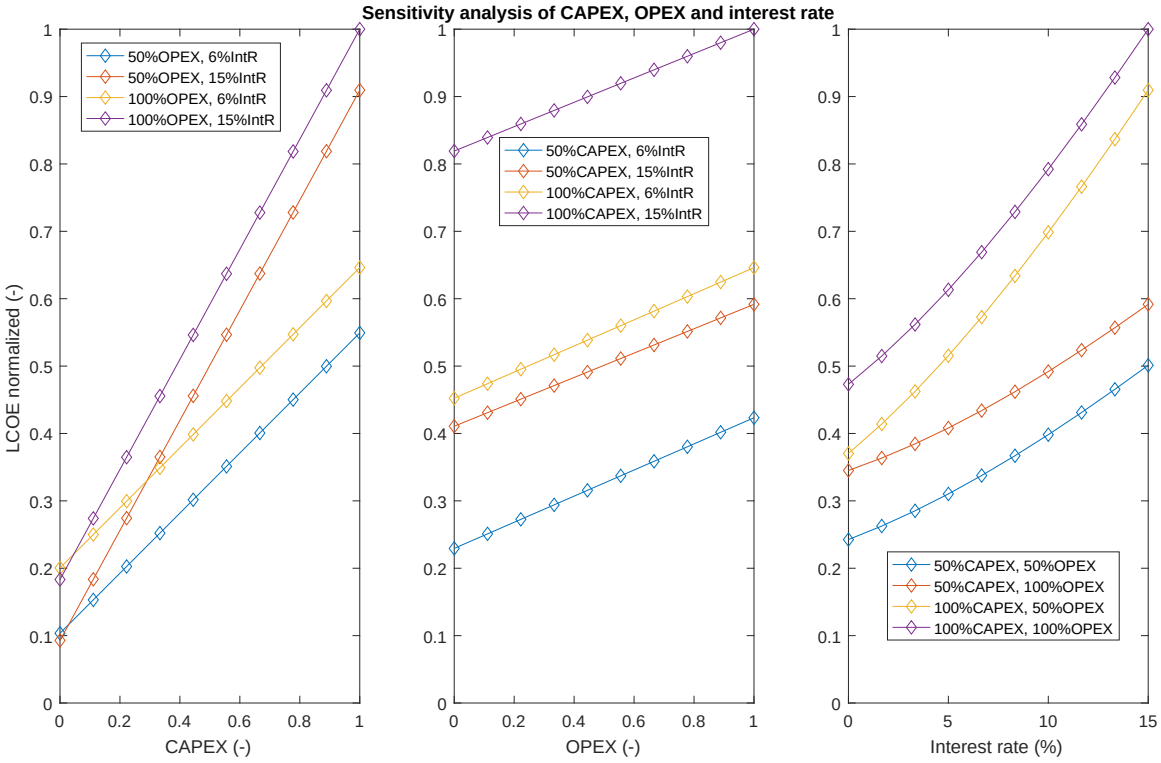

Figure 6.23: The influence of the key factors parameters influencing the LCOE for the optimal case found between the new design concepts.

6.8 Conclusions

Different layouts of multi-float configurations have been investigated in this chapter. The 6 float configuration is considered one of the most promising multi-float configuration as a result of chapter 5. The linear configuration investigated in chapter 5 is compared with the rectangular, triangular and circular configurations. The optimisation has been carried out for a single wave direction case but also for a more realistic multi-directional wave case. The comparison between the configurations has similar conclusion between the 2 different wave cases. The most appealing configuration result is the circular because it has the lowest LCOE and the highest rated power. Generally the lowest float spacing of each configuration has demonstrated to be the most interesting setting in terms of LCOE. The circular multi-float layout has been identified as the most promising configuration in terms of LCOE between the ones considered.

These results are very important in a commercial sense and they could give significant indications to MPS for the choice of the layout development of a multi-float configuration.

This research has a number of limitations. Some of them are related to the numerical model as discussed in chapter 3. There is uncertainty in the cost model related especially to the calculation of the CAPEX, OPEX and interest rate. It is expected that the future experience of MPS in the multi-float device production will increase accuracy in this calculation.

Future work will investigate more multi-float layouts. The inclusion of the hydrodynamic interaction between the devices in the wave farm is also still something to be considered. Finally, the PTO tuning of each single float is still topic of further research.

Chapter 7

Discussion

In this chapter, several different themes that have been developed throughout the whole thesis are reviewed and brought together. The strategy for this work is to automatically optimise for the lowest levelized cost of energy through use of a numerical approximation of the performance of a wave energy converter.

In this context, it is observed that, the numerical model chosen was able to satisfy the goals of this research project. In fact, the numerical model of a multi-float configuration of the WaveSub device was able to account for the hydrodynamic interactions between the multiple bodies of the device. More confidence in the numerical results has been achieved by comparison with experimental results.

The design of a single float WaveSub has been obtained from MPS. Multi-float configurations have been optimised considering the main design parameters influencing the energy produced from the device such as the float spacing, float reactor separation and PTO parameters. The design of a multi-float configuration is, however, limited to energy production purposes while a careful study of the loads acting on the WEC is not considered. A load analysis will be considered in a further design stage.

An appropriate numerical model has been investigated at the beginning of this work. The methodology is based on a BEM software (Nemoh) for the calculation of the hydrodynamic forces and on a time domain model for the dynamic system simulation that considers constraints, PTO and mooring forces. The BEM software considers a linear potential flow with different assumptions such as an inviscid, irrotational and incompressible flow. The inviscid flow is the main assumption of the adopted numerical methodology that will create inaccuracies on the results. The time domain model was able to address the requirements for a reasonably accurate calculation of the energy produced from the device. Hydrodynamic,

hydrostatic, PTO and mooring forces are all accounted. The availability of open-source codes (Nemoh and WEC-Sim) were making this choice easier. PTO and mooring forces have been simplified with a spring-damper and a spring respectively for optimisation reasons. However, more complexity could be included by utilisation of the WEC-Sim library of hydraulic and direct drive PTO and the use of a mooring lumped-mass system such as Moordyn [86].

The linear potential flow theory used in the numerical model does not consider the viscosity effect of the water. However, a drag force can be added during the simulation of the dynamic system. The main drawback of this method is that there are some uncertainties in the estimation of the drag coefficient. Previous research shows that the drag coefficient can be estimated in a reasonable way from literature or from experimental data. For example, in [13] the drag coefficient is estimated from literature for different WECs based on an estimated range of Keulegan-Carpenter numbers. This thesis has tried to obtain an experimental drag coefficient curve based on the Keulegan-Carpenter number. The benchmarking between the tank testing and the numerical results demonstrated a similar drag coefficient experimental curve with Sarpkaya work for cylinders [157]. Most of the drag coefficients obtained from the validation of the numerical model were between 0.5 and 1 giving an average around 0.7. Larger drag coefficients have been obtained for the lowest KC but these KC values are more rare because are generally related with lower period waves were the energy of the device is captured less.

One of the main limitations of the numerical methodology involved in the optimisation is probably the estimation of the drag coefficient that was based mainly on the tank testing benchmarking and on available literature. In fact, there is the assumption that the variation of the drag coefficient is reasonable independent of the float spacing, float reactor separation and float number. This assumption reduces significantly the simulation time because the theory can be simplified using a potential flow theory instead of for example using CFD. However, results of this optimisation will still be worthwhile because drag coefficients of the different floats for most of the KC numbers were in a similar range (See Figure 4.11).

Another area of uncertainty in the model is the amount of detail included in the representation of the PTO and mooring. In particular, PTO and mooring forces have been linearised to reduce the computational time and the complexity involved. Each PTO line model has a translational PTO that allows the application of a linear damping and a linear stiffness. However, a more realistic PTO should take in account the designed PTO system of the WaveSub device. Unfortunately, this was still not decided during the first stage of this

research project but later, an hydraulic PTO system was chosen. The PTO force of an hydraulic system was obtained using a Coulomb damping model in [13] to approximate the force given by the high and the low pressure accumulators. However, a linearised relationship between the PTO force and the line velocity could be obtained using a control system. The control system will give the required value of PTO force to obtain the optimal power produced from the device. As a result, the linearisation of the PTO will still give a good first approximation of the power produced. The simulation of the mooring system is another important component of a WEC especially in terms of reliability of the device. However, it is not expected that this will have a large influence on the power produced from the WaveSub device. High tensile forces are designed for the reactor component and this will consequently create a very steady structure. A taut mooring is foreseen for the WaveSub device and it could be reasonably linearised in the numerical model as demonstrated in the experimental curve of Figure 4.5. More complexity would be involved if MPS had chosen a catenary mooring design.

The numerical methodology used is sensible for the calculation of the energy produced from the device but it becomes less accurate when extreme sea state are considered [200]. Hydrodynamic forces based on a linear theory that can be used to evaluate reasonably the energy produced until moderate sea states if an appropriate drag force is also modelled. Nonlinear hydrodynamics and dynamics are expected to happen, for larger sea states. These sea conditions are necessary to simulate the survivability and to design the WEC. The extreme loading and dynamic response of the WEC are obtained as a result of this process [201] considering particularly the loads on the connection points and on the mooring lines. The numerical simulation of the WaveSub device under these extreme sea states was not part of this research project and it is left as a future work. A CFD model will be probably the most appropriate numerical model to simulate extreme events.

Finally, the optimisation involved different methods to investigate the optimal design parameters. A clear convergence to the optimum has not been achieved using the genetic algorithm but a sensitivity analysis approach helped to investigate further the space domain of the design variables. In-fact, the total number of simulations is limited to 100 due to practical limits on computer resources available. A similar sensitivity analysis approach has been used for optimisation purposes also in [194]. The genetic algorithm is used to refine the optimum found. Improvements to the genetic algorithm method has been investigated in this research but they should be understood more deeply, for example investigating more test functions. However, this was not the main purpose of this research and so the

time dedicated for this investigation has been limited to a reasonable satisfaction. An example of a further improvement of the genetic algorithm could be the coupling with a local optimisation method in the last part of the optimisation. In fact, local optimisation methods are generally much faster in the convergence to the optimum than global optimisation methods [195]. However, global optimisation methods are used if there could be more than one optimum.

The cost model is also limited to the experience of MPS and to literature related to wind farms. A sensitivity analysis of the key factors influencing the LCOE has been made demonstrating that the CAPEX and the interest rate have a large influence on the results. The main aim was, however, to compare different multi-float configurations and these costs are mostly independent from the design parameters; so there will be a similar conclusion of the optimal configuration. A significant part of the total cost is, in fact, related to the structure and PTO costs that is modular with the number of floats.

The main achievement of the optimisation has been to demonstrate that a multi-float configuration is better in terms of LCOE compared to a single one. A circular configuration is demonstrated to be more competitive compared to a linear, triangle and rectangular configurations. These results agree in some extent, for example with [65] where a linear configuration of a flap type device was found to be outperformed by a bowl or chevron configuration.

Another advantage of the multi-float configuration is that it is more reliable than a single one. In fact, the reliable factor for a multiple system is larger than a single one [202]. The reactor platform is more stable for a multi-float configuration due to the larger net buoyancy of the system. A multi-float configuration will also have less mooring components than a single one. So the probability that one of the mooring lines fails will be lower.

The optimisation was carried out in a specific site location for simplicity and because MPS indicated this location as the target of the optimisation. If a different location is chosen, it is expected a different design of the floats for an optimal performance of the device, especially if the energy matrix of the location is significantly different. The same optimisation methodology described in Section 5.3 could be still used with the only difference that there will be a different scatter matrix. However, the effect of the design of the float dependent on the location could be reduced using a different tuning of the PTO parameters for an optimal energy capture performance. It is expected that different sites will still have multi-float configurations outperforming a single float one because design parameters such as the float spacing can be optimised determining a positive WEC interaction factor [66]

while the total WEC farm cost will still favourite the multi-float configuration. As a result the LCOE will still be lower for multi-float configurations.

Chapter 8

Conclusions

The main aim of this thesis has been the investigation of an array layout of a multi-float configuration of the WaveSub device. Both the array layout and the multi-float configuration could have the potential to reduce the LCOE and therefore to increase the competitiveness of the device. An array of WECs has a reduced installation and grid connection costs compared to a single device because mainly of the shared infrastructure. A multi-float configuration of the WaveSub in the other hand, at the same level of total rated power of the WEC farm, has also lower costs related to the control system, to the mooring, to the OPEX and to the decommissioning because of the lower number of devices.
The work of this thesis has been related to a lower industrial phase (TRL 2-3) that investigates at a very low cost the multi-float configuration for a number of new layouts and new designs. The multi-float design concept requires a numerical model and to be validated against tank testing. Once there is confidence in the performance of the model, the optimisation of the design parameters is undertaken to estimate the further reduction of the LCOE.
The numerical and optimisation methodologies are of significant interest for the academia because they can be used for a large numbers of WEC types. The software used are open-source and so the access to them do not have economic issues and can be modified easily. The optimisation methodology uses a genetic algorithm that has been improved with various changes. These modifications demonstrated high performance of the algorithm to find the optimum of a test function. This same algorithm could be shared and used by several users. Finally, the results of the final optimisation chapters are the most important ones in a commercial sense because they could give important indications to MPS for the future development of the device in a multi-float configurations. In fact, they determined key de-

cisions for MPS regarding the choice of a multi-float configuration and of the layout of the floats. The optimal evaluation based on the LCOE is very critical for the company because both energy and cost determine the success of the device in the energy market.

8.1 Numerical model

The choice of the numerical model has been very critical for this thesis. For this reason a literature of available numerical models for WECs has been carefully investigated. The numerical model chosen accounts for a linear potential flow theory based on a Boundary Element Method (BEM) and for a time domain model for the simulation of the PTO, mooring and hydrodynamic bodies.
The BEM and dynamic system solver have been then compared with commercial codes (Wamit and WaveDyn). This comparison was reasonable and paved the way for the next assessment of the numerical model with the tank testing.
The fluid resistance generated by the device has been investigated first to understand the limitations of the numerical model. The drag force applied to the floats is obtained dependent on the square of the body velocity and on the drag coefficient. The characterization of the drag coefficient is very difficult to estimate due to the available literature that is limited only to simple regular body shapes and to bodies oscillating in a fluid at rest.
The visualization of the perturbed field has been an important tool to check the interaction between the WEC and the wave field. It was possible to visualize the perturbed wave field as well as the radiation and the scattered wave fields were possible to visualize. Time domain visualization of the WEC and of the perturbed wave field can give a realistic representation of the WEC under irregular and multi-directional waves. The visualization of the time domain perturbed wave field is something still not completely addressed in WEC-Sim and it was extended in this thesis. Then the total wave amplitude can be very useful to check the time averaged wave amplitudes along the domain.

8.2 Benchmarking

The benchmark between numerical model and tank testing of a 3 float WaveSub device was good especially in terms of mean total power with a relative difference of 10% for the different regular wave cases considered. A good characterisation of the drag coefficient was

very important for the accuracy of the estimation of the energy produced. The relationship between drag coefficient and KC number has shown a reasonable comparison with the Sarpkaya work for cylinders for the surge motion [157]. Tank testing heave motion relative to the multi-float configuration demonstrated a reduced heave motion probably because of mechanical friction of the central pulley system. An added damping force was added to the numerical model for the estimation of the mechanical friction.

8.3 Optimisation

After the accuracy of the numerical model through tank testing benchmarking was checked, the optimisation of multi-float configurations has been addressed. The optimisation was made in terms of number of floats, float spacing, float-reactor separation distance, stiffness and damping of the PTO.

The optimisation involved a novel optimisation approach that uses a genetic algorithm in combination with a Kriging surrogate model. Various improvements of an open source genetic algorithm [188] have been considered and investigated with application to a test function. Nemoh and WEC-Sim are used for the calculation of the energy produced from the device while a cost function is coupled together to obtain the LCOE. Then, a Taguchi and latin hypercube DOE are tested for sensitivity analysis purposes. Design parameters are investigated to understand their influence on the LCOE.

A number of floats between 1 and 6 is considered in the comparison. Larger number of float configurations were less feasible due to the more demanding simulation time required. A multi-float configuration demonstrated to have a lower LCOE compared to a single float configuration especially because of the reduction of the CAPEX for the same total rated power of the wave farm. This result is very important to answer the research problem of this thesis about the potentiality of a multi-float configuration in a commercial context. However the optimisation results showed that there is only a slight improvement in the minimum LCOE for configurations with a number of floats more than 3. Finally the 6 float configuration has been investigated with different layout concepts. The linear configuration has been compared with a rectangular, triangular and circular configurations. Three different float spacings are considered in the optimisation. Generally the lowest float spacing of each configuration outperformed the other ones. The stiffness and damping of the PTO were optimised determining reductions of the LCOE around 50%. The circular configuration demonstrated the most interesting application of a multi-float WaveSub because of its

lower LCOE and higher rated power generated.

8.4 Future work

Future work will be associated with improvements of Nemoh and WEC-Sim. The hydrodynamic coefficients of the WaveSub device have demonstrated some numerical errors especially for the thin cuboid shape of the reactor. This could be reduced using a dipole source method in the Nemoh code [148] but its implementation is not simple due to the complexity of the Nemoh code. Then hydrodynamic interactions in the WEC farm are still not accounted in the model because of the high computational cost. So, the numerical model should be updated to account the influence of the layout of the WECs on the productivity of the wave farm especially if the distance of the WECs is reduced. Then the PTO and the mooring need to be considered in more complexity. More specifically, the PTO will need to represent a more realistic hydraulic PTO while the mooring will be more realistic if for example slack events are accounted in the model. After that an extended validation of the numerical model against tank testing for different PTO settings and irregular waves will be necessary to represent the drag coefficient of the WaveSub device dependent on the KC number. Then the optimisation can be expanded to consider individual tuning per PTO line or per float to reach a larger overall system capture yield. Finally new multi-float design concepts can be still investigated to reach a competitive and optimised LCOE.

Appendices

Appendix A

The numerical-tank testing benchmark

The specification of the mass and displaced mass used in the simulation are given in the Table A.1. The inertia properties of the floaters and of the reactor were calculated related to their simplified geometry (A cylinder and 2 semi-sphere for the floater and a box for the reactor). In particular in this calculation the thickness of the simplified geometry of the floater was approximated to 2.5 mm to have the same mass as the tank testing model.
The floater and the reactor geometry features are shown in Table A.2. The height of the reactor was obtained from its simplified volume (Cuboid shape) equal to the real reactor physical volume characterized by the frame, ballasts and the PTO system. The float spacing and the float COG of the floaters in the simulation model was obtained as an average of the slight variations between the floaters in the testing set-up.
The location of the constraints related to the central floater is shown in Table A.3 with the convention of Figure A.1. The other constraint location are obtained by construction. In particular the reference system is set on the free surface above the COG of the reactor.
The stress-strain diagram of the different springs used during the tank testing are shown in Figure A.2 while the spring features are described in Table A.4. Constant spring coefficients have been used in the numerical model and these are reported in Table A.5. Finally Figure A.3 shows the relationship between the PTO line speed and the driving torque and Table A.6 the approximation of the mooring with a stiffness coefficient for each line.

Table A.1: Mass and displaced mass of the components of the WaveSub at the tank scale used in the numerical model.

	Mass (kg)	Displaced mass (kg)	Resultant (kg)
Float	6.8	92.3	256.5
Reactor frame	128.4	47.6	-80.8
Ballast tanks	2400	2400	0
Ballast	62.3	5.5	-56.8
PTO frame	150	55.6	-94.4
Sum	2747.5	2600.9	24.4

Table A.2: The floater and the reactor geometry characterization.

	Tank scale	Full scale
Float cylinder length (m)	0.19	4.75
Float diameter (m)	0.48	12
Reactor x dimension (m)	6.19	154.65
Reactor y dimension (m)	2	50
Reactor z dimension (m)	0.42	10.5
Reactor COG (m)	-1.81	-45.29
Float COG (m)	-0.42	-10.55
Float spacing COG (m)	1.56	39

Table A.3: The position of the constraint in the WEC-Sim model relative to the free surface.

	x (m)	y (m)	z (m)
T1	16.08	16.08	-42.87
TC	0	0	-16.55
F1	4.24	2.38	-14.79
FC	0	0	-42.87
R1	77.37	25	-42.87
M1	100	43.75	-75

Table A.4: Spring features of the multi-float configuration tested on July 2017.

	Target vertical load line (kg)	Spring free length (mm)	Spring length at static load (mm)	Line angle at static pos	Line tension (kg)	Static floater to reactor separation (mm)
Central spring	76.9	348 (x3)	985.4	90 (vertical)	76.9	812.4
Corner springs	2.14 (x4)	480	813.5	47.3	2.91	812.4

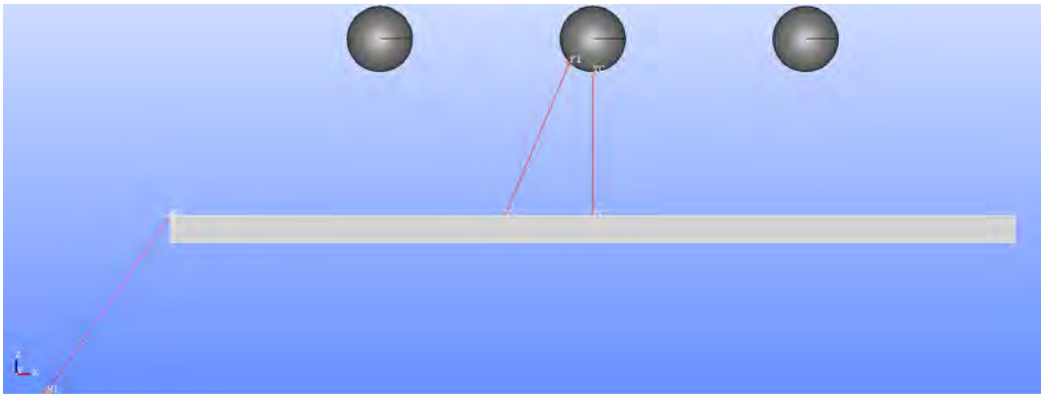

(a)

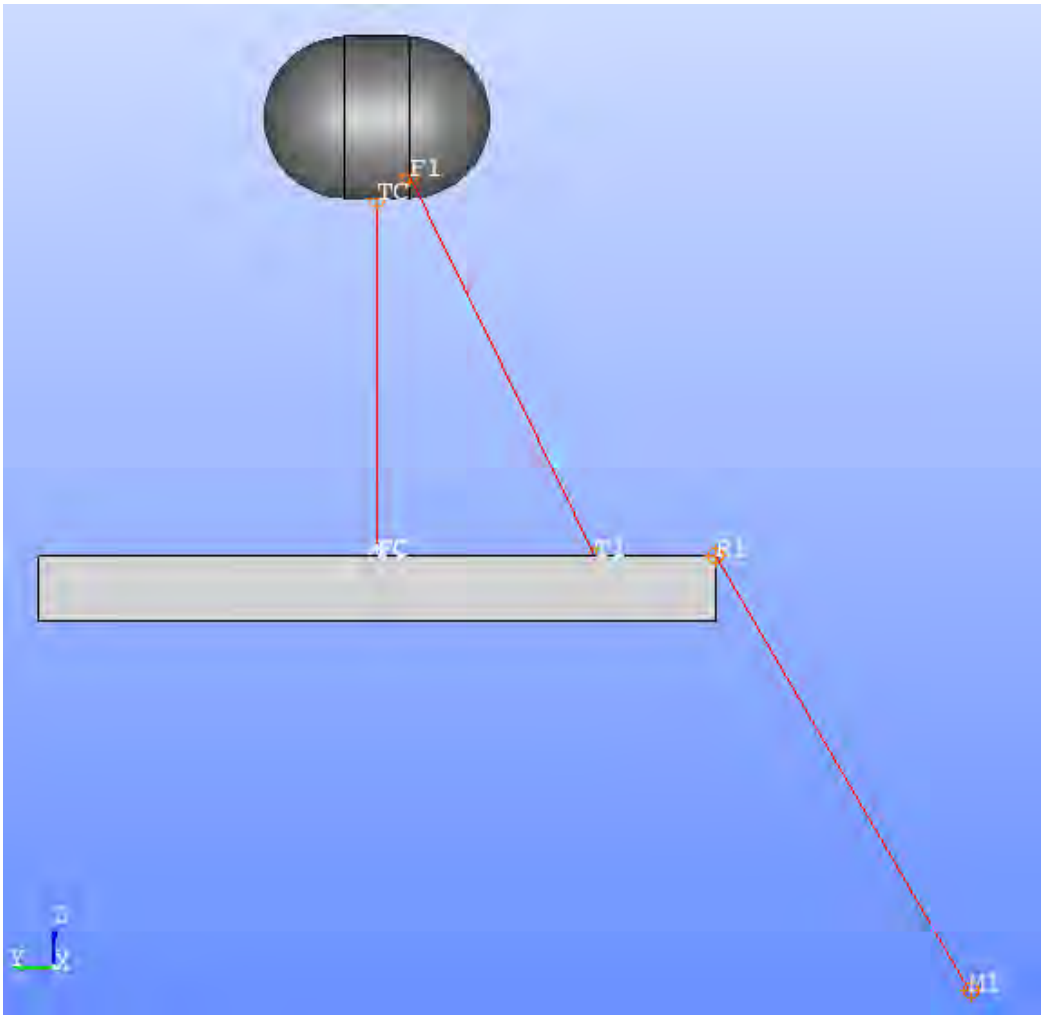

(b)

Figure A.1: Orthogonal projection of the WaveSub geometry on the xy plane (a) and on the plane yz (b) showing the design constraint.

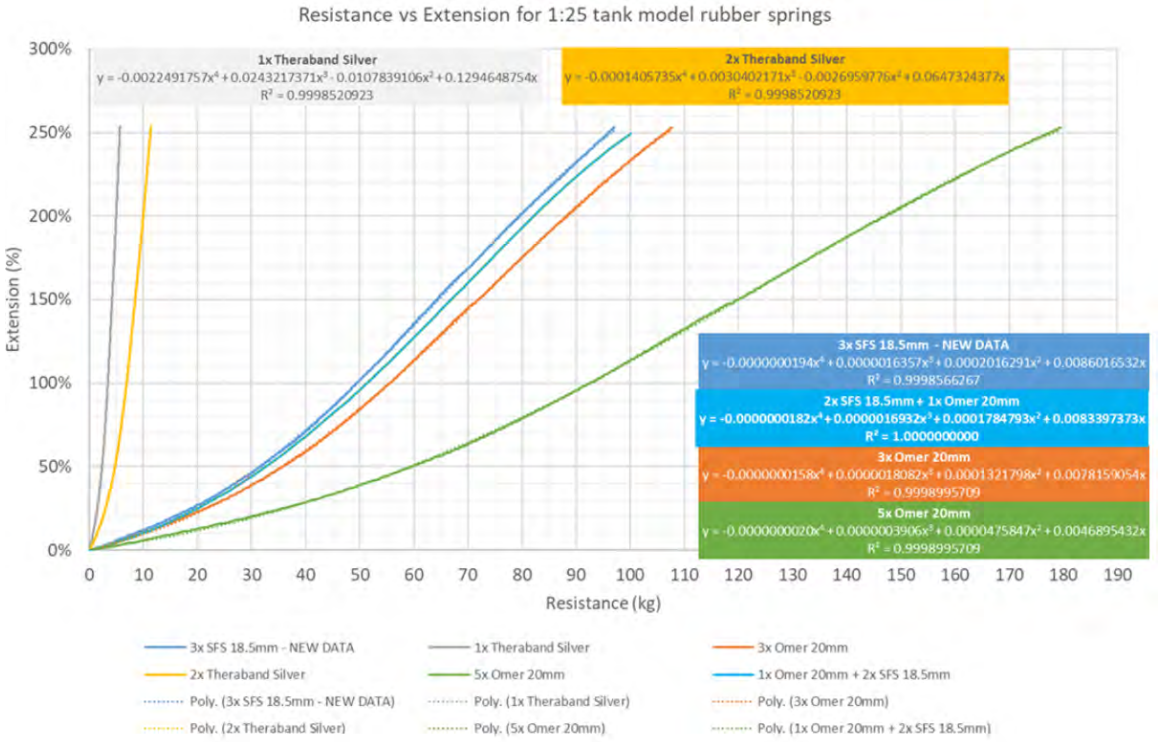

Figure A.2: The stress-strain diagram of different springs used in the tank testing.

Table A.5: The approximated stiffness used in the numerical model.

	Tank scale	Full scale
k (N/m) of 1x Theraband silver tube	52.11	32566.21
k (N/m) of 1x Omer 20mm band and 2x SFS 18.5mm band	937.60	586002.76

Table A.6: The mooring stiffness approximation used in the numerical model.

	Tank scale	Full scale
Rope free length 1 (m)	7.74	193.57
Rope free length 2 (m)	6.74	168.57
Rope free length 3 (m)	16.74	418.57
Rope free length 4 (m)	16.74	418.57
Stiffness 1 (kN/m)	7.75	4843.25
Stiffness 2 (kN/m)	8.90	5561.54
Stiffness 3 (kN/m)	3.58	2239.78
Stiffness 4 (kN/m)	3.58	2239.78

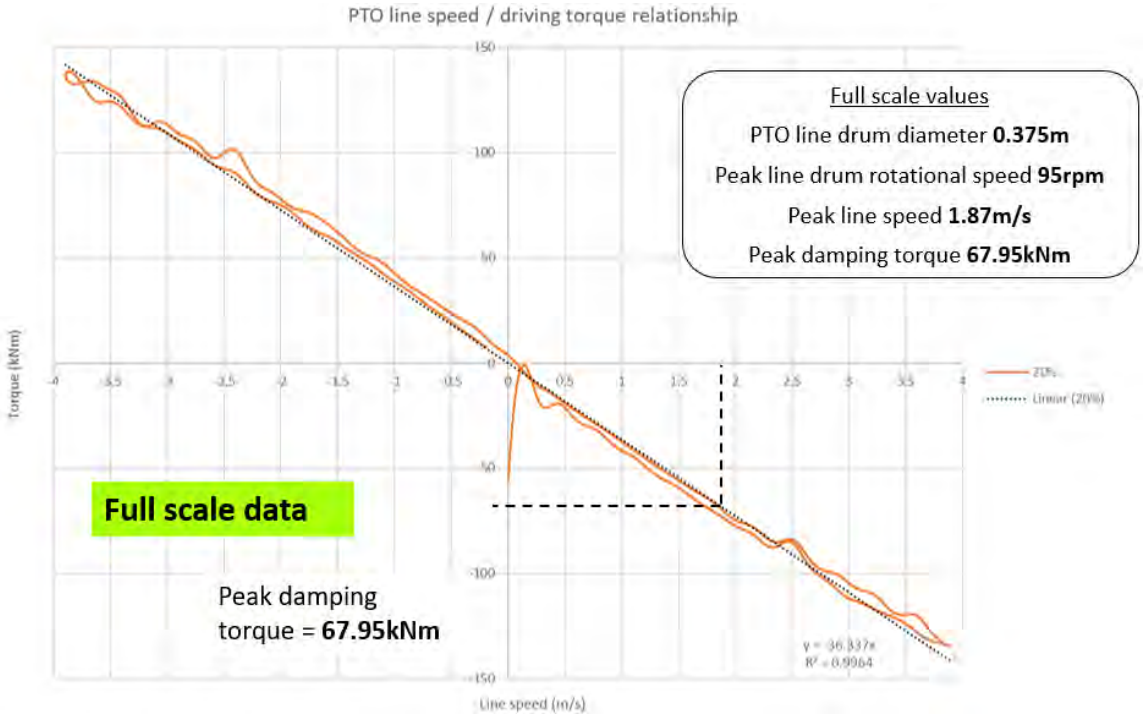

Figure A.3: The PTO line speed / driving torque relationship.

Bibliography

[1] Enerdata. Global Energy Statistical Yearbook 2019. [Accessed 1st August 2019]. [Online]. Available: https://yearbook.enerdata.net/world-electricity-production-map-graph-and-data.html

[2] Lewis A, Estefen S, Huckerby J, Musial W, Pontes T, Torres-Martinez J, "Ocean energy," *IPCC*, 2011.

[3] McCullen P, "Accessible wave energy resource atlas: Ireland: 2005," Marine Institute Sustainable Energy Ireland, Tech. Rep., 2005.

[4] Gunn K, Stock-Williams C, "Quantifying the global wave power resource," *Renewable Energy*, vol. 44, pp. 296–304, 2012.

[5] Yemm RW, Henderson RM, Taylor CAE, "The opd pelamis wec: Current status and onward programme," in *Proc. 4th European Wave Energy Conference, Alborg Denmark*, 2000.

[6] AQUARET. Wave. [Accessed 1st August 2019]. [Online]. Available: http://www.aquaret.com/images/stories/aquaret/pdf/chapter4.pdf

[7] Falcao AFO, "Modelling of wave energy conversion," *Instituto Superior Tecnico, Universidade Tecnica de Lisboa*, 2013.

[8] Cruz J, *Ocean wave energy: current status and future prespectives*. Springer Science & Business Media, 2007.

[9] Magagna D, Monfardini R, Uihlein A, "Jrc ocean energy status report 2016 edition," *Publications Office of the European Union: Luxembourg*, 2016.

[10] EMEC. Wave developers. [Accessed 1st August 2019]. [Online]. Available: http://www.emec.org.uk/marine-energy/wave-developers/

[11] Mankins JC, "Technology readiness levels," *White Paper*, vol. 6, no. 6, p. 1995, 1995.

[12] Folley M, "Numerical modelling of wave energy converters," *Elsevier*, 2016.

[13] Babarit A, Hals J, Muliawan MJ, Kurniawan A, Moan T, Krokstad J, "Numerical benchmarking study of a selection of wave energy converters," *Renewable Energy*, vol. 41, pp. 44–63, 2012.

[14] Hover F, Chin H, *Design of Electromechanical Robotic Systems*. MIT OpenCourseWare, 2009.

[15] PileBuck. Waves. [Accessed 1st August 2019]. [Online]. Available: http://www.pilebuck.com/highways-coastal-environment-second-edition/chapter-4-waves/

[16] ANSYS Aqwa, "Ansys aqwa theory manual," *Ansys, Canonsburg, Pa, USA*, 2013.

[17] Lee CH, *WAMIT theory manual*. Massachusetts Institute of Technology, Department of Ocean Engineering, 1995.

[18] Lee C, Newman JN, "Computation of wave effects using the panel method," *Numerical Models in Fluid Structure Interaction*, vol. 42, pp. 211–251, 2005.

[19] Faltinsen O, *Sea loads on ships and offshore structures*. Cambridge university press, 1993, vol. 1.

[20] Folley M, et al., "A review of numerical modelling of wave energy converter arrays," in *ASME 2012 31st International Conference on Ocean, Offshore and Arctic Engineering*. American Society of Mechanical Engineers, 2012, pp. 535–545.

[21] Newman JN, "Wave effects on multiple bodies," *Hydrodynamics in ship and ocean engineering*, vol. 3, pp. 3–26, 2001.

[22] Journee JMJ, Massie WW, *Offshore hydrodynamics First Edition*. Delft University of Technology, 2001.

[23] Chakrabarti SK, *Offshore structure modeling*. World Scientific, 1994, vol. 9.

[24] Cummins WE, "The impulse response function and ship motions," DTIC Document, Tech. Rep., 1962.

[25] Perez T, Fossen TI, "Time-vs. frequency-domain identification of parametric radiation force models for marine structures at zero speed," *Modeling, Identification and Control*, vol. 29, no. 1, pp. 1–19, 2008.

[26] Fenton JD, "Nonlinear wave theories," *the Sea*, vol. 9, no. 1, pp. 3–25, 1990.

[27] LHEEA Centrale Nantes. Nemoh website. [Accessed 1st August 2019]. [Online]. Available: https://lheea.ec-nantes.fr/logiciels-et-brevets/nemoh-presentation-192863.kjsp

[28] Wilson JF, *Dynamics of offshore structures*. John Wiley & Sons, 2003.

[29] Wikipedia. Navier Stokes equations. [Accessed 1st August 2019]. [Online]. Available: https://en.wikipedia.org/wiki/Navier%E2%80%93Stokes_equations#Compressible_flow

[30] Wolgamot HA, Fitzgerald CJ, "Nonlinear hydrodynamic and real fluid effects on wave energy converters," *Proceedings of the Institution of Mechanical Engineers, Part A: Journal of Power and Energy*, vol. 229, no. 7, pp. 772–794, 2015.

[31] Clement AH, "Dynamic nonlinear response of owc wave energy devices," *International Journal of Offshore and Polar Engineering*, vol. 7, no. 02, 1997.

[32] Koo W, Kim M-H, "Nonlinear time-domain simulation of a land-based oscillating water column," *Journal of waterway, port, coastal, and ocean engineering*, vol. 136, no. 5, pp. 276–285, 2010.

[33] Guerber E, Benoit M, Grilli ST, Buvat C, "A fully nonlinear implicit model for wave interactions with submerged structures in forced or free motion," *Engineering Analysis with Boundary Elements*, vol. 36, no. 7, pp. 1151–1163, 2012.

[34] Zhang Y, Zou Q-P, Greaves D, "Air–water two-phase flow modelling of hydrodynamic performance of an oscillating water column device," *Renewable Energy*, vol. 41, pp. 159–170, 2012.

[35] Luo Y, Nader J-R, Cooper P, Zhu S-P, "Nonlinear 2d analysis of the efficiency of fixed oscillating water column wave energy converters," *Renewable Energy*, vol. 64, pp. 255–265, 2014.

[36] Agamloh EB, Wallace AK, Von Jouanne A, "Application of fluid–structure interaction simulation of an ocean wave energy extraction device," *Renewable Energy*, vol. 33, no. 4, pp. 748–757, 2008.

[37] Palm J, Eskilsson C, Paredes GM, Bergdahl L, "Cfd simulation of a moored floating wave energy converter," in *Proceedings of the 10th European Wave and Tidal Energy Conference, Aalborg, Denmark*, vol. 25, 2013.

[38] Yu Y-H, Li Y, "Reynolds-averaged navier–stokes simulation of the heave performance of a two-body floating-point absorber wave energy system," *Computers & Fluids*, vol. 73, pp. 104–114, 2013.

[39] McNatt JC, Venugopal V, Forehand D, "The cylindrical wave field of wave energy converters," *International Journal of Marine Energy*, vol. 3, pp. e26–e39, 2013.

[40] Carbon Trust, "Accelerating marine energy," *Carbon Trust*, 2011.

[41] World-leading and trusted. Carbon trust. [Accessed 1st August 2019]. [Online]. Available: https://www.carbontrust.com/home/

[42] Catapult. The uk's leading technology innovation and research centre for offshore renewable energy. [Accessed 1st August 2019]. [Online]. Available: https://ore.catapult.org.uk/

[43] Carbon Trust, "Accelerating marine energy: The potential for cost reduction—insights from the carbon trust marine energy accelerator," *Carbon Trust: London, UK*, 2011.

[44] Pelamis Wave Power. Pelamis wave energy converter. [Accessed 13th December 2019]. [Online]. Available: https://en.wikipedia.org/wiki/Pelamis_Wave_Energy_Converter

[45] World Culture Pictorial. Pelamis wave farm. [Accessed 1st August 2019]. [Online]. Available: http://www.worldculturepictorial.com/blog/content/pelamis-portugal-world-first-most-ambitious-working-wave-farm-now-generating-electricity-1500-homes

[46] Seabased. 100mw contract ghana. [Accessed 1st August 2019]. [Online]. Available: https://www.seabased.com/100mwcontractghana

[47] WaveHub. Seabased completes 1st phase of 14-mw wave project in ghana. [Accessed 13th December 2019]. [Online]. Available: https://www.wavehub.co.uk/latest-news/seabased-completes-1st-phase-of-14-mw-wave-project-in-ghana

[48] Wikipedia. Wave farm. [Accessed 1st August 2019]. [Online]. Available: https://en.wikipedia.org/wiki/Wave_farm#cite_note-1

[49] WaveHub. Advancing offshore renewable energy. [Accessed 17th August 2019]. [Online]. Available: https://www.wavehub.co.uk/

[50] 40South Energy. Energia rinnovabile e ambiente. [Accessed 17th August 2019]. [Online]. Available: http://www.40southenergy.com

[51] Bombora Wave Power. Company announcements. [Accessed 17th August 2019]. [Online]. Available: https://www.bomborawave.com/our-media

[52] NEMOS. Nemos grows wave team. [Accessed 17th August 2019]. [Online]. Available: https://marineenergy.biz/2018/11/08/nemos-grows-wave-team/

[53] AMOG. Amog scouts for wave energy engineer. [Accessed 17th August 2019]. [Online]. Available: https://marineenergy.biz/2018/10/03/amog-scouts-for-wave-energy-engineer/

[54] Stratigaki V, et al., "Sea-state modification and heaving float interaction factors from physical modelling of arrays of wave energy converters," *Journal of Renewable and Sustainable Energy*, vol. 7, no. 6, p. 061705, 2015.

[55] Stratigaki V, et al., "Wave basin experiments with large wave energy converter arrays to study interactions between the converters and effects on other users in the sea and the coastal area," *Energies*, vol. 7, no. 2, pp. 701–734, 2014.

[56] Falnes J, Budal K, "Wave-power absorption by parallel rows of interacting oscillating bodies," *Applied Ocean Research*, vol. 4, no. 4, pp. 194–207, 1982.

[57] Giassi M, Göteman M, Thomas S, Engström J, Eriksson M, Isberg J, "Multi-parameter optimization of hybrid arrays of point absorber wave energy converters," in *12th European Wave and Tidal Energy Conference (EWTEC)*, 2017.

[58] De Andres AD, Guanche R, Meneses L, Vidal C, Losada IJ, "Factors that influence array layout on wave energy farms," *Ocean Engineering*, vol. 82, pp. 32–41, 2014.

[59] Mavrakos SA, Koumoutsakos P, "Hydrodynamic interaction among vertical axisymmetric bodies restrained in waves," *Applied Ocean Research*, vol. 9, no. 3, pp. 128–140, 1987.

[60] Mavrakos SA, "Hydrodynamic coefficients for groups of interacting vertical axisymmetric bodies," *Ocean Engineering*, vol. 18, no. 5, pp. 485–515, 1991.

[61] Mavrakos SA, McIver P, "Comparison of methods for computing hydrodynamic characteristics of arrays of wave power devices," *Applied Ocean Research*, vol. 19, no. 5-6, pp. 283–291, 1997.

[62] Sarkar D, Renzi E, Dias F, "Wave farm modelling of oscillating wave surge converters," *Proceedings of the Royal Society A: Mathematical, Physical and Engineering Sciences*, 2014.

[63] Zhang W, Liu H, Zhang X, Zhang L, Ashraf MA, "Optimal configurations of wave energy converter arrays with a floating body," *Polish Maritime Research*, vol. 23, pp. 71–77, 2016.

[64] Child BFM, "On the configuration of arrays of floating wave energy converters," *The University of Edinburgh*, 2011.

[65] Noad IF, Porter R, "Optimisation of arrays of flap-type oscillating wave surge converters," *Applied Ocean Research*, vol. 50, pp. 237–253, 2015.

[66] Budal K, "Theory for absorption of wave power by a system of interacting bodies," *Journal of Ship Research*, vol. 21, no. 4, 1977.

[67] Evans DV, "Some theoretical aspects of three-dimensional wave-energy absorbers," *First Symposium on Ocean Wave Energy Utilization*, 1979.

[68] McGuinness JP, Thomas G, "Hydrodynamic optimisation of small arrays of heaving point absorbers," *Journal of Ocean Engineering and Marine Energy*, vol. 2, no. 4, pp. 439–457, 2016.

[69] Child BFM, Venugopal V, "Modification of power characteristics in an array of floating wave energy devices," in *Proceedings of the 8th European Wave and Tidal Energy Conference, Uppsala, Sweden*, 2009, pp. 309–318.

[70] Goteman M, Engstrom J, Eriksson M, Isberg J, "Fast modeling of large wave energy farms using interaction distance cut-off," *Energies*, 2015.

[71] Goteman M, "Wave energy parks with point-absorbers of different dimensions," *Journal of Fluids and Structures*, vol. 74, pp. 142–157, 2017.

[72] Borgarino B, Babarit A, Ferrant P, "Impact of wave interactions effects on energy absorption in large arrays of wave energy converters," *Ocean Engineering*, vol. 41, pp. 79–88, 2012.

[73] Delhommeau G, "Seakeeping codes aquadyn and aquaplus," *19th WEGEMT School Numerical Simulation of Hydrodynamics: Ships and Offshore Structures*, 1993.

[74] Chakrabarti S, "Hybrid numerical method for wave–multibody interaction," *WIT Transactions on State-of-the-art in Science and Engineering*, vol. 18, 2005.

[75] McNatt JC. mwave. [Accessed 1st August 2019]. [Online]. Available: https://github.com/cmcnatt/mwave

[76] Sharp C, DuPont B, Bosma B, Lomonaco P, Batten B , "Array optimization of fixed oscillating water columns for active device control," in *Proceedings of the 12th European Wave and Tidal Energy Conference*, 2017.

[77] Stratigaki V, "Experimental study and numerical modelling of intra-array interactions and extra-array effects of wave energy converter arrays," Ph.D. dissertation, Ghent University, 2014.

[78] ITTC, "Ittc recommended guidelines: Wave energy converter model test experiments," in *27th International Towing Tank Conference*, 2014.

[79] ITTC, "Ittc recommended guidelines: Testing and extrapolation methods loads and responses, ocean engineering floating offshore platform experiments," in *24th International Towing Tank Conference*, 2005.

[80] Holmes B, *Tank testing of wave energy conversion systems: marine renewable energy guides*. European Marine Energy Centre, 2009.

[81] Holmes B, Nielsen K, "Guidelines for the development & testing of wave energy systems," *International Energy Agency Ocean Energy Systems*, 2010.

[82] Harris RE, Johanning L, Wolfram J, "Mooring systems for wave energy converters: A review of design issues and choices," *Marec2004*, 2004.

[83] Pecher A, Kofoed JP, *Handbook of ocean wave energy*. Springer London, 2017.

[84] Thies PR, "Advancing reliability information for wave energy converters," 2012.

[85] Uwihanganye B, Adenya CA, Ndiritu HM, "Review of numerical approach used in the optimization of mooring systems for floating structures." *International Journal of Engineering Technology and Scientific Innovation*, 2018.

[86] NREL. Moordyn. [Accessed 1st August 2019]. [Online]. Available: https://nwtc.nrel.gov/MoorDyn

[87] Davidson J, Ringwood JV, "Mathematical modelling of mooring systems for wave energy converters—a review," *Energies*, vol. 10, no. 5, p. 666, 2017.

[88] Martinelli L, Ruol P, Cortellazzo G, "On mooring design of wave energy converters: The seabreath application," *Coast. Eng. Proc*, vol. 1, no. 3, 2012.

[89] Payne G, "Guidance for the experimental tank testing of wave energy converters," *The University of Edinburgh: Newington, Edinburgh, UK*, 2008.

[90] University of Plymouth. COAST Laboratory. [Accessed 1st August 2019]. [Online]. Available: https://www.plymouth.ac.uk/research/institutes/marine-institute/coast-laboratory

[91] Cengel YA, Cimbala JM, "Fluid mechanics: Fundamentals and applications," *McGraw-Hill Education*, pp. 291–292, 2010.

[92] Qualisys. The swedish motion capture company. [Accessed 1st August 2019]. [Online]. Available: http://www.qualisys.com/

[93] Edinburgh Designs. Wave gauge. [Accessed 1st August 2019]. [Online]. Available: http://www.edesign.co.uk/product/wavegauges/

[94] Edesign. Wave generators. [Accessed 31st January 2020]. [Online]. Available: http://www4.edesign.co.uk/waves/some-wave-1/

[95] Edinburgh Designs. Flap wave generator. [Accessed 1st August 2019]. [Online]. Available: http://www.edesign.co.uk/product/ocean-flap-wave-generator/

[96] Edinburgh Designs. Wave generating software. [Accessed 1st August 2019]. [Online]. Available: http://www.edesign.co.uk/product/wave-generating-software/

[97] Baldini A, "A physical investigation into motion response and power performance of the wavesub wave energy converter to evaluate its annual energy yield at three different sites within the canary islands archipelago," Master thesis, Plymouth University, 2014.

[98] Short H, "An investigation into the geometric tuning capabilities of a novel wave energy converter under tank testing," Master thesis, Plymouth University, 2015.

[99] Torres DP, "Preliminary motion study of mps wavesub wec from regular waves and extreme sea states through physical modelling," Master thesis, Plymouth University, 2015.

[100] Paul L, "Investigating the effects that the new design of the wavesub has on its storm survivability," Master thesis, Plymouth University, 2016.

[101] Whitlam C, "Investigation of the effects that a new configuration of the wavesub wave energy convertor has on power output," Master thesis, Plymouth University, 2016.

[102] Howey B, "Tank testing investigation into the variable depth operation of a novel wave energy device," Master thesis, Plymouth University, 2015.

[103] SI Ocean, "Ocean energy: cost of energy and cost reduction opportunities," *Strategic Initiative for Ocean Energy (SI OCEAN) May*, 2013.

[104] Carbon Trust, "Cost estimation methodology," Carbon Trust, Tech. Rep., 2006.

[105] Fernandez-Chozas J, Kofoed JP, Jensen NEH, "User guide–coe calculation tool for wave energy converters," Department of Civil Engineering, Aalborg University, Tech. Rep., 2014.

[106] Neary V, et al., "Methodology for design and economic analysis of marine energy conversion (mec) technologies." Sandia National Lab.(SNL-NM), Albuquerque, NM (United States), Tech. Rep., 2014.

[107] Wikipedia. Net present value. [Accessed 1st August 2019]. [Online]. Available: https://en.wikipedia.org/wiki/Net_present_value

[108] Petrowiki. Key economic parameters. [Accessed 1st August 2019]. [Online]. Available: https://petrowiki.org/Key_economic_parameters_for_decision_making

[109] Wikipedia. Profitability index. [Accessed 1st August 2019]. [Online]. Available: https://en.wikipedia.org/wiki/Profitability_index

[110] Wikipedia. Contract for difference. [Accessed 17th August 2019]. [Online]. Available: https://en.wikipedia.org/wiki/Contract_for_difference#Invention

[111] DTOcean+. Providing advanced design tools for ocean energy systems. [Accessed 17th August 2019]. [Online]. Available: https://www.dtoceanplus.eu/

[112] MARINERG-i. Planning an integrated european research infrastructure. [Accessed 17th August 2019]. [Online]. Available: http://www.marinerg-i.eu/

[113] FORESEA. Project summary. [Accessed 17th August 2019]. [Online]. Available: http://www.nweurope.eu/projects/project-search/funding-ocean-renewable-energy-through-strategic-european-action/

[114] Wave Energy Scotland. Driving the development of wave energy technology in scotland. [Accessed 17th August 2019]. [Online]. Available: https://www.waveenergyscotland.co.uk/

[115] Badcock-Broe A, Flynn R, George S, Gruet R, Medic N , "Wave and tidal energy market deployment strategy for europe," *SI Ocean*, vol. 47, 2014.

[116] Ocean Energy Systems. Energy technology network. [Accessed 17th August 2019]. [Online]. Available: https://www.ocean-energy-systems.org/

[117] RES LEGAL Europe. Legal sourcs on renewable energy. [Accessed 17th August 2019]. [Online]. Available: http://www.res-legal.eu/search-by-country

[118] Boud R, "Uk wave energy resource," Carbon Trust, Tech. Rep., 2012.

[119] Marine Energy Wales. Wave energy cost reduction. [Accessed 1st August 2019]. [Online]. Available: https://www.marineenergywales.co.uk/wp-content/uploads/2018/05/ORE-Catapult-Tidal-Stream-and-Wave-Energy-Cost-Reduction-and-Ind-Benefit-FINAL-v03.02.pdf

[120] Debruyne Y, "User and theory manual: Free-surface visualisation tool," *Cruz Atcheson Consulting Engineering*, 2017.

[121] Adcock TAA, Taylor PH, "Estimating ocean wave directional spreading from an eulerian surface elevation time history," in *Proceedings of the Royal Society of London A: Mathematical, Physical and Engineering Sciences*. The Royal Society, 2009.

[122] Mitsuyasu H, Tasai F, Suhara T, Mizuno S, Ohkusu M, Honda T, Rikiishi K, "Observations of the directional spectrum of ocean wavesusing a cloverleaf buoy," *Journal of Physical Oceanography*, vol. 5, no. 4, pp. 750–760, 1975.

[123] Hasselmann K, et al., "Measurements of wind-wave growth and swell decay during the joint north sea wave project (jonswap)," *Ergänzungsheft 8-12*, 1973.

[124] Donelan MA, Hamilton J, Hui W, "Directional spectra of wind-generated ocean waves," *Philosophical Transactions of the Royal Society of London. Series A, Mathematical and Physical Sciences*, vol. 315, no. 1534, pp. 509–562, 1985.

[125] Banner ML, "Equilibrium spectra of wind waves," *Journal of Physical Oceanography*, vol. 20, no. 7, pp. 966–984, 1990.

[126] Ewans KC, "Observations of the directional spectrum of fetch-limited waves," *Journal of Physical Oceanography*, vol. 28, no. 3, pp. 495–512, 1998.

[127] Pierson WJ, Neumann G, James RW, "Practical methods for observing and forecasting ocean waves by means of wave spectra and statistics," Naval Oceanographic Office NSTL Station MS, Tech. Rep., 1971.

[128] Holthuijsen LH, *Waves in oceanic and coastal waters*. Cambridge university press, 2010.

[129] Marine Power Systems Ltd. WaveSub: The future of energy. [Accessed 1st August 2019]. [Online]. Available: http://marinepowersystems.co.uk/

[130] FaB Test. Fab test: A nursery site for marine renewable energy devices. [Accessed 1st August 2019]. [Online]. Available: http://www.fabtest.com/

[131] Codeaster. Salome-meca. [Accessed 1st August 2019]. [Online]. Available: http://www.code-aster.org/spip.php?article303

[132] Weywada PL, Debruyne Y, "Mesh quality and wec-sim guidance," *Cruzatcheson Consulting Engineers*, 2017.

[133] NREL, Sandia Corporation. Code structure. [Accessed 1st August 2019]. [Online]. Available: https://wec-sim.github.io/WEC-Sim/code_structure.html

[134] The HDF Group. HDF View. [Accessed 1st August 2019]. [Online]. Available: https://www.hdfgroup.org/downloads/hdfview/

[135] Cruz Atcheson. Cruz Atcheson Consulting Engineering. [Accessed 1st August 2019]. [Online]. Available: https://www.cruzatcheson.com/

[136] So R, Simmons A, Brekken T, Ruehl K, Michelen C, "Development of pto-sim: A power performance module for the open-source wave energy converter code wec-sim," in *ASME 2015 34th International Conference on Ocean, Offshore and Arctic Engineering*. American Society of Mechanical Engineers, 2015.

[137] Ruehl K, Michelen C, Kanner S, Lawson M, Yu YH, "Preliminary verification and validation of wec-sim, an open-source wave energy converter design tool," in *ASME 2014 33rd International Conference on Ocean, Offshore and Arctic Engineering*. American Society of Mechanical Engineers, 2014.

[138] Tom N, Lawson M, Yu YH, "Demonstration of the recent additions in modeling capabilities for the wec-sim wave energy converter design tool," in *ASME 2015 34th International Conference on Ocean, Offshore and Arctic Engineering*. American Society of Mechanical Engineers, 2015.

[139] Tom N, Lawson M, Yu YH, "Recent additions in the modeling capabilities of an open-source wave energy converter design tool," in *The Twenty-fifth International Offshore and Polar Engineering Conference*. International Society of Offshore and Polar Engineers, 2015.

[140] Combourieu A, et al., "Wec 3: Wave energy converter code comparison project," in *Proceedings of the 11th European Wave and Tidal Conference (EWTEC 2015). Nantes, France*, 2015.

[141] Lawson M, Yu YH, Ruehl K, Michelen C, "Development and demonstration of the wec-sim wave energy converter simulation tool," *Virginia Tech*, 2014.

[142] Lawson M, Yu YH, Nelessen A, Ruehl K, Michelen C , "Implementing nonlinear buoyancy and excitation forces in the wec-sim wave energy converter modeling tool," in *ASME 2014 33rd International Conference on Ocean, Offshore and Arctic Engineering*. American Society of Mechanical Engineers, 2014.

[143] Lawson M, Garzon BB, Wendt F, Yu YH, Michelen C, "Coer hydrodynamic modeling competition: Modeling the dynamic response of a floating body using the wec-sim and fast simulation tools," in *ASME 2015 34th International Conference on Ocean, Offshore and Arctic Engineering*. American Society of Mechanical Engineers, 2015.

[144] Yu YH, Li Y, Hallett K, Hotimsky C, "Design and analysis for a floating oscillating surge wave energy converter," in *ASME 2014 33rd International Conference on Ocean, Offshore and Arctic Engineering*. American Society of Mechanical Engineers, 2014.

[145] Lee CH, Newman JN, "Wamit user manual," *WAMIT, Inc*, 2006.

[146] Parisella G, Gourlay TP, "Comparison of open-source code nemoh with wamit for cargo ship motions in shallow water," in *Centre for Marine Science and Technology, Curtin University*, 2016.

[147] Penalba M, Kelly T, Ringwood JV, "Using nemoh for modelling wave energy converters: A comparative study with wamit," in *Proceedings of the 12th European Wave and Tidal Energy Conference (EWTEC2017), Cork, Ireland*, 2017, p. 631.

[148] Babarit A, Delhommeau G, "Theoretical and numerical aspects of the open source bem solver nemoh," in *11th European Wave and Tidal Energy Conference (EWTEC2015)*, 2015.

[149] LHEEA Centrale Nantes. Nemoh forum. [Accessed 1st August 2019]. [Online]. Available: http://130.66.47.2/redmine/boards/3/topics/635?r=647%23message-647

[150] Lunds Universitet, "Pressure and friction drag, lecture in hydromechanics," Lund University, Tech. Rep., 2017.

[151] Princeton University. Drag of blunt bodies and streamlined bodies. [Accessed 1st August 2019]. [Online]. Available: https://www.princeton.edu/~asmits/Bicycle_web/blunt.html

[152] Trytten DO, "Oscillating flow about yawed cylinders." Ph.D. dissertation, Monterey, California. Naval Postgraduate School, 1982.

[153] Sarpkaya T, "Vortex shedding and resistance in harmonic flow about smooth and rough circular cylinders at high reynolds numbers," Monterey, California. Naval Postgraduate School, Tech. Rep., 1976.

[154] Barltrop ND, Adams AJ, *Dynamics of fixed marine structures*. Butterworth-Heinemann, 2013, vol. 91.

[155] Sarpkaya T, *Wave forces on offshore structures*. Cambridge university press, 2010.

[156] Sarpkaya T, "Hydrodynamic forces on various multiple-tube riser configurations," in *Offshore Technology Conference*. Offshore Technology Conference, 1979.

[157] Sarpkaya T, "In-line and transverse forces on smooth and rough cylinders in oscillatory flow at high reynolds numbers," Monterey, California. Naval Postgraduate School, Tech. Rep., 1986.

[158] Reid V, "Biofouling simulation and analysis of the wave energy converter wavesub," Master's thesis, Exeter University, 2018.

[159] Keulegan GH, "Forces on cylinder and plates in an oscillating fluid," *J. Research of the National Bureau of Standards*, vol. 60, no. 5, pp. 423–440, 1958.

[160] Sarpkaya T, Shoaff RL, "A discrete-vortex analysis of flow about stationary and transversely oscillating circular cylinders," Monterey, California. Naval Postgraduate School, Tech. Rep., 1979.

[161] Sarpkaya T, Tuter O, "Periodic flow about bluff bodies. part 1: Forces on cylinders and spheres in a sinusoidally oscillating fluid," Monterey, California. Naval Postgraduate School, Tech. Rep., 1974.

[162] Mai TC, Wilms M, Hildebrandt A, Schlurmann T, "Comparison of drag and inertia coefficients for a circular cylinder in random waves derived from different methods," in *Proceedings of the Coastal Engineering Conference (2010)*. Reston: American Society of Civil Engineers, 2010.

[163] Bearman PW, Chaplin JR, "The loading on a cylinder in post-critical flow beneath periodic and random waves," *Sciences Engineering Medicine*, 1985.

[164] Bhinder MA, Babarit A, Gentaz L, Ferrant P, "Assessment of viscous damping via 3d-cfd modelling of a floating wave energy device," in *9th European Wave and Tidal Energy Conference*, 2011.

[165] Wikipedia. Airy wave theory. [Accessed 1st August 2019]. [Online]. Available: https://en.wikipedia.org/wiki/Airy_wave_theory

[166] WEC-Sim. Viscous Damping. [Accessed 1st August 2019]. [Online]. Available: https://wec-sim.github.io/WEC-Sim/theory.html#viscous-damping-and-morison-elements

[167] University of Cambridge. External flow and drag. [Accessed 1st August 2019]. [Online]. Available: http://www2.eng.cam.ac.uk/~mpj1001/learnfluidmechanics.org/LFM_blank_notes/handout_8_v3.pdf

[168] Faraggiana E, Masters I, Chapman J, Foster G, Stockman G, "Multi-directional waves and time domain perturbed field visualization of the wavesub device," *EWTEC 2019 Conference Proceedings*, 2019.

[169] Osgood B, "The fourier transform and its applications," *Lecture notes for EE*, vol. 261, p. 20, 2009.

[170] Ireland Ocean Energy Expertise. Atlantic marine energy test site (full scale). [Accessed 1st August 2019]. [Online]. Available: http://www.oceanenergyireland.ie/TestFacility/AMETS

[171] Tucker MJ, Pitt EG, *Waves in ocean engineering*. Sciences Engineering Medicine, 2001, no. Volume 5.

[172] Whitlam C, "The multi float wavesub wave energy convertor (wec)," in *IUK Project 132392*, 2017.

[173] Kitware Inc. Paraview. [Accessed 13th January 2020]. [Online]. Available: https://www.paraview.org/

[174] Faraggiana E, Whitlam C, Chapman J, Hillis A, Roesner J, Hann M, Greaves D, Yu YH, Ruehl K, Masters I, Foster G, Stockman G, "Computational modelling and experimental tank testing of the multi float wavesub under regular wave forcing," *Renewable Energy*, 2020.

[175] Maxon. Maxon EC 90 flat Ø90 mm, brushless, 90 Watt, with Hall sensors. [Accessed 1st August 2019]. [Online]. Available: https://www.maxonmotor.com/medias/sys_master/root/8825435389982/17-EN-271.pdf

[176] RLS. RM44 encoder-sensor base unit. [Accessed 1st August 2019]. [Online]. Available: https://www.rls.si/en/rm44-up-to-13-bit-encoder-base-unit

[177] Ohmite. Rheostats (Potentiometers) Wirewound. [Accessed 1st August 2019]. [Online]. Available: http://www.ohmite.com/cat/controls_rheostats.pdf

[178] TheraBand. Thera-Band Tubing 30m Silver (super Heavy). [Accessed 1st August 2019]. [Online]. Available: https://www.thera-bands.co.uk/thera-band-dispenser-boxes/104-thera-band-tubing-30m-tan.html

[179] NREL. OpenWarp. [Accessed 1st August 2019]. [Online]. Available: http://nrel.github.io/OpenWARP/

[180] Liros. Unlimited rope solutions. [Accessed 1st August 2019]. [Online]. Available: http://www.liros.com/en/products/productfinder/details/detail/liros-magic-speed.html

[181] Casey NF, Banfield SJ, "Factors affecting the measurement of axial stiffness of polyester deepwater mooring rope under sinusoidal loading," *InOffshore Technology Conference 2005 Jan 1. Offshore Technology Conference.*, 2005.

[182] Marine Power Systems Ltd, "Research of drag coefficients for the floater of the wavesub," Marine Power Systems Ltd, Tech. Rep., 2016.

[183] Faraggiana E, Chapman J, Williams AJ, Masters I, "Genetic based optimization of the design parameters for an array on device orbital motion wave energy converter," *Paper submitted to the Ocean Engineering Journal and currently under review*, 2020.

[184] Quoceant Ltd, "Power take-off: non-confidential summary report," Quoceant Ltd, Tech. Rep., 15 April 2016.

[185] Roy RK, *A primer on the Taguchi method*. Society of Manufacturing Engineers, 2010.

[186] Eberhart R, Kennedy J, "A new optimizer using particle swarm theory," in *Micro Machine and Human Science, 1995. MHS'95., Proceedings of the Sixth International Symposium on*. IEEE, 1995, pp. 39–43.

[187] Yarpiz. Particle swarm optimization. [Accessed 1st August 2019]. [Online]. Available: http://yarpiz.com/50/ypea102-particle-swarm-optimization

[188] Blasco X. Genetic algorithm. [Accessed 1st August 2019]. [Online]. Available: https://uk.mathworks.com/matlabcentral/fileexchange/39021-basic-genetic-algorithm

[189] MATLAB. parfor function. [Accessed 1st August 2019]. [Online]. Available: https://www.mathworks.com/help/parallel-computing/parfor.html;jsessionid=663e0ead6e3c90409fe51a99883a

[190] Faraggiana E, Masters I, Chapman J, "Design of an optimization scheme for the wavesub array," *RENEW 2019 Conference Proceedings*, 2018.

[191] Mahmoodabadi MJ, Nemati AR, "A novel adaptive genetic algorithm for global optimization of mathematical test functions and real-world problems," *Engineering Science and Technology, an International Journal*, vol. 19, no. 4, pp. 2002–2021, 2016.

[192] Couckuyt I, Dhaene T, Demeester P, "oodace toolbox: a flexible object-oriented kriging implementation," *The Journal of Machine Learning Research*, vol. 15, no. 1, pp. 3183–3186, 2014.

[193] Iooss B, Lemaitre P, "A review on global sensitivity analysis methods," in *Uncertainty management in simulation-optimization of complex systems*. Springer, 2015, pp. 101–122.

[194] Gonzalez-Gorbena E, Qassim RY, Rosman PC, "Multi-dimensional optimisation of tidal energy converters array layouts considering geometric, economic and environmental constraints," *Renewable energy*, vol. 116, pp. 647–658, 2018.

[195] Cavazzuti M, *Optimization methods: from theory to design scientific and technological aspects in mechanics*. Springer Science & Business Media, 2012.

[196] MATLAB. Orthogonal array MATLAB. [Accessed 1st August 2019]. [Online]. Available: https://uk.mathworks.com/matlabcentral/fileexchange/47218-orthogonal-array

[197] Leung YW, Wang Y, "An orthogonal genetic algorithm with quantization for global numerical optimization," *IEEE Transactions on Evolutionary computation*, vol. 5, no. 1, pp. 41–53, 2001.

[198] MATLAB. xcorr function. [Accessed 1st August 2019]. [Online]. Available: https://uk.mathworks.com/help/matlab/ref/xcorr.html

[199] James R, Ros MC, "Floating offshore wind: market and technology review," *Carbon Trust: UK*, p. 168, 2015.

[200] Penalba RM, Giorgi G, Ringwood J, "A review of non-linear approaches for wave energy converter modelling," in *Proceedings of the 11th European Wave and Tidal Energy Conference*. European Wave and Tidal Energy Conference 2015, 2015.

[201] Coe RG and Neary VS, "Review of methods for modeling wave energy converter survival in extreme sea states," 2014.

[202] Song S, Coit DW, Feng Q, Peng H, "Reliability analysis for multi-component systems subject to multiple dependent competing failure processes," *IEEE Transactions on Reliability*, vol. 63, no. 1, pp. 331–345, 2014.